Mineralogy, geochemistry and origin of the Neoproterozoic Xaudum iron-formation in Botswana

A thesis submitted to the Faculty of Science, Rhodes University, South Africa, in fulfilment of the requirements for the degree of Master of Science in Geology

Author: Mawande Ntantiso

Supervisors: Professor Hari Tsikos (RU)

Dr Peter Horvath (WITS)

DECLARATION

All work in this thesis is the original work of the author, except where specific acknowledgement is made to the work of others.

SIGNED

_____

JANUARY 2020
RHODES UNIVERSITY
GRAHAMSTOWN – SOUTH AFRICA

The LORD is my shepherd; I shall not want.

2 He maketh me to lie down in green pastures: he leadeth me beside the still waters.

3 He restoreth my soul: he leadeth me in the paths of righteousness for his name's sake.

4 Yea, though I walk through the valley of the shadow of death, I will fear no evil: for thou art with me; thy rod and thy staff they comfort me.

5 Thou preparest a table before me in the presence of mine enemies: thou anointest my head with oil; my cup runneth over.

6 Surely goodness and mercy shall follow me all the days of my life: and I will dwell in the house of the LORD for ever.

Psalm 23 KJV

Acknowledgements

Being involved in this project has been a truly life-changing experience in many aspects of my life. I am a better person from when I began this journey, and this would not have been possible without the support and guidance that I received from several people.

First and foremost, I would like to gratefully acknowledge CIMERA and ASSMANG for generously funding me to undertake this MSc project. None of this would be possible without your generous funds.

I would like to offer a massive thank you to my supervisor Professor Hari Tsikos. I am not the first and not the last student that you touched with your generous and caring heart, but the attention and guidance you offered made me feel like I was your only student. Thank you for believing in me and choosing me as a custodian of this wonderful project. Your supervision has gone beyond the academic sphere. Your constructive criticism has built my confidence in science and in writing, I know that I am nowhere near being a good writer, but I know that I am better than what I was before we embarked on this journey. Our lengthy discussions on science equipped me with knowledge that made it possible for me to complete this journey. If it were possible, I would continue writing praises the size of this thesis for the huge impact that you played in my life however this platform does not permit. The former South African president Nelson Mandela once said, “If you talk to a man in a language he understands, that goes to his head. If you talk to him in his language, that goes to his heart.” By those few words I would like to say:

Σας ευχαριστώ για όλα όσα έχετε κάνει για μένα καθηγητή.

Many thanks also to Dr. Peter Horvarth for assisting me with the petrographic and mineralogy of this project and Dr. Alistair Jeffcoate for his time and support in Botswana and for all the useful resources he provided.

I am also grateful for the brotherhood that we shared in the Rhodes University Postgraduate Research in Iron-Manganese Ore Resources (PRIMOR). This space allowed the fruitful sharing of ideas, information and resources amongst each other for the betterment of scientific research. Dr. Xolane Mhlanga, thank you for not being tired of assisting me with this project, Donald Motilaodi thanks for being a friend indeed in tough times. I would also like to thank the Rhodes University technicians, Andile Pikoli and Thulani Royi for their wonderful work in the labs.

Everyone in my family has played an integral role in this journey, without their prayers, support and love God knows where I would be right now. I would like to thank my grandmother Eunice “Mamtolo” Lexie Ntantiso, my dad Zamikaya Alex “Ta-Zet” Ntantiso and my aunt Thobeka “Dabs” Tshiki and my brother Wandile Ntantiso for emotionally supporting me. You are my heroes. Tata thank you, for being the most wonderful dad anyone can ask for, thank you for everything you have done in my life. I love you and God bless you. I would also like to thank my go to person when I feel overwhelmed by everything. Dr. Rachael Magwaza thank you for being a wonderful partner, friend and so much more. Thank you for pushing me to greater heights, for believing in me and showing me that nothing is impossible. You are candle in a dark room. I love you “Munxuza”.

Saving the best for last, without God I would not even exist. Thank you, God, for this wonderful planet and the people that inhabit it. You have said it all in Psalm 23 and I am a living testimony to that.

Key words: Snowball Earth Hypothesis, Paleoproterozoic, Neoproterozoic, Neoproterozoic iron-formation (NIF), Xaudum iron-formation (XIF), Manganese, Cobalt, Redox state, detrital input, oxygen levels.

ABSTRACT

Banded iron-formations (BIF) formed in three different geological periods in the Earth's history, namely the Archean, Paleoproterozoic and Neoproterozoic. Each of these periods has a corresponding index BIF type attributed to them. The oldest is the Archean Algoma-type BIF which is typically dominated by smaller-volume BIF deposits associated with volcanic rocks and greenstone belts. The next is the volumetrically far more abundant Superior-type BIF of the Paleoproterozoic lacking any obvious volcanic relation. The youngest BIFs were deposited after a hiatus of a billion years in the Neoproterozoic and are believed to be genetically linked to Marinoan ice-age. The global re-introduction and distribution of BIF in the Neoproterozoic highlights a shift in the Earth's tectonics, climate, biosphere and ocean chemistry from the older Archean and Paleoproterozoic counterparts. Various models have been postulated by researchers in attempts to explain how Neoproterozoic iron-formations formed. In all the available models, the Snowball Earth Hypothesis initially proposed by Kirshvink (1992) is an overarching concept.

In this study, four cores from the Neoproterozoic Xaudum iron-formation (XIF) in Ngamiland, northwest of Botswana, were sampled and analysed following a partnership between Postgraduate Research in Iron and Manganese Ore Resources (PRIMOR) and Tsodilo Resources Ltd. The study sets out to explore the mineralogy and chemistry of XIF in order to determine its origin, constrain the redox conditions in the paleo-basin, assess it in the context of other Neoproterozoic iron-formations and older Archean and Paleoproterozoic iron-formations, and inform metallurgical processing. The mineralogy of XIF consists of magnetite, quartz, amphibole, garnet, biotite and chlorite in decreasing abundance. This mineral assemblage is characteristic of medium grade metamorphosed iron-formations. Algoma and Superior-type BIFs which experienced late-diagenetic and very low-grade metamorphism have a complex mineral assemblage consisting of hematite, magnetite, quartz, and several carbonate (dolomite-ankerite series and siderite) and silicate phases (greenalite, riebeckite and stilpnomelane). The geochemical results show that XIF has higher Mn_3O_4 and Al_2O_3 average contents when compared to Algoma and Superior type BIF. The detrital components in XIF correlate with High Field Strength Elements (HFSE) suggesting increased delivery of siliciclastic material during deposition. This trend is comparable to other NIF deposits suggesting a global high input of siliciclastic material into Neoproterozoic

paleodepositional environments. This trend is different from Archean and Paleoproterozoic BIF deposits which are close to pure chemical sediments lacking measurable detrital contributions.

In the XIF, bulk-rock Mn_3O_4 and Al_2O_3 in drillcore SW have higher averages of 2.4 and 2.6 wt. % respectively, compared to the other three cores. The Mn_3O_4 shows a positive statistical relationship with Co, suggesting that Neoproterozoic oceans and atmosphere were possibly more oxic than in the Archean and Paleoproterozoic. The Mn_3O_4 shows an antithetic relationship with Fe_2O_3 suggesting that the paleobasin was chemically heterogeneous in terms of redox conditions, with Fe_2O_3 depositing presumably in deeper parts removed from a detrital source, and Mn_3O_4 depositing possibly more proximal to a paleo-shoreline in a shallower setting where there was higher delivery of siliciclastic material from the continent due to correspondingly higher Al_2O_3 and TiO_2 contents.

The REE patterns of XIF show positive-sloping trends of depletion in LREE and enrichment in HREE which resemble those of seawater. However, the REE slope becomes a lot flatter and resembles closer the signature of PAAS and adjacent diamictite facies, which agrees with the idea of high siliciclastic input in the paleobasin comparable to other NIF. XIF also appears to lack clear Ce or Eu anomalies. The lack of the former points to the oceans possibly not being oxic enough to drive the fractionation of Ce into Mn oxides like in the modern oceans, or that the Ce behaviour is obscured by the high siliciclastic input in XIF. Similarly, the lack of positive Eu anomaly shows a weak to absent hydrothermal signal into to modern shallow seawater where Fe and Si were sourced, or detritally derived REE contamination. Extensive weathering under hot and humid climate during glacial retreat is shown by the low K_2O/Al_2O_3 ratios and high CIA values ranging from 80-99. Re-glaciation signifies the return of cold and arid and it is represented by high K_2O/Al_2O_3 ratios and low CIA values ranging from 64-78.

The previous genetic models of NIF by Klein (1993), Baldwin *et al*. (2012) and Lechte and Wallace (2015) provide an essential foundation for the development of a XIF genetic model. The genetic model of XIF proposes deposition on an open continental shelf characterized by a steady influx of detrital material. The seawater has been anoxic since the Paleoproterozoic and further induced by basin stagnation due to the ice covering the basin. Two overlapping oxidative stages are assumed for the precipitation of Fe and Mn across lateral redox gradients in the paleobasin. The exact oxidative pathways and mechanisms for the above processes remains unconstrained.

TABLE OF CONTENTS

TABE OF FIGURES

LIST OF TABLES

1. INTRODUCTION AND GEOLOGICAL SETTING

1.1 Background

Banded iron formation (BIF) is the principal and most important commercial source of iron ore, accounting for greater than 60% of iron reserves globally (Nadoll *et al.,* 2014; Trendall, 2011). BIF is of particular interest because it is one of the oldest known sedimentary rock types with a very specific time distribution confined to the Precambrian. Therefore, studying BIF provides insights into geological and broader paleoenvironmental processes during early Earth history. BIF consists of successive layers (from mm to cm-scale) of iron oxides (magnetite Fe_3O_4 and/or hematite Fe_2O_3) alternating with bands primarily composed of chert and lesser Fe-rich minerals. These rocks typically have iron content greater than 15wt%, and thicknesses commonly of up to hundreds of meters (James, 1954).

The time when BIF formed can be subdivided into three geological periods in Earth's history, namely the Archean, the Paleoproterozoic and lastly the Neoproterozoic. Each of these geological time intervals has a corresponding "index" BIF type attributed to them. The Archean is dominated by *Algoma*-type BIF which is generally smaller in volume by comparison to its younger counterparts and is typically associated with volcanic rocks in greenstone belts, pointing to a likely submarine exhalative origin (James, 1983). The second type is the *Superior*-type BIF which is the most abundant type by volume and lateral extent of BIF sediment deposited. *Superior*-type BIFs are deposited in stable continental shelf basins and lack volcanic relation (James, 1954; Trendall, 2011). Lastly is the glacially associated, *Rapitan*-type BIF deposited in the Neoproterozoic (James, 1983; Bekker *et al*., 2010).

1.1.1 Archean BIF

Many mid-Archean (3.5-3.0 Ga) occurrences of BIF generally lack strict classification due to their structural and metamorphic complexity. The greatest preserved deposits of this time are those in the Guyana Shield of Venezuela and its West African correlatives in Liberia, Sierra Leone and Ivory Coast (James, 1983). The precise age of the mid-Archean Venezuelan BIF deposits remains undetermined due to the superimposed metamorphism, but they are estimated to be in the range of 3.0-2.5 Ga (James, 1983). Dating correlative Liberian BIF using Rb-Sr and Pb-Pb dating methods have provided an age bracket between 2.97 and 2.75 Ga (James, 1983)

Most parts of the world experienced extensive cratonisation in the late Archean (2.9-2.5 Ga), characterized by extensive volcanism, igneous intrusions into thin crust, and sedimentary processes influenced by a volcanogenic component. Krapez (1997) explains cratonisation in the late Archean as a result of a four-stage tectonic evolution where the terrane suffered (1)

initial intracontinental rifting linked to mantle plumes followed by (2) continental break up with intrabasinal plumes. The continent later underwent rapid drifting with plume breakout (3); and dispersal continued until maximum rifting was achieved (4). Algoma-type BIF was deposited as a result of intrabasinal magmatic and hydrothermal activity in greenstone belt basins (Barley, 1997). Algoma-type BIF are widely distributed on every continent, with classic examples seen in greenstone belts of South Africa, Canada, Australia, and Brazil. It should be noted that not all Archean-age BIFs fall into the Algoma-type category, such as the BIF in the 3.1-2.7 Ga Witwatersrand Supergroup of South Africa (Klein, 2005).

1.1.2 Paleoproterozoic BIF

The period from the late Archean to the early Paleoproterozoic (2.6-2.2Ga) was a time of great iron sedimentation in the Earth's history (James, 1983). During this period, giant Superior-type BIF were deposited in several stable continental shelves around the world, including two of the largest BIF of the Transvaal (South Africa), Hamersley (Australia), Minas Gerais (Brazil), Lake Superior (U.S.A) and Krivoy Rog-Kursk (Ukrainian shield) (James, 1983; Beukes and Gutzmer, 2008; Bekker *et al*., 2010; Trendall, 2011). A period of evolution in ocean-atmosphere redox conditions leading up to an oxic state around 2.4 Ga, forms the background for the deposition of the Paleoproterozoic BIF listed above (Bekker *et al.*, 2010). This shift to oxic conditions is known as the Great Oxygenation Event (GOE) and continues to constitute a topic of intensive research (Canfield *et al*., 2013). Post GOE Paleoproterozoic BIF is seen mainly in North America (Biwabik, Gunflint), whereas the Mesoproterozoic (1.6-1.0 Ga) contains some BIF in the Bushmanland Group of South Africa and the Penganga Group of India (Beukes and Gutzmer, 2008), although these BIF are smaller-scale deposits widely interpreted to be of a direct sedimentary-exhalative origin.

1.1.3 Neoproterozoic BIF

The Neoproterozoic (1.0 Ga to 0.54 Ga) was a great transition period in the Earth's tectonic activity, climate, biosphere and ocean chemistry. This change is highlighted by the 1-billion-year hiatus in the sedimentary record, where BIF reappeared in the Neoproterozoic era for a third depositional period (Klein, 2005; Cox *et al.,* 2013). Contrary to Archean-Paleoproterozoic BIF, which were deposited at a time of low atmospheric pO_2 and prevalent anoxic deep oceans (Bekker, 2004; Canfield 2005), Neoproterozoic iron-formation (NIF), formed at a time when pO_2 is expected to have been comparatively higher (Holland, 2006; Frei *et al*., 2009; Cox *et al*., 2013).

NIF is different from Archean-Paleoproterozoic BIF in several respects. Archean and Paleoproterozoic BIF appear to have a wider spatial distribution than NIFs (Ilyin, 2009; Basta *et al*., 2011; Xu *et al*., 2014). The latter generally lack or has poorly developed banding, and when banding is present, it commonly comprises hematite (Fe_2O_3) and jaspilite (iron-rich chert) layers (Cox *et al.,* 2013). A significant contrast between Archean/Paleoproterozoic BIF and NIF is in terms of iron mineralogy. In unmetamorphosed NIF, iron occurs almost exclusively as hematite. Magnetite (Fe_3O_4) is also present, but not as the principal iron-bearing phase, except for metamorphosed occurrences (Freitas *et al*., 2011; Cox *et al.,* 2013). By contrast, Archaean and Paleoproterozoic BIFs are characterized by much more varied iron mineralogy that comprises several iron carbonates (ankerite, siderite) and iron silicate minerals (greenalite, minnesotaite) and is also dominated by magnetite relative to hematite.

Rapitan-type BIF (after the homonymous locality in Canada) is associated with widespread Neoproterozoic glacial events. Geochronologic constraints and stratigraphic correlations suggest that the Sturtian and Marinoan glaciations are temporally associated to most NIFs, whilst only a few are associated with mafic volcanism and thus show a more volcanogenic affinity (Kendall *et al*., 2009; Bekker *et al.,* 2010). These glacial events marked the return of widespread basin anoxia and a shift from euxinic to ferruginous oceanic basins, which relates to tectonic and extreme climate changes in the Cryogenian stratigraphy (Cox *et al*., 2015). Numerous data and geological evidence presented have led researchers to postulate that NIF deposition occurred in a completely frozen Earth known as Snowball Earth (Ilyin, 2009; Cox *et al.*, 2013)

Regions that host NIF are characterised by various metamorphic grades, primary rock features and stratigraphic configurations (Ilyin, 2009). However, all regions have two important shared features, namely:

1. Stratigraphic sections comprising one or two glaciogenic formations i.e. tillites and diamictites associated with the NIF (Ilyin, 2009)
2. A laterally extensive, thick dolomite sequence, termed *cap dolomite* in the literature (Hoffman *et al*., 1997), developing above the upper (youngest) glacial formation corresponding to the last phase of glaciation.

Best-documented NIFs are the Rapitan type deposit of northwest Canada (Klein and Beukes, 1993; Young, 2002), Adelaide Geosyncline of Australia, Jacadigo Group of South America

and the Damara Group of Namibia (Table.1 and Fig.1) (Freitas *et al*., 2011). Below are more comprehensive accounts to these classic NIF occurrences.

Chuos iron-formation (Namibia)

The Chuos iron-formation is abundantly located in northwest Namibia with a few localities also found in central and southeast Namibia (Hoffmann and Prave, 1996). The Chuos iron-formation-bearing sequence consists of lithologies of highly variable thickness and type across different structural zones within the Damara Orogen (Breitkopf, 1988; Cox *et al.*, 2013). The lithology comprises glacial diamictite, schist, quartzite and dolomite of variable thicknesses, and thick siliceous iron-formation rich in both hematite and magnetite (Breitkopf, 1988). The high lithological variability is attributed to the glacial influence of the Chuos and its deposition during rifting on the southern margin of the Congo craton at 0.75-0.65 Ga (Cox *et al.*, 2013). Breitkopf (1998), distinguished two types of iron-formation in the Chuos sequence, namely diamictite-associated iron-formation and amphibole-associated iron-formation. Chemically, the diamictite-associated iron-formation reflects low manganese and low aluminium values, whereas the amphibole-associated iron-formation contains low manganese, and high phosphorus and aluminium oxide contents (Breitkopf, 1988). In the past, the Chuos iron-formation has been tentatively correlated to the manganese-bearing iron-formation at Otjosondu (Bühn *et al.*, 1995).

Braemar iron-formation (Australia)

The Braemar iron-formation is part of the Umbertana Group in the eastern part of the Adelaide Geosyncline which hosts glaciomarine sequences of Sturtian age, calcareous and manganiferous siltstone, and dolomites (Lottermoser and Ashley, 2000). The Braemar iron-formation was metamorphosed to upper greenschist facies (Lottermoser and Ashley, 2000). It has a complex mineral assemblage consisting of magnetite and hematite as chief iron oxides, biotite, muscovite, quartz, carbonate, minor chlorite, plagioclase and apatite (Cox *et al.*, 2013). The chemical composition of the Braemar iron-formation shows low manganese content and moderate aluminium abundance (Lottermoser and Ashley, 2000).

Jacadigo iron-formation

The Jacadigo Group is located in southwestern Brazil and hosts the famous NIF in South America and its depositional age is poorly constrained (Klein and Ladeira, 2004; Freitas *et al.*, 2011). Like the Chuos iron-formation in Namibia, the Jacadigo Group was deposited in a rift system that developed on the boundary between the Rio Apa block and the south-east margin of the Amazon craton (Cox *et al.*, 2013). The Jacadigo Group is subdivided into the basal

Urucum Formation and the upper Santa Cruz Formation. The basal Urucum Formation consists of different carbonate-cemented siliclastic deposits such as sandstone, black shale and glacial diamictite. The Santa Cruz Formation is predominantly made up of iron-formation, ferruginous sandstone and manganese-rich lithologies (Klein and Ladeira, 2004). The manganese horizons within the Santa Cruz Formation contain complex silicate-oxide assemblages consisting of braunite, cryptomelane, pyrolusite, and aegirine (Klein and Ladeira, 2004). The iron-formation itself consists almost entirely of hematite and chert with variable stratigraphic thickness over 100 meters (Klein and Ladeira, 2004). Compositionally, the iron-formation chemistry here has low aluminium and manganese contents.

Rapitan iron-formation

The Rapitan Group in northwest Canada hosts the famous Neoproterozoic syn-glacial iron-formation also known as Rapitan iron-formation. The Rapitan iron-formation is estimated to have formed formed between 0.75-0.71 Ga, and its deposition was greatly influenced by multiple N-NE trending faults active for the duration of glaciation (Klein and Beukes, 1993; MacDondald *et al*., 2010a). This resulted in the iron-formation having variable lateral thickness and multiple unconformities (Armstrong *et* al., 1982; Cox *et al.*, 2013). Mineralogically, the Rapitan iron-formation consists almost entirely of hematite and chert (Klein and Beukes, 1993). Development of the Rapitan Group is closely attributed to rifting during the breakup of Rodinia. This resulted in the Rapitan diamictites being temporally linked to volcanic rocks (Mount Harper Volcanic Complex and Pleasant Creek Volcanics) (Cox *et al.*, 2013).

Against the background of the NIFs described in the above paragraphs – which have been comprehensively studied and reported in the literature – lies a relatively recent discovery of a NIF in northern Botswana. This magnetite-rich iron-formation is known as the Xaudum iron-formation (XIF), named after the Xaudum River that runs through Ngamiland region in the North-West District of Botswana and covers an area of more than 36 km (Fig.1.1). For this study, XIF will be used to refer to the iron formation in this study, and NIF will refer to general Neoproterozoic iron formations. The XIF is hosted in a sequence which signifies a Neoproterozoic rift basin-fill sequence, characterised by stratigraphic pinch-outs along basement highs and abrupt facies change. Manifestations of the XIF deposit are found in several horizons sandwiched within two discrete diamictite units above and below the XIF. The sequence also contains various types of intrusive rocks and was folded and metamorphosed to amphibolite facies with local kyanite development during the Damara and Luffilian orogenic events (Singletary *et al.*, 2003)

Table 1.1: Classification of global NIF based on mineralogy and facies association. The facies associations include glacially influenced (Rapitan-type), mafic volcanic-associated and hybrid deposits. The deposits host varying iron mineralogy and occasional manganese association. Compiled after Buhn *et al.*1982; Baldwin, 2014; Basta *et al.* 2011; Breitkopf, 1988; Cox *et al.* 2013; Feng *et al*. 2016; Frimmel, 2011; Klein and Beukes, 1993; Klein and Ladeira, 2004; Lottermoser and Ashley, 2000; Tang *et al*. 1987; Zhang *et al*. 2011.

LOCATION	LITHOFACIES ASSOCIATION	IRON MINERALOGY
Canada (Rapitan Gp)	Dropstones, exotic clasts & till pellets	Hematite
Australia (Umbertana Gp)	Diamictites lonestone horizons	Hematite, magnetite (+Mn)
Namibia (Chuos Fm)	Striated clasts, dropstones, diamictites & volcanic detritus	Hematite, magnetite (+Mn)
Namibia (Numees Gp)	Poorly stratified diamictites & dropstones	Hematite
Brazil (Jacadigo Gp)	Diamictites and dropstones	Hematite (+Mn)
Egypt (Wadi Karim & Um Anab Fm)	Wackes, tuffs, lapilli, subordinate volcanic flows (basalts, andesites, dacites)	Hematite, magnetite
China (Fulu Fm)	Altered basalts, tuffs, tuffaceous arkoses and massive diamictites	Hematite

Figure 1.1: XIF location and global distribution of NIF. Red star denotes study area, Xaudum iron-formation, Botswana. (1) Tindir Formation (Alaska, United States); (2) Rapitan Group (Canada); (3) Kingston Peak Formation (California, United States); (4) Jacadigo Group (Brazil); (5)Yerbal Group (Argentina); (6) Yara Group (Togo); (7) Menhouhou Group (Morocco); (8) Central Eastern Desert (Egypt); (9) Chuos Group (Namibia); (10) Damara orogen (Namibia) ;(11) Jazir deposit (Oman); (12) Yamata deposit (Russia); (13) Erzin basin (Mongolia); (14) Buren manifestation (Russia); (15) Malyi Khingan Formation (Russia); (16) Yangtze Platform (China); (17) Yudnamutana Group (Australia); (18) Adelaide Geosyncline and (Australia).Modified from (Ilyin, 2009).

1.2 Neoproterozoic Snowball Earth

1.2.1 Background

The global resurgence of glacial-associated NIF after an interval of a billion years sparked great interest among iron-formation researchers for a long time. During this time, there already had been ongoing research on Neoproterozoic glacial deposits which commenced in the late 1800s. Notable pioneer research is the work of Thomson (1871, 1877) who interpreted the Port of Askaig Tillite in Scotland as the first Neoproterozoic glaciogenic formation. Subsequently, more discoveries of Neoproterozoic glacial formations were observed in Australia (Woodward 1884), Norway (Reusch 1891) and Svalbard (Garwood & Gregory 1898). The research took a hiatus until paleomagnetic data produced in a series of publications from 1942-1964 suggested that glacial deposits with cap carbonates were equatorially aligned in the Neoproterozoic (Irving, 1956; Harland and Rudwick 1964). Between 1965-1981, globally distributed Neoproterozoic syn-glacial iron and manganese formations were recognized and incorporated into Neoproterozoic glacial deposit research for the first time (Ziegler 1960; Martin 1965a; Walde et al. 1981; Whitten 1970). Iron and manganese ores were essential tools for post-World War II reconstruction, and as a result, glacial associated NIF and manganese mineralization from Brazil, Canada, Namibia and Australia received great attention.

During the same period, hot research topics relating to paleomagnetism, plate tectonic movement and global distribution of glacial deposits and cap carbonates were greatly debated by scientists in various fields. This transdisciplinary research produced climatic models based on simple energy balance calculations and the geochemical cycle of carbon that proved global glaciation was possible in the Neoproterozoic (Walker *et al.,* 1981; North, 1990; Hoffman, 2011). From this period onwards, new developments were made regarding NIF and associated glacial deposits (Hoffman, 2011). Developments included expanding knowledge on the use of carbon isotopes as correlation tool, glaciomarine processes and causative theories for low paleolatitude glaciation. One interesting finding came from the Elatina Formation in South Australia (Hoffman, 2011). This formation is made up of reddish sandstone, 10m thick repetitive layers of siltstone and a diamictite (Embleton and Williams, 1986; Hoffman, 2011). The siltstone laminae were extensively studied for its palaeomagnetic signals and provided reliable results which proved glaciation at low paleolatitudes during the Neoproterozoic (Embleton and Williams, 1986; Raub and Evan, 2006).

1.2.2 Evidence for Neoproterozoic Snowball Earth

Several geological and geochemical features serve as key pieces of evidence to the popular Neoproterozoic Snowball Earth model proposed (Evans, 2000). Presented below are these multiple lines of evidence.

1. **Iron-formations**

Ice-covered oceans could have allowed accumulation of dissolved iron through a progressively more reduced hydrosphere (Basta *et al.,* 2011; Young, 2002). Hydrosphere reduction could have been a consequence of diminished riverine sulphate delivery to the oceans due to glaciation, producing a change from the anhydrite-magnetite redox buffer of hydrothermal fluids and resulting in a higher Fe/S ratio in the fluids (Kump and Seyfried, 2005). Scouring of the continental interior by widespread glaciation could thus have delivered sediments with a high Fe/S ratio. Furthermore, lower sea levels globally could have depressurised mid-ocean ridges inducing higher Fe/S ratio in hydrothermal fluids (Kump and Seyfried, 2005). Deposition of BIF could have occurred following re-oxygenation of the hydrosphere as the ice cover melted and revived ocean circulations that mixed deep, anoxic waters with oxic surface waters (Kirschvink, 1992; Basta *et al.,* 2011; Basta *et al.*, 2011).

2. **Glacial deposits**

The omnipresent occurrence of glacial deposits such as diamictites containing abundant dropstones as well as faceted and striated clasts, are indicative of glacial transport in Neoproterozoic successions and constitute the hallmark of the environment of formation of NIF (see also Table 1). Carbon isotope chemostratigraphic evidence suggests that these glacial deposits correspond to the Sturtian and Marinoan glaciations were broadly synchronous globally (Halverson, 2005; Hoffman, 2005). This is further supported by paleomagnetic data from various regions that show the equatorial alignment of glacial marine successions from the two glacial events (Evans, 2000). Glacial marine deposits in various regions are associated with thick, shallow-water carbonate successions (Hoffman, 2005). Such successions favourably deposit in warmest parts of the surface ocean due to reverse carbonate solubility (Broecker and Peng, 1982). The paleomagnetic data for these carbonates reveals a normal meridional climate gradient (warmest at the equatorial region) while glacial invasion resulted in an abrupt temperature decline in the warmest places (Hoffman, 2005).

3. Cap carbonates and their isotope signature

The carbonate sequences that directly overlie the Neoproterozoic glacial deposits without hiatus or subglacial unconformity are known as *cap carbonates* (Hoffman and Schrag, 2002; Hoffman, 2005). These cap carbonates contain unusual sedimentary structures (interpreted as large ripples by Allen and Hoffman (2005)) and are interpreted to have been deposited on continental margins and inland seas (Hoffman, 2005). Unlike widespread Neoproterozoic glaciers, regional glaciers have poorly developed or absent cap carbonates, suggesting that cap carbonate deposition is a result of a significant change in ocean chemistry in the Neoproterozoic (Hoffman, 2005). These postglacial cap carbonates are widely associated with negative excursions in $\delta^{13}C$ (-5‰), indicating a strong perturbation in the Earth's carbon cycle (Kaufman, Knoll and Narbonne, 1997; Hoffman and Schrag, 2002; Hoffman, 2005, 2011).

The formation mechanism of cap carbonates and their associated negative carbon excursions has been widely debated. As a result, several authors have proposed various models to account for these phenomena. An early explanation by Kaufman *et al*. (1993) proposed that Neoproterozoic cap carbonates with negative $\delta^{13}C$ isotope values were a result of stratification of the ocean where organic carbon low in $\delta^{13}C$ accumulated in sediments below anoxic deep-water during glaciation. Post-glaciation induced upwelling resulted in the delivery of anoxic deep water depleted in isotopically heavy carbon and high alkalinity to shallow water, and subsequent precipitation of cap carbonates. In the Snowball Earth Hypothesis (explained later), Hoffman *et al*. (1998) suggested that Neoproterozoic cap carbonates recording a $\delta^{13}C$ value of -5‰ were a result of a prolonged marine ecosystem shut down due to the complete coverage of the ocean surface with ice. Subsequently enhanced silicate weathering which sequestered atmospheric CO_2 (120 000 ppm) delivered excess alkalinity to the oceans and precipitated as cap carbonates during deglaciation. An alternative explanation by Kennedy *et al*. (2001) proposed that cap carbonate deposits are associated with the destabilization of methane hydrates trapped in low altitude terrestrial permafrost, due to rapid postglacial warming and flooding of widely exposed continental shelves and interior basins.

Following the multiple sources of evidence advocating for the Snowball Earth, the next step was to establish how NIF and associated glacial deposits formed. Several models have been proposed. One of the first proposed and arguably most prevailing model is the Snowball Earth Hypothesis, proposed by Kirshvink (1992) and later modified by works of Hoffman, Schrag and Kaufman, incorporating information from Proterozoic geology, oceanic modelling and

chemostratigraphy respectively (Hoffman *et al.*, 1998; Myrow and Kaufman, 1999; Hoffman and Schrag, 2002). Subsequently, other models that contradict and/or are exclusive to Snowball Earth Hypothesis, have also been proposed.

1.2.3. Snowball Earth Hypothesis

The two most severe glaciations in Earth's history, namely the Sturtian (0.71 Ga) and Marinoan glaciations which ended at approximately 0.63 Ga, were responsible for the so-called Snowball Earth event (Hoffman, 2005). The onset of these glaciation events is believed to be a product of equatorial continental distribution during the Neoproterozoic (Hoffman and Schrag, 2002). Consequently, this led to a significantly higher subtropical albedo that provided a cooling mechanism for ice accumulation (Kirschvink, 1992). The gradual increase in glaciation provided positive feedback which meant substantial albedo increase and decreasing sea levels, exposing inland seas and continental shelves (Kirschvink, 1992). Furthermore, the high precipitation and weathering in tropical continents resulted in sequestration of atmospheric carbon dioxide (CO_2) by silicate breakdown, additionally cooling the Earth (Kirschvink, 1992). Early energy-balance climate models (Fig. 1.2) predicted that if half of the Earth was glaciated, there would be overpowering albedo feedback leading to a drastic decline in surface temperatures and tropical glaciation. The energy-balance models by Caldeira and Kasting (1992) and Ikeda and Tajika (1999) use an albedo of 0.6 for ice cover and modern-day meridional heat transport. Snowball Earth event is indicated by digits 1-7 in both diagrams (Fig. 1.2): Part (A) shows three stable climate states represented as solid lines, namely ice-free, partly ice-covered, and ice-covered. A move from point (1) to (2), which shifted the state to a lower altitude, was instigated by a decline in energy absorption by greenhouse gases such as pCO_2 or other solar flux reducing factors. Albedo effect promoted a discontinuity and the system moved to an ice-covered state (3) with mean temperatures of -50° (B). This state had minimum energy and mass transfer between atmosphere and hydrosphere, reduced hydrological cycle and stagnant chemical weathering. Accumulation of volcanic-derived gases over a period of 3-30 million years leading to gradual warming and hydrological cycle intensification was achieved in this state. The gradually warming atmosphere drove the system to jump from (4) to (5) due to albedo reversal leading to deglaciation and formation of cap carbonates. Enhanced silicate weathering removed excess CO_2 and was released into oceans as alkalinity, forming cap carbonates (Hyde *et al.*, 2000; Hoffman and Schrag, 2002). 6) Subsequently, the system shifts to the original state (7).

Part (B) shows temperature changes through the Snowball Earth event. The approximate 5Ma period is conservative for an albedo of 0.6, based on the predicted outgassing flux of CO_2 and subsidence analysis (Hoffman *et al*., 1998b). The amount of CO_2 required to thaw the snowball Earth was estimated to be 350 times of today's atmospheric CO_2 levels (approximately 14% of the atmosphere) (Crowley *et al*., 2001). Through the function of microbes converting organic CO_2 confined beneath the ice to gas and volcanoes emitting CO_2 and CH_4 over a period of 3 to 30 million years, there was enough gas to initiate glacial retreat (Pierrehumbert, 2005). Deglaciation was reinforced by the release of methane hydrates that were trapped by low latitude permafrost, translating to stronger positive feedback for warming (Kennedy, Mrofka and Von Der Borch, 2008). During this period, substantial amounts of glaciers on continents released glacial deposits which weathered and eroded the continents. The resulting nutrient-rich sediments were transported to the sea and, together with the rising CO_2 levels, were conducive to cyanobacterial population blooms responsible for rapid oxygenation of the hydrosphere and atmosphere (Kirschvink, 1992; Hoffman and Schrag, 2002).

1.2.3 Alternative models

Slush-ball Earth

The Slush-ball is a counter-premise to Snowball Earth hypothesis based on a model by Hyde *et al.* (2000), which does not completely disregard the Snowball Earth Hypothesis but seeks to modify its 'irregular' ideas. This model argues that the Earth was not entirely frozen during extreme glaciation as per Snowball Earth Hypothesis; it rather postulates that floating ice masses covered around 60% of the Earth, leaving the equatorial regions open to safeguard eukaryote survival (Hyde *et al.*, 2000; Fairchild and Kennedy, 2007). A Slush-ball Earth would have been initiated and terminated by moderate fluctuations in greenhouse gases and, unlike with the Snowball Earth, global surface temperatures would have equilibrated around 0° rather than -50° (Fairchild and Kennedy, 2007). Active weathering and erosion in equatorial continents would have facilitated nutrient supply to open equatorial oceans and coastlines (Lewis, Weaver and Eby, 2007). An active hydrological cycle would have permitted upwelling acting as effective nutrient transport agent (Link and Christie-Blick, 2011). All these conditions would have ensured the survival of multicellular organisms (Hyde *et al.*, 2000).

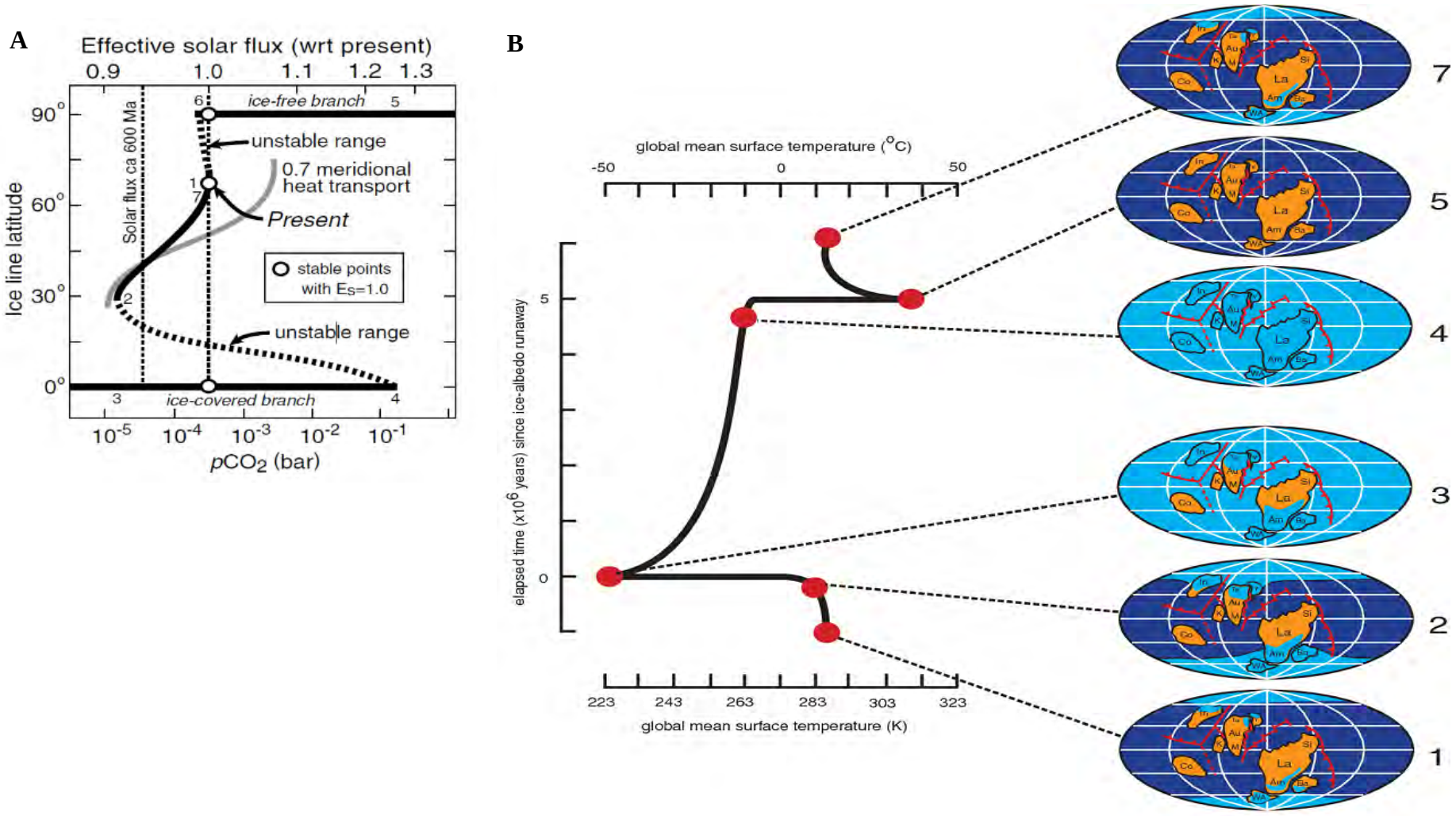

Figure 1.2: (A) Variations in Earth state predicted by the Snowball Earth model (Hoffman & Schrag 2002) derived from energy-balance models by Caldeira and Kasting (1992) and Ikeda and Tajika (1999) and using an albedo of 0.6 for ice cover and modern-day meridional heat transport. Snowball Earth event is indicated by digits 1-7 in both diagrams. (B) Shows temperature changes through Snowball Earth event. The approximated 5-million-year period is conservative for an albedo of 0.6, based on the predicted outgassing flux of CO2 and subsidence analysis (Hoffman et al., 1998b)

Zipper Rift

Zipper Rift is a mutually-exclusive model postulating that deposition of iron-formation in the Neoproterozoic occurred in inland seas as a result of two episodes of continental rifting (Eyles and Januszczak, 2004). The first rifting phase occurred on the supercontinent Rodinia, resulting in the proto-Pacific Ocean. The second rifting phase separated the continent Baltica from Laurentia forming the proto-Atlantic, and coincided with the Neoproterozoic glaciation periods (Eyles and Januszczak, 2004). Eyles and Januszczak (2004) suggest that these inland seas are subject to different conditions and complex chemistries. High evaporation rates allow the Fe(II) ions to concentrate, and during a periodic absence of water circulation the bottom water would become anoxic. The iron-formation would be deposited following susbsidence of the inland sea.

1.3 Regional geology

The geology of Botswana provides a holistic insight into the geological dynamics of the Precambrian crust of southern Africa. The crust experienced a tectonic evolution that produced a system of Proterozoic orogenic belts surrounding and disconnecting older Archean nuclei (Fig. 1.1) (Singletary *et al.*, 2003). Precambrian basement rocks in Botswana that are located in the central Kalahari Desert are virtually obscured by Carboniferous to Jurassic Karoo lithologies and are overlain by vast Cenozoic sediments of the Kalahari Group (Singletary *et al.*, 2003). The sediments provide a challenge to understanding the tectonic evolution and distribution of the underlying basement lithologies of Botswana. This challenge is solved through inference from geophysical applications and correlation with adjacent geology through geochronology and stratigraphy (Singletary *et al.*, 2003). This section will explore the geology of Botswana starting from regional considerations to local scale geology.

1.3.1 Archean cratonic terranes

The basement geology of Botswana is made up of Archean cratonic rocks. A portion of the Zimbabwean Craton occupies the eastern part of Botswana, rocks of the Congo Craton occupy the

northwest portion, and the Kaapvaal Craton occurs in the southeast part of Botswana and stretches to neighbouring South Africa (Key and Ayres, 2000; Haddon, 2005a). Archean Kaapvaal lithostratigraphy is classified according to older cratonic domains consisting mostly of tonalitic and trondhjemitic gneissic granitoids (TTG), metamorphosed mafic volcanics forming greenstone belts, as well as late to post-orogeny associated mafic-ultramafic volcanic, plutonic and sedimentary rocks metamorphosed to greenschist facies (Carney *et* al., 1994;Poujol *et al.*, 2003; Singletary *et al.*, 2003; Haddon, 2005b). Such sequences comprise the following, listed in approximate order of decreasing age: 1. Kraaipan Greenstone Belt, 2. Kanye Volcanic Formation, 3. Gaborone Granite, and 4. Lobatse Volcanic Suite (Carney *et* al., 1994).

1. The Kraaipan Greenstone (3.2 Ga) occurs as a narrow and elongated belt with an NNW-strike that extends from southeast Botswana to South Africa that overlies Archean basement granite (3.2 Ga) (Key and Ayres, 1994; Poujol *et al.,* 2003). The Kraaipan Greenstone Belt consists of mafic volcanic rocks interlayered with thick BIF and ferruginous chert and is surrounded by TTG, granitoids and adamellites (Ramatoroko *et al.,* 2016; Ranganai *et al*., 2017).

2. The Kanye Volcanic Formation is made up of alkali porphyritic rhyolites and felsite deposits that are extensively distributed in the southeast of Botswana (Carney, Aldiss and Lock, 1994; Haddon, 2005). The precise age of the Kanye Volcanic Formation remains enigmatic, however, dating studies by Anhaeusser and Walraven (1999) provide a bracketing age of 2.78 Ga (see below).

3. The Gaborone Granite Complex covers an area of some 14 000 km^2 in southeast Botswana where it intruded a portion of the Kanye Formation. It is thus surrounded by the Kanye Formation on a regional scale, including some areas in the North-West Province, South Africa (Carney, Aldiss and Lock, 1994; Franchi and Mapeo, 2019). The Gaborone Granite has a concentric structure comprising the Thamanga Granite at the centre and the Ntlhantlhe Microgranite at the margins of the structure (Franchi and Mapeo, 2019). The transitional zone from the central porphyritic alkali feldspar and rapakivi Thamanga Granite to the marginal Ntlhantlhe Granite is known as the Kgale Granite (Mapeo *et al.*, 2004; Franchi and Mapeo, 2019). The Thamanga and Kgale granites are thought to be

contemporaneous and are therefore treated as a single unit termed the Gaborone Granite which is dated to be 2.78 Ga (Anhaeusser and Walraven, 1999). A younger unit of the Gaborone Granite called the Mmathethe pluton is situated south of Gaborone Granite (Carney, Aldiss and Lock, 1994; Franchi and Mapeo, 2019)

4. The Lobatse Volcanic Group is exposed at the southwest of Botswana and is also known as the Ventersdorp Supergroup due to its wide distribution in South Africa (Table. 1) (Van der Westhuizen, De Bruiyn and Meintjes, 1991; Carney, Aldiss and Lock, 1994). In Botswana, the older Klipriviersberg Group is eroded and only the Platberg and Pniel Groups exist (Carney, Aldiss and Lock, 1994). The remaining Platberg and Pniel Groups are represented as a single unit consisting of mafic lava, rhyolite, pyroclastic material, conglomerate and shale known as the Lobatse Volcanic Group (Van der Westhuizen, De Bruiyn and Meintjes, 1991; J. N. Carney, Aldiss and Lock, 1994; Franchi and Mapeo, 2019). The Lobatse Group, like the Gaborone Granite, exhibits intrusive relationships into the Kanye Group (Key and Ayres, 2000). Pb-Pb zircon dating of the Lobatse Group produced an age of 2.8 Ga which is broadly contemporaneous with the Kanye Group and Gaborone Granite Complex (Franchi and Mapeo, 2019). The Lobatse is divided into Nywane Formation made up of volcanics and sedimentary rocks and into the Mogobane Formation consisting of fine-grained sedimentary rocks (Carney, Aldiss and Lock, 1994).

The Lobatse Volcanic Group is unconformably overlain by the Taupone Group which was deposited after a hiatus of 0.2 Ga (Franchi and Mapeo, 2019). The Taupone Group is the stratigraphic equivalent of the Malmani Group of the Transvaal Supergroup is South Africa. A stratigrahic juxtaposition of the Transvaal Supergroup and the equivalent Kanye Basin in Botswana, is shown for convenience in (Fig 1.3) below.

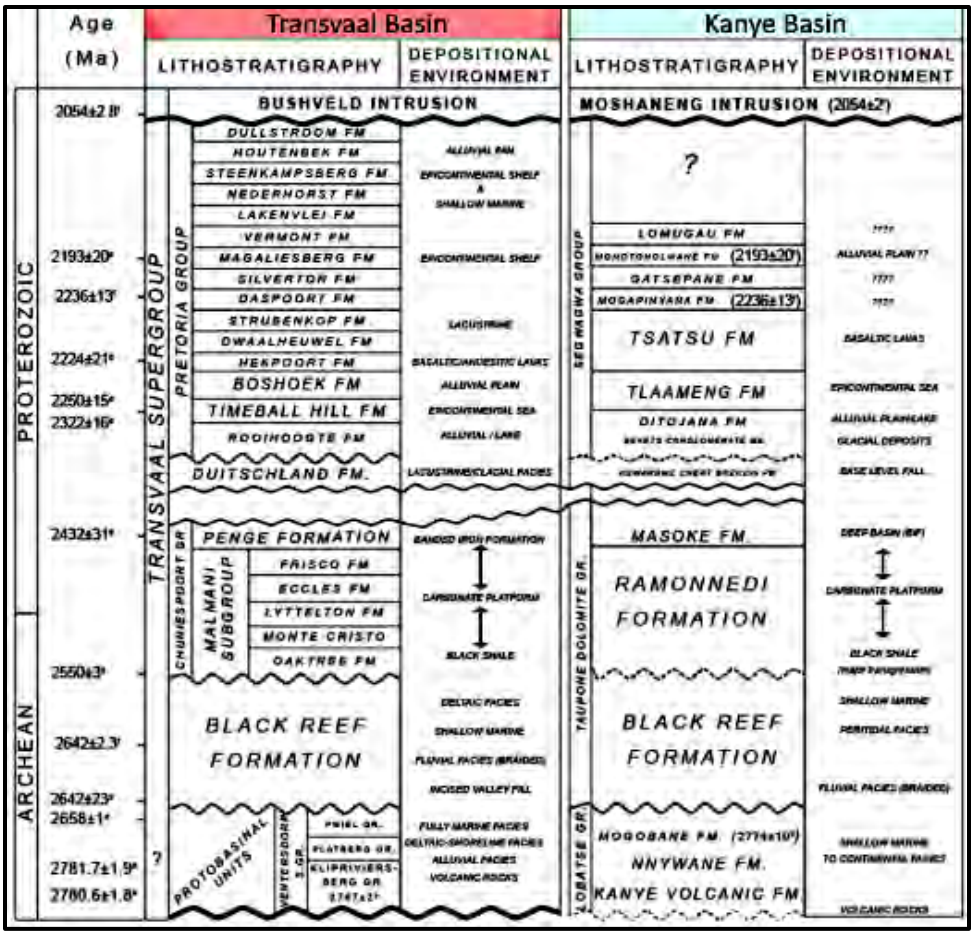

Figure 1.3: Lithostratigraphic chart of the Transvaal Supergroup (red) in South Africa and its equivalent Kanye Basin (blue) of Botswana. Modified from Franchi and Mapeo *et al*. (2019).

1.3.2 Proterozoic Complexes

Proterozoic terranes in south-western Botswana, South Africa and Namibia, are well exposed and allow for intersite strata correlation (Fig.1). This is contrary to central Botswana's Proterozoic terranes which are completely concealed by Phanerozoic sequences (Singletary *et al.*, 2003; Haddon, 2005). In this case, geophysical studies play a vital role in the understanding of central Botswana's concealed Proterozoic terranes.

According to Barton *et al.,* (1994), the Central Zone of the Limpopo Mobile Belt (Fig. 1.4) consists of Paleoproterozoic lithologies of about 2.0 Ga, which diverges from the idea that such sequences it is entirely Archean (Key and Ayres, 2000). The Mahalapye Complex (2.0 Ga) further south is

made up of the Mahalapye Granites and Migmatites and Mokgwane Granite (McCourt and Armstrong, 1998; McCourt *et al.*, 2004). The date of the Malahapye Complex suggests an Eburnian event in eastern Botswana (Key and Ayres, 2000).

The Okwa Complex (Fig.1.3) is situated south of the Ghanzi Group where it is bounded by the Tsan Fault Zone and the Kalahari Line (Haddon, 2005). The Complex is made up of porphyritic felsites, seritic quartzites leucogranites, augen granite and gneisses and metadolerite (Aldiss and Carney, 1992; Majaule *et al.*, 2001; Haddon, 2005). Due to the nature of the Okwa Complex, it has been accepted that the Okwa Complex and Magondi Belt were laterally continuous (Brett *et al*., 2000; Ramokate *et al*., 2000; Haddon, 2005) or that Okwa Complex granitic rocks display an extension of the Kheis Belt (Key and Rundle, 1981). The Kheis Belt (Fig. 1.4) is situated in the southwestern area of the province and comprises low grade metasedimentary and metavolcanic rocks exposed in Northen Cape, South Africa and southern Botswana. Towards the north, the Kheis Belt is connected to the fault bound Okwa block that has limited 2.05 Ga outcrops metarhyolite and orthogneiss in the Okwa Valley (Key and Ayres, 2000; Singletary *et al.*, 2003; Haddon, 2005). The north-eastern region of the province is made up of the Magondi Belt, consisting of high-grade paragneiss extending from Zimbabwe (Key and Ayres, 2000; Singletary *et al.*, 2003; Haddon and McCarthy, 2005).

The Ghanzi Group consists of clastic and carbonate rocks which unconformably overlying the Kgwebe Formation volcanics within the Northwest Botswana Rift. Towards the north, the Northwest Rift basin is called the Ghanzi-Chobe Ridge and has experienced metamorphism and deformation (Singletary *et al.*, 2003). The Ghanzi-Chobe zone is characterized by northeast-trending aeromagnetic signatures distinct fold structures (Key and Ayres, 2000). The Kwando Complex (1.2 Ga), northwest of the Ghanzi-Chobe zone is a geophysically distinct subsurface area (Carney, Aldiss and Lock, 1994).

The Rooibok Complex, located west of the Kwando Complex, is characterized by distinct northeast structural trends and is like the Matchless Amphibolite Belt of Namibian Damara Belt (Lüdtke, Eberle and van Der Boom, 1986; Singletary *et al.*, 2003). The Rooibok Complex has abundant amphibolites, granitic gneiss, pelitic and mafic schists (Carney, Aldiss and Lock, 1994). The Koanaka Group greenschist facies marbles are structurally juxtaposed with meta-

igneous rocks from the Chihabadum Complex north of the Rooibok Complex. The Aha Hills further north consist of lower grade chert-rich limestone and dolomite (Singletary *et al.*, 2003).

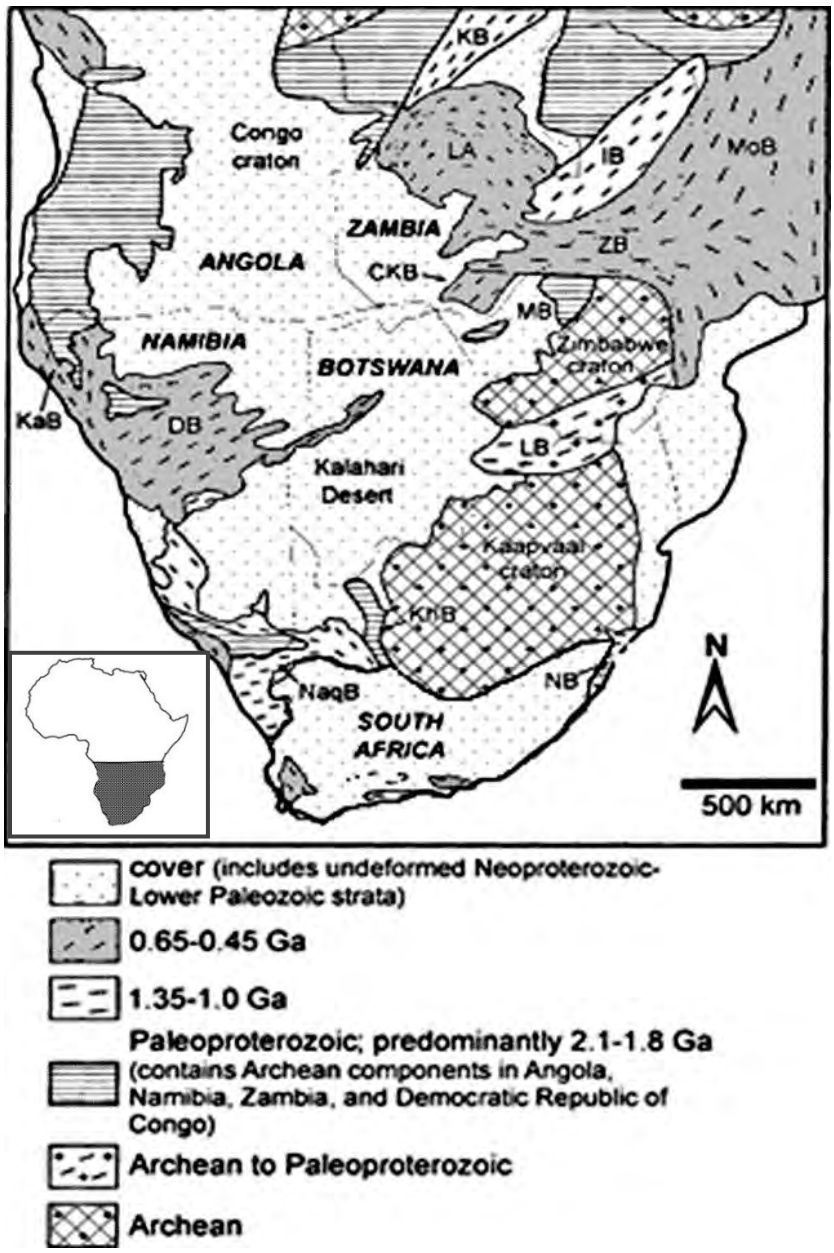

Figure 1.4: Southern Africa inset showing outcropping Archean cratonic nuclei and Proterozoic orogenic belts. CKB, Choma-Kalomo block; DB, Damara belt; IB, Irumide belt; KaB, Kaoko belt; KB, Kibaran belt; KhB, Kheis belt; LA, Lufilian arc; LB, Limpopo belt; MB, Magondi belt; MoB, Mozambique belt; NaqB, Namaqua belt; NB, Natal belt; ZB, Zambezi belt, modified from Singletary et al., (2003).

The Quangwadum Complex situated in Ngamiland District, Northwest Botswana (Fig. 1.4) is represented by granitic-gneiss lithologies. Metasedimentary rocks of the Xaudum (1.01 Ga) and Tsodilo Hills Group (0.49 Ga) located north of the Quangwadum Complex, show prominent north to northwest structural trends (Key and Ayres, 2000; Mapeo, Kampunzu and Armstrong, 2000; Singletary *et al.*, 2003). The Xaudum Group consists of chert-bearing carbonate, low-grade sandstone and siltstone, whilst the Xaudum Iron Formation (XIF) of the Tsodilo Hills Group consists of ferruginous meta-quartzites, meta-conglomerates and quartz-mica schists altered to amphibolite metamorphic grade (Singletary *et al.*, 2003; Wendorff, 2005)

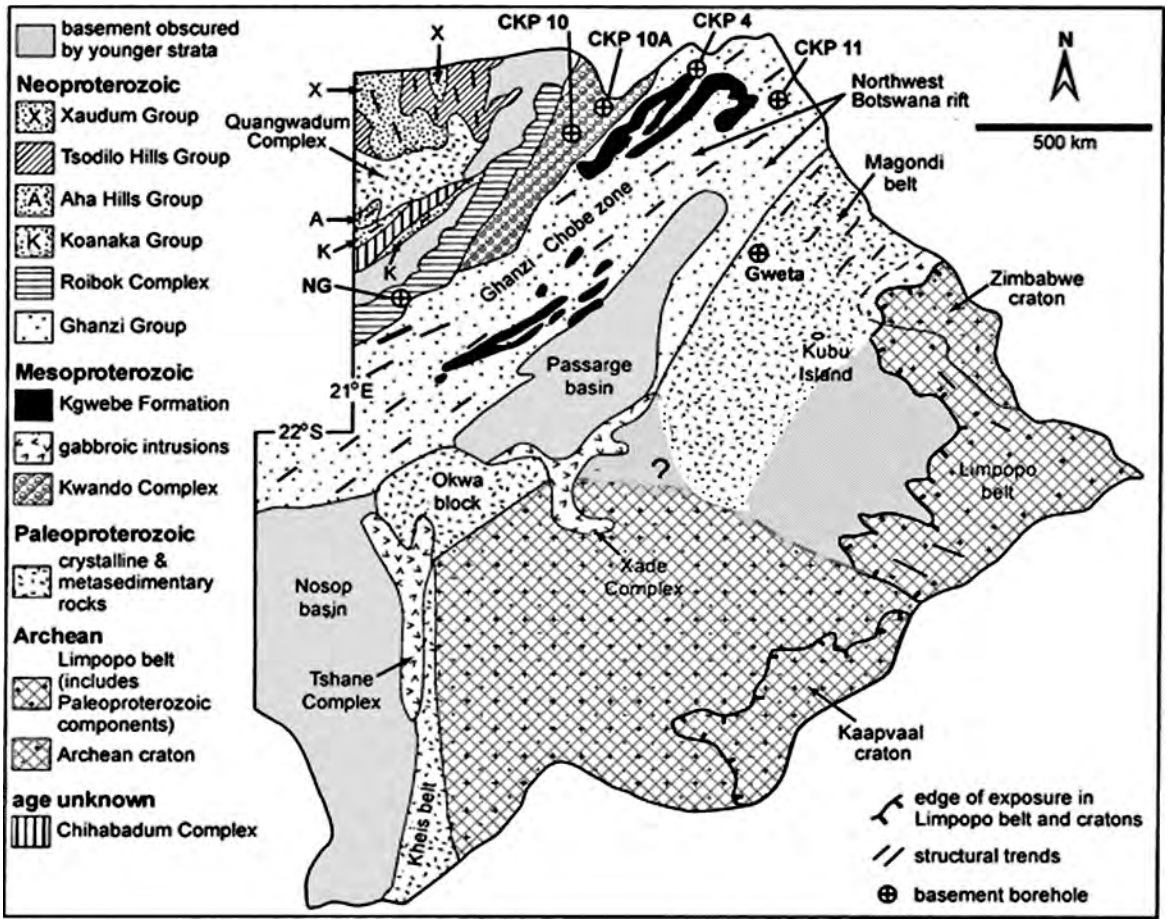

Figure 1.5: Basement Precambrian geology of Botswana with major structural features, (from Singletary, 2003).

1.3.3 Phanerozoic Lithologies

The Phanerozoic lithologies that conceal the Precambrian basement in Botswana belong to the Karoo Supergroup and overlying Kalahari beds which will not be discussed in this study (Carney, Aldiss and Lock, 1994; Key and Ayres, 2000). The Karoo Supergroup rocks were deposited on the Gondwana supercontinent following the Damara orogeny which caused a rift in the Kalahari and Congo cratons (Carney, Aldiss and Lock, 1994). The lithological sequences of the Karoo Supergroup consist of sedimentary and volcanic rocks that cover a vast area of the Southern Africa subcontinent (Carney, Aldiss and Lock, 1994; Catuneanu *et al.*, 2005). The stratigraphy of the Karoo Supergroup comprises the basal Dwyka Group which is overlain by the younger Ecca, Beaufort and Stormberg Groups.

1. The Dwyka Group is the oldest unit, it has variable thickness and comprises lithologies that were deposited during the Permian-Carboniferous glaciation (Carney, Aldiss and Lock, 1994; Catuneanu *et al.*, 2005).
2. The Ecca Group units consist of mudrocks, black (organic) shales and sandstones which were deposited during the Permian. The basal Prince Alfred Formation of the Ecca Group comprises shallow-water carbonates and is overlain by organic-rich black shales of the Whitehill Formation. Mudrocks interbedded with tuff beds are featured in the overlying Collingham Formation (Johnson *et al.*, 1996; Catuneanu *et al.*, 2005; Alexander and Wheeler, 2015).
3. The Beaufort Group, which is believed to have been deposited around the P-T boundary, is made up of fluvio-deltaic mudstone, sandstone, conglomerate and granulestones (Alexander and Wheeler, 2015).
4. The Stormberg Group is the youngest unit of the Karoo Supergroup: it consists of sedimentary and volcanic rocks that were deposited and erupted in the Triassic (Johnson *et al.*, 1996; Catuneanu *et al.*, 2005). The lowermost unit of the Stormberg Group is the Molteno Formation which consists of fluvial sandstones. The Stormberg Group is overlain by the fluvial and floodplain fine-grained mudstone and sandstones of the Elliot Formation and the uppermost aeolian sandstones of the Clarens Formation, which are in turn covered

by Drakensberg lavas (Johnson *et al.*, 1996; Catuneanu *et al.*, 2005; Alexander and Wheeler, 2015).

Smith (1984) correlated Phanerozoic lithologies of Botswana to the Karoo Supergroup of South Africa and noted similarities between them, and highlighted the aelioan sands of the Molteno, Elliot and Clarens Formations of the Stormberg Group as a separate lithological group in Botswana (Carney, Aldiss and Lock, 1994). Fig.1.5 below shows the correlated Karoo Supergroup stratigraphy in Botswana and South Africa.

<table>
<tr><th>GROUPS</th><th>SOUTH WEST BOTSWANA</th><th>KWENENG & WESTERN CENTRAL KALAHARI</th><th>MMAMABULA</th><th>MORUPULE & SE KALAHARI</th><th>NE BOTSWANA & NORTHERN BELT</th><th>NORTH WEST BOTSWANA</th><th>TULI BASIN</th></tr>
<tr><td>STORMBERG LAVA</td><td colspan="5">STORMBERG LAVA GROUP (Undivided)</td><td>Bobonong Lava Formation</td></tr>
<tr><td rowspan="2">LEBUNG</td><td>Nakalatlou Sandstone</td><td colspan="4">Ntane Sandstone Formation</td><td>Bodibeng Sandstone Fm.</td><td>Tsheung Sandstone Formation</td></tr>
<tr><td>Dondong Fm.</td><td colspan="3">Mosolotsane Formation</td><td>Ngwasha Fm.
Pandamatenga Fm.</td><td>Savuti Fm.</td><td>Thune Formation
Korebo Formation</td></tr>
<tr><td>BEAUFORT</td><td>Kule Fm.</td><td>Kwetla Fm.</td><td colspan="3">Tlhabala Formation</td><td>?</td><td rowspan="3">Seswe Formation</td></tr>
<tr><td rowspan="3">ECCA</td><td rowspan="2">Otshe Fm.</td><td rowspan="2">Boritse Fm.</td><td>Korotlo Fm.</td><td>Serowe Fm.</td><td rowspan="2">Tlapana Fm.</td><td rowspan="2">Marakwena Formation
Tale Formation</td></tr>
<tr><td>Mmamabula Fm.</td><td>Morupule Fm</td></tr>
<tr><td>Kweneng Fm.</td><td>Mosomane Fm</td><td>Kamotaka Fm.</td><td>Mea Arkose Fm.</td><td>?</td></tr>
<tr><td>Kobe Fm.</td><td>Bori Fm.</td><td>Bori Fm.</td><td>Makoro Fm.</td><td>Tswane Fm.</td><td>?</td><td>Mofdiamogolo Formation</td></tr>
<tr><td rowspan="3">DWYKA</td><td>Middlepits Fm.</td><td colspan="4" rowspan="3">Dukwi Formation</td><td rowspan="3">?</td><td rowspan="3">?</td></tr>
<tr><td>Khuis Fm.</td></tr>
<tr><td>Mmalogong Fm.</td></tr>
</table>

Figure 1.6: Lithostratigraphy of the Karoo Supergroup correlated to its equivalent rocks in Botswana adapted from Smith (1984).

1.4 Local Geology

Neoproterozoic sequences that contain iron-formation occur in the Ngamiland District, Northwestern Botswana (Fig.1.6). The Quangwandum Complex, Xaudum Group and Tsodilo Hills Group comprise the basement rocks in this area. The XIF is hosted in a metasedimentary sequence that is divided into two units, namely Xaudum Group and Tsodilo Hills Group (Key and

Ayres, 2000). The Xaudum Group and Tsodilo Hills Group outcrop at Shakawe and Tsodilo Hills whilst the Quangwandum Complex have been delineated by aeromagnetic surveys (Key and Ayres, 2000). The Lebung Group, Drakensberg basalts and Kalahari sediments are the overlying younger lithologies (Singletary *et al.*, 2003).

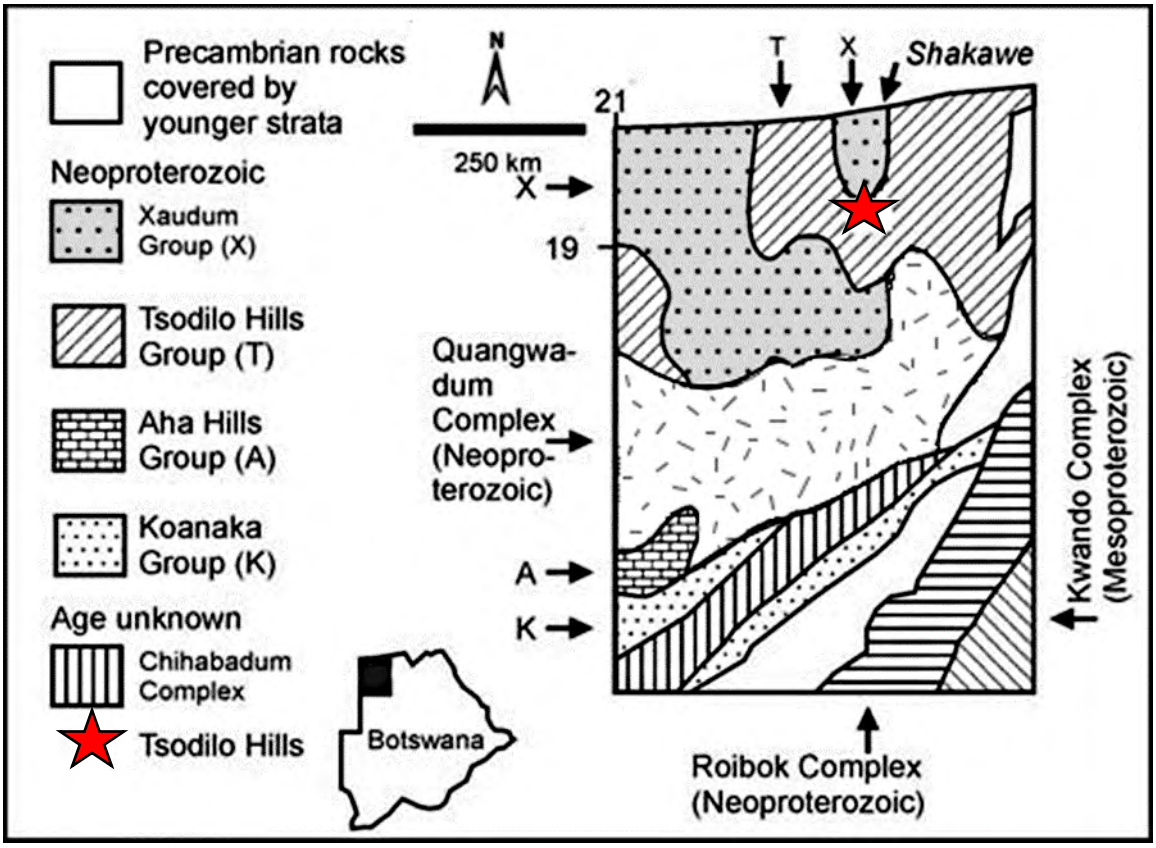

Figure 1.7: Geology of northwestern Botswana showing Neoproterozoic units. The star denotes the sampling area (Tsodilo Hills). Inset: Location of the map in Botswana (after Wendorff, 2005).

The Quangwandum Complex consists of augen gneiss, porphyritic granite and muscovite-biotite granite (Singletary *et al.*, 2003). The augen gneiss has prominently foliated quartz, feldspar and biotite, whereas the porphyritic granite has cm-scale potassium feldspar megacrysts surrounded by medium-grained foliated matrix enclosing gneiss xenoliths (Key and Ayres, 2000; Singletary *et al.*, 2003; Wendorff, 2005). Augen gneiss records an age of 2.55 Ga, indicating an Archean component in gneiss formation (Key and Rundle, 1984). Muscovite and biotite K-Ar dates yielded

ages of 0.65-0.5 Ga, signifying Pan-African orogenic overprint (Key and Rundle, 1984; Singletary *et al.*, 2003).

The Xaudum and Tsodilo Hills Groups are amphibolite-grade metamorphosed successions. The Xaudum Group outcrops at the Nxau Nxau Valley and was metamorphosed through regional folding and tectonism related to the Damaran orogeny (Singletary *et al.*, 2003). Wendorff (2005) suggests that the Xaudum Group could be the equivalent of the Nosib Group of the Namibian Damara Succession.

An Ar-Ar 0.49 Ga age of Tsodilo Hills derived from muscovite dating (Singletary *et al.*, 2003; Wendorff, 2005), implies deposition of the Tsodilo Hills Group before the end of Pan-African orogenesis. This age links the Tsodilo Hills Group coevally to other sedimentary sequences within the Pan-African orogenic system, spreading from the Damara Belt in the west to the Lufilian Arc in the northeast (Wendorff, 2005). Due to the high iron content and lithological similarities, Singletary *et al*. (2003) suggest that the XIF-hosting Tsodilo Hills Group can be correlated to the Chuos Iron Formation of the Damara Supergroup in Namibia and the Grand Conglomerat Formation of the Katangan Supergroup in Zambia.

The Lebung Group sediments capping the aforementioned stratigraphy lack exposure, however geophysical data and drill cores have assisted in delineating their distribution. Drakensberg basalts (0.18 Ga) overlie these sediments.

1.5 Objectives and Methodology

Tsodilo Resources Ltd is a TSX-V listed exploration and mineral development company based in Botswana. The company acquired prospecting licenses on the magnetite iron-rich Xaudum area in Ngamiland, northwest of Botswana in 2008 which was later renewed in 2012 due to more interest by Tsodilo Resources Ltd into magnetite iron ore (Baker, 2014). The interest of Tsodilo Resources Ltd in the magnetite iron ore led to a research partnership with Rhodes University Postgraduate Research in Iron and Manganese Ore Resources (PRIMOR) which is headed by Professor H. Tsikos. The ensuing partnership between Tsodilo Resources Ltd and PRIMOR took the form of the present MSc project which commenced in February of 2017. The following overarching

objectives were proposed, namely to further geological understanding of the XIF by producing new data and insights into the redox and environmental conditions of the paleobasin wherein it was deposited; and, where possible, offer deeper insights into the economic potential of the XIF as an iron ore resource. These objectives were further broken down into the following four milestones:

1. Re-construct the primary compositional character of the Xaudum IF by unravelling the complex metamorphic overprint;

2. Compare and contrast the XIF to other BIF on a regional and global scale.

3. Constrain the redox conditions in the paleo-basin and overall paleoclimatic regime during IF deposition.

4. Gain a better understanding of the distribution (speciation) of iron to inform metallurgical processing and overall economic viability

In April 2017, the author accompanied by Professor Tsikos of PRIMOR, visited the premises of Tsodilo Resources Ltd and obtained generous access to their core yard in Shakawe, Botswana where drillcores were accessed, logged, and sampling was carried out. A total of four drill cores, namely L9600_10W_31Q, 1821B116E_78W, 1821B91AV3 and 1821B91AV3 were specifically selected and logged. The cores were selected based on their spatial distribution to achieve a representative sampling strategy of the area of structural development of XIF and ultimately of its original paleo-depository. Subsequently, the four cores were conveniently re-labelled to Core N, S, SW and SS for this thesis, according to their relative geographic positions, this information can be further accessed in the Appendix A1 and A2. Macroscopic observations of the various rock types, their textures and relationships were recorded during the core-logging. Core sampling followed the observations made from logging the four cores. A total of 67 XIF and 34 diamictite samples were collected across the four cores for further geochemical and petrographic analysis. Methodological details on all analytical techniques used can be found in the Appendix A.

1.5.1 Sample preparation and analysis

1.5.1.1 Petrographic microscope

XIF and diamictite samples selected based on macroscopic observations were cut and made into polished thin sections. The thin sections were studied through transmitted light for silicates and reflected light microscopy for oxides and, where present, sulphides.

1.5.1.2 Electron probe micro-analysis (EPMA)

Eight thin sections representing IF and diamictite facies were selected based on observations made under the petrographic microscope. These samples were subsequently carbon coated and analysed using a JEOL electron microprobe (EPMA) at Rhodes University, to acquire precise and quantitative elemental analyses of representative rock-forming minerals. Members of the silicates, oxides and carbonate mineral groups present were targeted.

1.5.1.3 Whole rock geochemistry

The entire total of 67 XIF and 34 diamictite samples were crushed to fine powder and sent to Stellenbosch University for whole rock geochemical analysis. X-Ray Fluorescence (XRF) spectroscopy was for major and minor element analysis on used beads of the original sample powders, whereas Laser Ablation Inductively Coupled Plasma Mass Spectrometry (LA-ICPMS) was used to determine trace element contents, including rare-earth elements (REE).

2. PETROGRAPHY OF THE XAUDUM IRON FORMATION

A vast body of literature on the mineralogy and petrography of Archean and Paleoproterozoic BIF has been published by several researchers (see Klein, 1983; Klein, 2005, for original references). This literature contains diverse information on BIF ranging from mineral chemistry, phase equilibria, mineral compatibilities, natural mineral reactions and mechanisms for deposition of primary Fe-rich precipitates (Klein 1966; Klein, 1974; Klein and Fink, 1976); Klein, 1978; Ewers and Morris 1981; Klein and Gole 1981). An important aspect discussed in the literature is mineral phases forming under diagenetic and/or metamorphic processes of various grades. With respect to metamorphosed BIF like the XIF, this kind of information is especially pertinent to the identification and characterisation of mineral species that are indicative and diagnostic of the various metamorphic grades and facies in BIF (Klein, 2005).

Archean BIF lithologies are characterised by various metamorphic grades and only a few are of low metamorphic grade. Conversely, the younger, Paleoproterozoic BIF counterparts of the Superior type, including those of the Kaapvaal Craton, South Africa and Hamersley Basin, Western Australia, belong to late diagenetic to very low metamorphic grades (Klein, 1983, Klein, 2005). The NIFs, similarly to Archean BIFs are characterised again by various metamorphic grades. The XIF tackled in this study is metamorphosed to medium grade amphibolite facies.

A striking difference between Algoma and Superior-type BIF compared to the NIF is in terms of bulk mineralogy. In Algoma and Superior-type BIF, iron exists as ferrous iron in magnetite, carbonates and silicates, which contrasts to the iron mineralogy in NIF which is dominated by oxides (mainly hematite) together with chert. Clearly, the latter mineralogy characterises unmetamorphosed iron formations such as the Rapitan and Urucum iron formations in Canada and Brazil respectively (Klein and Beukes, 1993, Cox *et al.,* 2013). Since a wide spectrum of mineral phases (silicates, carbonates and oxides) are expected to be produced from diagenetic to medium-grade metamorphic conditions, this section will review mineral phases applicable to XIF based on its evident metamorphic grade.

Silicates: Iron-silicate minerals (greenalite, stilpnomelane, minnesotaite and riebeckite) that are present in diagenetic and low metamorphic grade Paleoproterozoic iron formations of the Superior

type are not present in the XIF owing to its medium-grade metamorphism (Klein, 2005). If present, these iron-silicates are thought to have reacted at medium metamorphic grade to produce amphiboles (cummingtonite/grunerite series) and garnets (almandine and Mn-rich spessartine) as documented later in this study (see also Konhauser *et al*., 2017). This is broadly illustrated in Fig. 2.1 below where diagenetic and low grade metamorphic mineral assemblages give way with increasing metamorphic grade to produce new minerals stable under the new conditions. For comparison, the grey shaded area in Fig.2.1 represents a diagenetic mineral assemblage as documented from the Paleoproterozoic Hotazel BIF in South Africa (Tsikos and Moore, 1997); the red shaded area represents a classic medium grade metamorphic mineral assemblage expected to be encountered in BIFs such as XIF.

SiO_2 is a major chemical component in iron-formations with its crystal form manifesting commonly as very fine-grained chert, which recrystallises to coarser quartz during progressive burial. Typically, diagenetic iron formations will contain very fine-grained chert (conventionally < 0.05mm SiO_2 particles), whereas discrete quartz grains will be larger than 0.05mm (Klein, 1983).

Magnetite: Apart from quartz, magnetite is the most abundant mineral phase in iron formations around the world (Klein, 2005). Magnetite commonly exists as moderate to well-shaped, medium-sized grains arranged as homogenous magnetite laminae/banding and/or disseminated grains in chert or iron-rich silica/carbonate assemblages (Klein, 2005). Earlier theories attributed the common size and shape of coexisting magnetite and carbonate to a possible cogenetic history in the diagenetic/low metamorphic environment (James, 1954). This idea opened conflicting schools of thought on the genetic origin of magnetite in iron formations. A theory supported widely (Gross, 1973; Perry & Tan, 1973; Klein, 1974; Klein & Bricker, 1977; Klein, 1978) proposes that magnetite is a product of diagenetic recrystallization of a precursor hydromagnetite. An alternative theory by French (1968, 1973), Floran and Papike (1978) and Han (1988) suggest that magnetite is product of low-grade metamorphic reactions that consume iron silicates, iron carbonates or iron oxides. Textural observations by Klein and Fink (1976) revealed cross-cutting relations between magnetite and other coexisting minerals from the Sokoman iron-formation, which were interpreted as recrystallization product of an earlier iron oxyhydroxide precursor.

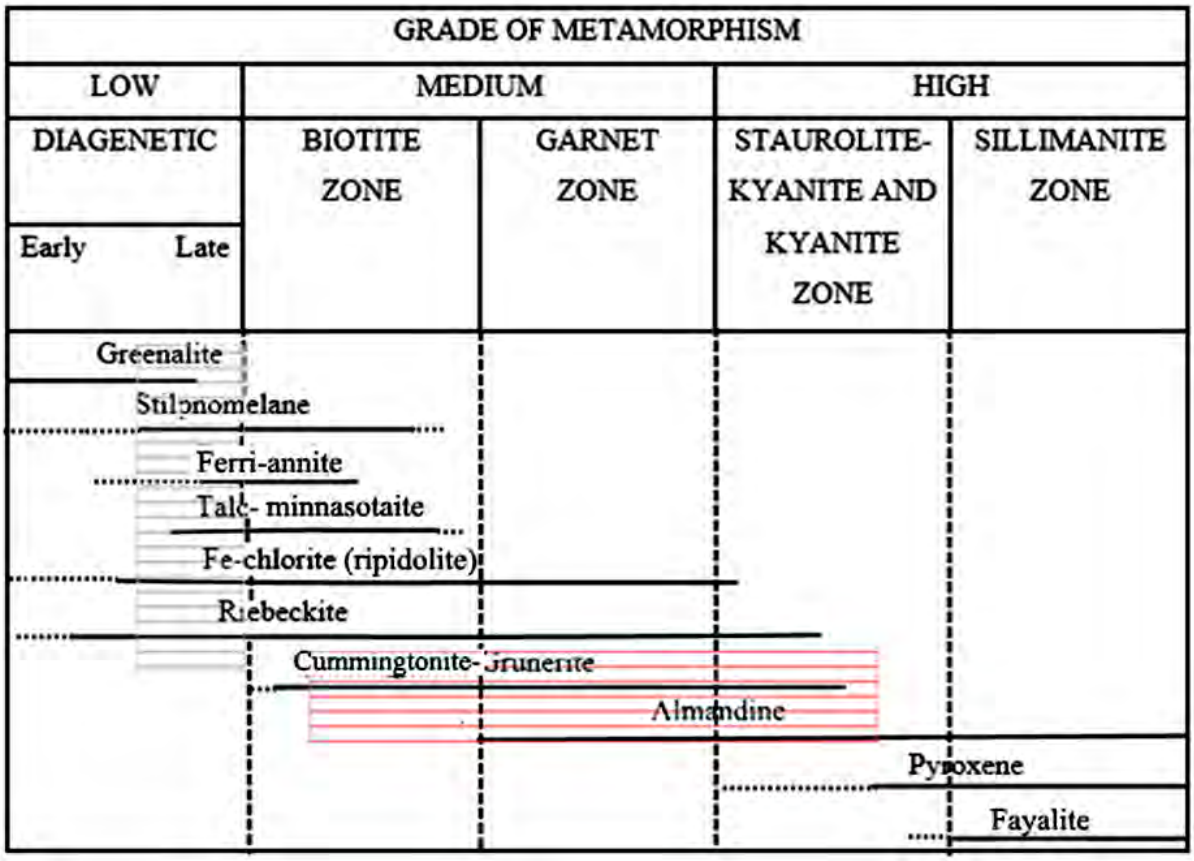

Figure 2.1: Relative stabilities of iron-silicates in metamorphosed iron formations as a function of metamorphic grade, modified from (Klein, 1983). The grey shaded area represents Hotazel iron-formation mineral assemblage. The red shaded area represents medium metamorphic grade XIF mineral assemblage.

Hematite: Contrary to the common presence of hematite in unmetamorphosed NIF, ferrous oxides are far less common in most late diagenetic to low-grade metamorphic BIFs, unless supergene oxidation has overprinted the rocks. When present as a primary component, hematite usually coexists with magnetite and tends to be much finer-grained than the latter. The hematite occurs typically as microbands/laminations and irregular bleb-like concentrations (Klein 2005). Ferric hydroxide [$Fe(OH)_3$] or hydrous ferric oxide ($Fe_2O_3.nH_2O$) are the suggested sedimentary precursors to observed crystalline phases (French, 1973; Klein & Bricker, 1977; Lesher, 1978; Mel'nik, 1982; Konhauser et al., 2017)

Pyrite: Sulphide-rich iron formations are generally rare and owe their origin to hydrothermal sulphidation (Klein, 2005). In sulphide-poor iron formations, pyrite is a common albeit very minor

phase (James, 1954). It exists as well shaped grains which appear coarser than the other coexisting mineral phases such as greenalite, carbonates and chert (Klein & Fink, 1976; Klein, 2005).

Amphiboles: Iron-rich amphiboles of the cummingtonite-grunerite series are the most notable mineral group in medium grade metamorphosed BIF. This series is thought to be product of reactions between iron-rich carbonates and quartz (*equation 1 and 2*) or dehydration breakdown of lower-grade iron silicate minerals such as minnesotaite (*equation 3*) (Klein, 2005). The amphiboles tend to develop as medium to large grains with moderate to well-developed crystal faces often arranged in bands. The grains have a schistose texture with some of the grains exhibiting polysynthetic and simple twinning (Klein, 2005).

$$7Ca(Fe,Mg)(CO_3) + 8SiO_2 + H_2O \rightarrow (Fe,Mg)_7Si_8O_{22}(OH)_2 + 7CaCO_3 + 7CO_2 \quad (1)$$

Ferrodolomite Quartz Grunerite Calcite

$$8(Fe,Mg)CO_3 + 8SiO_2 + H_2O \rightarrow (Fe,Mg)_7Si_8O_{22}(OH)_2 + 7CO_2 \quad (2)$$

Siderite Quartz Grunerite

$$7Fe_3Si_4O_{10}(OH)_2 \rightarrow 3Fe_7Si_8O_{22}(OH)_2 + 4SiO_2 + 4H_2O \quad (3)$$

Minnesotaite Grunerite Quartz

Garnets: Whereas iron-rich garnets (almandine) are not absent in medium-grade metamorphic BIFs, they are nevertheless very rare due to the inherently low Al_2O_3 content of the majority of BIF. Contrary to most BIFs, XIF has a relatively high Al_2O_3 content (particularly in core SW selected for this study), as such, garnet is one of the most abundant mineral constituents in the study rocks. Otherwise, the expectation is that most metamorphosed BIFs under amphibolite facies will develop low-Al, andraditic garnet by reaction of pre-existing iron silicate phases (or oxides and chert), with coexisting carbonate minerals.

2.1 Mineralogical and textural descriptions

2.1.1 Xaudum IF

The sampled XIF mineralogy comprises magnetite, quartz, amphibole, garnet, biotite and chlorite in decreasing abundance as shown in Table 4.1. Carbonate minerals are relatively uncommon and exist as calcite and dolomite. Sulphides, mainly pyrite, are present as minor trace components.

Table 2.1: Bulk mineral composition of XIF as determined by petrographic microscope and EPMA. XXX represents the most abundant component with modal abundance greater than 50%, XX represents the common phase with modal abundance greater than 20% and X represents minor trace components with abundance less than 5%.

Mineral group	Mineral component	Abundance
Oxides	Magnetite	XXX
	Rutile	X
Silicate	Quartz	XXX
	Amphibole	XXX
	Garnet	XXX
	Biotite	XX
	Chlorite	XX
Carbonates	Calcite	X
	Dolomite	X
Sulphides	Pyrrhotite	X
	Chalcopyrite	X

Magnetite

Magnetite displays a variety of textures and grain sizes and is ubiquitously distributed throughout the XIF. The most common magnetite texture is well-shaped equant magnetite crystals with grain sizes ranging from 0.5 to 1 mm. They form distinct bands with variable thicknesses and constitute arguably the most economically interesting concentrations of iron in the study rocks. Magnetite

bands are occasionally deformed and thus show slight variation in magnetite distribution on small scales (Fig.2.2 A, B and C). Another observed texture of magnetite is as medium- to fine-grained inclusions in garnet (Fig. 2.2B) and amphiboles. Fine to medium-sized sub-equant magnetite grains also occur interstitially in a variety of mineral assemblages of XIF (Fig. 2.2D). The distribution of magnetite grains is usually random but may record crude alignment on fine scales (Fig. 2.2E).

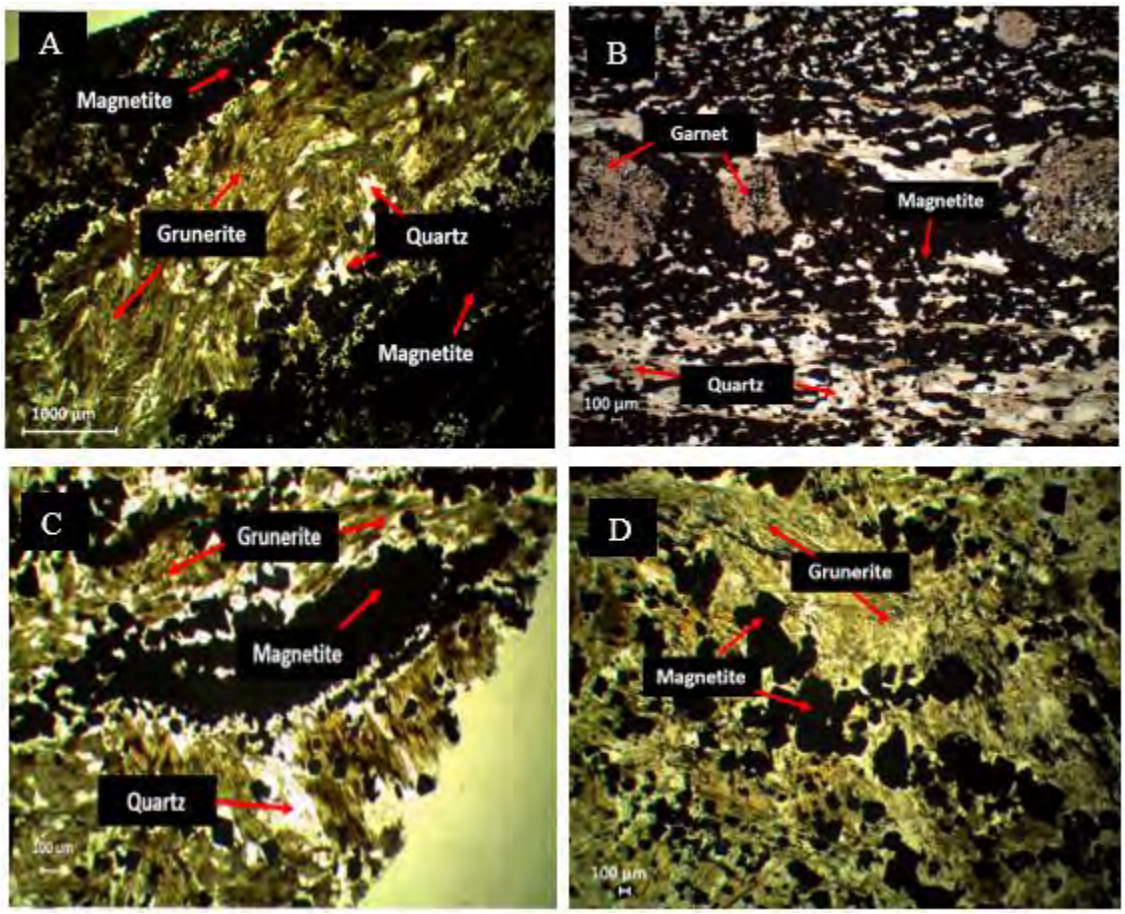

Figure 2.2 A-D: Photomicrographs illustrating various textures and grain sizes of Xaudum Iron-formation magnetite under plane polarized light. (A) Altered grunerite band flanked by distinct magnetite bands with very fine-grained quartz occupying the interstitial space. (B) Quartz-rich band alternating with deformed magnetite band wrapping medium-grained garnet with quartz inclusions and interstitial quartz. (C) Highly deformed magnetite band alternating with grunerite. The grunerite interstitial space hosts fine well crystalline magnetite gains. (D) Medium, moderately shaped magnetite grains occupying interstitial space in grunerite-rich matrix.

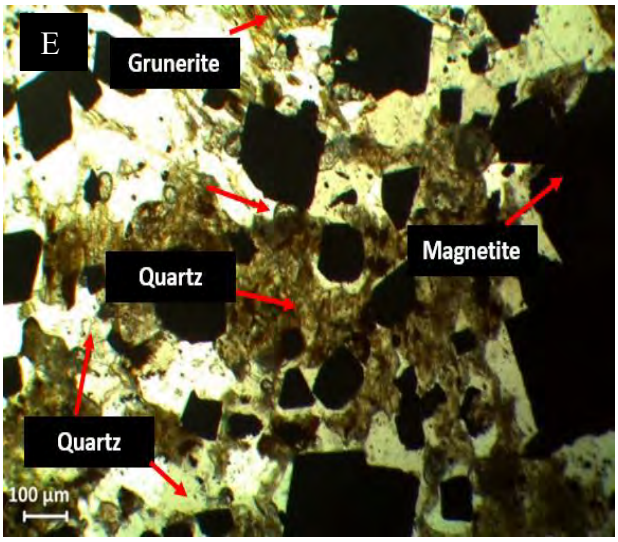

Figure 2.2E: Photomicrographs illustrating various textures and grain sizes of Xaudum Iron-formation magnetite under plane polarized light (E) Medium to coarse-grained magnetite showing random distribution and locally crude alignment in a grunerite-rich matrix.

Amphibole

Amphibole exists as grunerite-cummingtonite solid solution series in Core-SW. The Fe-rich end member grunerite is common in Core-N, Core-S and Core-SS less so in Core-SW. It is defined by coarse bladed grains with distinctive yellow-brown colour and moderate birefringence (Fig. 2.3B). Rarer Mg-rich cummingtonite occurs in core SW as tabular and elongated crystals with pale green colour. The cummingtonite shows distinctive polysynthetic twinning (Fig. 2.3C).

The observed amphibole exist as bands of distinct well shaped grains that may record deformation effects. The amphibole crystals making up the bands exhibit three often overlapping textures: amphibole crystal clumps with an apparent radial fan shaped texture (Fig. 2.3B), disseminated grains lacking specific orientation (see Fig. 2.3C), or banded crystal aggregates defining a crude foliation pattern (Fig.2.3A). Amphibole crystals can often develop as relatively large grains in a finer matrix, in which case they may contain fine magnetite inclusions. The matrix itself occurs as 0.5 to 1.2 mm bladed grunerite crystals formed in apparent textural equilibrium with tabular to elongated biotite (Fig. 2.3B).

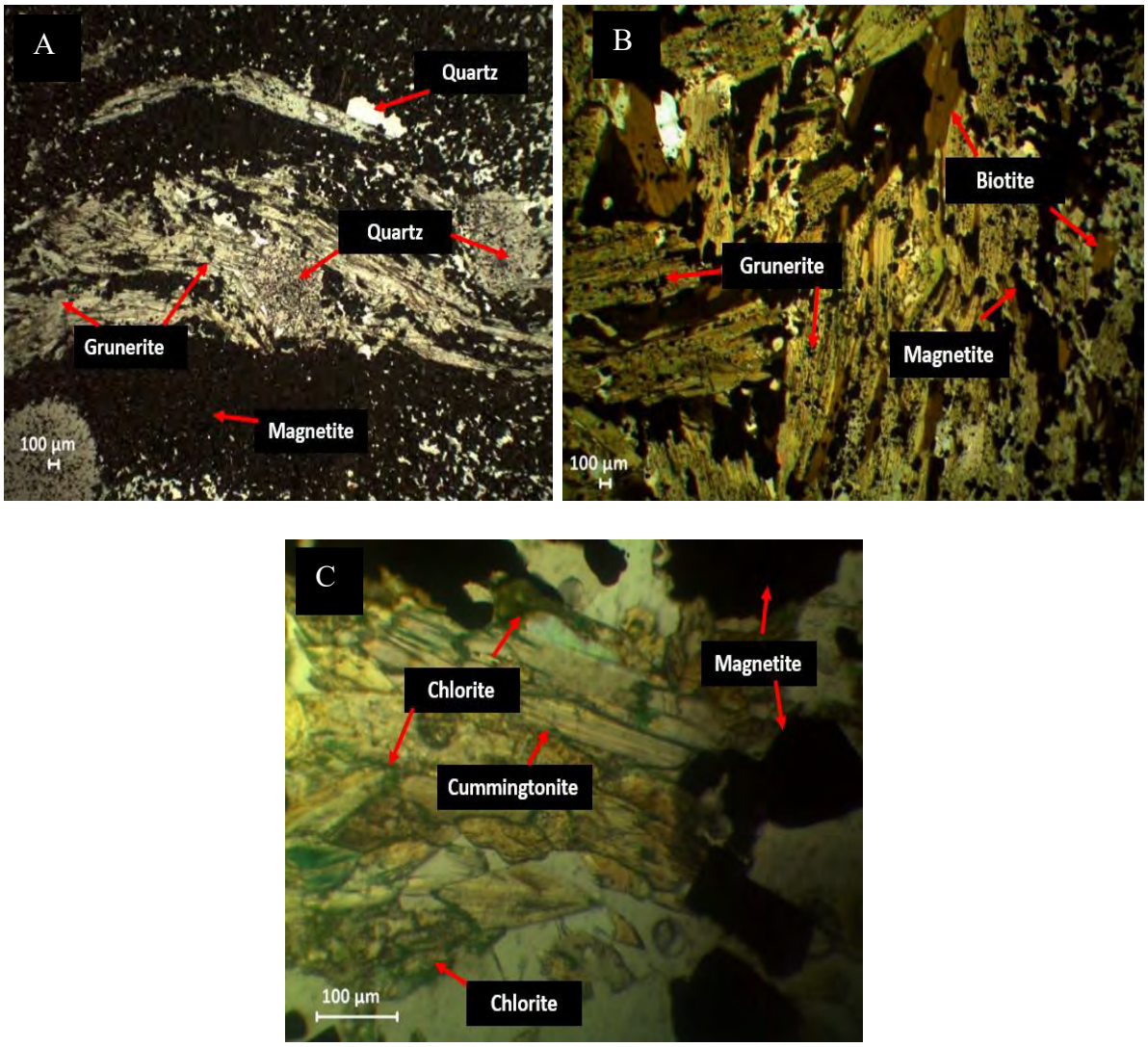

Figure 2.3: Photomicrographs illustrating various textures and grain sizes of Xaudum Iron-formation amphibole under plane polarized light. (A) Deformed amphibole band consisting of acicular cummingtonite crystals that crudely define foliation. Medium-sized garnet with magnetite inclusions is enveloped by cummingtonite-rich bands containing magnetite. (B) Coarse and tabular grunerite grains with fine magnetite inclusions in textural equilibrium with medium tabular biotite. The biotite hosts fine-grained grunerite. (C) Tabular to elongated cummingtonite crystals showing moderate orientation. Chlorite is present along the cummingtonite rims and interstitial spaces and appears to be the result of retrograde alteration.

Garnet

Garnet is a significant component of the XIF throughout the study area. This high distribution is sometimes evident macroscopically in the form of multiple, thick garnet rich bands in hand

samples. In thin section, the garnets show various grain sizes, textures and subtle color variability. Garnet exists as Fe-rich almandine in Core-N, Core-S and Core-SS and only occurs as the Mn-rich variety spessartine in Core-SW.

Garnet bands comprising moderate- to well-crystalline garnet grains commonly containing fine magnetite (Fig. 2.4A and B) and acicular amphibole inclusions (Fig. 2.4B). These garnets show the typical high relief under the petrographic microscope. Zoning is another prominent texture exhibited by many garnet grains; the zonation itself is manifested by the internal distribution of fine to medium-grained magnetite inclusions. This is illustrated in Fig. 2.4C where magnetite inclusions show high-density distribution at the core which declines sharply at the rim. This is, however, not an omnipresent feature as other garnet grains may not exhibit magnetite inclusions at all (Fig. 2.4D) or, if they do, it is not systematically developed from rim to core (Fig. 2.4C). Another form of zoning develops as a result of partial alteration of garnets grains with characteristic chlorite rims and heterogeneous cores containing large magnetite inclusions. Most other garnet crystals are randomly distributed with variable shapes and sizes but dominated mostly by the typical equant "stubby" habit. Many of these garnet grains show at least partial alteration and deformation (Fig. 2.4E).

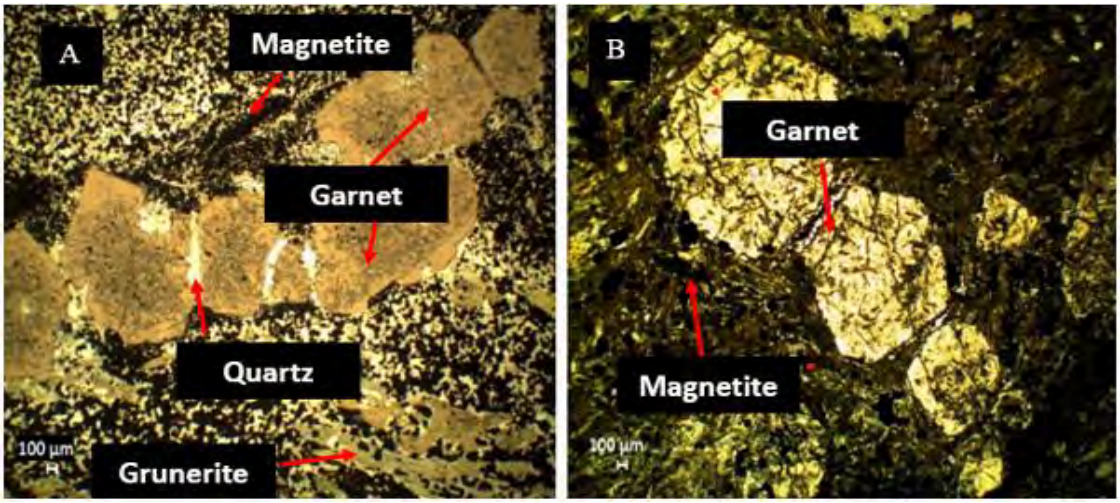

Figure 2.4 A-B: Photomicrographs illustrating various textures and grain sizes of Xaudum Iron-formation garnets under plane polarized light. A and B show garnet bands formed by different garnet solid-solution end-members. (A) Almandine garnet band. (B) Spessartine garnet band with fine acicular amphibole crystals included in garnet grains.

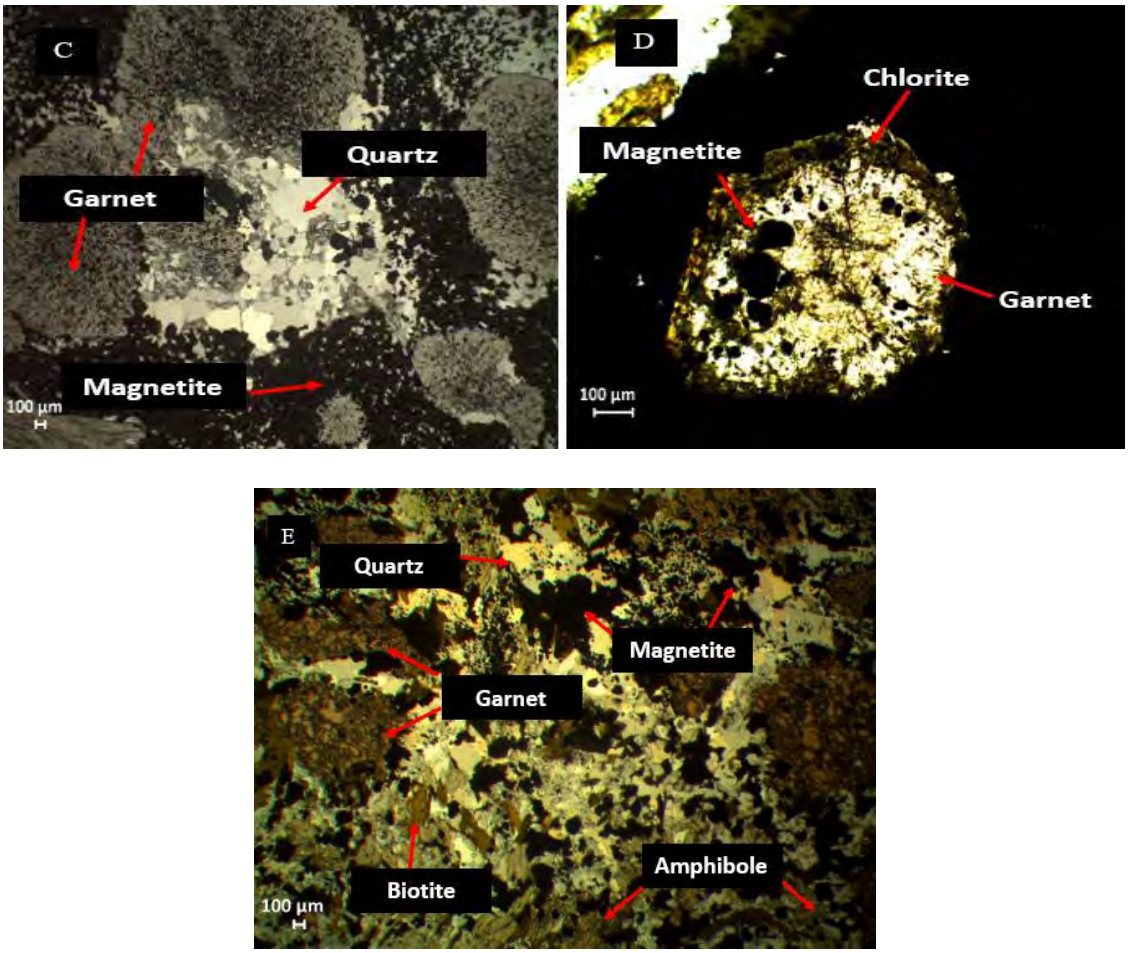

Figure 2.4 C-E: Photomicrographs illustrating various textures and grain sizes of Xaudum Iron-formation garnets under plane polarized light. (C) Zoned garnet with magnetite-free rim and magnetite rich core. (D) Zoned garnet with unaltered core and few magnetite inclusions and chlorite alteration at the rim. (E) Medium-sized, anhedral garnet grains containing magnetite inclusions. Fine-grained quartz, magnetite, amphibole and/or biotite crystals form the matrix in all instances.

Biotite

Biotite is a relatively uncommon phase. It occurs as moderate to well-shaped grains ranging from 0.5 to 1 mm in size, exhibiting dark brown to yellow pleochroism (see Fig. 2.3B), with some grains hosting fine magnetite inclusions. Biotite crystals are found in quartz and amphibole-rich bands either as sparsely distributed grains with no preferred orientation (see Fig. 2.8B) or defining a schistose texture. In some instances, biotite pressure-shadows appear to form around equant garnet grains (Fig. 2.6B).

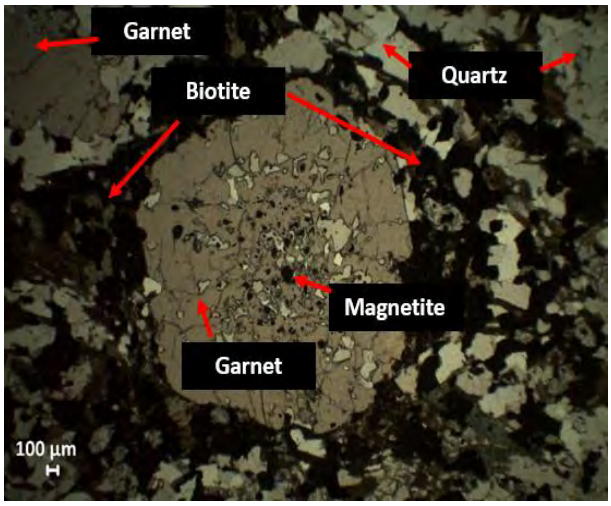

Figure 2.5*:* PPL photomicrograph illustrating biotite defined foliation enveloping surrounding garnet grains forming pressure shadows.

Chlorite

Chlorite is the least abundant mineral phase. When it does occur in local abundance, it displays fine, usually orientated subhedral aggregates as "flakes" with characteristic green pleochroism, usually in quartz matrix (Fig. 2.7A). Another common occurrence of chlorite, as indicated above, is in the form of retrograde alteration rims after garnet grains (Fig. 2.7B).

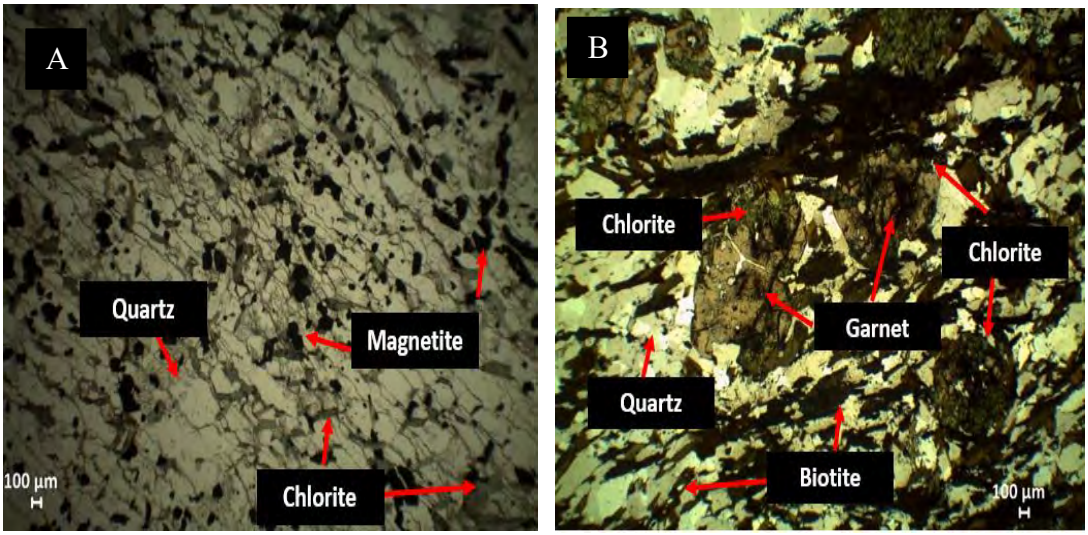

Figure 2.6: Photomicrographs illustrating various textures and grain sizes of Xaudum Iron-formation garnet under plane polarized light. (A) Fine foliated chlorite flakes in quartz matrix. Fine-grained magnetite randomly distributed throughout the quartz matrix. (B) Illustrating chlorite (green) replacing garnet grains. Foliated biotite enwrapping garnet in quartz matrix.

Accessory minerals

Accessory minerals present in the XIF are apatite, sulphides (pyrite, pyrrhotite and chalcopyrite) and rutile. Apatite forms fine equant crystals that may develop in sparsely populated bands or localized granular mosaics in association with coexisting calcite, magnetite and quartz. Sulphides are very uncommon and randomly distributed, with pyrrhotite characteristically occurring as medium-grained anhedral grains and aggregates associated with granular quartz and chlorite wisps (Fig. 2.8). Finally, rutile occurs as occasional, fine, high-relief grains and aggregates with characteristically deep orange to yellow internal reflections under reflected light.

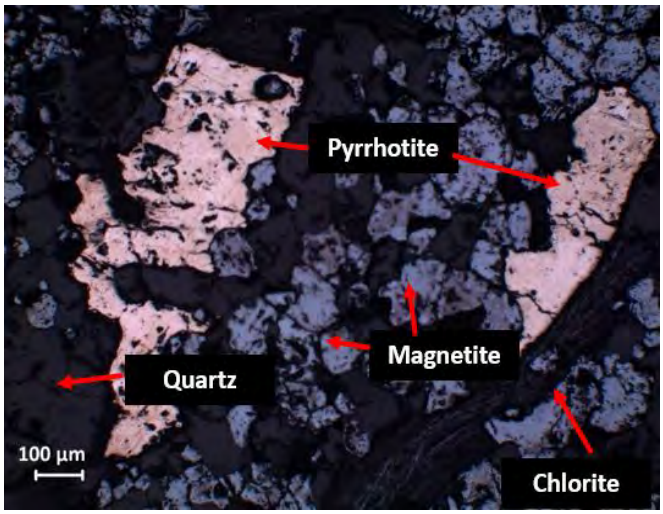

Figure 2.7: Reflected light PPL photomicrograph illustrating medium sized pyrrhotite crystals aligned with chlorite wisps in a quartz matrix.

2.1.2 Diamictite

Diamictite facies comprise typically mixed material in terms of texture and mineralogy. This ranges from abundant phyllosilicates (muscovite, biotite), quartz, magnetite, garnet, feldspar (mainly plagioclase) and lesser calcite, while mm- to cm-sized granitoid fragments appear to be the dominant dropstone material floating in the afore-mentioned matrix. All these phases show clear effects of re-crystallisation and annealing (e.g. granoblastic textures) as well as preferred orientation (foliation) typical of the metamorphic overprint affecting the rocks. Of note is the locally very high abundance of magnetite grains which locally approximate that in the XIF.

In the diamictites, quartz occurs as equant poor to moderately shaped crystals with grain sizes ranging from 0.1 to 1 mm. They commonly form granoblastic mosaics throughout the rock with some grains hosting fine magnetite inclusions (Fig. 2.8B). Magnetite is closely associated with quartz: it occurs as either fine disseminations occupying quartz interstitial space (Fig. 2.8A), as medium-grained granoblastic grains in quartz matrix or as apparent magnetite bands defining crude foliation and enveloped by quartz (Fig. 2.8B). Garnet occurs as medium to coarse grains with individual grains dominated by equant shapes yet varying widely due to local alteration and deformation.

Granitic clasts are dominated by feldspar (plagioclase) suggesting a largely plagio-granitic composition as large tabular grains. Interestingly, some of the plagioclase grains hosts fine magnetite and quartz inclusions (Fig. 2.8D)

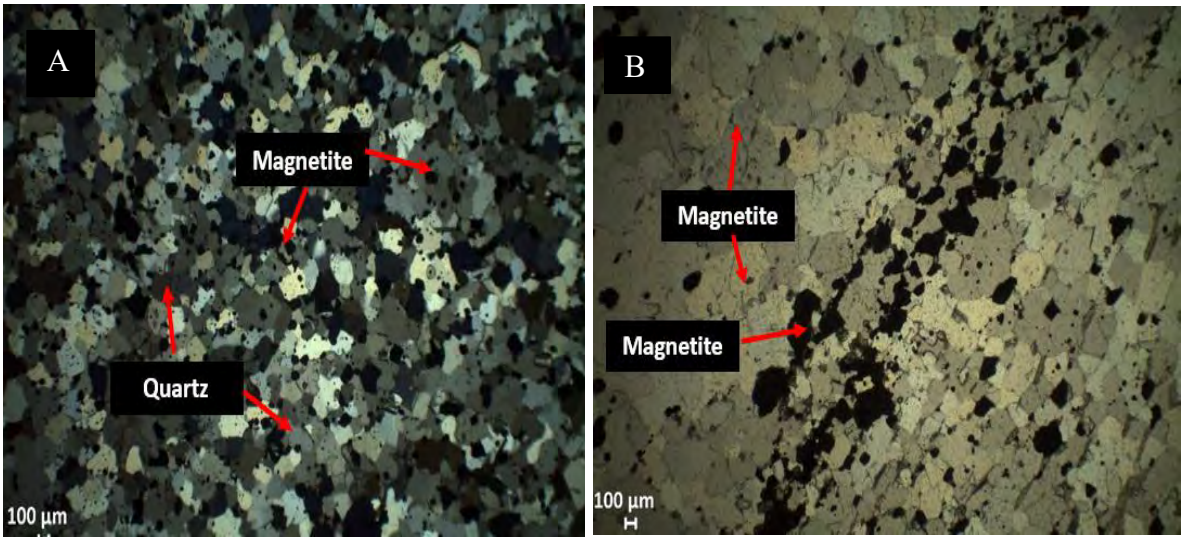

Figure 2.8 A-B: Photomicrographs illustrating mineral phases and textures in the diamictite. (A) Fine-grained granoblastic quartz matrix with magnetite inclusions. Disseminated magnetite also occupy quartz interstitial spaces. Image is in XPL for clearer quartz boundary identification. (B) Magnetite lamination mimicking biotite defined foliation. The lamination is separated by fine to medium-grained quartz bands developing granoblastic mosaics.

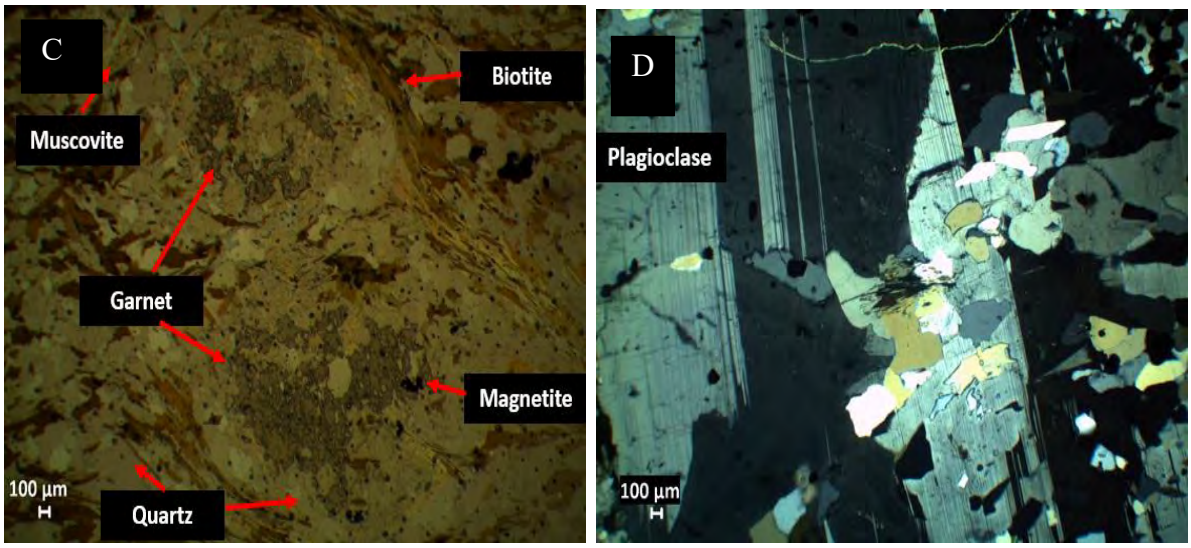

Figure 2.8 C-D: Photomicrographs illustrating mineral phases and textures in the diamictite. (C) Deformed garnet enveloped by foliated muscovite and biotite-rich matrix. (D) Large plagioclase crystals from granitic clasts.

2.2 Mineral chemistry

2.2.1 Results

Mineral chemical results of the main rock-forming minerals in the XIF are presented in Tables 2.2 and 2.3 below. Averaged results from individual mineral phases in drillcores N, S and SS are specifically presented in Table 2.2, whereas those of core SW are shown in Table. 2.3. This was done in order to highlight certain compositional differences between the mineralogy in drillcore SW against that of samples from the other three cores.

In terms of the prevailing mineral compositions shown in Table 2.2, the two dominant silicate minerals, namely garnet and amphibole, have compositions that approximate closely those for ideal almandine and grunerite respectively. The main chemical difference between the two is that the garnet is the main host of aluminum, whereas grunerite is essentially free of Al and is the second richest in Si silicate mineral after quartz. Chlorite and biotite are additional Al-rich phases. With regards to iron, highest abundances in weight percentage are contained in grunerite, whereas manganese is contained in relatively high amounts only in almandine garnet, at an average of about 3 wt%. The only other silicate mineral with manganese content higher that 1wt% is chlorite, and

this seems to agree with the fact that garnets are commonly altered into chlorite at their rims and therefore some of the Mn in garnet is taken up by retrograde chlorite.

Table 2.2: Average EPMA results (in wt.%) for major minerals in drillcores N, S and SS.

	Garnet (n= 62)	Amphibole (n= 15)	Biotite (n= 25)	Chlorite (n= 9)
SiO_2	37.99 ± 0.44	52.21 ± 0,04	38.24 ± 1,20	32.55 ± 0,61
Al_2O_3	20.24 ± 0.33	0.35 ± 0,15	17.91 ± 0,95	12.37 ± 0,89
TiO_2	0.05 ± 0,04	0.01 ± 0,02	1.83 ± 0,27	0.06 ± 0,03
Na_2O	0.01 ± 0,01	0.02 ± 0,02	0.17 ± 0,06	0.05 ± 0,02
MgO	1.53 ± 0,74	8.03 ±0,08	10.90 ± 1,04	24.47 ± 1,37
FeO	33.03 ± 4,56	37.78 ± 0,21	18.28 ±0,36	16.58 ± 1,40
MnO	3.23 ± 3,98	0.04 ± 0,03	0.14 ± 0,09	1.12 ± 0,14
CaO	4.12 ± 2.20	0.02 ± 0.01	0.03 ± 0.03	0.11 ± 0.06
K_2O	0.02 ± 0.01	0.03 ± 0.01	8.25 ± 0.90	0.12 ± 0.04
Total*	100.27	99.77	95.88	87.61

*Totals reported without H_2O for hydrous phases

Table 2.3 shows the mineral chemistry of minerals in drillcore SW. Contrary to low MnO values in the other three cores (Table 2.2), drillcore SW has clearly higher MnO values. MnO abundances are highest in garnet, which has a composition that appears intermediate between pure almandine and pure spessartine end-members, at a FeO/MnO ratio very close to the value of 1. In terms of the amphiboles, high-Mg cummingtonite compositions are now seen along with more typical Fe-rich varieties (grunerite), but both compositions are also enriched in Mn with contents of MnO ranging between 3 and 4wt%. Biotite is not very Mn-rich but its average content at 0.67 wt% is still much higher compared to biotite from the other 3 cores which have an average at 0.14 wt%. This suggests that core SW locally records an anomaly in manganese which through metamorphic mineral-forming reactions is reflected in the whole suite of metamorphic minerals observed.

Table 2.2: Averaged EPMA analysis results in (wt.%) for Core-SW minerals.

	Garnet	Amphibole		Biotite
	Spessartine (n=28)	Grunerite (n=22)	Cummingtonite (n=6)	(n=11)
SiO_2	37.78 ± 0.44	52.21 ± 0.68	55.6 ± 0.31	39.02 ± 0.01
Al_2O_3	19.60 ± 0.67	0.23 ± 0.06	0.14 ± 0.05	14.63 ± 0.08
TiO_2	0.11 ± 0.05	0.02 ± 0.02	0.01 ± 0.01	1.62 ± 0.90
Na_2O	0.01 ± 0.01	0.03 ± 0.01	0.02 ± 0.01	0.10 ± 1.60
MgO	0.96 ± 0.40	8.70 ± 1.24	16.16 ± 0.36	12.16 ± 0.07
FeO	19.77 ± 2.52	33.19 ± 1.86	21.20 ± 0.53	19.12 ± 0.09
MnO	18.81 ±1.35	3.84 ± 0.10	4.82 ± 0.22	0.67 ± 0.01
CaO	3.20 ± 0.56	0.22 ± 0.05	0.61 ± 0.21	0.01 ± 0.57
K_2O	0.03 ± 0.01	0.02 ± 0.01	0.03 ± 0.01	8.83 ± 0.00
Total	99.58	100.00	98.60	96.29

*Totals reported without H_2O for hydrous phases

The diagrams 2.4 and 2.5 below summarize and illustrate the characteristic signatures discussed above with regard to Al and Mn concentrations respectively in the studied rocks. The only additional piece of information is results from selected analyses of calcite in core SW as well, which also carries elevated Mn like the coexisting silicate minerals, attesting to the manganese anomaly mentioned above.

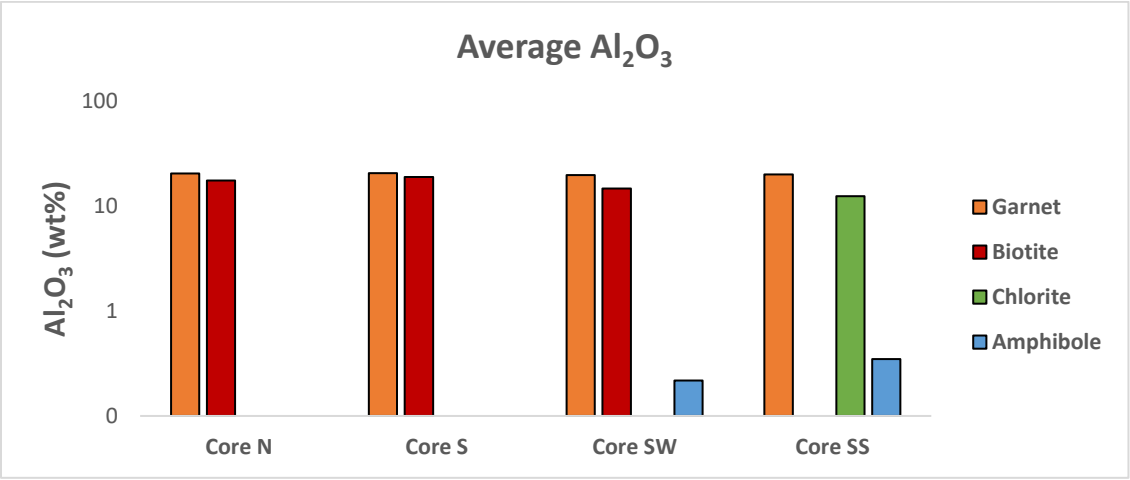

Figure 2.9: The average Al_2O_3 distribution in silicate minerals across the four cores.

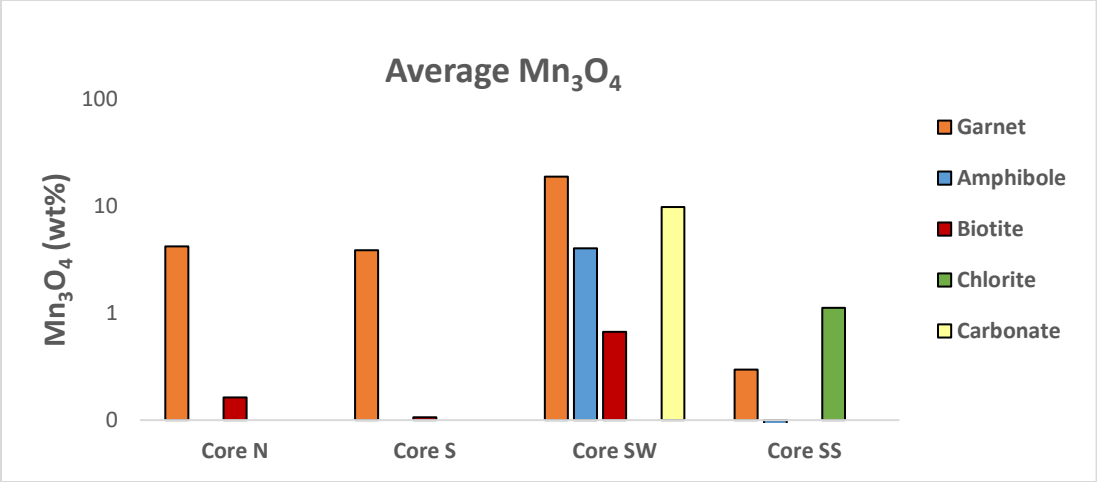

Figure 2.10: The average Mn_3O_4 distribution in the various minerals across the four cores.

2.3 Summary

The mineralogical and petrographic examination of the XIF presented, and that of the stratigraphically associated diamictites, was not aimed to provide a full and detailed account of every mineralogical and textural variability across all drillcores. It was intended instead to provide the essential background for the comprehensive geochemical examination of the same samples that will be presented in the next chapter. Therefore, a relatively condensed picture of the examined rocks was presented here. The key findings are as follows: firstly, the XIF is dominated by a typical assemblage of medium-grade metamorphic minerals that constitute amphibolite-facies metamorphosed IF. Dominant iron phase is magnetite, followed by amphibole, garnet, biotite, lesser chlorite and minor carbonate. The enclosing diamictites are dominated by abundant quartz, muscovite, biotite, feldspar and appreciable interstitial to banded magnetite. Dropstones are dominated by plagioclase-rich granite fragments.

Magnetite grains show various textures and sizes across the XIF, predominantly occurring as deformation bands with various thicknesses alternating with bands rich mainly in quartz and amphibole. Amphibole also occurs as characteristic blade-like crystals and aggregates, and frequently also occurs as bands of various thicknesses. Main amphibole phase is grunerite to grunerite-cummingtonite solid solution seen in drillcore SW only. Garnet mostly occurs as medium- to coarse-grained crystals that forms distinct bands. It exists as almandine towards more

spessartine-like compositions in drillcore SW. Biotite and chlorite are additional silicate phases of lesser modal abundance.

Compositionally, garnet is the main host of aluminum, followed by biotite and chlorite. This generates the expectation that the XIF is a relatively Al-rich iron formation facies which should reflect in the geochemical results that follow in the next chapter. Another element of interest is manganese, which shows enrichments in minerals of drillcore SW. This is where garnet approaches spessartine composition and the amphibole (grunerite-cummingtonite) is also more manganese-rich compared to the other drillcores. This means that there are lateral compositional variations in the XIF, especially with respect to manganese.

3. BULK GEOCHEMISTRY

3.1 Introduction

In the past, rare earth element (REE) and light stable isotope geochemistry have been the dominant applications used in understanding the origin and paleoenvironmental significance of BIFs (Perry et al., 1973; Fryer 1977a; Kaufman et al., 1990; Bau et al., 1997). During that same time, major and trace element geochemical data of BIFs were given relatively little attention in this field and this is apparent in the relevant literature (Davy, 1983). The main usage of bulk geochemistry was mainly as investigative tools in conjunction with mineral petrography of BIF (as they still are in the modern-day) and to outline geochemical features of BIFs around the world in an average sense (Gole, 1981; Gross, 1990; Horstmann and Halbich, 1995). In recent times, the reporting and availability of major and trace elements in BIF literature has increased considerably, and therefore such data have become more and more accessible and utilisable in determining the origin of NIFs (Cox *et al*., 2014). In this vein, trace and major element geochemistry will play a significant role in this study as they will be applied to constrain where possible the origin of XIF as an important objective of this study.

The few studies that have been carried out on the XIF contain relatively little geochemical information at bulk-rock level (Mojaki, 2009; Gaisford, 2010; Gerner, 2011; Witbooi, 2011; Mongalo, 2013; Baker, 2014; van Vuuren, 2015). In addressing this deficiency, this chapter will provide new information into major element and trace element geochemistry of XIF, includes some data on the associated diamictites. The bulk of this chapter will deal primarily with results and interpretations from the XIF itself, representing the total of 66 samples analysed (see Appendix B for all raw data). With regard to trace element geochemistry, the chapter will contain specific subsections dealing with transition metals, large ion lithophiles (LILE) and rare earth elements (REE). Much emphasis will be placed on aspects related to identifying statistically significant associations and their possible controls, constrain sources of elements where possible, and understanding redox processes in the primary environment through redox-sensitive elements and their behaviour.

3.2 Major Element Chemistry

3.2.1 Comparative considerations

In order to gain a perspective of how XIF element chemistry compares to Archean and Paleoproterozoic BIF and other contemporaneous NIF deposits around the world, a spider-gram showing the average major element chemistry of the various BIF and NIF is presented in Fig. 3.1 below. The data distribution shows high SiO_2 and Fe_2O_3 content, typical of BIF, with averages ranging broadly from 28 to 55 wt% and 12 to 55 wt % respectively. In this context, the XIF has the lowest SiO_2 value (28.6 wt %) and a second highest Fe_2O_3 value (54.8 wt %) after the Isua IF.

The element oxides CaO, MgO Mn_3O_4, Al_2O_3, Na_2O and K_2O are present typically in much lower amounts (less than 10 wt. %) in all these iron formations. The average CaO and MgO concentrations range from 1.8 to 7.7 wt % and 1.1 to 7.2 wt % for all the iron-formations, while the XIF has values of 2.1 wt % and 1.2 wt % respectively. Isua IF constitutes an exception because of its exceptionally high MgO content of 7.2 wt %. In unmetamorphosed BIF, the CaO and MgO concentrations are accounted for by the presence of carbonate phases (siderite, dolomite-ankerite and minor calcite) and Fe-Mg silicates (greenalite and minnesotaite) (Fig. 3.1). In the metamorphosed XIF, the CaO content is reflected in minor calcite as the carbonate phase and MgO content reflects the combined control by mica, chlorite, amphibole and, much less so, garnet. The latter, in the form of a manganese-rich end-member spessartine garnet accounts for the bulk Mn_3O_4 content in XIF: XIF has in fact the highest average value of 0.9 wt. % compared to all the NIF and BIF included in Fig. 1.3.

The elements Al_2O_3, Na_2O and K_2O are present in low concentrations generally, and in diagenetic to low metamorphic grade BIF are contained in silicate phases such as stilpnomelane, riebeckite, greenalite and ferri-annite. The XIF is of medium metamorphic grade and thus contains amphibole and garnet-rich mineral assemblages as Al carriers instead of the aforementioned mineral assemblages. NIFs have Al_2O_3 content ranging from 0.9 to 5.5 wt. % which is generally higher than Archean and Paleoproterozoic BIF which ranges from 0.2 to 0.5 wt. %. An exception to this

is the aluminous and graphitic sample of the Archean Isua BIF which has an exceptionally high Al_2O_3 average value of 4.5 wt. % above the XIF average value of 1.7 wt. %. The high Al_2O_3 in NIF and XIF suggests a high detrital input in the paleobasin during the Neoproterozoic period. The Algoma and Superior-type BIF lack this detrital signature signifying that they are essentially pure chemical sediments. Regarding the alkalis (Na_2O and K_2O) their concentrations share similar characteristics with respect to all the iron-formations. The Hotazel BIF has the lowest values, followed by the Rapitan IF and the XIF with values of 0.1 and 0.2 wt. % respectively. This trend changes at the highest end of alkali concentrations, where Braemar IF has the highest K_2O of 1.1 wt. % and the Chuos BIF has the highest Na_2O values of 2 wt. %.

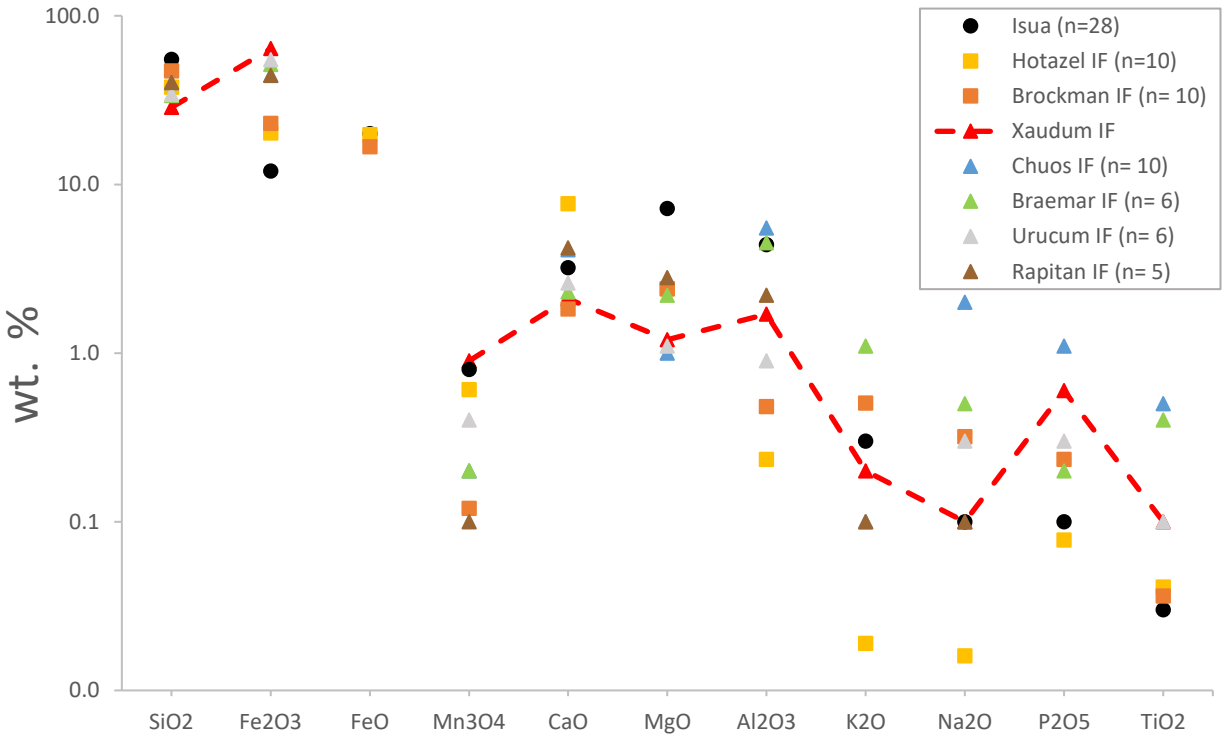

Figure 3.1: Spidergram illustrating average major element data for different Archean (circle shaped), Paleoproterozoic (square shaped) and Neoproterozoic (triangle shaped) iron-formations. Archean BIF is by represented the Isua BIF (Dymek and Klein, 1988), Paleoproterozoic BIF are represented by the Hotazel iron-formation (Tsikos and Moore, 1997) and Brockman iron-formation (Dales Gorge Member) (Trendall and Brockley, 1970). Neoproterozoic iron-formations are represented by the Chuos iron-formation (Breitkopf, 1988), Braemar iron-formation (Lottermoser and Ashley, 2000), Urucum iron-formation (Klein and Ladeira, 2004) and the Rapitan iron-formation (Klein and Beukes, 1993).

Archean and Paleoproterozoic BIFs generally have very low TiO_2 content and low P_2O_5 (down to ppm level) compared to the XIF and NIFs in general. Low TiO_2 in Archean and Paleoproterozoic BIFs further supports the dearth of detrital input into the Algoma and Superior-type BIF, contrary to the somewhat high average value of up to 0.5 wt. % in Chuos IF. XIF and Urucum IF have equal average values of 0.1 wt. %. Mineralogically, the P_2O_5 and TiO_2 contents reflect accessory apatite and rutile grains in XIF.

Before engaging with the inter-element relationships of XIF in the following section, it is important to point out that samples from drillcore SW show, as expected, the highest range in manganese oxide concentrations. These reach the maximum of 11.6 wt. % at an average of 2.8 wt. % with regards to Mn_3O_4 (Fig. 3.2). This will be explored further in the following sections.

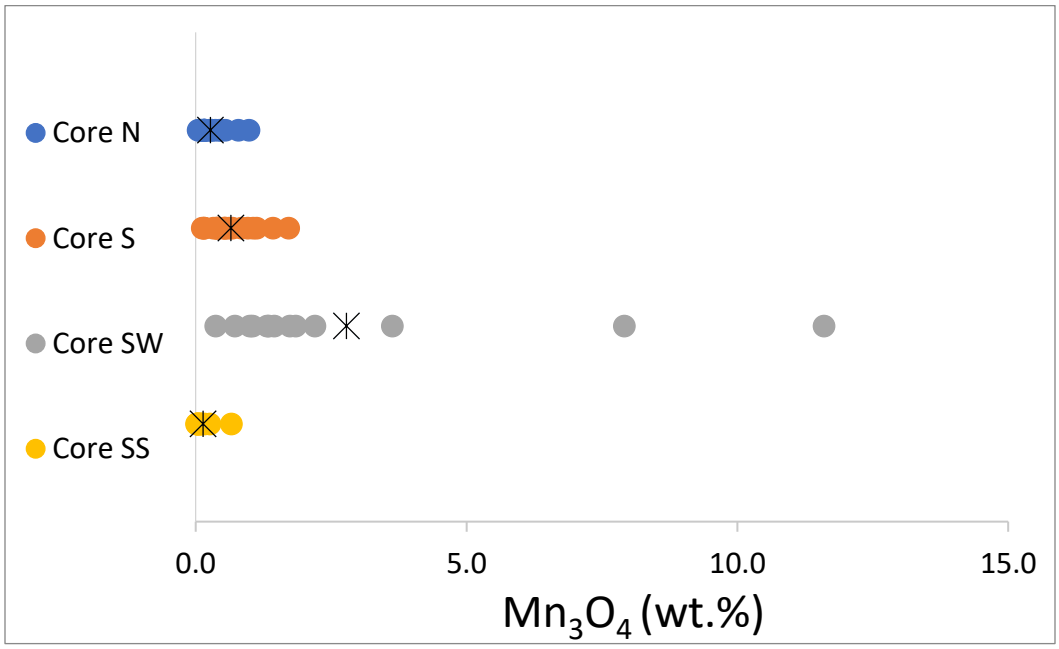

Figure 3.2: Plot showing Mn_3O_4 content in the selected XIF cores.

3.2.2. Inter-elemental relationships

The inter-elemental relationships against Fe_2O_3 of the XIF are presented on the bivariate plots of Fig. 3.3 A-F, to further investigate major element geochemical relationships of potential value. The analytical results are plotted the same way as reported in Appendix B, namely as the major oxide (in order of declining abundance) Fe_2O_3, SiO_2, CaO, Al_2O_3 and Mn_3O_4. As expected, the

oxides Fe_2O_3 and SiO_2 (Fig. 3.3 A) make up the bulk of the sample mass. The concentration of Fe_2O_3 ranges from 11.5 to 90.1 wt. % (see appendix B). The sample SW-164.20, which has the lowest Fe_2O_3 at 11.5 wt. %, is poor in magnetite and has abundant garnet and amphibole. By contrast, the drillcores S and N in particular host a magnetite rich domain that was sampled independently and expectedly registered Fe_2O_3 content up to 89.2 and 90.1 wt. % respectively in the two drillcores. The strong antithetic correlation of Fe_2O_3 against SiO_2 is related to the well-known closure effect in BIFs between iron and silica.

The Mn_3O_4 content in three cores (N, S and SS) ranges from 0.1 to 1.7 wt. % (Fig. 3.2 B), whereas drillcore SW has a Mn_3O_4 range of 0.4 to 3.6 wt. %. This core contains samples SW-145.90 and SW-164.20 which have atypically high values of 11.6 and 7.9 wt. % correspondingly. The high Mn_3O_4 in core SW reflects abundant spessartine garnet and lesser cummingtonite. The Mn_3O_4 spike in Core SW and the broad anti-correlation relationship between Mn_3O_4 and Fe_2O_3 shown in (Fig 3.2 and 3.3B) may be suggestive of lateral variation in Mn:$Fe_{(aq)}$ conditions in paleobasin, which will be re-visited later.

The CaO content in the XIF is relatively low compared to most of the featured BIF and NIF in Fig. 3.1, and ranges from 0.2 to 7.5 wt. % with an outlying high value of 11.3 wt. % in sample N-166.70 (Fig. 3.2 C). This impacts the overall CaO average in the same core which reaches the value of 2.6 wt %, that is higher than the rest of the cores. Bulk MgO values range from 0.1 to 3.8 wt. % in all the cores and has a maximum value of 6.2 wt. % in the same sample N-166.70 which also has the highest CaO value. The high CaO and MgO correspond to minor dolomite grains present in the sample. This correlation is not recorded in the rest of the samples from other cores. There, MgO is controlled mainly by silicate minerals such as mica, chlorite and amphibole that contain minor to no CaO. Minor calcite grains are present in drillcore N corresponding to its high CaO average.

The Al_2O_3 content of XIF is considered atypically high compared to Paleoproterozoic BIFs with a range from 0.2 to a maximum of 6.6 wt. % (Fig. 3.3 D). Two samples namely S-141.80 and SW-164.20, are outliers with very high values of 11.9 and 9.7 wt. % respectively. Amongst all the cores, drillcore SW has the highest Al_2O_3 average of 2.6 wt. % followed by an average of 2.1 wt. % in Core-SS. The high 11.9 wt. % of Al_2O_3 corresponds to high MgO content in sample S-141.80

and is accounted for by abundant biotite. The second highest Al_2O_3 value is in sample SW-164.20 with abundant spessartine garnet as mentioned earlier. Like Mn_3O_4 in drillcore SW, Al_2O_3 shows a broadly antithetic relationship with Fe_2O_3 but does not show any such relationship in the other cores. Finally, TiO_2 is an accessory element oxide with values ranging from 0.01 to 0.8 wt. % (Fig. 3.3 E).. High values reflect samples with accessory rutile seen mainly in drillcores SS and SW.

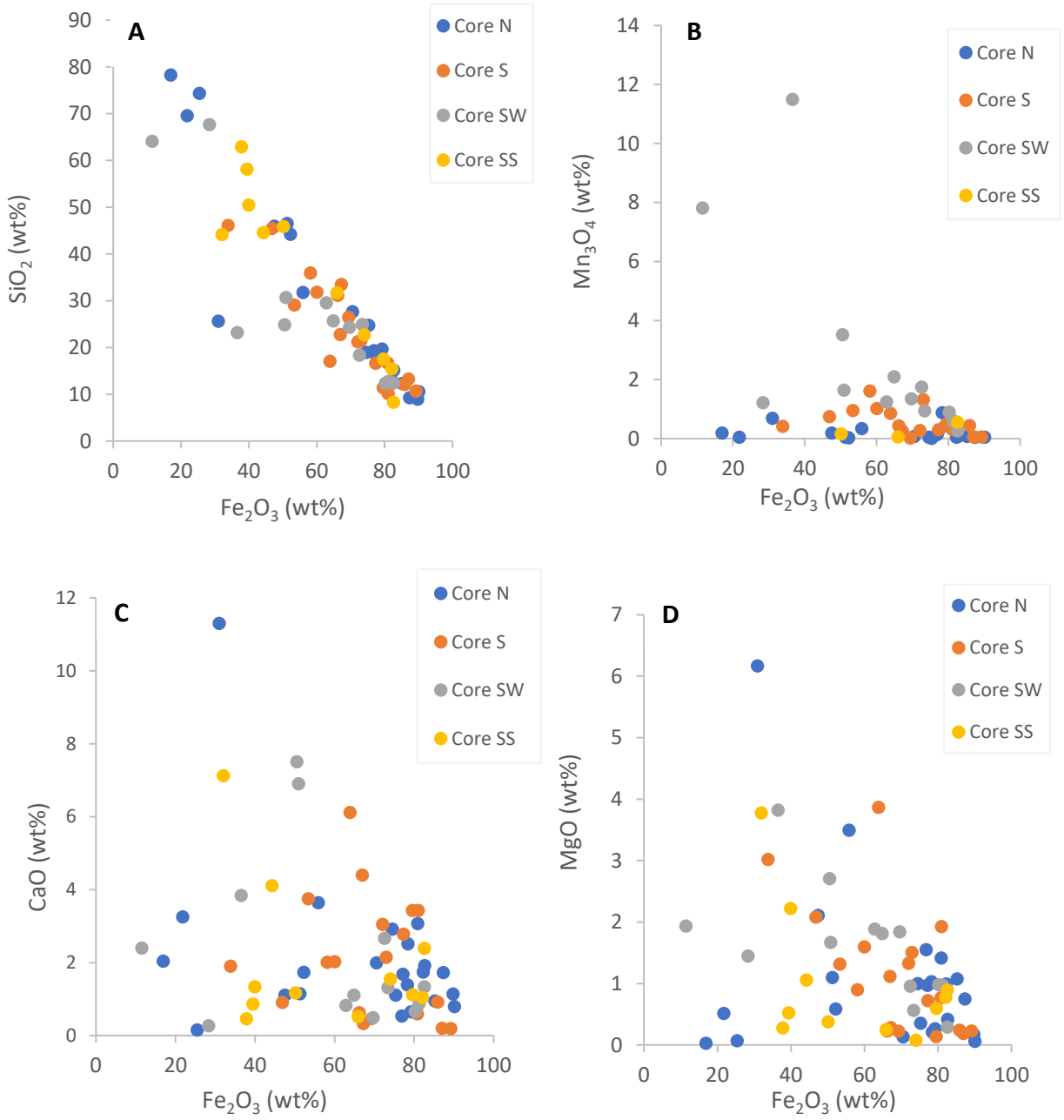

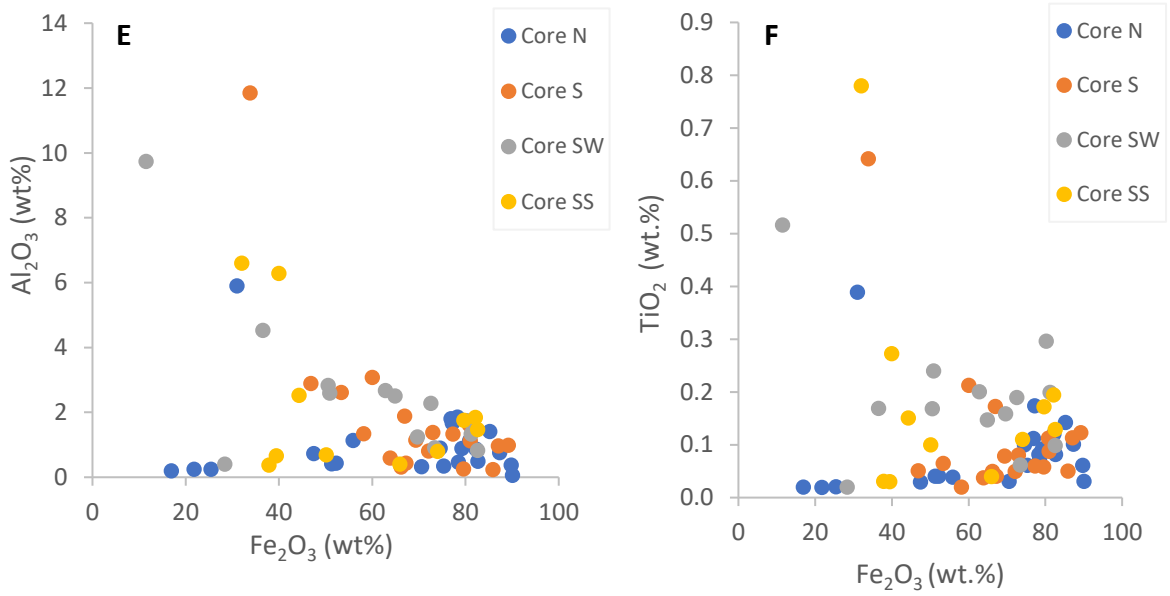

Figure 3.3: Bivariate diagrams showing XIF geochemical relationships of major elements in relation to Fe_2O_3.

3.3 Trace Element Chemistry

Chemical elements are referred to as trace elements when their concentration is below 0.1 wt. % of the whole rock composition. As low as their abundance is, trace elements are a very useful tool in BIF studies towards interpreting the physicochemical conditions in the environment of deposition and constraining the source of materials (Reddy and Sashidhar, 1989; Klein and Beukes, 1993; Klein, 2005; Cox *et al.*, 2016). For example, the contamination of BIF chemical sediments by volcanic ash, exhalative material and terrigenous clastic particles can be gleaned from the trace element geochemical signatures and specifically abundances and relative ratios of large ion lithophile elements (LILE), high field strength elements (HFSE) transition metals and rare earth elements (REE)(Bau and Dulski, 1993). The application and utility of trace elements in BIF is therefore central in meeting key objectives of this study. This chapter will therefore explore trace elements subdivided in the above groupings, that is, LILE, HFSE, transition metals and REE of the XIF with a view to constraining the redox state and conditions of the paleonevironment of deposition, and where possible, the source of the different elements.

In contextualizing the trace element geochemistry of XIF (excluding the REE) in global terms, a spidergram showing its average trace element chemistry against that of selected Algoma and Superior-type BIF and NIF deposits is shown in Fig. 3.4 below. It is important to note that the metal molybdenum (Mo) which will be discussed later in this chapter, has not been included in the spidergram due to the lack of data from most of the source publications used.

The average value of trace elements in all the BIFs and NIFs shown in Fig. 3.4 below is generally less than 100 ppm. On a broader scale, XIF and other NIF trace elements behave comparably. For transition metals, XIF shows an overall depletion relative to other BIF and NIF, particularly for Zn, Ni, Cu and Cr that are commonly associated with volcanogenic hydrothermal input. Exception here is the Archean Isua BIF has high Ni content due to higher influx of hydrothermal fluids from Ni-rich komatiites into Archean oceans as suggested by Konhauser *et al*, (2011). Unlike the depleted transition metals, the abundance of Co in XIF shows a relatively high value of 11.8 ppm, which is higher than most Paleoproterozoic BIF. High Co abundances in XIF may be attributed to high manganese contents and possibly offer constraints on the redox regime of the paleobasin during the Neoproterozoic. Relative to all the other BIF and NIF, XIF is also highly enriched in the transition metals V and less so Sc. Vanadium, in particular, shows a second-highest value of 57 ppm compared to the other BIFs and NIF displayed, suggesting a possible control by the abundant magnetite with which it is commonly afiliated.

With regard to LILE concentrations in XIF, particularly elements such as Rb, Cs and Ba, their average abundances are around 100ppm or higher which are broadly comparable to other NIF deposits. High LILE values often correspond to extensive adsorption onto clay minerals (Rudnick, 1998), and therefore are expected in metamorphic phyllosilicate minerals, such as biotite and muscovite, that derive from them. Contrary to the above elements, Sr abundances in the XIF are low at an average of 26.2 ppm which is probably owed to the lack of Ca-Mg carbonate phases in the rocks. Finally, concerning HFSE, the element Zr has highest average value of 94 ppm compared to other BIF and NIF, attesting to increased terrigenous detritus in the rocks which agrees with the high Al_2O_3 values seen earlier. Mineralogically, the Zr in the XIF corresponds to minor zircon grains and substitutions for Ti in accessory ilmenite and rutile grains. The remaining HFSE are all below 10 ppm and show a broad similarity to the Rapitan IF. The Isua BIF shows extremely low LILE and HFSE values compared to all the BIF and NIF.

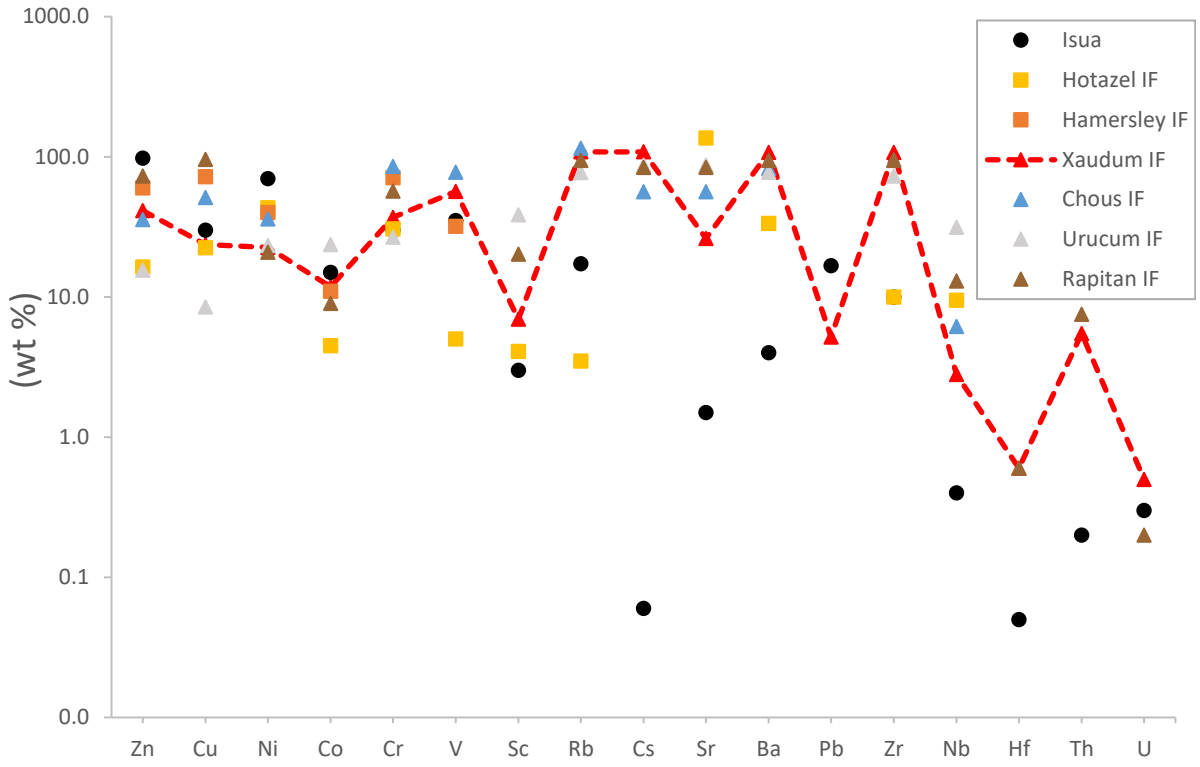

Figure 3.4: Spidergram illustrating average trace element data for different Archean (circle shaped), Paleoproterozoic (square shaped) and Neoproterozoic (triangle shaped) iron-formations. Archean BIF is represented by the Isua BIF (Dymek and Klein, 1988), Paleoproterozoic BIF are represented by the Hotazel iron-formation (Tsikos and Moore, 1997) and Hamersley iron formation (Trendall and Brockley, 1970). Neoproterozoic iron-formations are represented by the Chuos iron-formation (Breitkopf, 1988), Braemar iron-formation (Lottermoser and Ashley, 2000) and Rapitan iron-formation (Klein and Beukes, 1993).

3.3.1 Large Ion Lithophiles (LILE) and High Field Strength Elements (HFSE)

LILE are trace elements with a large ionic radius to charge ratio and ionic radii bigger than those of Ca^{2+} and Na^{+}, two major cations common in rock-forming minerals (Rudnick, 1998). These elements comprise Rb, Cs, Sr, Ba and Pb, tend to be concentrated in the melt phase of igneous systems during crystallization (i.e. are incompatible) and are usually mobile during weathering and metamorphism (Rudnick, 1998). In chemical sedimentary environments, they are commonly associated with carbonates and underpin the chemical nature of BIFs. The LILE concentrations of XIF (see Appendix B for the raw data) including K_2O, are plotted against Fe_2O_3 in Fig. 3.5 below. The data show broad scatter in almost all instances (ranges from 5 to 105 ppm), a high proportion of very low values especially for Ba and Cs, and no statistical correlation with bulk-rock Fe.

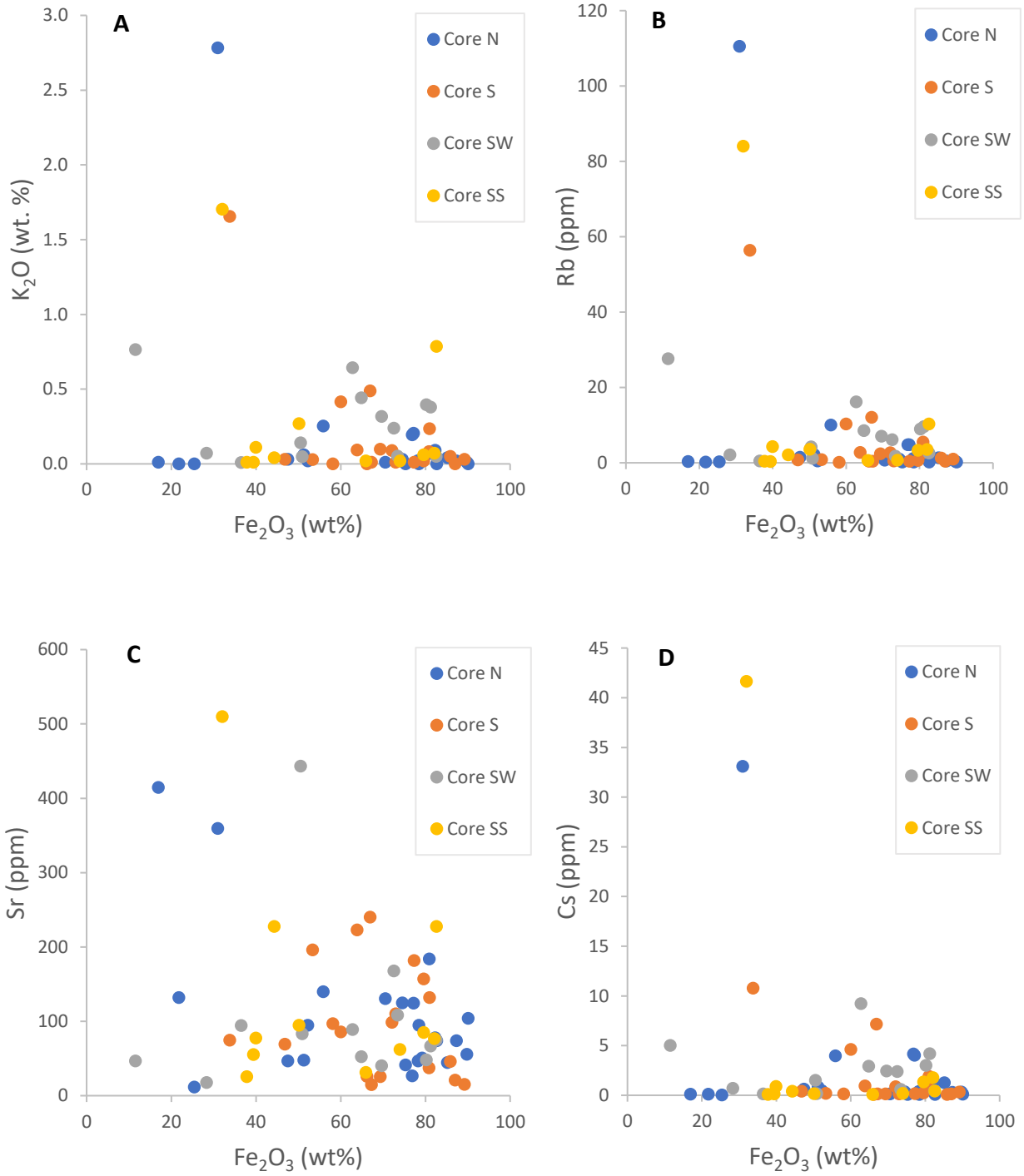
A
B
C
D
Core N
Core S
Core SW
Core SS
K_2O (wt. %)
Rb (ppm)
Sr (ppm)
Cs (ppm)
Fe_2O_3 (wt%)

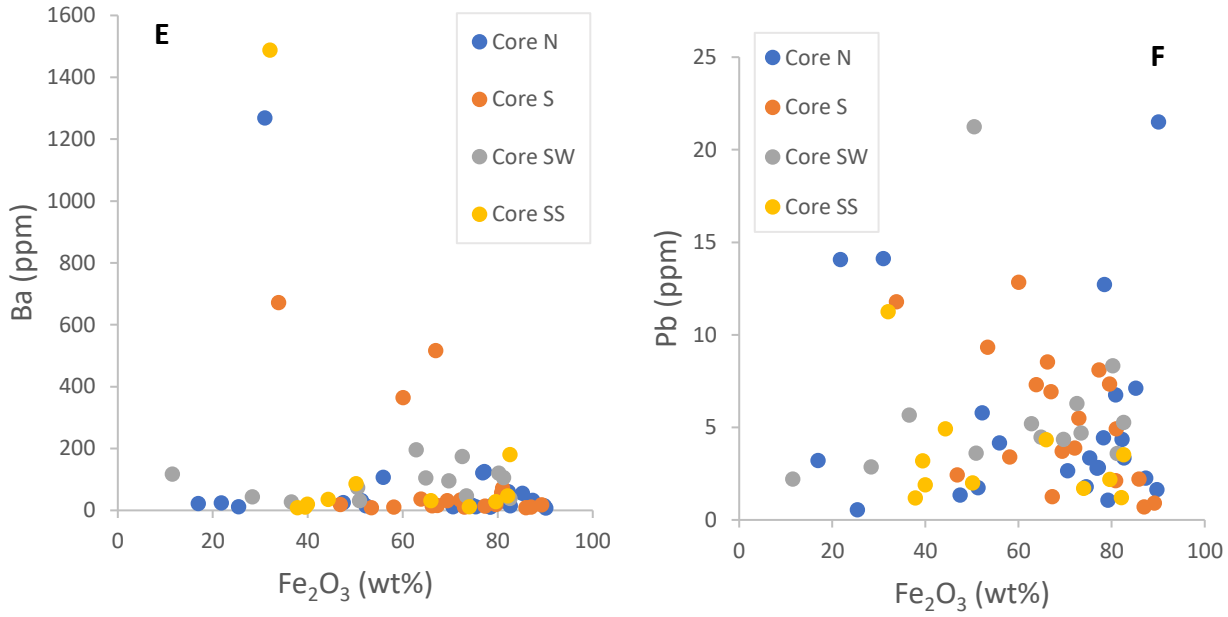

Figure 3.5: Bivariate diagrams illustrating the relationship between LILE and Fe_2O_3

The HFSE are elements with a high ionic charge and relatively small radius (Rudnick, 1998). They include the elements Th, Zr, Hf, Nb, U and Ta which are generally insoluble in fluids by virtue of their high ionic charge to radius ratio. Consequently, these elements tend to be immobile during weathering and metamorphism (Rudnick, 1998). Therefore, the presence of HFSE and their correlation to detrital species such as Al_2O_3 in geochemical studies denotes the levels of terrigenous clastic contamination. For that reason, the HFSE abundances of XIF (see appendix B for the raw data) have been plotted against Al_2O_3 in the binary diagrams A-F of Fig. 3.6 to attest for possible detrital origins.

The values of HFSE range widely from 1 to 94 ppm, with U having the lowest and Zr the highest concentrations. The TiO_2 vs Al_2O_3 diagram (Fig. 3.6 A) has been included and shows a positive linear relationship with a R^2 value of 0.75 in XIF. The relationship corresponds to the overall common origin of the two species through detrital input. Similar relationship is seen in the Zr, Hf and Nb vs Al_2O_3 diagrams of Fig. 3.6 B and D, with a strong positive correlation of a R^2 value of 0.83 and 0.88 for the first two respectively, whereas the Nb relationship appears to be compromised by a single outlier.

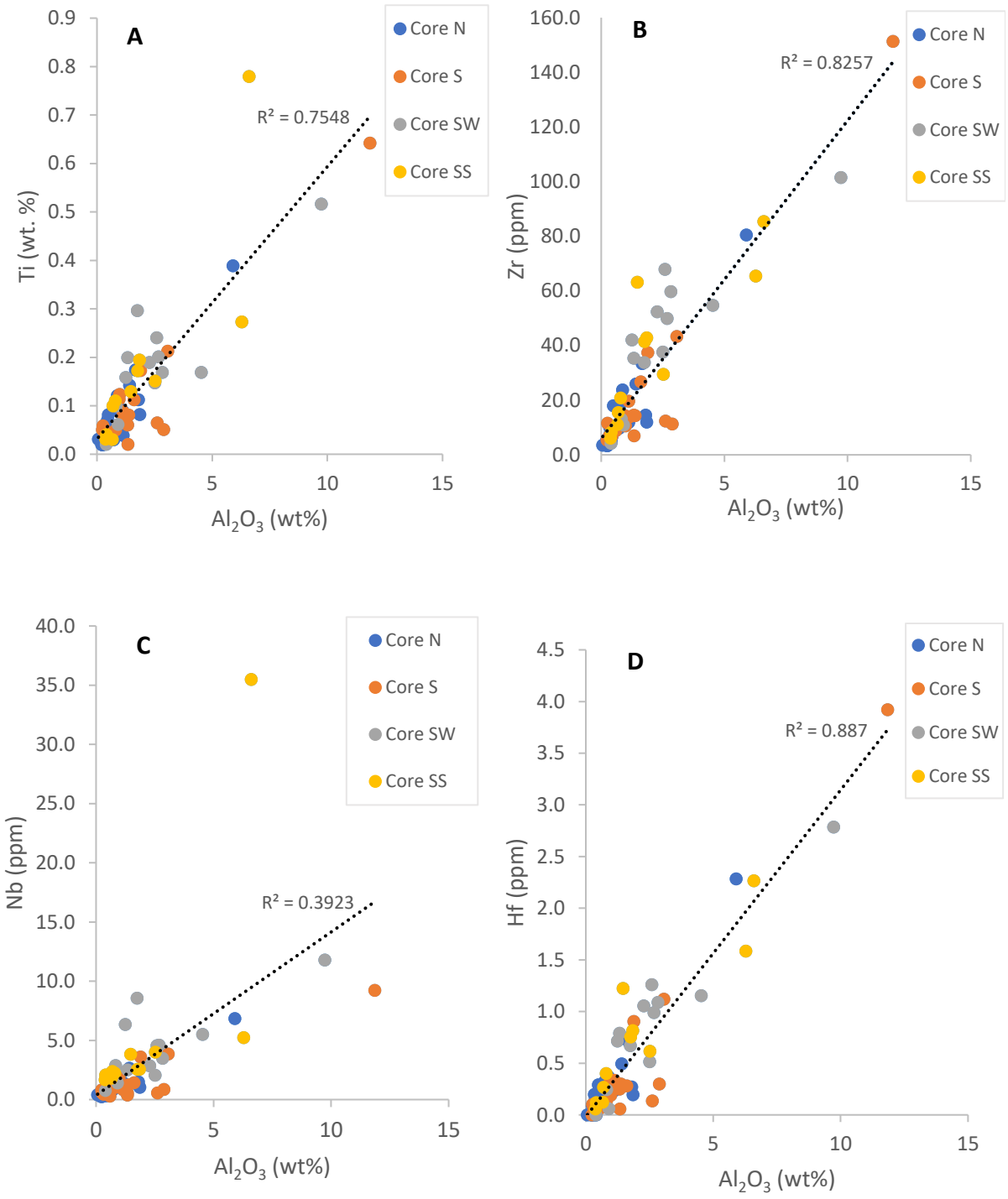
A
Core N
Core S
Core SW
Core SS
R² = 0.7548
Ti (wt. %)
Al2O3 (wt%)
B
R² = 0.8257
Zr (ppm)
C
R² = 0.3923
Nb (ppm)
D
R² = 0.887
Hf (ppm)

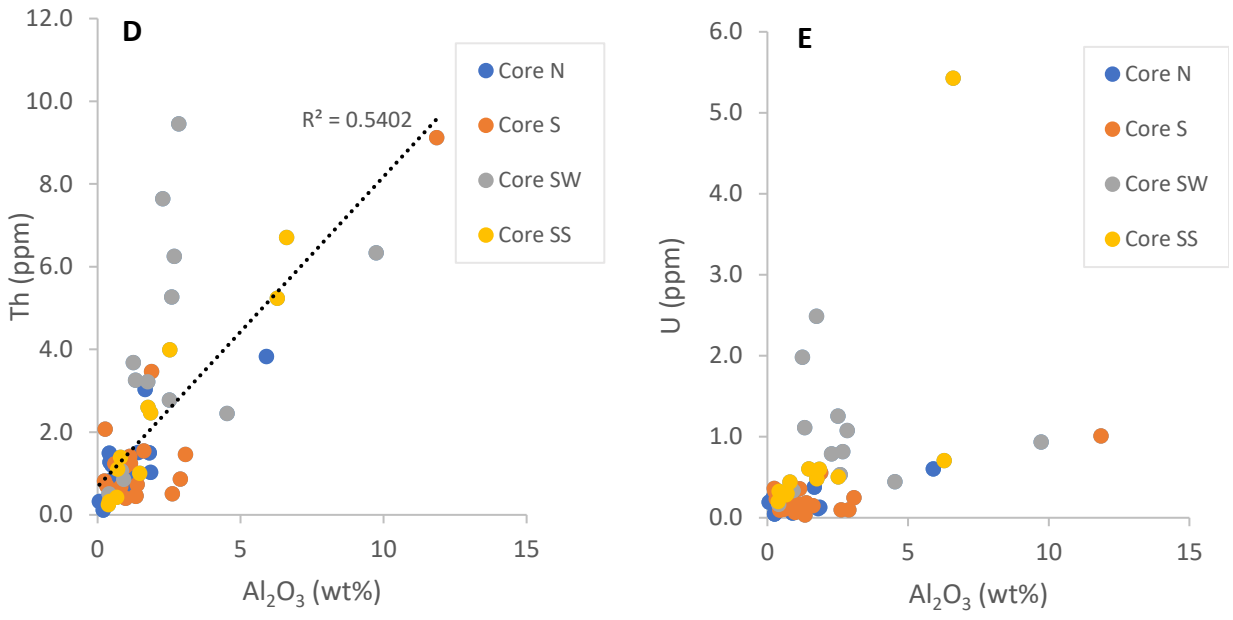

Figure 3.6: Bivariate diagrams illustrating the relationship between HSFE and Al_2O_3

3.3.2 Transition metals

The transition metal group includes iron and manganese as major element components and typically the elements Zn, Ni, Cu, Cr, Co, Mo and V as trace components. Iron and manganese are the most important transition metals because of their high abundance and their similar chemistry to each other, which gives them also the close affiliation to the trace transition metals listed above. The behavior of the trace transition metals Co, Cr, Ni, Cu, Zn, and Mo towards iron and manganese may vary as a function of the dominant redox conditions in the ocean (Anbar, 2008). These metals are insoluble under oxic conditions, however, under anoxic conditions they become reduced to soluble species with lower valencies (Calvert and Perderson, 1993). Co and Mo are well-known redox proxies, and their redox-controlled partitioning towards iron and manganese has been extensively studied in case studies of ancient and modern sedimentary systems alike (Bertine, K.K., Turekian, 1973; Crerar and Barnes, 1974; Burns, 1976; Anbar, 2008; Armstrong, 2008; Cornu *et al.*, 2011; Scholz, McManus and Sommer, 2013; Swanner *et al.*, 2014).

In order to bond metals such as Co and Mo to iron and/or manganese under anoxic environments, certain thermodynamic conditions (Eh, pH and temperature) in the oceans must be met. Dissolved Co^{2+} would have to be oxidized to Co^{3+} in the same Eh–pH space where Mn^{2+} oxidation takes place, thereby producing the oxidation of Co^{2+} and adsorption of Co^{3+} to precipitated Mn^{3+} and Mn^{4+} oxides (Swanner *et al.*, 2014). A similar process followed for adsorption of Co^{3+} to Fe^{3+}, however at lesser Eh and pH for Fe^{3+} compared to Mn^{2+} and Mn^{4+} (Swanner *et al.*, 2014; Kurzweil *et al.*, 2016). For adsorption of Mo to Mn^{3+}, similar thermodynamic conditions would have been required (Crerar and Barnes, 1974). This adsorption is linked to a change from tetrahedral (MoO_2^{-4}) to octahedral coordination (adsorbed Mo) in the absence of H_2S (Kurzweil *et al.*, 2016). This section will therefore explore the relationships of Fe_2O_3 and Mn_3O_4 against Mo, Co, as well as Zn, Cu, Ni, Cr, V and Pb in bivariate diagrams. This will be achieved by plotting the data first against Fe_2O_3 and then against Mn_3O_4, with more attention given particularly to Co and Mo to assess any potential correlations which could be used as redox proxy during XIF deposition.

The abundance of transition metals in XIF is relatively low with regards to NIF and Algoma and Superior-type BIF. Concentration ranges are from as low as 11 ppm to as high as 56 ppm for Co and V respectively. The only elements that appear to show some degree of correlation (Fig. 3.7) with Fe_2O_3 abundances are Co and V (Fig. 3.7 E and H respectively), while the remaining transition metals plotted do not show any systematic relationship with respect to Fe_2O_3. It is noteworthy that core-specific data from drillcores SS and SW show a relatively stronger positive correlation of V against Fe_2O_3 compared to the entire dataset, with corresponding R^2 values of 0.75 and 0.61 respectively. As previously mentioned, this relationship is most probably mineralogically controlled and linked to the affinity of V to substitute for Fe in magnetite grains.

The Co vs Fe_2O_3 plot (Fig. 3.7 E) shows no apparent statistical relationship but if only the samples from drillcore SW are considered, it actually appears to show a crudely antithetic relationship with an R^2 value of 0.53. This relationship suggests that Co is probably associated with a major phase that correlates antithetically with Fe. Considering the relationship between transition metals and Mn_3O_4 as shown in Fig. 3.8 A-H below, similarly to the Fe_2O_3, the bulk of the transition metals do not show any statistical relationship to Mn_3O_4. However, Co shows a good positive relationship with Mn_3O_4 (Fig. 3.8 E) at an R^2 value of 0.68. This suggests that Co is affiliated with primary Mn-rich precipitates that are now captured mainly in the metamorphic garnets and amphiboles.

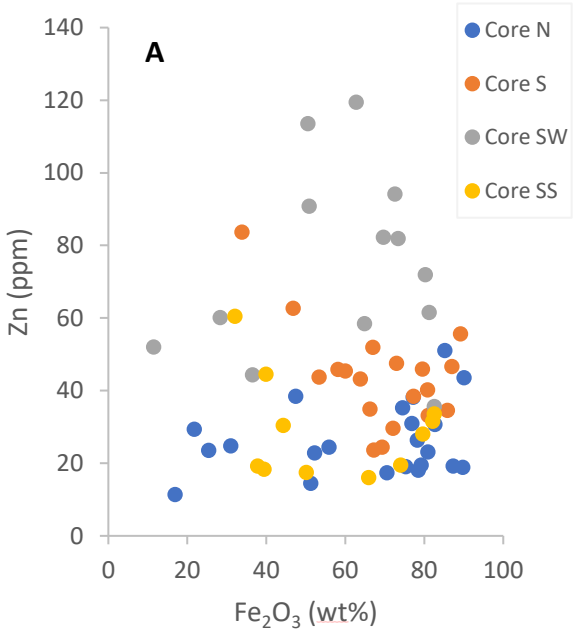
A
Core N
Core S
Core SW
Core SS
Zn (ppm)
Fe_2O_3 (wt%)
0
20
40
60
80
100
120
140

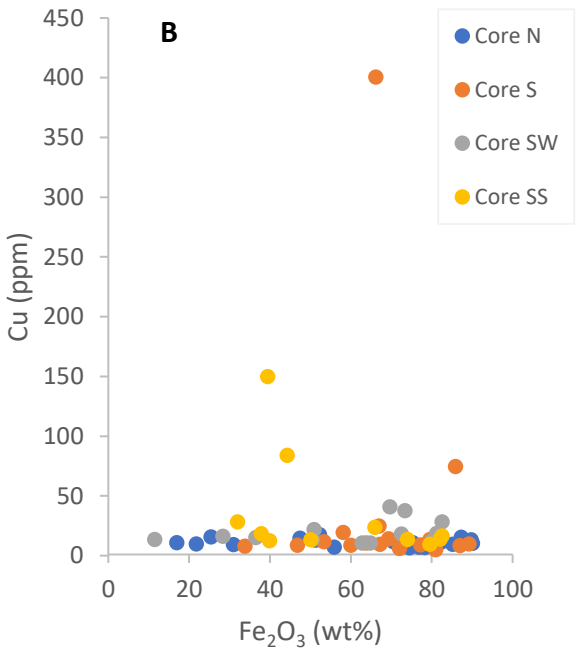
B
Core N
Core S
Core SW
Core SS
Cu (ppm)
Fe_2O_3 (wt%)
0
50
100
150
200
250
300
350
400
450

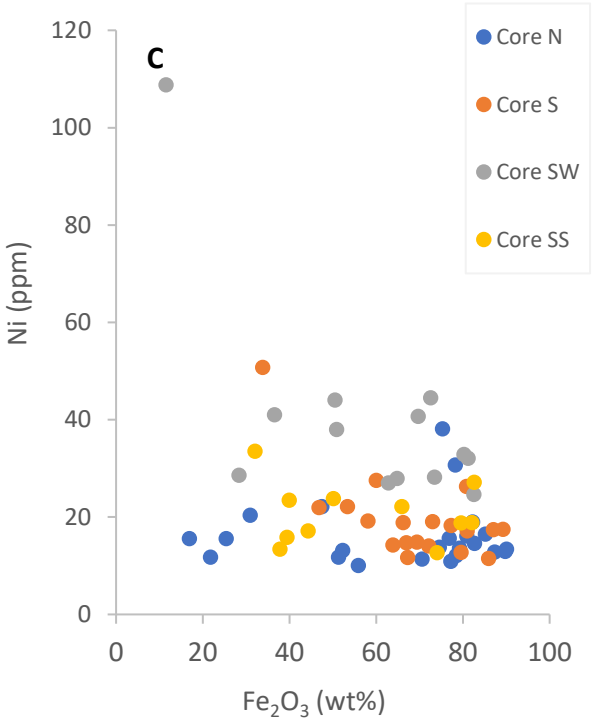
C
Core N
Core S
Core SW
Core SS
Ni (ppm)
Fe_2O_3 (wt%)
0
20
40
60
80
100
120

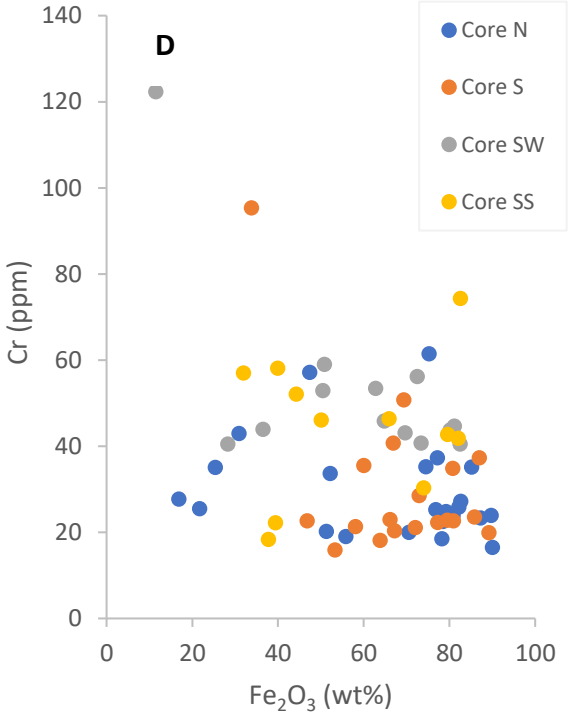
D
Core N
Core S
Core SW
Core SS
Cr (ppm)
Fe_2O_3 (wt%)
0
20
40
60
80
100
120
140

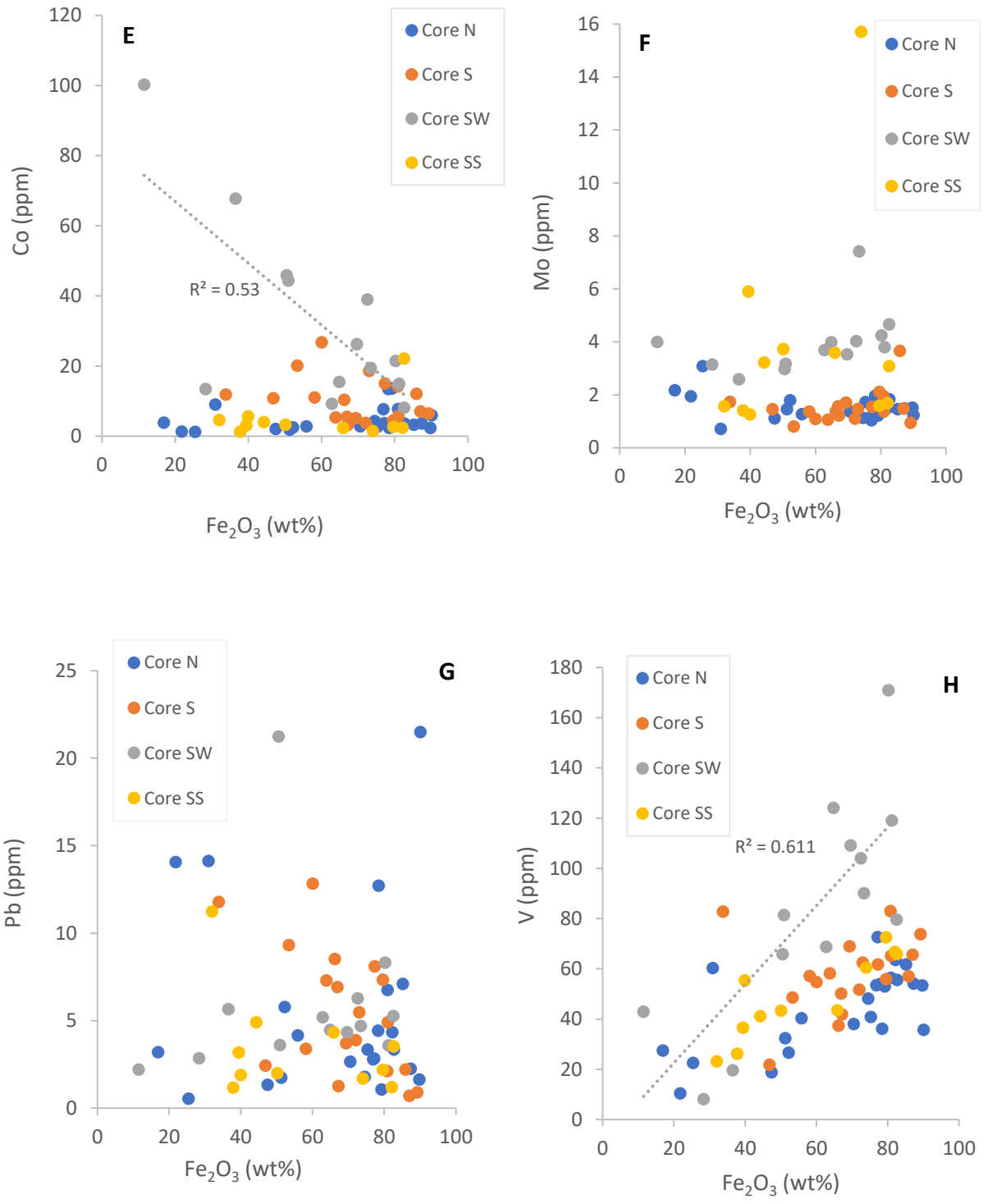

Figure 3.7: Bivariate diagrams showing relationships between transition metals and Fe_2O_3.

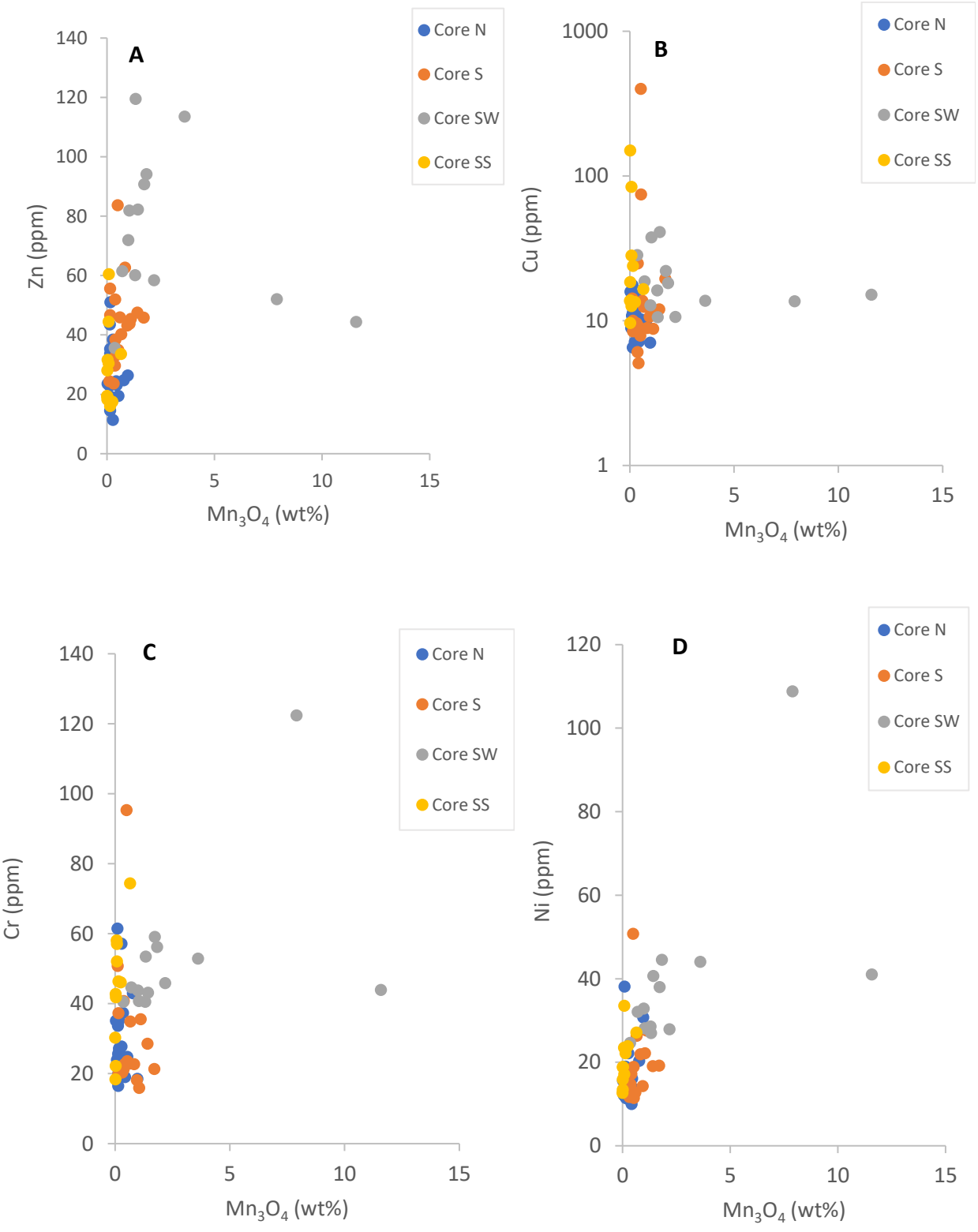
A
Zn (ppm)
Mn_3O_4 (wt%)
Core N
Core S
Core SW
Core SS
B
Cu (ppm)
Mn_3O_4 (wt%)
Core N
Core S
Core SW
Core SS
C
Cr (ppm)
Mn_3O_4 (wt%)
Core N
Core S
Core SW
Core SS
D
Ni (ppm)
Mn_3O_4 (wt%)
Core N
Core S
Core SW
Core SS

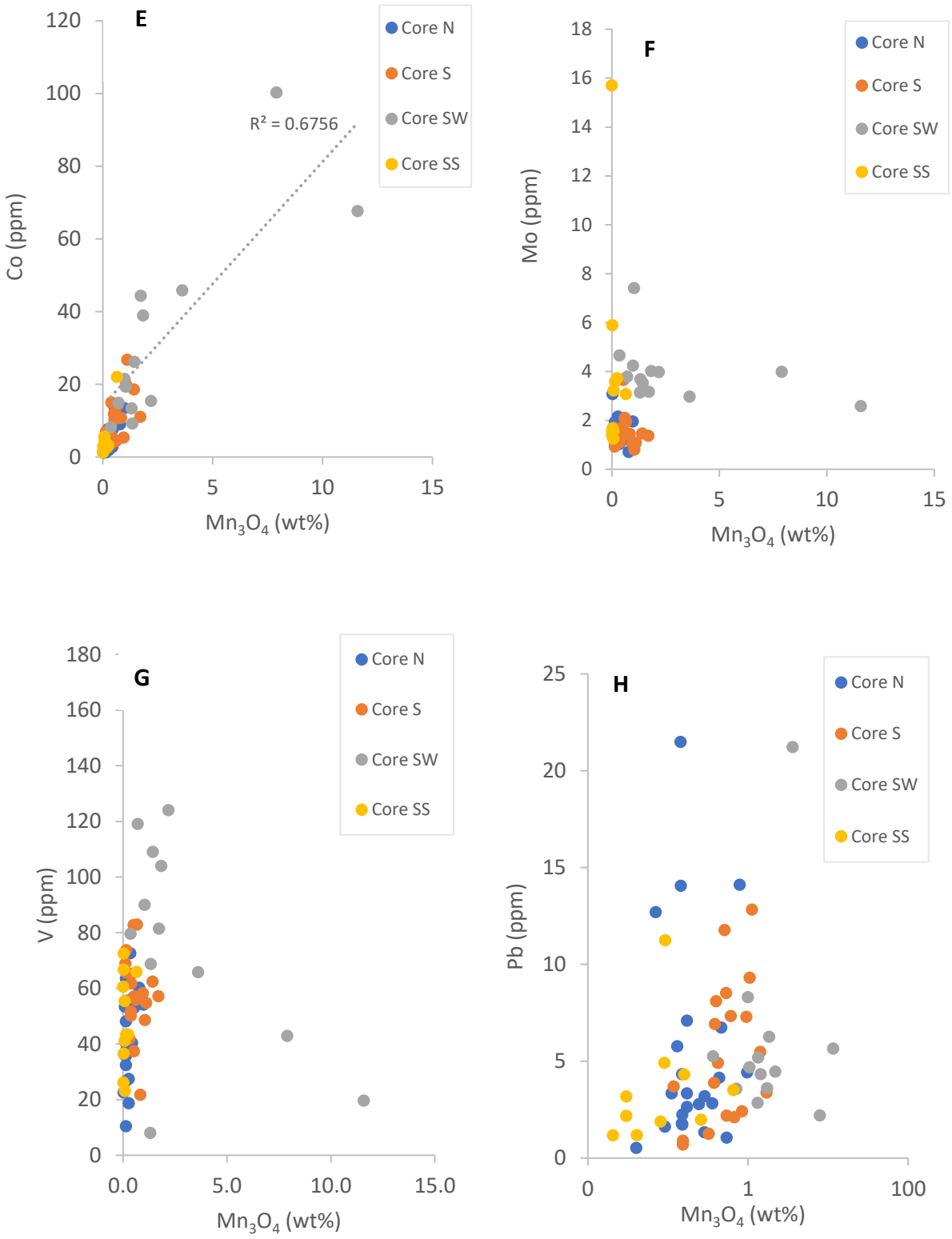

Figure 3.8: Bivariate diagrams showing relationships between transition metals and Mn_3O_4.

3.3.3 Rare Earth Elements (REE)

Rare earth elements (REE) are an assemblage of fourteen trace elements that form a chemical spectrum from the lightest lanthanum (La) to the heaviest lutetium (Lu). The REEs are delivered to the oceans from various sources namely, continental rivers, wind transport and hydrothermal vents (Tostevin *et al.*, 2016). The REE share a similar chemical behavior owing to their very similar oxidation states and ionic radii (Bau and Dulski, 1993). As a result, a coherent and predictable distribution trend is expected in the REE spectrum when normalized against conventional compositions such as that of Post Archean Australian Shale (PAAS) (Elderfield and Greaves, 1982; Olivarez and Owen, 1991; Bau and Dulski, 1993; Cox *et al.*, 2013; Tostevin *et al.*, 2016). However, cerium (Ce) and europium (Eu) diverge from this trend due to their additional oxidation state of 4+ for Ce and 2+ for Eu (Bau and Dulski, 1993; Cox *et al.*, 2013). A deviation from the 3+ oxidation state in Ce or Eu will result in fractionation relative to adjacent REEs thus producing negative and positive anomalies respectively in normalized plots (Cox *et al.*, 2013). This fractionation is caused by scavenging of Ce and/or Eu onto hydrous Fe-Mn oxides and clay materials (Tostevin *et al.*, 2016). Mn-oxides commonly show a positive Ce anomaly due to their multi-valence states which allows it to oxidise Ce^{3+} to Ce^{4+} and to immobilize the less soluble Ce^{4+} (Takahashi *et al.*, 2000, 2007; Loges *et al.*, 2012). The REE anomalies are indicative of processes involved in mobilization and/or precipitation of REE in the paleoenvironment and in-turn inform us of the redox state of the paleoenvironment (Ohta and Kawabe, 2001).

The enrichment or depletion of REE with regards to light REE (LREE) and/or heavy REE (HREE) is used to determine the various sources of REE material, namely seawater, hydrothermal vents or riverine water (Tostevin *et al.*, 2016). REE from modern seawater will have a signature that is strongly depleted in LREE, has a negative Ce anomaly and progressive enrichment in HREE (Cox *et al.*, 2013; Tostevin *et al.*, 2016). The strong depletion of LREE in seawater is a result of preferential scavenging of LREE relative to middle REE (MREE) and HREE by seawater (Cox *et al.*, 2013). The REE signature originating from hydrothermal vents shows depletion in HREE and positive Eu anomaly. Lastly, the REE signature from rivers with substantial detrital material is characterized by flat shale-normalized distribution pattern (Tostevin *et al.*, 2016).

The following section will deal with the REE geochemistry of the XIF to evaluate the source of material and to further constrain possible redox conditions of the paleobasin during deposition. In achieving this, the REE data from the four cores will be plotted separately showing the minimum, average and maximum values normalized against PAAS. Seawater compositions from Zhang and Nozaki (1996) (Fig. 3.9 to 3.12) will be included for comparisons. It was chosen to show the XIF data in that way for convenience, as the large dataset obtained would render difficult the handling of all data in a single plot.

Furthermore, with reference to data from drillcore SW (Fig. 3.11), the sample SW-145.9 (highest Mn content) is featured in order to check whether a Ce anomaly is present, which would in turn inform the specific redox conditions during high Mn deposition. The averages of the four cores are later combined in a single diagram together with averages of the upper and bottom diamictite facies (more details on these in the following section) and averages from the Hotazel IF and Braemar IF (Fig. 3.12). The key objectives of this treatise is to evaluate the degree of detrital component of the XIF by comparing it to the clastic diamictite facies, and secondly to assess the XIF REE signature in the context of other BIF globally.

The two cores N and S contain REE values that range from 0.015 (Eu) to 1.34 (Lu) and 0.024 to 1.47 (Lu) respectively. The respective averages of both cores show depleted LREE and progressively enriched HREE with atomic weight, resulting in broadly positive slopes. This LREE distribution pattern is comparable to the chemical signature of seawater, although no sharp negative Ce anomaly is seen. Similarly, both averages show essentially no Eu anomaly. This chemical signature might suggest that the sediment captured in these cores was relatively distal from a detrital source (e.g. shoreline). Cores SW and SS have a range of 0.01 (La) to 1.35 (Lu) and 0.049 (Ce) to 1.96 (Eu) respectively. Contrary to cores N and S, the cores SW and SS show relatively more enriched LREE and depleted HREE, resulting in characteristically flatter patterns of REE distribution. Again, these cores exhibit no clear anomalies in terms of both Ce and Eu. The REE signature is therefore very similar to that of PAAS, signifying detrital input in cores SW and SS controlling REE behavior to a large degree. This also agrees, as seen earlier, with the high major element Al_2O_3 and HFSE content in these two cores, suggesting a closer proximity to a detrital source. Regarding the high Mn sample SW-145.9, there appears to be no associated positive Ce anomaly associated with primary Mn oxides in the paleobasin.

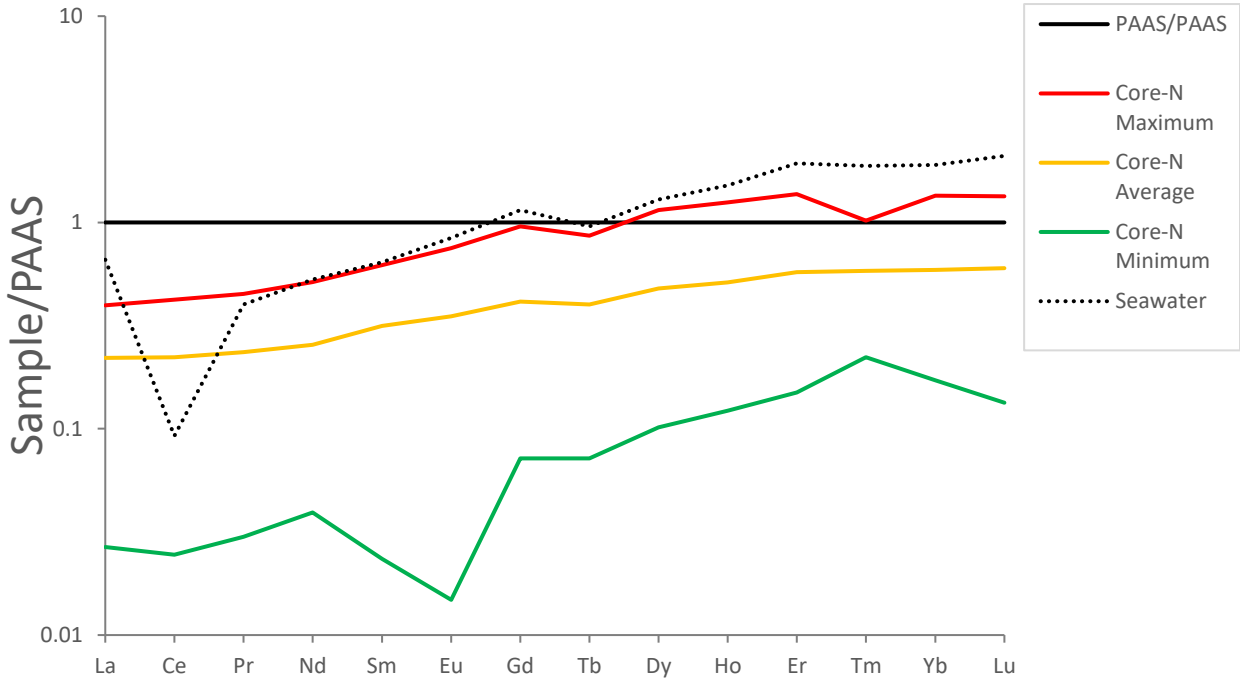

Figure 3.9: Spidergram illustrating REE relationships for drillcore N (average, max and min). Seawater composition from Zhang and Nozaki (1996) and PAAS values from Taylor and McLennan (1985).

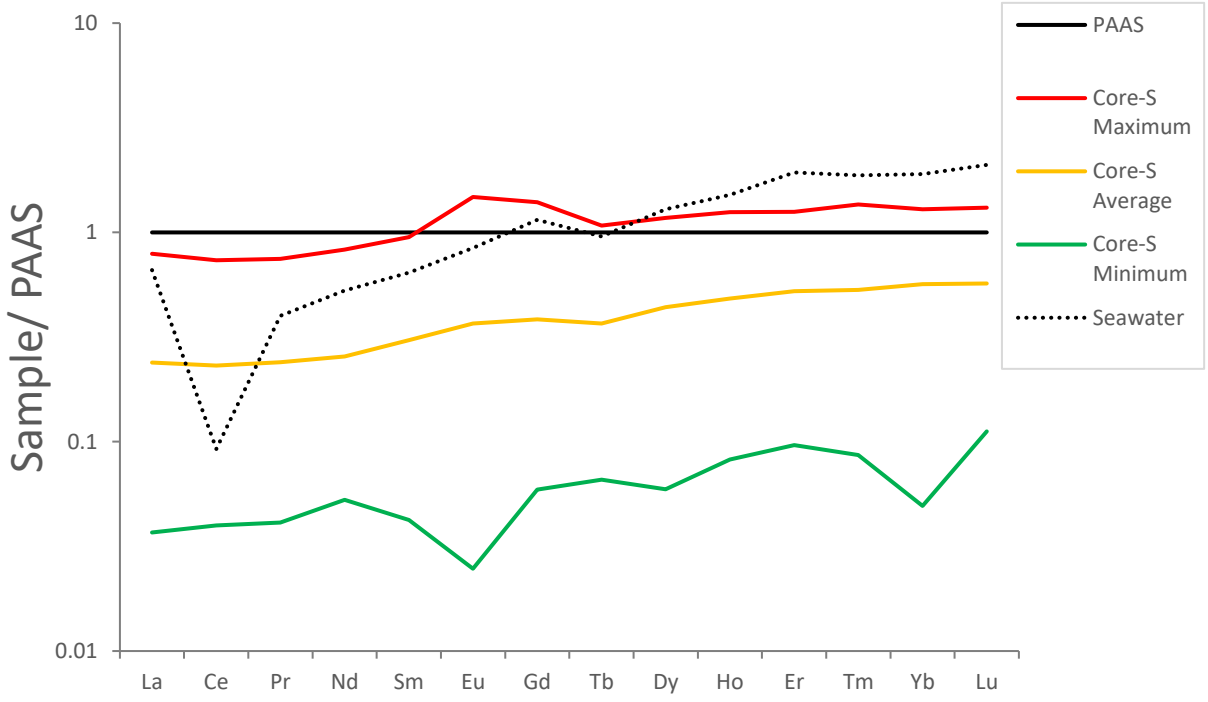

Figure 3.10: Spidergram illustrating REE relationships for drillcore S (average, max and min). Seawater composition from Zhang and Nozaki (1996) and PAAS values from Taylor and McLennan (1985).

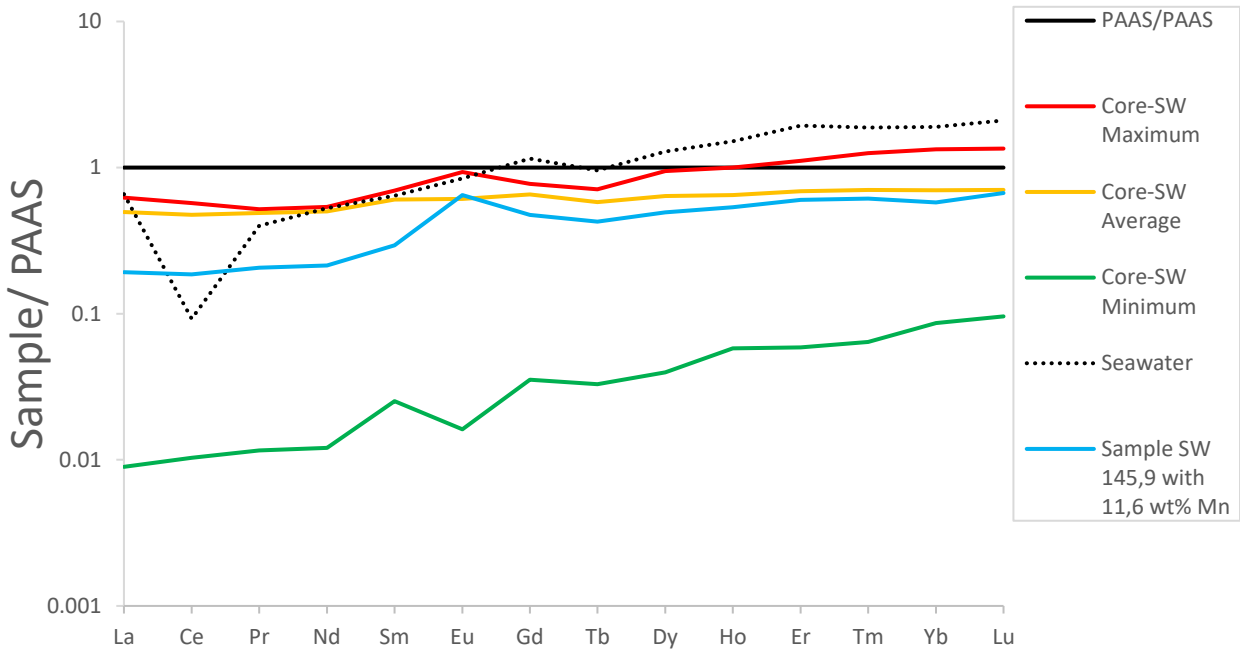

Figure 3.11: Spidergram illustrating REE relationships for drillcore SW (average, max and min), including sample SW-145.90 with highest Mn-concentration. Seawater composition from Zhang and Nozaki (1996) and PAAS values from Taylor and McLennan (1985).

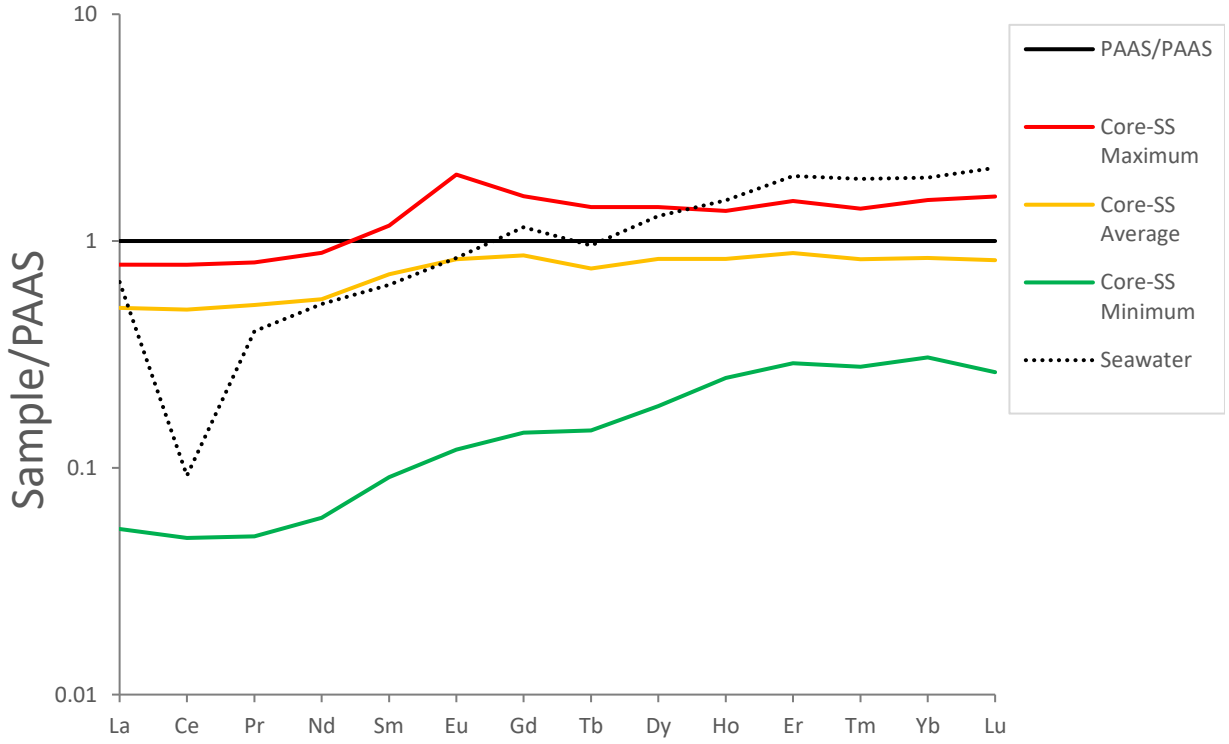

Figure 3.12: Spidergram illustrating REE relationships for drillcore SS (average, max and min). Seawater composition from Zhang and Nozaki (1996) and PAAS values from Taylor and McLennan (1985).

The averages of the four XIF cores, along with those for the upper and bottom diamictites and those for the Hotazel and Braemar BIFs are plotted in Fig. 3.13 below. The diamictite facies comprising the upper and bottom diamictite are, as expected, essentially flat in terms of REE distribution. This signal of the diamictite facies is very similar to the REE signature of cores SW and SS which are consequently controlled mainly by clastic detritus. The slightly steeper patterns of Core N and S is are clearly more indicative of subdued terrigenous control and preservation of the ambient seawater signal (Fig 3.13). On broader terms, the overall REE signature of the XIF is comparable to the Neoproterozoic Braemer iron-formation which might suggest similar paleoenvironmental conditions. The Hotazel BIF, only has La value (0.96) as the highest average value, the rest of the REE average values are lower relative to XIF and Braemar. The Hotazel is different from both the Neoproterozoic XIF and Braemar iron-formations in terms of REE geochemistry which could be revealing different paleoenvironment conditions.

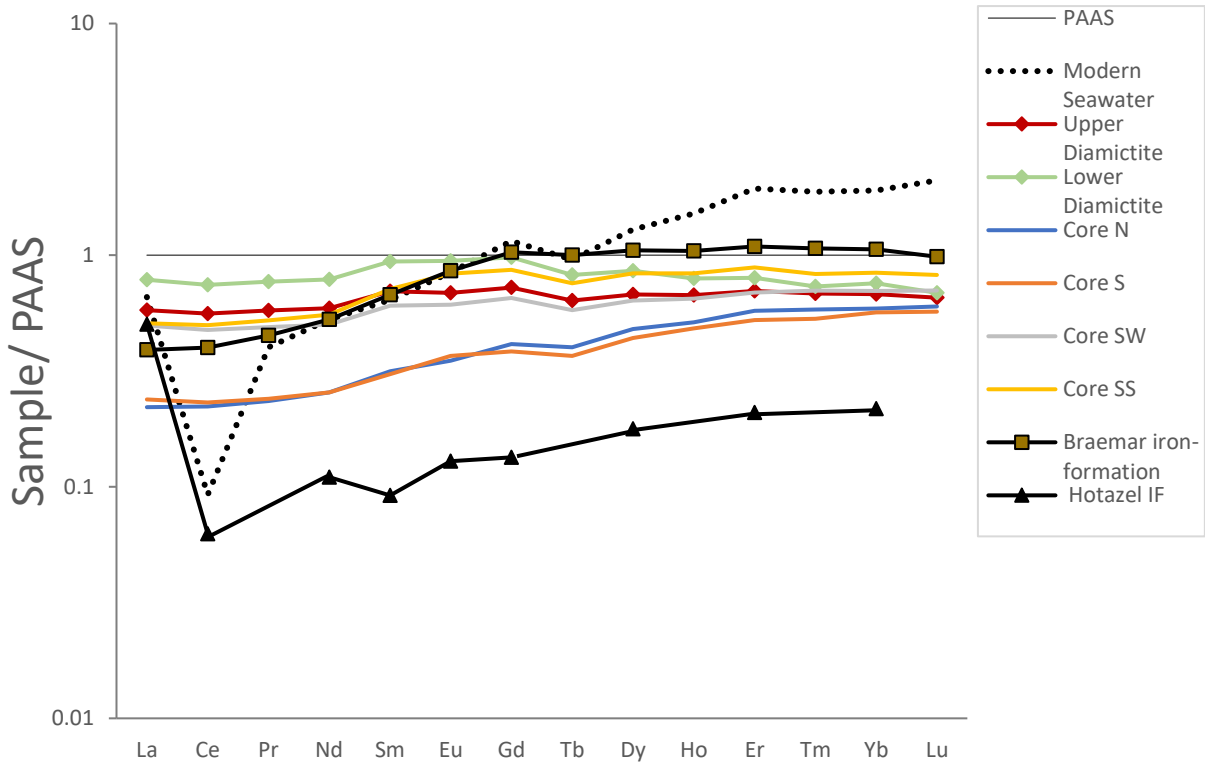

Figure 3.13: Spider diagram illustrating REE signatures for the XIF, top and bottom diamictite, average Hotazel and Braemar BIFs. Seawater composition from Zhang and Nozaki (1996).

3.3.4 Geochemical comparisons with other NIFs

In earlier sections of this chapter, the average major element geochemistry of the XIF was explored against other compositional averages of BIF and NIF, to provide an overall context for comparative considerations. The data displayed in the spidergram of Fig. 3.1 showed that the XIF and NIF in general had higher concentrations of Al_2O_3 and TiO_2 than older Paleoproterozoic BIFs. In this section, XIF will be evaluated exclusively against other NIFs using bivariate plots involving major element oxides (Fig. 3.12 A-F). These assess further the evidently high detrital component in Neoproterozoic iron formations and possibly other relationships of potential interest. The XIF major element geochemical data will specifically be compared to the neighbouring Chuos IF of Namibia (Breitkopf, 1988), Braemar IF (Lottermoser and Ashley, 2000), Urucum IF (Klein and Ladeira, 2004) and Rapitan IF (Klein and Beukes, 1993).

All of the iron-formations plotted in Fig. 3.12A, show a strong antithetic relationship between Fe_2O_3 and SiO_2 due to the typical closure effect that characterises iron-formations. The Al_2O_3 vs Fe_2O_3 binary plot of Fig. 3.11E also shows a broadly antithetic relationship between these two element oxides for all the NIF and XIF. The Al_2O_3 concentration in these iron-formations has a wide range of values with a maximum reaching the value of 11.9 wt. %. This essentially defines a broad continuum in Al_2O_3 concentrations across all the iron-formations, with the Urucum IF at the lowest end of the spectrum having a highest value of 2.6 wt. %. The Rapitan IF is next with a highest value of 5.5 wt. %, followed by the Braemar IF at 7.8 wt. %. The Chuos IF is the second-highest in the above spectrum with a value of 8.9 wt. % and lastly is the XIF with highest value at 11.9 wt. %. The antithetic relationship between bulk-rock iron and aluminium concentrations displayed by these iron-formations, signifies the interplay between chemical export of material from seawater versus variable fluxes of detritus from a terrigenous source. This association is further strengthened by the antithetic relationship of TiO_2 vs Fe_2O_3 as seen in the plot in Fig. 3.12F. We have already seen the strong relationship of Al_2O_3 with most HFSE earlier that supports the notion of high detrital input in XIF.

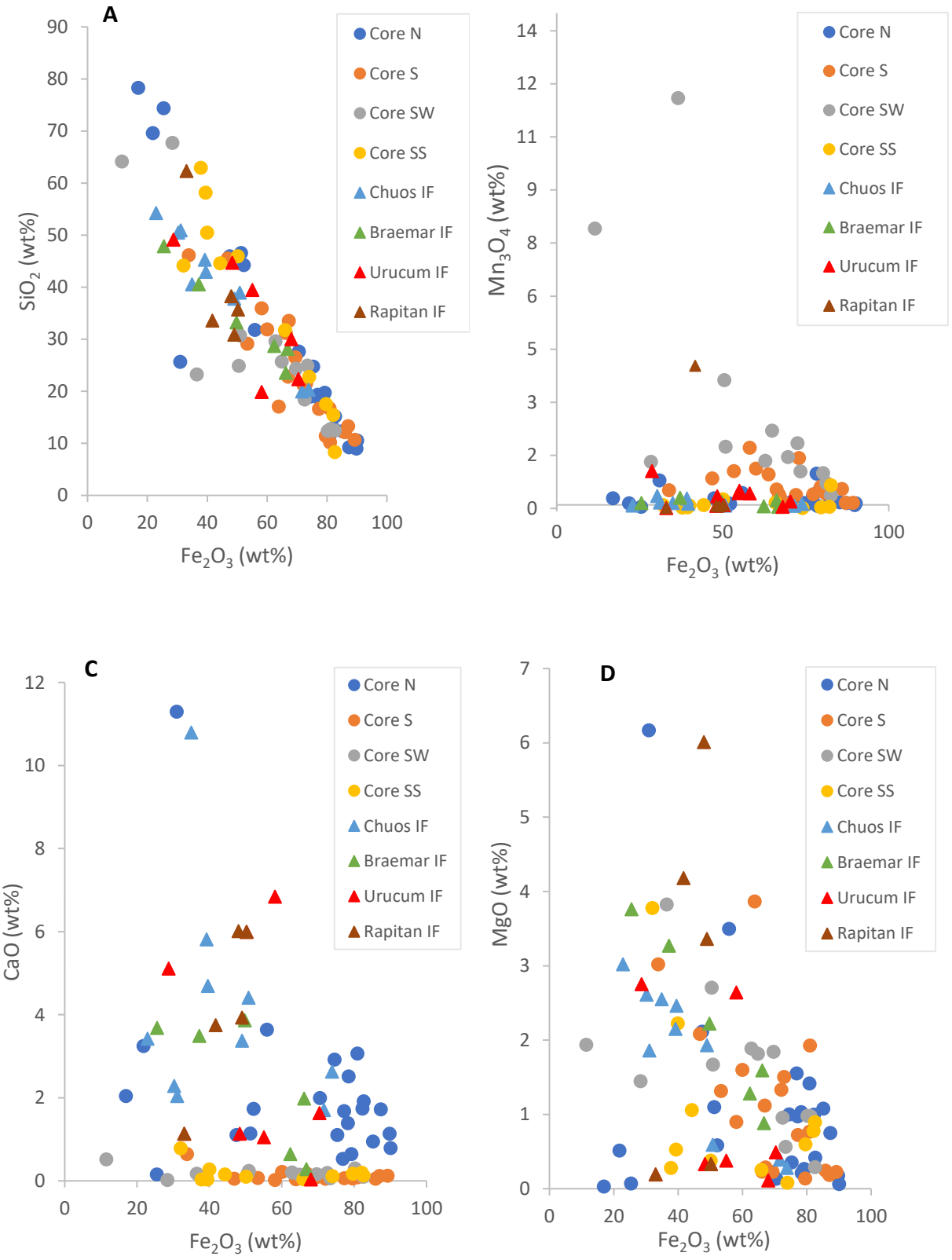
A
SiO_2 (wt%)
Fe_2O_3 (wt%)
Mn_3O_4 (wt%)
C
CaO (wt%)
D
MgO (wt%)
Core N
Core S
Core SW
Core SS
Chuos IF
Braemar IF
Urucum IF
Rapitan IF

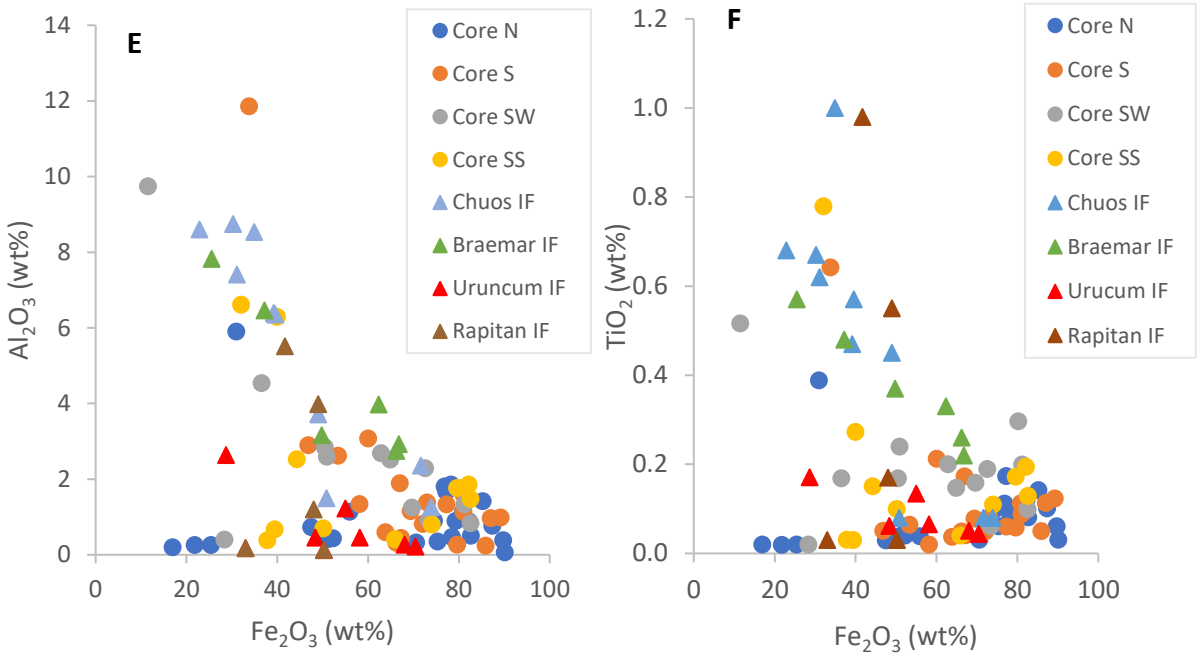

Figure 3.14: Bivariate diagrams showing XIF major element geochemistry compared to other NIF.

3.4 Geochemical relationships in diamictites

This section will briefly deal with the geochemistry of the diamictites enveloping the XIF. In doing so, only a few selected binary plots signifying the siliciclastic nature of the diamictite are shown, essentially focusing on constraining possible differences in provenance. Diagrams that further explore diamictite geochemistry showing relationships between transition metals and Al_2O_3, Fe_2O_3 and Mn_3O_4 are plotted and included in the appendix. The top and bottom diamictites are plotted and compared to other global diamictites namely, Ghaub formation (around 0.63 Ga) in Namibia (from Hoffman *et al.*, 2004), and Smalfjord and Mortensnes Formations both (around 0.63 Ga) in Norway (from Rice et al. 2011).

The plots of Fig. 3.13A-F below illustrate relationships highlighting the nature of siliciclastic control in geochemistry between the top and bottom diamictite. The diagrams and statistical correlations where evident, collectively indicate only slight compositional differences, essentially suggesting similar sources for the detritus making up each diamictite member.

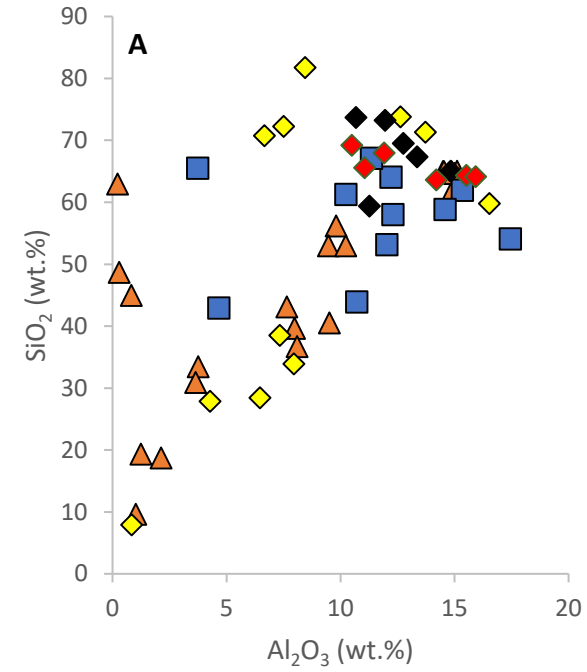
A
SiO2 (wt.%)
Al2O3 (wt.%)
0
10
20
30
40
50
60
70
80
90
0
5
10
15
20

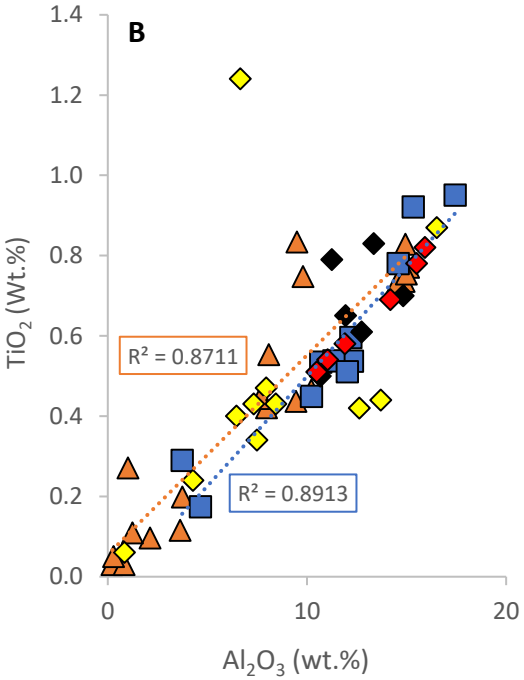
B
TiO2 (Wt.%)
Al2O3 (wt.%)
R² = 0.8711
R² = 0.8913
0.0
0.2
0.4
0.6
0.8
1.0
1.2
1.4
0
10
20

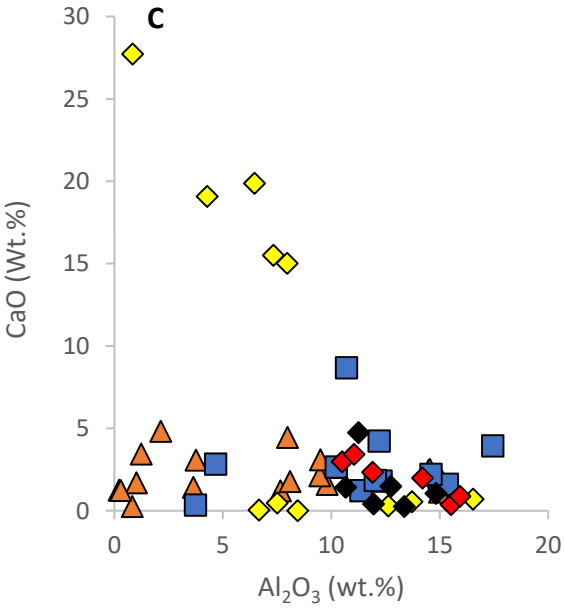
C
CaO (Wt.%)
Al2O3 (wt.%)
0
5
10
15
20
25
30
0
5
10
15
20

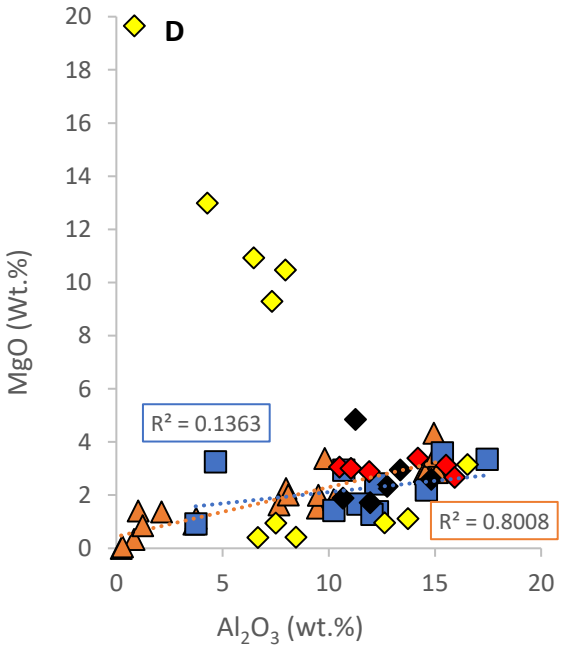
D
MgO (Wt.%)
Al2O3 (wt.%)
R² = 0.1363
R² = 0.8008
0
2
4
6
8
10
12
14
16
18
20
0
5
10
15
20

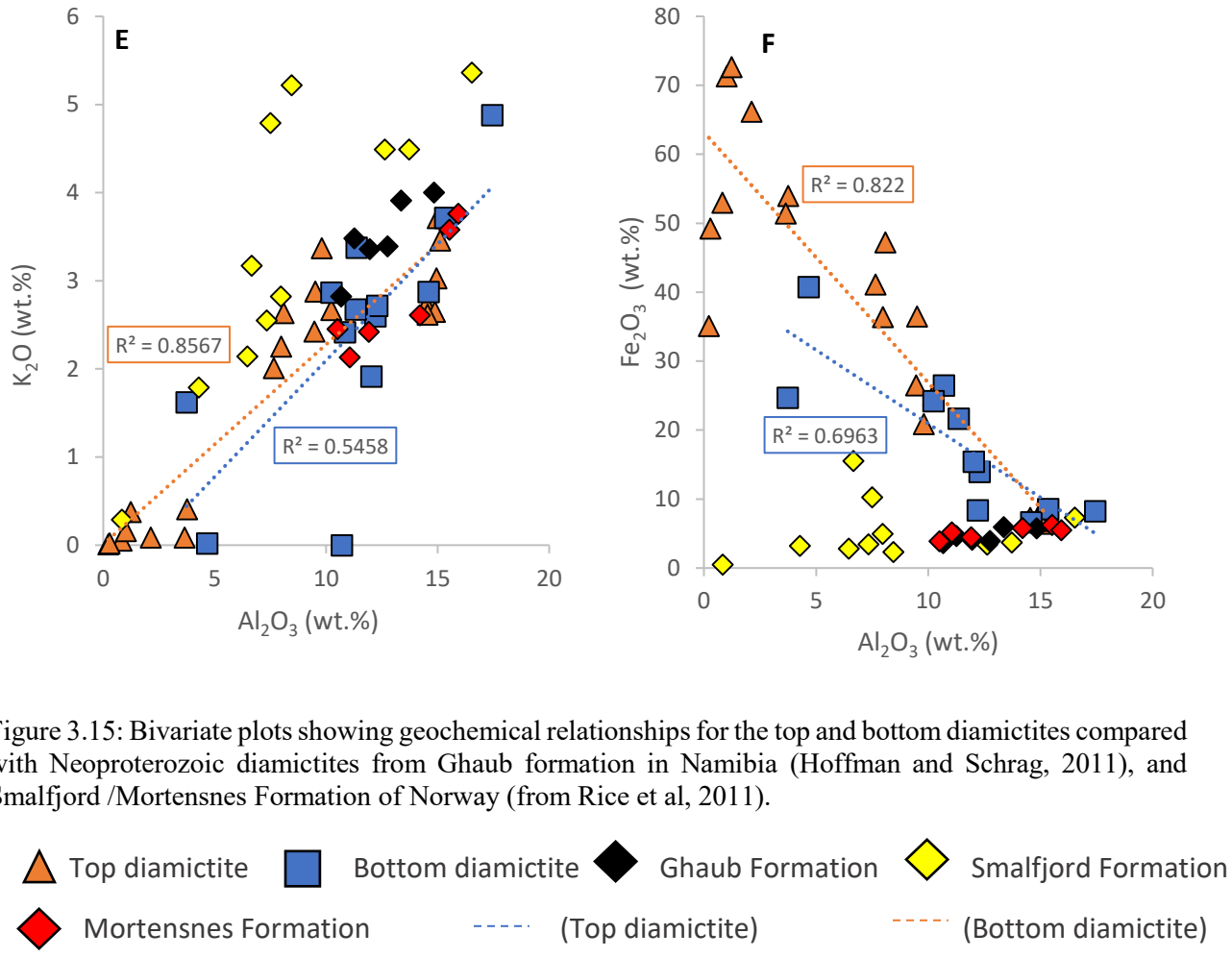

Figure 3.15: Bivariate plots showing geochemical relationships for the top and bottom diamictites compared with Neoproterozoic diamictites from Ghaub formation in Namibia (Hoffman and Schrag, 2011), and Smalfjord /Mortensnes Formation of Norway (from Rice et al, 2011).

3.5 Summary of results

The information derived from the major and trace element geochemical data presented in this chapter is summarized below.

- Algoma and Superior-type BIF generally contain very low Al_2O_3 average values ranging from 0.2 to 0.5 wt. %, except for the Archaean Isua IF which is unusually aluminous and graphitic. NIF averages range from 0.9 to 5.5 wt. % and XIF has an average of 1.7 wt. %. This suggests that older BIF are essentially lithified products of pure chemical sediments lacking detrital input, contrary to NIF and XIF. This

idea is strengthened by the extremely low TiO_2 values of both Archean and Paleoproterozoic BIFs present on a ppm scale, while NIF abundances range from 0.1 to 0.4 wt. %. In XIF, Al_2O_3 values range from 0.2 to 6.6 wt. % with very high values of 11.9 and 9.7 wt. % in cores S and SW respectively. Drillcore SW also happens to have the highest Al_2O_3 average of 2.6 wt. %.

- The XIF has the highest Mn_3O_4 average than all the BIFs and NIFs to which it was compared. The average of XIF is 0.9 wt. %. The high Mn_3O_4 in XIF is accounted for by spessartine garnet and cummingtonite amphibole grains containing wt% level Mn in their structures. Core SW in XIF has the highest Mn_3O_4 average of 2.4 wt. % than all the cores, and occasionally very high values of 7.9 and 11.6 wt. %. It should be noted that this is also the same core with the highest Al_2O_3 average.

- The CaO and MgO averages in XIF are the lowest amongst NIF and BIF, with values of 2.1 wt % and 1.2 wt % respectively. Contrary to BIF and other NIF which have carbonate phases such as dolomite, ankerite and calcite, the CaO in XIF is related mainly to minor calcite and dolomite. In the case of MgO, silicate minerals are the preferred hosts, which is the case of unmetamorphosed BIFs would be minerlas such as greenalite and minnesotaite whereas the XIF is dominated by biotite, chlorite and garnet.

- With regard to transition metals, XIF shows an overall depletion relative to other BIF and NIF, especially in terms of Zn, Ni, Cu and Cr that are commonly associated with volcanogenic hydrothermal input. XIF is instead highly enriched in Co and V; the former is higher in concentration than that in Paleoproterozoic BIF, whilst the latter is highest compared to Archean and Paleoproterozoic BIF and NIF. The high Co value in XIF shows a broadly antithetic relationship to Fe_2O_3 and a positive relationship with Mn_3O_4. It is thus inferred that primary Mn oxides would have controlled Co deposition in the original environment, possibly representing a transiently more oxic stage in the paleobasin during XIF deposition. Metamorphism

led to replacement of the primary oxides (plus silica and aluminum) by garnet and amphibole, thus preserving the original signal.

- Concentrations of LILE in XIF (such as Rb, Cs and Ba) are broadly comparable to other NIF deposits and higher than both Archean and Paleoproterozoic BIFs. The LILE did not show any specific relationship to bulk-rock Fe_2O_3. For the HFSE, the elements Zr and Th have the highest abundances which are atypical of older BIF and more similar to NIF, corresponding to elevated Al_2O_3 contents. Most of the HFSE show a good positive relationship with Al_2O_3 attesting to the argument for detrital input into the paleobasin during deposition of XIF. Overall, The XIF has comparable LILE and HFSE signatures with most NIF.

- The REE results show that samples from cores N and S have depleted LREE and enriched HREE signatures typical of seawater but lacking clear Ce or Eu anomalies. Low inputs of clastic component in these cores suggests that the initial sediments are mostly hydrogenous chemical precipitates away from a detrital source. By contrast, the averages of cores SS and SW, show less steep REE patterns (i.e. subdued enrichments in HREE relative to LREE) which result in flatter slopes resembling PAAS, signifying relatively higher input of continental clastic material in the samples from these two cores. This suggests that they were deposited more proximal to a detrital source.

- As expected, the top and bottom diamictites show a REE signature that is closely comparable to PAAS. The REE signature of the Braemar IF largely resembles that of XIF, reinforcing the idea that the two NIF were deposited under similar paleodepositional conditions. This is also in agreement based on relationships with Al_2O_3 concentration, as gleaned from the geochemical comparison of the XIF with other NIFs, from across the world.

4. DISCUSSION

4.1 The Xaudum IF in the global IF perspective

The mineralogy of unmetamorphosed NIF deposits is known to be relatively simple compared to the iron-formation of the Algoma-type and Superior-type. The mineralogy commonly consists of hematite as the main iron bearing phase, along with much chert, and variable clastic detrital material (Klein, 2005; Cox *et al.*, 2013). Metamorphosed NIF, including the XIF, comprises magnetite, quartz, garnet, amphibole, biotite and chlorite, with carbonate grains appearing as a minor phase in some NIFs and more abundant in others (Trendall, 2011; Cox *et al.*, 2013). The Algoma and Superior-type BIF that have experienced late-diagenetic and very low- grade metamorphism have a more complex mineral assemblage that consists of magnetite, a variety of carbonate phases (members of the dolomite-ankerite series, siderite, calcite) and several silicates (chert, greenalite, riebeckite and stilpnomelane)(Klein, 2005). The Isua BIF of Greenland is a bit of an exception in that it experienced a complex metamorphic history combining high grade metamorphism and contact metamorphism, and thus contains quartz, magnetite, hornblende, stilpnomelane, chlorite, calcite, almandine-rich garnet, ferroan talc, and minor sulphide (Dymek and Klein, 1988).

The average bulk chemistry of XIF and NIF is broadly comparable to that of Algoma and Superior-type BIF with regards to Fe_2O_3 and SiO_2, with values ranging from 20-40 wt. % and 43-56 wt. % respectively (Klein, 2005). The XIF has the lowest CaO and MgO average values than all other BIFs and NIF owing to the lack of carbonate phases particularly dolomite in the XIF mineral assemblage. The XIF has the highest average Mn_3O_4 content compared to Algoma and Superior-type BIF and other NIF. The high manganese in XIF is particularly prominent in Core-SW where it is manifested as spessartine garnet and manganiferous amphibole. The XIF and all other NIFs have average Al_2O_3 values that are greater than Superior-type BIF. This suggests a clear effect of high detrital input into Neoproterozoic IF paleobasins. This is absent in the Archean and Paleoproterozoic counterparts because the iron-formation deposits from these times are pure chemical sediments that lack detrital components (Klein, 2005). The high Al_2O_3 content present in all samples and especially those from drillcore SW suggest relative proximity to a detrital

source, whereas the anticorrelation between Fe_2O_3 and Mn_3O_4 is indicative of a spatial chemical heterogeneity in terms of Fe versus Mn deposition, which further supports the idea of localized variabilities in redox conditions of the paleobasin.

The contents of transition metals Zn, Cu, Ni, and Cr are amongst the lowest in XIF compared to other NIF, Algoma-type and Superior-type BIF. By contrast, Co and V are relatively more enriched compared to most BIF, including NIF. The V in XIF shows a sympathetic relationship with Fe_2O_3 whereas Co shows a positive relationship with Mn_3O_4. The V is most probably controlled by the abundant magnetite in the rocks whereas Co is related towards Mn-rich primary oxides that were later replaced by spessartine and amphibole during metamorphism. The affinity of Co towards Mn in XIF suggests that the conditions in the paleobasin must have been oxic enough to promote the oxidation of Co^{2+} to Co^{3+} and consequently adsorption to MnO_2. Research by Burns (1975) suggests that the Co^{2+} ions are adsorbed onto the surface of Mn^{4+} oxides in the area of vacancies present in the sheets or chains of the edge shared [MnO_6] because of the compatibility between the ionic radii of Co^{2+} and Mn^{4+}. This results into the Co^{3+} being fixated onto the [MnO_6] vacancies displacing the reduced Mn^{3+} after oxidation. The oxidation of Co^{2+} by $Mn4^{+}$ takes place under higher thermodynamic conditions (higher Eh and pH) compared to oxidation of Co^{2+} by Fe^{3+} as shown by Fig. 4.1 below (Swanner *et al.*, 2014; Kurzweil *et al.*, 2016). This means that, under much higher Eh and pH, Co^{3+} will preferentially adsorb to Mn^4 compared to Fe^{3+}, which is probably the case in XIF. As a result of such oxic conditions, Co can be permanently buried with Fe^{3+} oxyhydroxides and Mn^{3+}/Mn^{4+} oxides in sediments where oxygen can penetrate at least 1 cm below the sediment-water interface (Brumsack, 1989; Swanner *et al.*, 2014).

The availability of transition metals in seawater is a reflection of the balance between fluxes and sinks of these elements through the processes of precipitation and adsorption (Carr and Turekian, 1961; Swanner *et al.*, 2014). These elements are mainly delivered to the marine environment by riverine and hydrothermal fluxes. The riverine flux of Co is estimated to be 5.5 X 10^{12} g kyr^{-1} whereas the hydrothermal flux is estimated to be around 1.3 X 10^{12} g kyr^{-1} into modern seawater (Gaillardet *et al.,* 2003). The riverine Co from the continents is sourced mainly from mafic and ultramafic material. Some researchers believe that prior to 2.5 Ga, the continental flux of Co was likely higher due to the predominantly mafic compositions of the crust that time (Condie, 1993; Swanner *et al.*, 2014), and likely declined through time. It is possible that the Co in XIF was

delivered mainly by riverine fluxes during a period of high detrital input into the paleobasin, as attested also by the relatively higher Al content in the same rocks. This is in part also a function of Co fluxes to oxic continental margins being greater than those in the deep sea (Koschinsky and Hein, 2003; Swanner *et al.*, 2014).

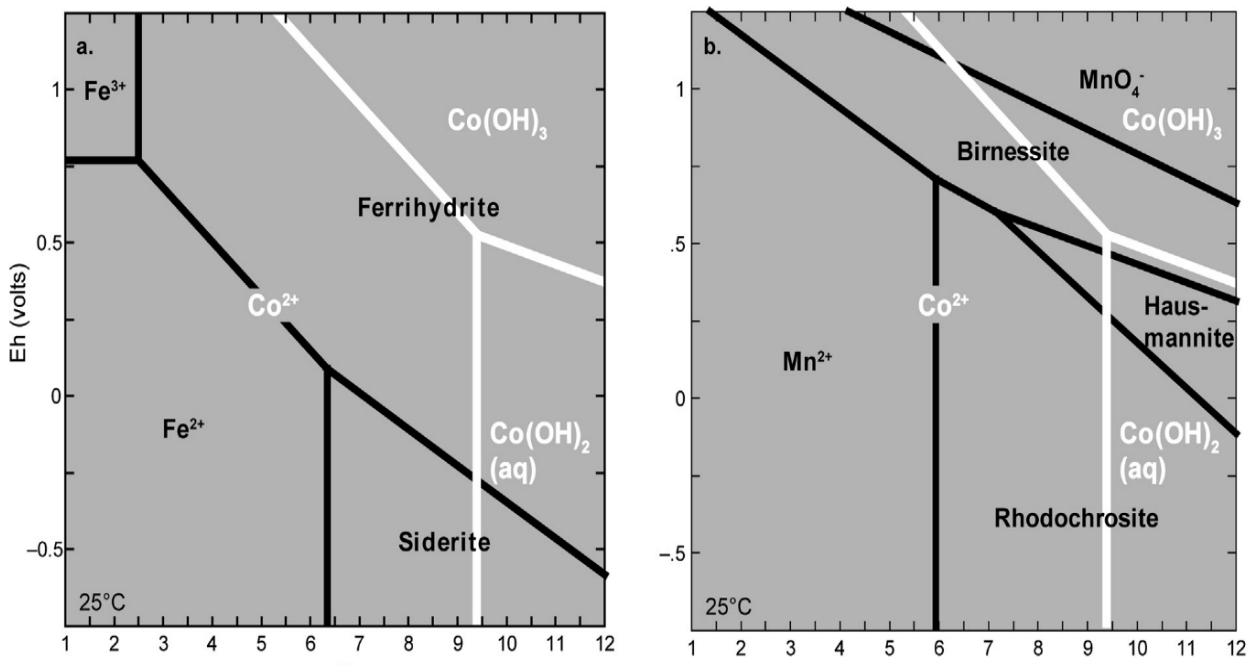

Figure 4.1: (A) The speciation diagram of Co (white) and Fe (black) under different Eh–pH conditions. The Co^{2+} is stable under assumed marine Eh and pH conditions (7–8) in the Precambrian ocean. When carbonate is absent, Fe^{2+} is soluble. (B) Speciation diagram of Co (white) and Mn (black) showing the similar redox potential for Mn^{2+} and Co^{2+} oxidation, which are both higher than that of Fe(II) oxidation. Adapted from Swanner *et al*. (2014).

The comparative analysis of the REE signature of the XIF with other BIF (i.e. Paleoproterozoic Hotazel IF and the coeval Braemar IF) revealed an overall similarity between the XIF and the Braemar IF. Both of these NIF show relative departures from the standard seawater-like pattern of most BIF, and flatter PAAS-normalised spidergrams signifying the high detrital input in global Neproterozoic paleobasins as also evidenced by major element geochemistry and particularly HFSE relationships. The detrital input in XIF is particularly prominent in the REE distribution of samples from drillcores SW and SS, whereas drillcores N and S show REE distribution and behavior that is more comparable to that of seawater. In short, variability in REE behavior from core to core indicates variability in REE inputs from seawater versus detrital sources.

Modern seawater has a notable negative Ce anomaly with respect to PAAS. This depletion occurs when Ce^{3+} is oxidised to Ce^{4+} and subsequently incorporated into ferromanganese nodules and crusts which conversely attain a positive anomaly (Elderfield and Greaves, 1982). Therefore, Ce is an important redox proxy of the oceanic water column. The XIF lacks Ce anomaly, which is a feature that is similar to those shown by the Rapitan and other NIFs globally (Klein and Beukes, 1993; Cox *et al.*, 2013; Gaucher, Sial and Robert, 2015; Feng *et al.*, 2016). Baldwin *et al*. (2012) argued that the lack of Ce and Eu anomalies in NIF suggests that the primary iron source in the NIFs originates from iron oxyhydroxide nanoparticles that were further bacterially reduced under ferruginous conditions with additional distal hydrothermal sources from the deep ocean. The absence of negative Ce anomalies in the XIF may suggest that the depositional environment was not oxic enough to fractionate Ce by adsorption to Mn^{4+} oxides in a localised oxygen-rich region of the primary depositional environment. This may be simply because Mn did not oxidise fully to Mn^{4+} but mainly to Mn^{3+} oxides, which yet controlled Co behavior. The lack of negative Ce anomaly should also not be viewed necessarily as proxy for anoxia, as the REE are controlled largely by detrital input and therefore Ce anomalies may be obscured (Cox *et al*., 2013). This is a shared feature in other NIF such as the Braemar IF as shown in reviews by Klein (2005) and Cox *et al.,* (2013).

The absence of the negative Ce anomaly in XIF and other NIF adds to the complexity of constraining oxygen levels in the Neoproterozoic atmosphere and oceans using geochemical proxies. This is arguably different from the more conclusive utility of mass independent fractionation (MIF) of sulphur isotopes that mark the beginning of the G.O.E in the Paleoproterozoic (Canfield, 2005; Pierrehumbert *et al.*, 2011). Jones (2016) adds that establishing the timing and extent of changes in oxygen levels in the Neoproterozoic is intricated by differential responses of each geochemical proxy, uncertainties or ambiguities in the applied models that connect proxy measurements to quantitative approximations of oxygen in the environment, and questions related to possible diagenetic alteration of the proxies.

Anomalies in Eu are also applied to evaluate the presence or the absence of hydrothermal input in chemical sediments (Elderfield and Greaves, 1982). Hydrothermal fluids achieve high enrichment in REE signature via high temperature reactions with oceanic crust during fluid-rock interactions leading to leaching of minerals (Klinkhammer *et al*., 1994). The dissolved plagioclase influences

the distribution of REE elements in hydrothermal fluids since plagioclase contain similar chondrite-normalised compositions to MOR hydrothermal fluid (Klinkhammer *et al*., 1994; Craddock *et al*., 2010). Consequently, hydrothermal fluids display positive Eu anomalies owing to albitization of plagioclase which consists of a positive Eu because of its incorporation of significant amount of Eu^{2+} (Klinkhammer *et al*., 1994; Drake and Weill, 1995). Therefore, positive Eu anomalies present in high temperature hydrothermal fluids make them perfect proxies for high temperature hydrothermal fluid involvement (Olivarez and Owen, 1991). The magnitude of the positive Eu anomaly decreases with decreasing temperatures of the hydrothermal fluids, therefore a weak positive Eu anomaly is thought to imply low temperature hydrothermal fluids (Bau and Möller, 1993; Klein, 2005). Studies have shown that the magnitude of Eu anomalies has progressively decreased from Archean to Paleoproterozoic iron formations, due to decreasing hydrothermal temperatures which were ultimately controlled by declining upper mantle temperatures (Bau and Möller, 1993; Klein, 2005). The Paleoproterozoic Hotazel and Kuruman IF (not reviewed in this study) show a slight positive Eu indicating minor hydrothermal fluid influence in the overall modern shallow-seawater REE patterns (Beukes and Klein, 1990; Tsikos and Moore, 1997). XIF and other NIFs on the other hand do not show Eu anomalies suggesting a lack of hydrothermal input into shallow seawater that has interacted with terrigenous material as shown by the REE pattern (Klein and Beukes, 1993; Cox *et al.*, 2013; Gaucher, Sial and Robert, 2015). It should be noted however, that the absence of a positive Eu anomaly in XIF may not necessarily mean a lack of hydrothermal input, because hydrothermal plumes may mix or interact with other REE reservoirs such as basaltic crust, seawater and continental sediment that could dilute or mask the original hydrothermal signal (Cox *et al.*, 2013).

4.2 Paleoclimatic constraints

A clear picture of Neoproterozoic climate conditions is a crucial component in understanding and possibly linking the presented data in this study to proposed Neoproterozoic Snowball Earth models. To this end, the new information and arguments built in this thesis have potential to also shed light into the severity of climatic variations during the Neoproterozoic which remain a

contentious subject to this day. In order to make inroads into that objective, the chemical index of alteration (CIA) has been applied as an additional possible constrain to Neoproterozoic climate.

4.2.1 Chemical Index of Alteration

Severe paleoclimatic conditions are preserved in bulk mineralogical and chemical compositions of associated clastic sedimentary rocks. These compositions serve a role in providing constraints on the rock provenance and intensity of physical and chemical paleo-weathering (Nesbitt and Young, 1982). One of the tools that can be used to assess paleo-weathering trends is the CIA, a chemical proxy useful in understanding paleoclimates (Nesbitt and Young, 1982). The CIA is based on the idea that, during progressive chemical weathering on silicate minerals, mobile cations such as Ca^{2+}, Na^{+} and K^{+} are easily removed relative to elements such as Al^{3+} and Ti^{4+} that are more stable under surface weathering conditions (Nesbitt and Young, 1982; Bahlburg and Dobrzinski, 2011). Persistent weathering of silicates followed by erosion and deposition in basins, will ultimately produce sedimentary rocks rich in clay minerals such as illite and kaolinite (Bahlburg and Dobrzinski, 2011). The CIA is calculated as the effective ratio of immobile Al_2O_3 over the sum of the oxides of mobile cations Ca^{2+}, Na^{+} and K^{+}:

$$CIA = \left(\frac{Al_2O_3}{Al_2O_3 + Na_2O + K_2O + CaO^*}\right) X100 \qquad (1)$$

The major oxides are given are molecular proportions. CaO* represents CaO incorporated in silicate rocks, thus differentiating it from carbonates that form authigenically in marine systems. Caution must therefore be exercised to the potential involvement of clastic carbonate grains or cement minerals in the rocks under investigation, otherwise CIA values may be grossly underestimated and become spurious. CIA values close to 100 are indicative of the highest weathering in warm and humid climates producing pure kaolinite (Table 4.1). Low CIA values on the other hand are representative of minimal or absent weathering under either cool or arid climates (Nesbitt and Young, 1982; Rieu *et al.*, 2007).

The use of the CIA can reveal a lot of hidden information about paleoclimate and paleo-weathering trends in the Neoproterozoic. A recent study by Liivamägi et al. (2014) shows that cyclically increased atmospheric CO_2 during the late Edicaran period of the Neoproterozoic led to intense weathering of continental silicates in the Baltic paleosols, which produced kaolinite and iron-oxyhydroxide (Rieu *et al.*, 2007). This piece of evidence presents the novel prospect of finding lateritic paleosols that are typically associated with hot climates, in what is believed to be a cold Neoproterozoic climate. Lateritic paleosols are generally very scarce from this period due to their low preservation potential (Liivamägi *et al.*, 2014). This raises the question of how evidence of intense chemical weathering can illuminate extreme climatic changes associate with a Neoproterozoic Snowball scenario.

Table 4.1: Relationship between climate conditions and weathering intensities (CIA values) and their respective minerals/rocks (Bahlburg and Dobrzinski, 2011).

CIA values	Minerals/Rocks	Climate
90 to100	Kaolinite	Warm and humid
90	Illite	
75	Muscovite	Cool and arid
50	Feldspar	
45 to 55	Fresh granite and grandiorite	
30 to 45	Fresh basalts	

It should be also noted that although CIA caters as an efficient tool for constraining paleoclimate conditions, CIA values alone are worthless if not linked to the stratigraphic framework and/or facies of the analysed sedimentary rocks (Bahlburg and Dobrzinski, 2011). To increase the potential value of the CIA application, inclusion of the top and bottom diamictites into consideration was deemed necessary.

The major element K_2O/Al_2O_3 ratio was also used in combination with the CIA to help classify weathering products and to assist in constraining the possible type of climate that prevailed during weathering and XIF deposition. The Fig.4.2 below, illustrates low K_2O/Al_2O_3 ratios reflecting

presence of predominantly kaolinite and smectite, along with very high CIA values from 80-99 and a few outlying lower values (see also Appendix for details). This information combined suggests very high degree of chemical weathering in a warm and humid climate during XIF deposition.

By contrast, diamictite weathering analysis shows high K_2O/Al_2O_3 ratios plotting along the muscovite line (Fig. 4.3) coupled with lower CIA values from 64-78 and a few outlying higher values (see appendix for more details). These values confirm that the diamictites were deposited during a cool arid climate which produced minimal weathering. Interestingly enough, the bottom diamictite has an overall higher K_2O/Al_2O_3 ratio than the top diamictite, suggesting that the climate may have been even colder in the glacial re-advance and regression events following XIF deposition.

Concerning the Neoproterozoic Snowball Earth, the above data suggests that the climatic conditions in the Neoproterozoic varied from cool and arid to interglacial warm and humid during XIF deposition and back to extremely cool and arid glaciation for top diamictite. The information provided above supports some of the more recent ideas proposed by the Snowball Earth Hypothesis: these state that, following interglaciation, substantial amounts of glaciers on continents released weathered and eroded continental material and transported it to the sea. Furthermore, lateritic deposits formed under intensive weathering from the equatorial continents during warm and arid conditions, after the continental glaciers thawed in the interglacial period (Liivamägi *et al.*, 2014). Subsequent to interglacial period, climatic conditions during glacial re-advance were probably even cooler than initial glaciations.

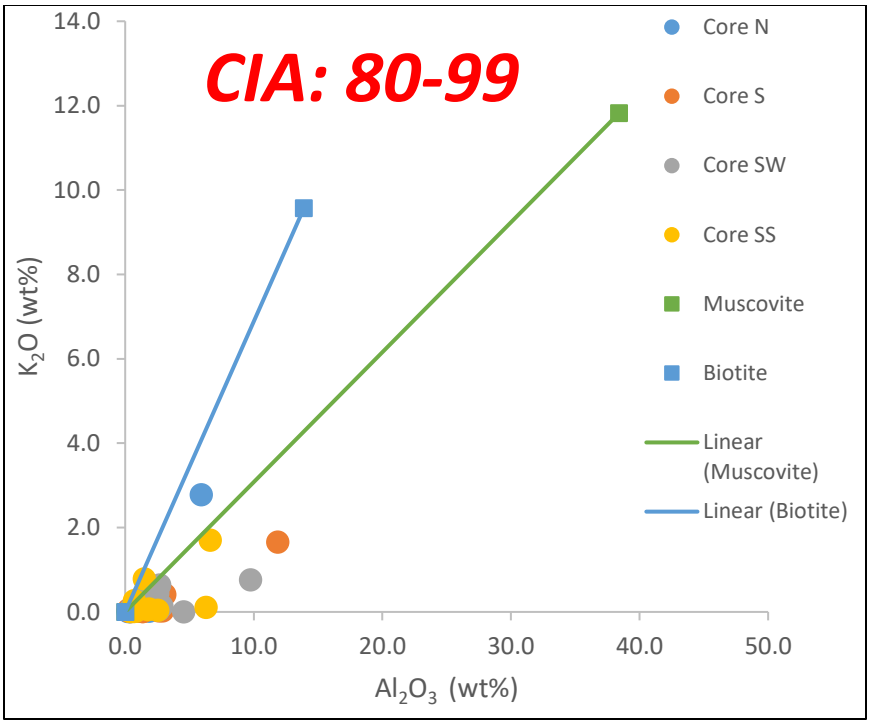

Figure 4.2:Bivariate plot showing K_2O/Al_2O_3 for XIF ratios and high CIA values indicating extreme weathering in warm and arid climate.

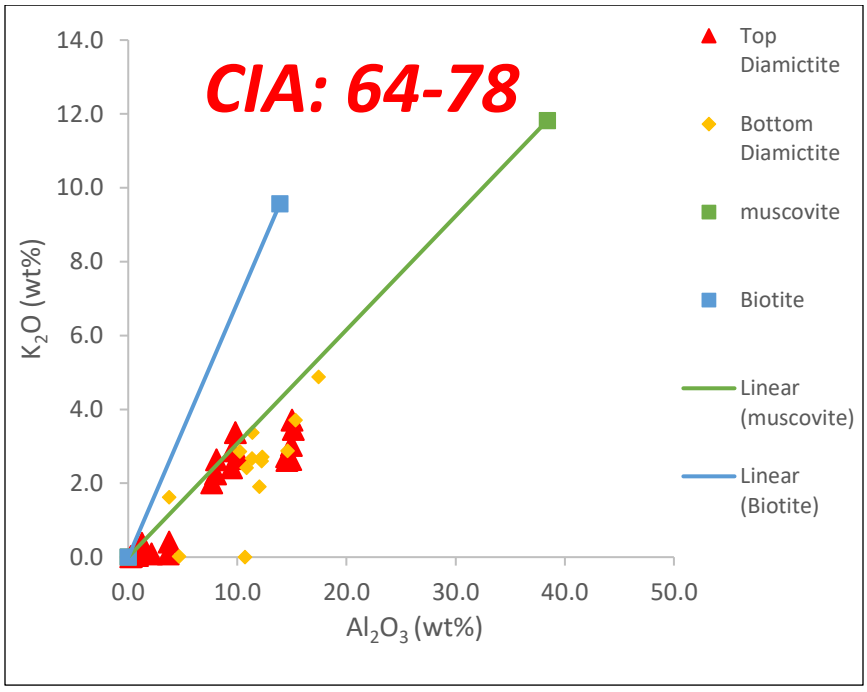

Figure 4.3: Bivariate plot showing K_2O/Al_2O_3 diamictite ratios and low CIA values indicating minimal weathering in cool and arid climate.

4.3 Depositional and genetic modelling of the Xaudum IF

A variety of BIF genetic models have been proposed owing to the lack of consensus amongst researchers. The difficulty in arriving at a universal genetic model is complicated by the fact that BIFs are a product of multiple and diverse processes during major evolutionary changes in the Earth's atmosphere and oceans through time (Lyons *et al.,* 2014). The reappearance of NIF after a billion-year hiatus does not grant any immunity to the above statement. The coeval nature and similarity in lithological features of NIF still does not guarantee a convergent genetic model.

In order to appreciate all the possible parameters affecting genetic modelling of the XIF the principal points that were used by Klein and Beukes (1993) to produce a genetic model for the Rapitan IF will be employed here as well. These include the character of the paleo-depositional basin, possible sources and transport modes of silica and iron, and physico-chemical conditions of precipitation- all these will be explored and discussed in the following sections.

4.3.1 Paleo-depositional basin

Various BIF deposits around the world were deposited in correspondingly variable environments throughout the geological time. Reconstruction of Archean depositional environments is challenging since most Archean BIFs are subjected to highly metamorphosed and deformed greenstone belts (Klein, 2005). However, evidence shown by poorly preserved lamination and micro-banding in Archean BIF suggests a deep basin depositional setting due to the lack of detrital input (Klein, 2005; Trendall, 2011). Like Archean BIF, Paleoproterozoic BIF also lack detrital input, however they were deposited in stable continental shelf basin where preserved textures such as cross bedding and ripples suggest often shallow water marine settings. Due to the extensive geotectonic activity resulting from the assemblage and breakup of Rodinia, most of NIFs are deposited in large scale ice covered rift basins (Klein and Beukes, 1993; Lottermoser and Ashley, 2000; Cox *et al.*, 2013). Contrary to other NIFs, the Holowilena iron-formation in Australia formed in a small-scale half graben which was characterized by physicochemical conditions unlike those of rift basin (Lechte and Wallace, 2015). Research by Wendorff (2005) shows that the XIF was likely deposited on an open continental shelf that was influenced by tides and supplied with detrital

material sourced from the elevated coast. This is supported by the mineral compositions, textures, facies trends, sedimentary structures and paleo-currents.

4.3.2 Source of iron and silica

The ultimate source of Fe in BIFs remained contentious for a long time (Frei and Polat, 2007; Pecoits *et al.*, 2009). Over the years, several hypotheses that point to terrigenous and hydrothermal Fe and Si sources have been proposed (Frei and Polat, 2007). Volcanogenic sources have also been invoked, however only terrigenous and hydrothermal origins of Fe and Si will be reviewd for the scope of this study.

Sakamoto (1950) suggested that Fe and Si were derived from the continents resulting from weathering and lateritization. The idea of terrigenous source for Archean-Paleoproterozoic BIFs is considered infeasible by many, because terrigenous Fe and Si could not account for the huge volume of some of these BIFs, coupled with the general lack of classic detrital minerals in them (Holland, 1984). A terrigenous source is perhaps more practically acceptable when considering NIFs for two reasons:

1. NIFs are generally smaller in size relative to Archean-Paleoproterozoic BIFs;
2. Extreme weathering and laterization in equatorial continents promoted by peak atmospheric CO_2 during interglaciation/deglaciation in Snowball Earth was contemporaneous with iron-formation deposition

Extensive research on REE in BIF, led to researchers to postulate that hydrothermal fluids (alteration of Fe^{2+} bearing igneous rocks, mainly seafloor basalt) were the source of Fe and Si in BIFs (Fryer, 1963; Klein, 2005). These studies found that hydrothermal fluids rich in Fe and Si were released deep in the stratified ocean and were later transferred into shallower parts of the oceans by upwelling (Klein, 2005). The review by Klein (2005) shows that iron-formations from the Archean were predominantly sourced from high temperature hydrothermal fluids as indicated by sharp positive Eu anomalies. In the Paleoproterozoic, the iron-formations have REE patterns that are similar to modern shallow seawater REE signals with a less distinct Eu anomaly suggesting a dilute hydrothermal fluid component compared to the Archean. Most NIFs including XIF show

REE patterns that are similar to modern shallow seawater mixed with terrigenous-sourced REE, while absence of Eu anomalies suggest a far lower to absent hydrothermal fluid component.

4.3.3 Conditions of precipitation

The required conditions for the deposition of iron and manganese formations demand a reducing environment to allow for the accumulation and transport of soluble Fe^{2+} and Mn^{2+} within the reservoir (Holland, 1973; Cox *et al.*, 2013). A powerful oxidant such as molecular oxygen is later required in the reservoir to transform the dissolved Fe^{2+} and Mn^{2+} into iron and manganese oxides and precipitate them (Holland, 1973). The processes accountable for the oxygenation of the ocean to precipitate iron and manganese oxides remains enigmatic and they will be discussed later (Holland, 2006). Similarly evasive are the processes responsible for significant transitions in the oxidation state of the atmosphere–ocean system (Lyons and Reinhard, 2009; Lyons *et al.,* 2014) . For billions of years starting from the Archean to the Neoproterozoic, the oceans have likely experienced fluctuations in redox states in satisfying the conditions that allow deposition of iron and manganese formations (Catling and Claire, 2005).

Multiple sources of evidence from continental and marine environments such as paleosols, redbeds, detrital grains and BIF, confirm the presence of very low levels of oxygen localized in shallow ocean and atmosphere during the Archean (Catling and Claire, 2005; Holland, 2006; Lyons and Reinhard, 2009). Further evidence by MIF in the sulphide and sulphate isotopic signal (expressed in terms of $\Delta^{33}S$) in sedimentary rocks older than 2.4 Ga show oxygen content as of 0.1% than present atmospheric level (P.A.L) (Kasting and Siefert, 2003; Bekker *et al.*, 2006; Holland, 2006). The MIF signal seems to have disappeared in the sedimentary rock record deposited from 3.0 to 2.8 Ga and resurfaced again around after 2.8 Ga (Fig.4.4). The disappearance of MIF at this stage was because the atmosphere and oceans were oxidizing sulphur species to sulphates thereby terminating the transfer of the MIF signal into pyrite of the Timeball Hill and Rooihoogte Formation, South Africa (Bekker *et al.*, 2006). These small amounts of oceanic oxygen prior to the G.O.E are famously labelled “whiffs of oxygen”, and proved to have persisted until the late Archean, 50 million years preceding the G.O.E (Anbar *et al.*, 2007; Lyons *et al.*, 2014).

This is supported by redox-sensitive transition metals such as molybdenum (Mo) and rhenium (Re) delivered to the Archean oceans via oxidative weathering of sulphide minerals in the crust and subsequently enriched in the 2.5 Ga Mt McRae shale in Australia (Anbar *et al.*, 2007). Despite the above evidence of Archean transient oxygenation, in the grand scheme of things, the Archean deep oceans and atmosphere were predominantly anoxic as indicated by widespread BIF and ultimately manganese deposits (Hotazel Formation) which required reducing conditions for accumulation of Fe^{2+} and Mn^{2+}.

The beginning of the Paleoproterozoic coincided with the termination of Archean BIF deposition in the ocean and inversely a spike of atmospheric oxygen around 2.4 Ga (Lyons *et al.,* 2014). The reasons for termination of BIF deposition are still elusive (Holland, 2006). Researchers believe that absence of BIF contributed to the change in the operation of the Earth's system by removing a powerful oxygen sink and promoting extreme atmospheric oxygenation (Canfield, 2005; Holland, 2006). High phosphorus (P) in the ocean budget would have facilitated photosynthesis during the absence of BIF as an oxygen sink (Holland, 2006). The increasing oxygen would have then led to increased sulphate concentrations promoting sulphate reduction rates resulting in sulphide which titrated iron from the oceanic reservoir (Canfield, 2005). While the atmosphere was progressively oxygenating, the shallow oceans were mildly oxygenated and deep ocean remained anoxic (Holland, 2006).

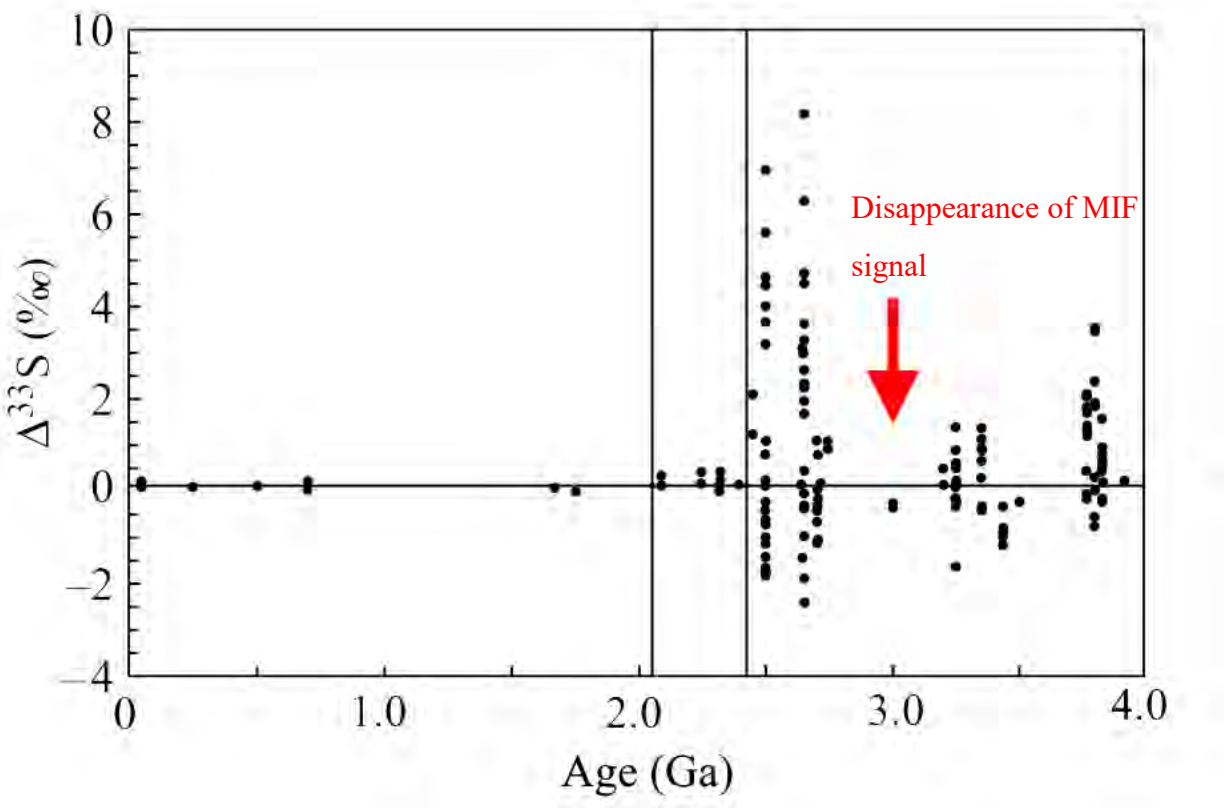

Figure 4.4: The mass-independent fractionation (MIF) signal of sulphur in pyrite and barite in deep oceans over time as expressed by $\Delta^{33}S$. There is a hiatus in the MIF signal from 3.0 to 2.8 Ga in the sedimentary sequence due to oxygenation of sulphur to sulphates which terminates the MIF signal transfer into minerals barite and pyrite. Modified from Holland, (2006).

During the near end of the Neoproterozoic, an atmospheric oxygen increase of more than 10% PAL is thought to have occurred (Canfield, 2005). Alternative research by Blamey *et al.* (2016) shows an increase of up to 50% PAL in the Neoproterozoic atmospheric oxygen, measured from Neoproterozoic (0.81 Ga) aged gas inclusions in evaporite sedimentary rocks from Officer Basin, Australia. The exact cause of the increase in atmospheric oxygen is still widely argued (Canfield, 2005; Pierrehumbert *et al.*, 2011; Lyons *et al.,* 2014). Some researchers believe that continental break up due to a shift in global tectonics and high sedimentation rates during the Neoproterozoic caused increased organic carbon burial and a consequent rise in atmospheric oxygen (Knoll *et al.*, 1986; Derry *et al.*, 1992; Kaufman *et al.*, 1997). Other researchers are further divided by the causality dilemma between the rise of atmospheric oxygen and evolution of life in the Neoproterozoic similarly to the classic 'egg and chicken' question. This causality dilemma

challenges researchers to reveal if the rise of atmospheric oxygen in the Neoproterozoic caused the evolution of life in the Neoproterozoic or whether the evolution of life in the Neoproterozoic oceans caused the rise of atmospheric oxygen in the Neoproterozoic. The likes of Xiao and Laflamme, (2009), Erwin *et al*. (2011), Lenton *et al*.(2014), Cohen and Macdonald, (2015) and others believe that the evolution of life in the oceans caused a rise of oxygen in Neoproterozoic atmosphere; conversely Canfield *et al*. (2007), Partin *et al*. (2013), Reinhard *et al*. (2013) and others believe the opposite. Butterfield (2015) suggested that the concurrent evolution of life and the rise in atmospheric oxygen in the Neoproterozoic could be merely a coincidence. Despite the lack of agreement amongst researchers on what caused a rise in the atmospheric oxygen of the in the early and late Neoproterozoic, there is an apparent consensus that indeed the oxygen levels did significantly increase compared to the Paleoproterozoic as shown in Fig. 4.5 below. Lyons *et al.* (2014) acknowledge the rise of atmospheric oxygen in the late Archean and late Neoproterozoic which they named 'state changes' (red boxes). They further acknowledge the complexity in explaining how the processes develops and suggest more work is still needed to be done in resolving this complexity.

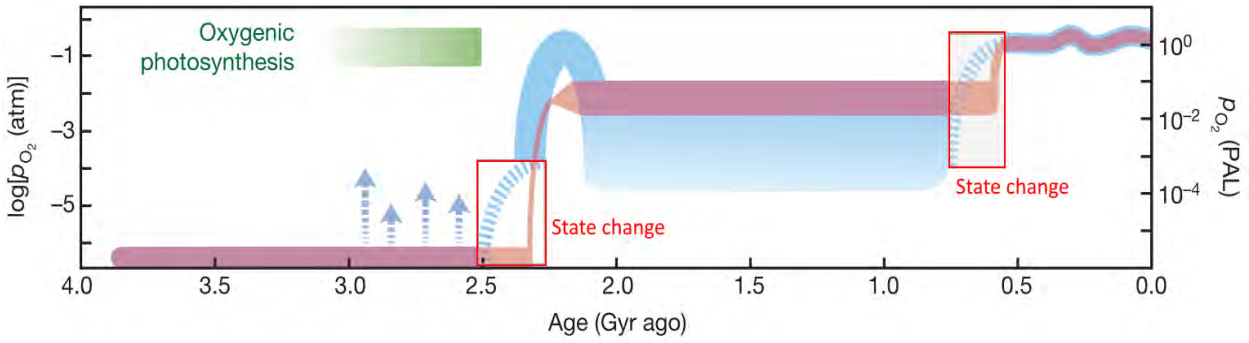

Figure 4.5: The advancement of the Earth's atmospheric oxygen over time. The pink curve denotes a 'classical, two-step' approach of atmospheric evolution, while the blue curve shows the developing model (atmospheric partial pressure of O_2, pO_2) in the right axis. The left axis shows log pO_2. The blue arrows illustrate possible 'whiffs' of O_2 late in the Archaean as discussed earlier which were influenced by oxygenic photosynthesis labelled in green. The red boxes denote the state changes where the late Archean and Neoproterozoic experienced an increase in atmospheric oxygen. Modified from Lyons *et al.* (2014).

As the Ediacaran period of Neoproterozoic atmosphere was getting more enriched in oxygen, the shallow oceans were also getting more oxygen while the deep oceans remained anoxic under

extensive ice cover (Holland, 2006). The deep ocean's reducing conditions allowed for accumulation of dissolved iron and manganese. Later on, they precipitated in NIF and associated manganese deposits around the world such as in Jacadigo Group, Brazil and the Otjosondu ferromanganese deposits in Namibia, when oxygen was supplied during deglaciation or interglacial periods (Klein and Ladeira, 2004; Cabral *et al.*, 2011).

The exact oxidative mechanism required to transform dissolved Fe^{2+} and Mn^{2+} to iron and manganese formations in the reducing ocean is not well constrained (Bekker *et al.*, 2010; Posth, Konhauser and Kappler, 2013). Abiotic and biotic mechanisms are both possible oxidative pathways. These mechanisms are both considered and summarized below.

4.3.3.1 Abiotic pathways

Abiotic pathways have two mechanisms of oxidising reduced Fe^{2+} to Fe^{3+}. The first mechanism is oxygenic photosynthesis and it uses free oxygen in the photic zone that is derived from cyanobacterial photosynthesis to oxidise dissolved Fe^{2+} (*equation 4*). Although strictly abiotic, since the cyanobacteria is not directly involved in oxidising the dissolved Fe^{2+}, this mechanism would have been linked to biology in confined environments rich in cyanobacterial produced oxygen "oxygen oases" (Klein and Beukes, 1989). Oxidation of dissolved Fe^{2+} would have occurred after the transport of bottom anoxic waters in ferrous solution produced by hydrothermal activity to shallower levels through an upwelling mechanism, which promoted mixing and oxidation of the dissolved Fe^{2+} and ultimately its delivery as particulate iron oxide to the basin floor, in the form of ferric oxy-hydroxide precursors. This model has been proposed for Paleoproterozoic basins where BIF was deposited in oxic relatively shallow-water shelves (Klein and Beukes, 1989). However, this mechanism has been challenged to account for Archean BIF because of the inconclusive evidence presented for the debut of free molecular oxygen in the early history of the Earth (Koehler *et al.*, 2010)

$$2Fe^{2+} + O_2 + 4H_2O \rightarrow 2Fe(OH)_3 + 2H^+ \qquad (4)$$

The second abiotic mechanism is UV photo-oxidation and it accounts for iron oxidation without the direct involvement of oxygen. Cairns-Smith (1978) proposed that this could be achieved when

dissolved Fe^{2+} in the anoxic water column is exposed to excessive UV-radiation in the absence of a shielding ozone layer during early Earth history. The ferrous iron would have absorbed radiation in the range of 200-400 nm and hydrolyzed to produce ferric hydroxide at neutral pH (*equation 5*) (Braterman *et al.,* 1983). Based on experimental results by Konhauser *et al.,* (2007) this mechanism was discredited as being responsible for Archean BIF oxidation. Konhauser *et al.* (2007) argued that precipitation of silicates and carbonates would have outcompeted this process and rather opted for an anaerobic mechanism.

$$2Fe^{2+}_{(aq)} + 6H_2O + hv \rightarrow 2Fe(OH)_3 + 4H^+ + H_2 \quad (5)$$

4.3.3.2 Biological pathways

Biotic mechanisms are categorised into aerobic and anaerobic processes. They are generally ecosystem-specific and are more varied compared to their abiotic counterparts. Aerobic mechanisms are effective at acid mine drainage sites and circum-neutral pH at hydrothermal vents, therefore they will not be discussed further.

Anaerobic biotic oxidation has various mechanisms using different terminal acceptors for the oxidation of dissolved ferrous iron. Denitrifying bacteria oxidising ferrous iron in the water column is one example (Straub *et al.,* 1996). One of the most important biotic oxidation mechanisms (anoxygenic, phototrophic Fe^{2+} oxidation) is the use of ferrous iron as an electron donor in carbon dioxide rich photic zone to produce ferric iron via photosynthesis (*equation 6*) (Hartman, 1984; Widdel *et al.,* 1993).

$$4Fe^{2+} + 11H_2O + CO_2 + hv \rightarrow CH_2O + 4Fe(OH)_3 + 8H^+ \quad (6)$$

This mechanism is proposed to be a viable alternative to the formation of BIFs in anaerobic conditions in the Paleoproterozoic ocean-atmosphere system (Hartman, 1984). Experiments by Kappler *et al.,* (2005) have demonstrated the ability of bacteria to oxidise ferrous up to 100m water depth to produce iron-formation the size of Superior-type.

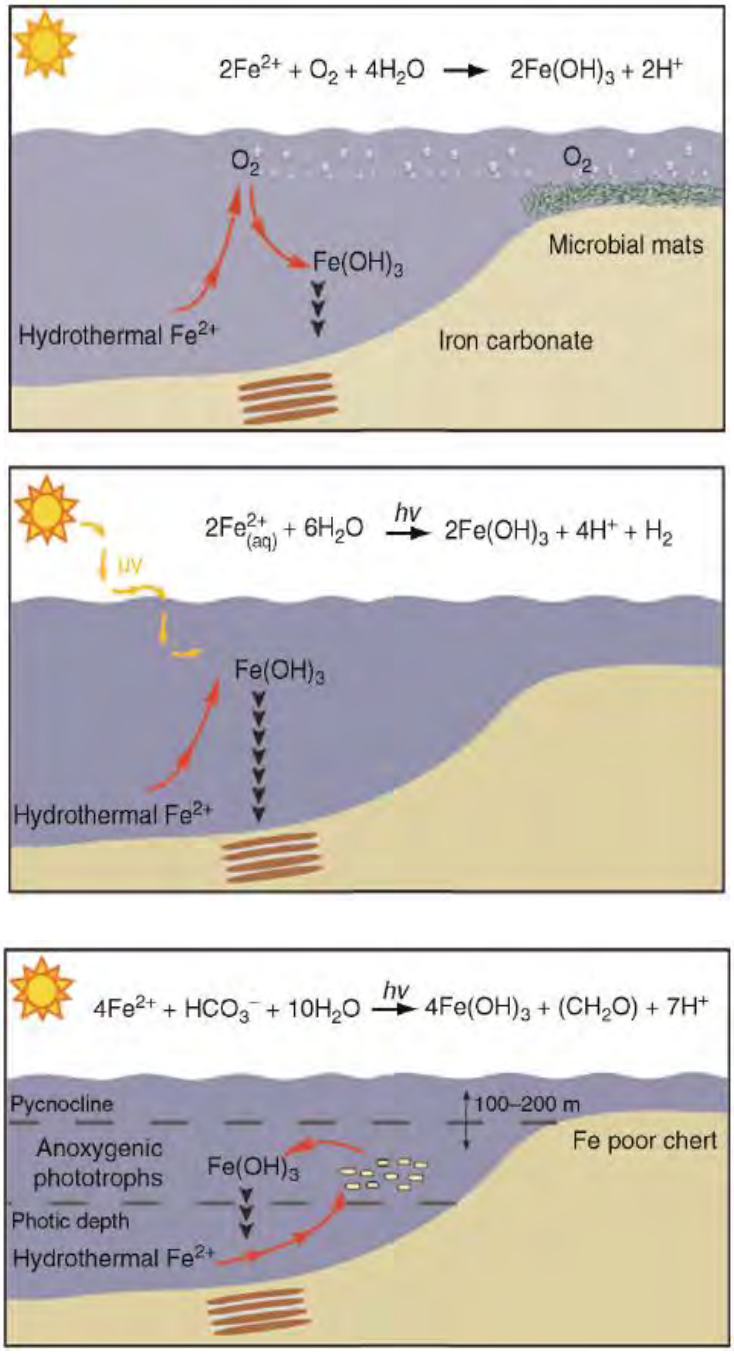

Figure 4.6: The models of banded iron formation deposition: (A) The traditional model of BIF deposition includes the production of oxygen by cyanobacteria in the shallow water photic zone, which is released into the water column to chemically react with hydrothermal dissolved Fe^{2+}. The two proposed mechanisms of deposition in an anoxic ocean water column are the abiotic Fe(II) photo-oxidation by UV light, which has been discounted (Konhauser et al., 2007) (b), and direct microbial Fe(II) oxidation via anoxygenic Fe^{2+} oxidizing phototrophy (c). Adapted from Posth *et al*. (2011).

An oxidative process strictly suited for Neoproterozoic glacial oceans is the introduction of fresh oxic water through subglacial meltwater plumes to anoxic deep waters, consequently converting the dissolved ferrous iron to ferric iron (Hoffman, 2005). The quantity of ferrous iron produced via this process has not been estimated.

The reasons for the rejection of abiotic pathways (oxygenic photosynthesis and UV photo-oxidation) as oxidative mechanisms during the Archean-Paleoproterozoic should not be applied to the Neoproterozoic without careful evaluation of the different time periods in question. The disqualification of oxygenic photosynthesis in the Archean may not be applicable to the Neoproterozoic because of the atmosphere and shallow ocean oxygen levels of the latter have been suggested to have drastically increased since the former (Holland, 2006), thereby placing oxygenic photosynthesis as one of the candidates for ferrous oxidation in the Neoproterozoic. UV photo-oxidation was rejected based on experimental Archean conditions simulated by Konhauser *et al.* (2007) which may not be valid for Neoproterozoic conditions. A questionable parameter in the experiment is the Fe^{2+} discharged from a shallow seamount-type system almost directly into the photic zone of the ocean. This was clearly not the case during the Neoproterozoic because iron rich hydrothermal fluids had low temperatures based on the absent positive Eu anomaly and the dissolved Fe^{2+} was delivered to the shallow oxic water by upwelling rather than direct emplacement by seamount-type system. Therefore, UV photo-oxidation is possibly another resurrected oxidative candidate for ferrous iron-formation during the Neoproterozoic. Thus, it is suggested that it is plausible that a combination between abiotic and biotic pathways could have been the responsible oxidative mechanisms for ferric iron deposition in the Neoproterozoic.

4.3.4 Current NIF models

Klein and Beukes (1993) pioneered NIF genetic modelling using results from the Rapitan iron-formation. Nearly two decades later, Baldwin *et al.* (2012) suggested an alternative genetic model using results from the Rapitan iron-formation as well. This new model only agreed with the idea that introduction of oxygen to the anoxic deep basin was influenced by glacial retreat from the classical model by Klein and Beukes (1993) but contradicted every other aspect of the model.

Lechte and Wallace (2015) invoked a different model with results from the Holowilena ironstone in Australia. Their model had a similar, small scale localised geo-tectonic basin setting like the Baldwin *et al.* (2012) model. The model also agreed that oxygen was introduced to the anoxic deep basin during glacial retreat however the oxygen was only introduced by dense oxic waters expelled from dynamic distal ice sheets and not by biotic oxidative mechanisms.

The classic NIF genetic model of Klein and Beukes (1993) (Fig. 4.7) proposes that during Neoproterozoic ice ages, the sea stand would have been extremely low, and oceans would have been stagnant because of extensive ice cover over the oceans. Consequently, highly anoxic and reducing conditions developed and facilitated accumulation of dissolved Fe^{2+} and/or Mn^{2+} derived from hydrothermal fluids or dissolved material from the basin floor. The inception of interglaciation or post glaciation stage resulted in transgression, introduction of oxygen in the photic zone and restoration of ocean circulation. Ocean circulation promoted the mixing of reduced Fe^{2+} and/or Mn^{2+} with oxygenated water and precipitated Fe^{3+} rich iron-formation and manganese formations.

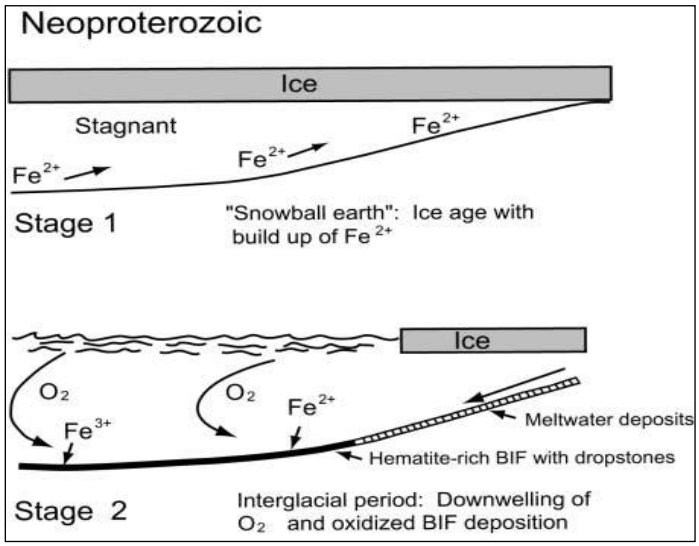

Figure 4.7: Klein and Beukes (1993) NIF genetic model showing two stages of iron sedimentation. Stage one is the accumulation of dissolved iron and manganese in ice covered anoxic deep oceans. Stage two is the oxygenation of the deep anoxic ocean following glacial retreat and subsequent precipitation of iron-formation. Adapted from (Klein and Beukes, 1993).

The alternative model by Baldwin *et al.* (2012) proposed an entirely different geo-tectonic setting where the basin is restricted by an extensional bathymetric sill. Extreme displacement of the

hanging wall during normal faulting event in the sill resulted to a localised deep basin (Fig.4.8A). Anoxia developed in the newly formed basin because of restricted water exchange with the above shallow ocean water with limited oxygen due to ice cover. The ice cover played a crucial role in supplying sediment and dissolved sulphate to the basin via subglacial outwash. The ice cover simultaneously provided highly reactive iron oxyhydroxide nanoparticles $Fe_{(HR)}$ to the basin. $Fe_{(HR)}$ was reduced to Fe^{2+} in the basin by bacteria, increasing dissolved ferrous iron content in the basin to levels suitable for iron-formation deposition (Fig.4.8B). Glacial retreat would have exposed the photic zone to atmospheric oxygen resulting in oxidation of dissolved Fe^{2+} and precipitation of iron-formation (Fig.4.8C).

The Lechte and Wallace (2015) model takes a holistic approach and explains the deposition of basal diamictite facies (Pualco Tillite) famously observed in most of NIF as the initial stage of the Sturtian glacial phase (Fig.4.9A). Previous models have omitted or failed to account for this diamictite facies even though it is a prominent distinguishing feature in NIFs (Ilyin, 2009). Lechte and Wallace (20105) explain that the ferruginous Pualco Tillite was deposited in a tectonically active basin floor due to the abundance of poorly sorted clasts which developed as a result of reworking of unconsolidated ferruginous silt and clastic detritus which deposited as muddy debris flow. Furthermore, Lechte and Wallace (2015) believe that this basal diamictite is not of glacial origin compared to other NIFs due to lack of evidence of dropstones and other glacial indicators. Subsequent to glacial retreat, a syntectonic half graben which makes up the restricted and anoxic primary basin of deposition developed in the deep ocean. In this restricted basin, anoxia was not a result of stagnation or tectonic processes as the previous models have elucidated. Lechte and Wallace (2015) explain the anoxia and ferruginous deep ocean condition as a global Neoproterozoic trend inherited from the Paleoproterozoic. Oxygenation of the anoxic and ferruginous oceans was a result of dense oxic plumes released from dynamic distal ice sheets that settled into the oceanographic depression of the half-graben and not a result of glacial retreat as previous models suggested. Upwelling of dissolved Fe^{2+} basin water to dense oxic fluids in the half graben facilitated mixing of the two fluids and precipitated out Holowilena ironstones (Fig.4.9B). Dynamic glacial activity deposited the Wilyerpa Formation overlying the Holowilena ironstone leading to closing the half-graben (Fig.4.9C).

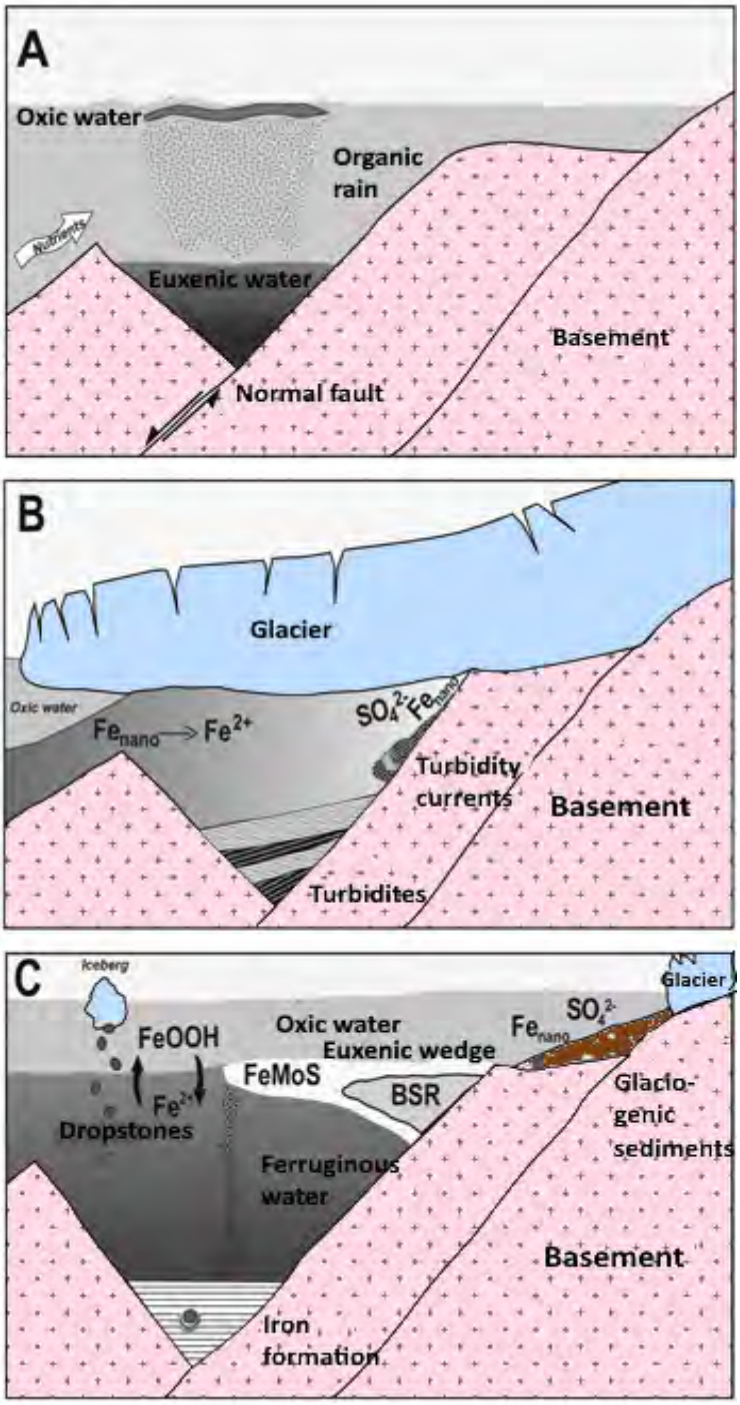

Figure 4.8: Modified Baldwin *et al.* (2015) NIF genetic model. (A) Normal fault in a bathymetric sill resulting in formation of a restricted deep basin consequently developing anoxia. (B) Glacial cover supplying sediment and highly reactive iron oxyhydroxide nanoparticles $Fe_{(HR)}$ to the basin. (C) Glacial retreat and subsequent oxidation.

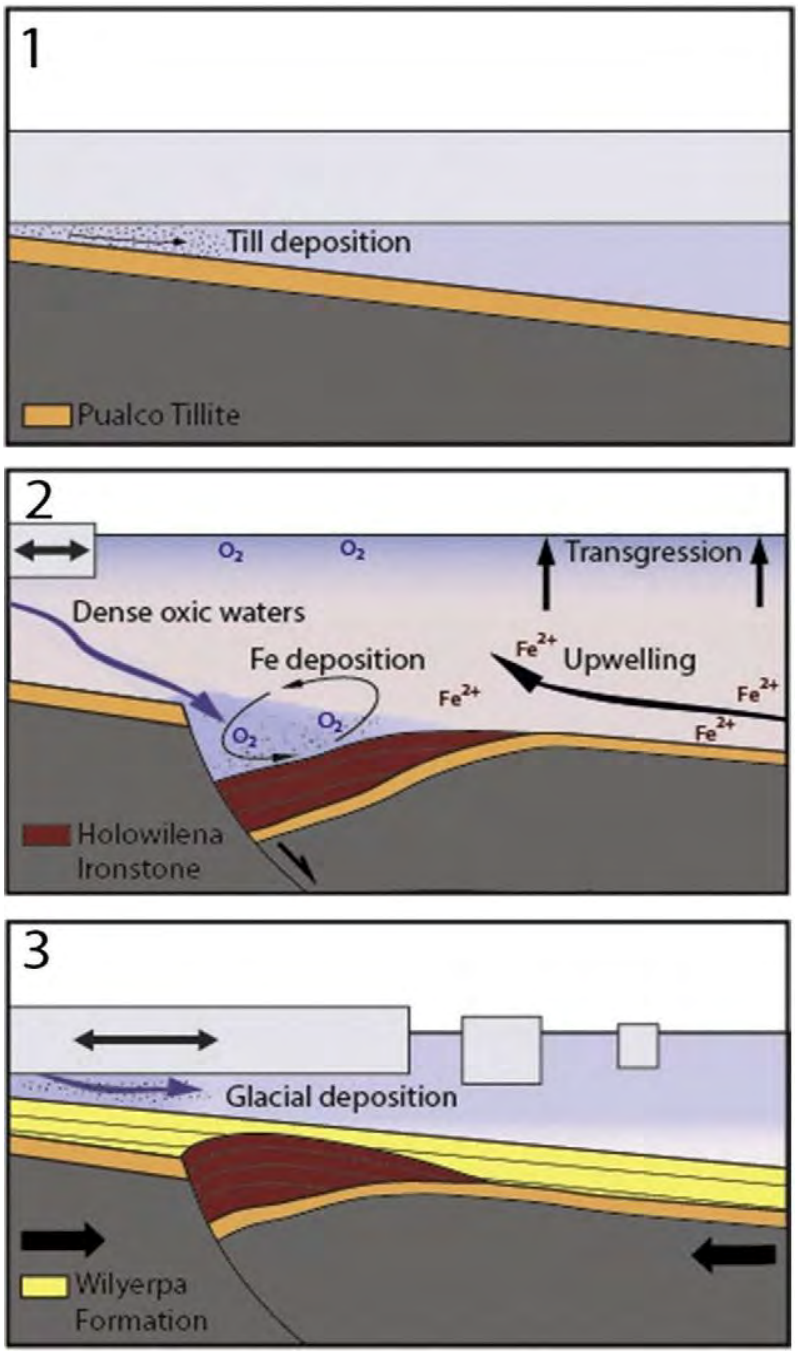

Figure 4.9: Lechte and Wallace (2015) NIF genetic model of Holowilena ironstone. (1) Initial stage of Sturtian glaciation which led to the deposition of the Pualco tillite in an anoxic and ferruginous basin. (2) Deposition of Holowilena ironstone due to mixing of dense oxic fluids expelled from distal sheets with ferrous water. (3) Deposition of the Wilyerpa Formation following dynamic glacial activity during glacial readvance.

4.3.5 Genesis of XIF

The conditions of precipitation discussed above are fundamental building blocks of a genetic model. Of further importance are of course the previous NIF genetic models because they may offer a plausible template for explaining the genesis of the XIF. Thus, development of the XIF model will involve close consideration of the presented factors and models in foregoing sections.

The basal diamictites were deposited in a large anoxic glaciomarine basin covered with extensive albedo-inducing ice during the initial stage of Sturtian glaciation. The anoxic conditions of the basin would have been largely inherited from the Paleoproterozoic as suggested by Holland (2006), or perhaps basin stagnation as a result of extensive ice cover as suggested by Klein and Beukes (1993) would have intensified the preexisting anoxic state of the basin. The anoxic deep basin would have acted as a reservoir for the accumulation of dissolved Fe^{2+} and Mn^{2+} initially sourced from seawater with no evident hydrothermal component and later contaminated by detrital material. The basin maintained a spatial chemical heterogeneity with respect to the observed decoupling between Fe^{2+} and Mn^{2+}, in order to account for the apparently heterogeneous distribution of manganeses in the basin and anticorrelation with Fe.

Increasing atmospheric temperatures prompted interglaciation which led to the release of dense oxic plumes by melting ice sheets to oxidise dissolved Fe^{2+} and Mn^{2+} to Fe^{3+} and Mn^{3+} respectively. The introduction of oxygen by dense oxic plumes was the first-generation oxidation event in the basin because there was still a large remnant of basin ice cover at this point which inhibited UV-photo oxidation, anoxygenic photosynthesis and oxidative photosynthesis pathways (Fig.4.10A). Iron, and locally manganese too, precipitated as oxides across the basin. The melting ice cover also released dropstones to the basin floor which consequently reworked the precipitated iron oxides to produce the ferruginous diamictites.

High atmospheric temperatures must have dominated during the post glacial period as supported by the high CIA values. As a result, intensely weathered detrital material eroded from the equatorial continents was transported to the transgressed basin and contaminated any dilute hydrothermal signature. The hydrological cycle and various anaerobic or aerobic oxidative mechanisms were initiated around this period, overlapping the first-generation oxidation event.

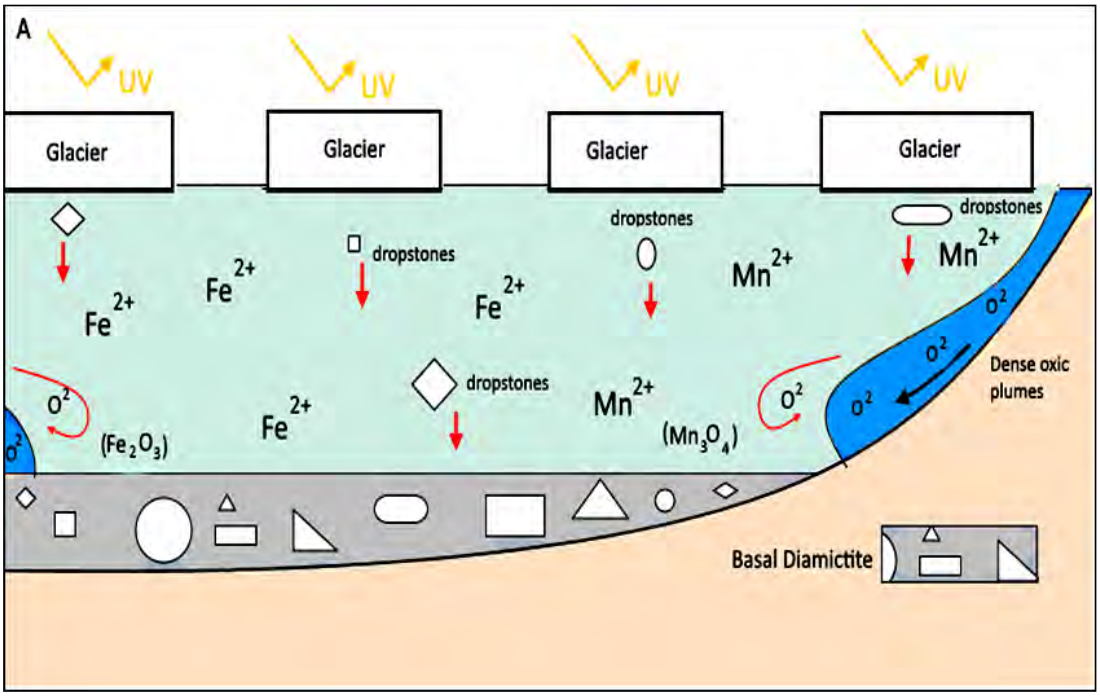
A
UV
UV
UV
UV
Glacier
Glacier
Glacier
Glacier
dropstones
dropstones
dropstones
dropstones
Fe^{2+}
Fe^{2+}
Fe^{2+}
Fe^{2+}
Mn^{2+}
Mn^{2+}
O^2
O^2
O^2
O^2
O^2
O^2
O^2
(Fe_2O_3)
(Mn_3O_4)
Dense oxic plumes
Basal Diamictite

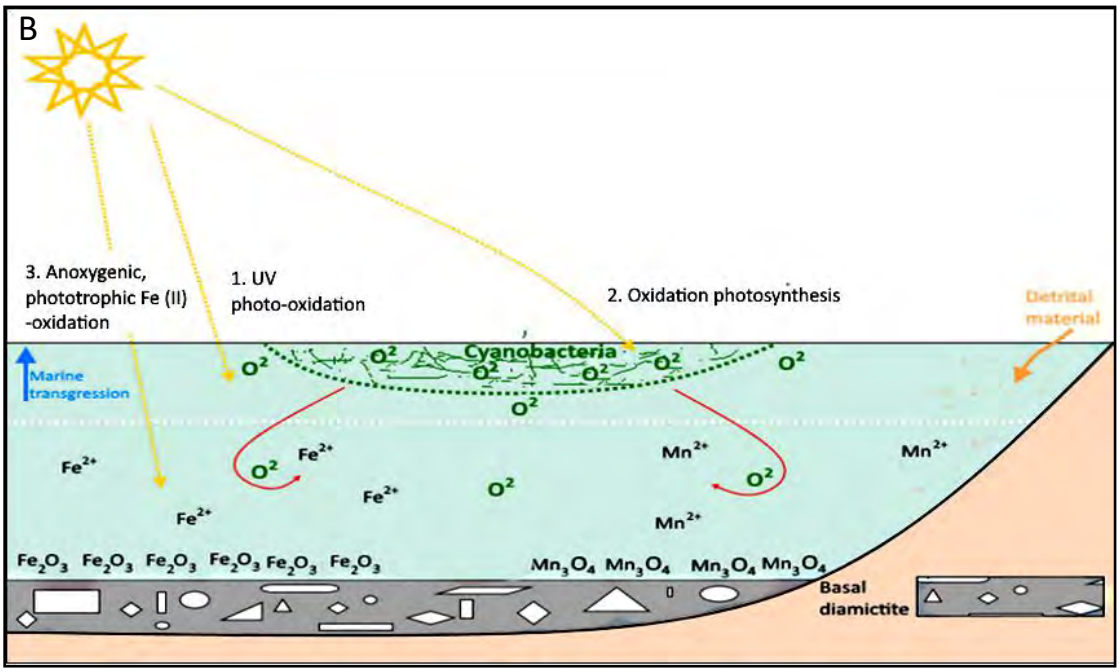
B
3. Anoxygenic, phototrophic Fe (II) -oxidation
1. UV photo-oxidation
2. Oxidation photosynthesis
Detrital material
Cyanobacteria
Marine transgression
O^2
Fe^{2+}
Mn^{2+}
Fe_2O_3
Mn_3O_4
Basal diamictite

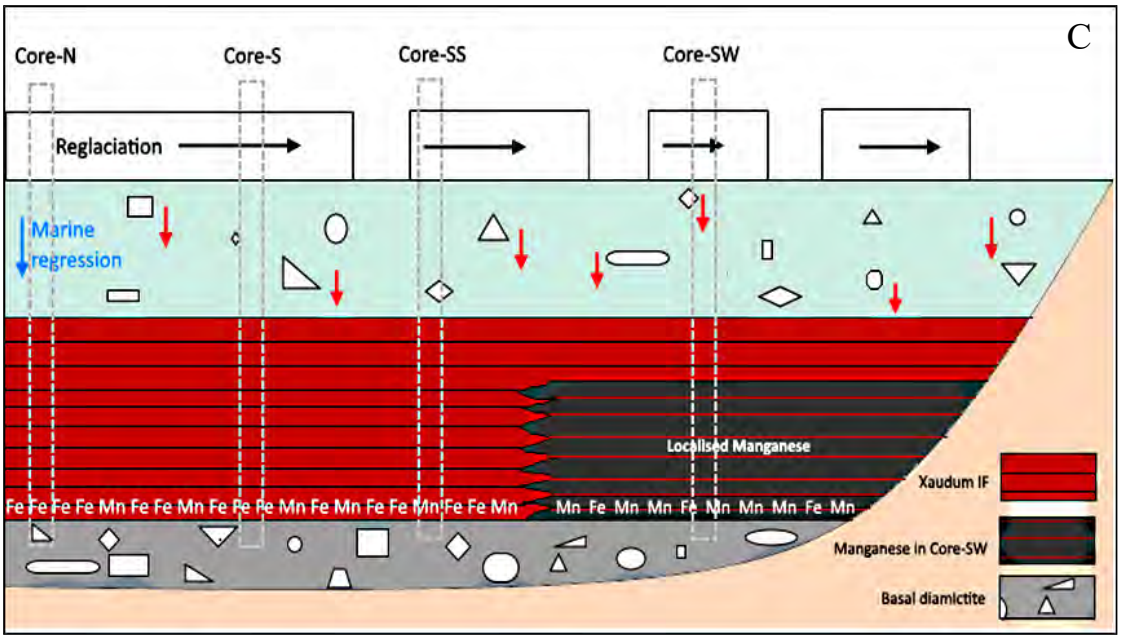

Figure 4.10: Genetic model for the Xaudum iron-formation. (A) Melting of the ice cover deposited the initial stage of Sturtian glaciation facilitated expulsion of dense oxic plumes and release of dropstones in the basin. The dense oxic plumes oxidised dissolved Fe^{2+} and Mn^{2+} to iron and manganese oxides respectively. (B) Very hot post glacial temperatures induced intense weathering and transport of detrital material to the basin. Possible oxidative mechanisms and the hydrological cycle facilitated further oxidation of dissolved Fe^{2+} and Mn^{2+} as high-valence oxides. (C) Decreased temperatures promoted marine re-glaciation and regression. Dropstones falling on XIF reworked it and produced ferruginous diamictites. The estimated relative locations of the four cores are shown in the paleobasinal context.

UV-photo oxidation, anoxygenic photosynthesis and oxidative photosynthesis may have further oxidised dissolved Fe^{2+} and Mn^{2+} to Fe^{3+} and Mn^{4+} respectively in the second-generation oxidation event. The hydrological cycle facilitated mixing of photic zone dioxygen and dissolved Fe^{2+} and Mn^{2+} fron the deep waters, which consequently precipitated as oxides. Manganese likely precipitated as Mn^{3+} and Mn^{4+} oxides, as supported by the manganese-cobalt positive correlation, (Fig.4.10B). Very simple primary mineralogy possibly consisting mainly of hematite and chert was precipitated from the water column and incorporated a detrital signature producing XIF with shale-like REE signatures.

Climatic condition reverted to an even colder extreme state compared to the initial phase of Sturtian glaciation as shown by the CIA results. The freezing conditions promoted marine regression and marine re-glaciation. Ice cover was deposited on extensively distributed XIF with

manganese enrichments locally (Fig.4.10C). The entire stratigraphic sequence was later subjected to the Damara orogeny which folded and metamorphosed the sequence to amphibolite facies. During this process, primary deposited Fe and Mn oxides and silicates were converted to the current mineral assemblage.

4.4 Significance of manganese in NIF

The relationship between Co and ferromanganese nodules has been extensively studied for their potential as ore deposits (Burns, 1976). An essential reason relating to this study is that Co concentration variations in ancient sediments can be used as a proxy for changes in redox conditions in the oceans and atmosphere over time (Konhauser *et al.*, 2009). This is achieved simply because Co can be scavenged type by oxidation and adsorption onto Mn^{3+} and Mn^{4+} oxides as they precipitate (Murray and Dillard, 1979). Experimental work by James and Dillard (1979) shows that oxidation of Co^{2+} by O_2 in bulk solution of seawater concentration cannot be achieved. Oxidation of Co^{2+} can only be successful near a powerful electric field at the MnO_2-solution interface. This makes the Co-Mn relationship a potentially powerful tool for evaluating change in redox conditions in marine basins of the past.

In the case of XIF Co^{2+} was possibly oxidised to Co^{3+} during the second-generation oxidation event because of the absence of Mn^{2+} oxidising bacteria in the dense oxic plumes and probably because of the lower redox potential (Eh) of first-generation compared to the second-generation oxidation (Murray *et al.,* 2007; Swanner *et al.*, 2014). The second-generation oxidative event thus provided a conducive environment for oxidation of Co^{2+} to Co^{3+} which adsorbed to Mn^{3+} and Mn^{4+} and not so with Fe^{3+}. The preferential adsorption of Co^{3+} to Mn^{3+} and Mn^{4+} is because Co^{2+} is suitably oxidised to Co^{3+} in the same Eh-pH field (Swanner *et al.*, 2014).

The evidence shown by the manganese-cobalt relationship in XIF presents a fresh perspective on the redox state of the Proterozoic. The G.O.E is believed to be the period in the Paleoproterozoic where the atmosphere and oceans reached peak oxic levels. The Hotazel sequence is known for thick and laterally extensive interlayers of Mn-rich sedimentary rock in BIF which were deposited around the G.O.E, implying possibly oxic enough conditions to precipitate primary Mn as oxide.

Unpublished results courtecy of Mhlanga (2019) who examined the chemostratigraphic behavior of Fe, Mn and Co (Fig.4.11) show in fact peak Co concentrations coinciding with hematite-rich (Fe^{3+}) transition zone between hematite free BIF and Mn-rich layers. The peak Co does not, however, coincide with the Mn-rich layer recording Mn maxima which also has hematite, albeit in much lesser amount. The above can possibly be interpreted as evidence that the Neoproterozoic primary depositional basin where XIF formed, was possibly more oxic than the Paleoproterozoic basin forming the Hotazel Formation around the GOE. This broadly conforms with the secular oxygen evolution model of Lyons *et al*. (2014) across the Precambrian (see also Fig. 4.5).

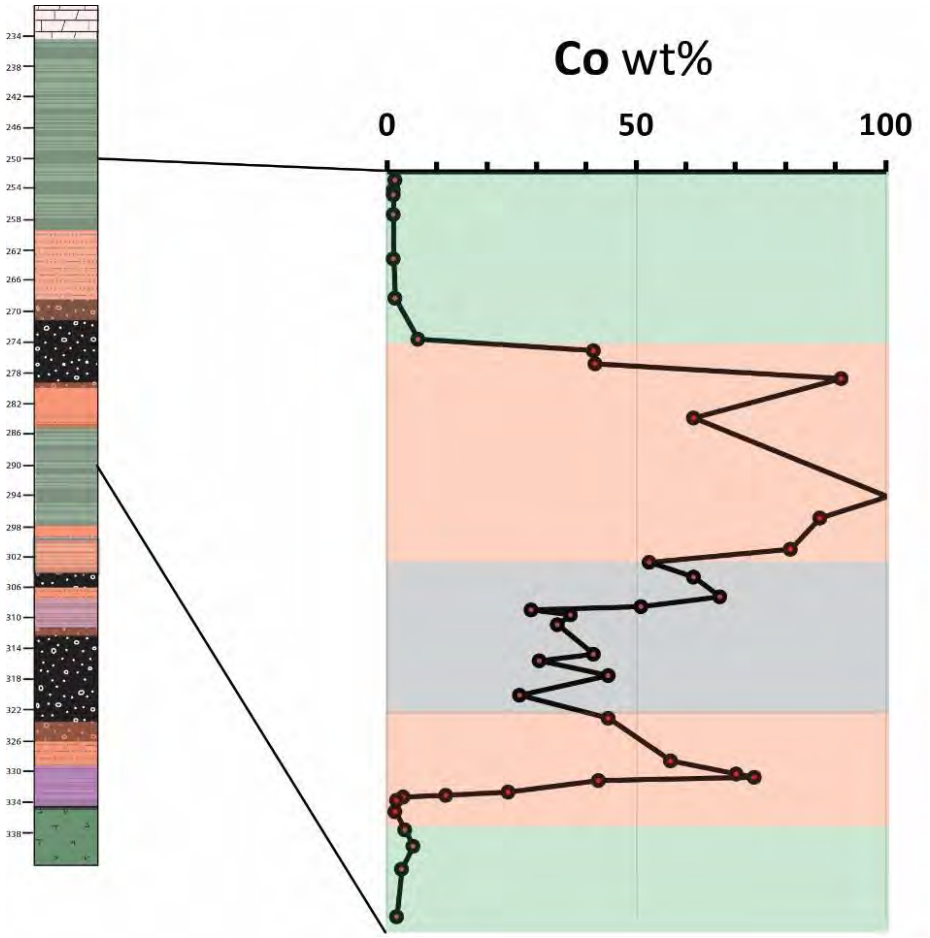

Figure 4.11: Chemostratigraphic variation in whole rock Co abundance of the 2.4Ga Hotazel Formation across the transition from BIF (striped) to intermediate hematite-rich lutite (pink) and ultimately to Mn-rich lutite (black). Note maxima in Co concentration coincidental with maximum hematite in hematite lutite. Plot courtesy of Mhlanga (2019), unpublished.

4.5 Fe/Mn speciation of the Xaudum IF and geo-metallurgical implications

Prior to metamorphism, the XIF is thought to have consisted of simple mineralogy consisting of hematite, chert and clastic material. Due to subsequent metamorphism, a new mineral assemblage resulted and chemical elements from the original sediments were redistributed into the newly formed mineral phases.

The XIF is recognized by the collaborating company *Tsodilo Resources* as a potential resource of iron ore by virtue of its high magnetite content. Nevertheless, not all Fe in the XIF is metallurgically viable, as much of the Fe is hosted in silicate minerals. For that reason, a simple modal mineral calculation was made to estimate how much of the bulk iron in the compositional grand average of XIF from this study, is magnetite-hosted and therefore extractable through magnetic separation techniques. Calculations were made using average mineral compositions of all key Fe-hosting minerals as obtained through EPMA. The results of the exercise are shown in (Table. 4.2) below.

Table 4.2: Major element oxide abundance and speciation in XIF mineral assemblage.

	Fe_2O_3	Mn_3O_4	TiO_2	CaO	K_2O	P_2O_5	SiO_2	Al_2O_3	MgO	Na_2O	
	(wt.%)	(wt%)	(wt%)	(wt%)	(wt%)	(wt%)	(wt%)	(wt%)	(wt%)	(wt%)	
Overall	68.00	1.00	0.10	2.00	0.20	0.40	25.00	1.50	1.30	0.20	99.70
2% apatite				1.40		0.40					
2% biotite	0.4		0.1		0.2		0.8	0.4	0.2		
5.2% garnet	0.8	0.6		0.6			2	1.1	0.1		
10% grunerite	3.1	0.4					5.5		1		
63.7% magnetite	63.70										
16.7% quartz							16.70				

Although the calculations above are somewhat imprecise, they provide insights into the feasibility of the XIF as an iron metal resource. As expected, from the 68% of bulk-rock iron oxide determined through geochemical analyses of this study, the very bulk of it is magnetite-hosted.

Magnetite is estimated to account for a bit less than 64wt% of the bulk iron oxide in the rock, which means that the non-recoverable silicate-hosted iron makes up a bit less than 6% of the total iron oxide on average. That iron partitions into the major silicate hosts, namely amphibole (grunerite), garnet and biotite, with the first taking up the bulk of it. Finally, concerning the Mn, it is effectively all hosted in garnet and amphibole, therefore the Fe/Mn ratio in the extractable magnetite ore is expected to be extremely high, thus providing an essentially pure product to the steel market.

5. CONCLUSIONS

In this thesis, results are presented on the petrography and geochemistry of the Neoproterozoic XIF in Botswana. The XIF and other NIF deposits around the world have been genetically attributed to a glacial influence, like the famous Rapitan-type iron-formation. The formation process of these NIF deposits is widely explained by the Snowball Earth Hypothesis, as typically manifested by the stratigraphy of the iron formation facies and direct association with glacial diamictites. Four drill cores of the XIF were targeted for detailed study. The mineralogy of the rock was examined and the metamorphic overprint to amphibolite grade facies was confirmed. The mineralogy of the XIF consists of magnetite, quartz, amphibole, garnet, biotite and chlorite in decreasing modal abundance. Amphibole exists as grunerite-cummingtonite solid solution series with magnesian compositions containing percentage level Mn seen in drillcore SW. The same drillcore contains spessartine garnet accounting for much of the containing Mn, unlike the other cores which are dominated by almandine and are therefore Mn-poor.

The geochemistry of XIF shows the well-known closure effect between Fe_2O_3 and SiO_2 in BIFs and a broad antithetic correlation between Fe_2O_3 and Mn_3O_4 in drillcore SW. The antithetic correlation between Fe_2O_3 and Mn_3O_4 suggested a chemical decoupling between Fe and Mn in the paleoenvironment of deposition. Drillcore SW has the highest Mn_3O_4 and Al_2O_3 content compared to other drill cores with averages of 2.4 wt. % and 2.6 wt. % respectively. When compared to contemporaneous NIF and older Algoma and Superior-type BIF, XIF has the highest bulk-rock Mn_3O_4 average and the highest Al_2O_3 average value among other NIFs. The Al_2O_3 and HFSE in XIF show strong positive relationship supporting the high detrital input into the Neoproterozoic paleobasin. Conversely, the XIF has the lowest CaO average values of 2.1 wt. % than all of the iron-formations as shown by the dearth of carbonate minerals. The V and Co in XIF have the highest values compared to other BIF and NIF and are the only transition metals that show statistical relationships with bulk Fe_2O_3 and Mn_3O_4. In all the four cores Fe_2O_3 shows a positive relationship with V which is explained by the affinity of V to magnetite grains in the XIF. The Co on the other hand shows an antithetic relationship with Fe_2O_3 and sympathetic relationship with Mn_3O_4. This is interpreted as a primary association of the Co exists with Mn oxides which were metamorphically transformed to the present assemblage. The affinity of Co to Mn_3O_4 in XIF

suggests that the Neoproterozoic oceans were possibly more oxic than those of the Paleoproterozoic around the G.O.E, to fractionate Co as Co^{3+} into Mn^{4+}.

The REE signature of XIF was compared to the coeval Braemar IF and the Paleoproterozoic Hotazel IF. The REE signature of the XIF and Braemar IF were comparable and show relatively flat REE patterns similar to the PAAS REE pattern and the top and bottom diamictite facies. This indicates high influx of detrital material in the Neoproterozoic paleobasin. On the contrary, the Hotazel IF shows depleted LREE and enriched HREE in positive-sloping patterns that mimic seawater and suggest pure chemical sedimentation effectively devoid of siliciclastic input. The XIF does not exhibit an apparent negative Ce anomaly which is commonly associated with oxic basin conditions during deposition. No positive Ce anomaly is seen in high Mn samples either, suggesting either no primary control of Mn^{4+}over Ce, or obliteration of the anomaly by detrital REE input. The XIF also appears to lack a positive Eu anomaly suggesting that hydrothermal influence was either absent in the XIF (like in other NIF) or masked by the detrital REE input.

The combination of CIA index and K_2O/Al_2O_3 ratio were applied to reconstruct the paleoclimatic conditions of the Neoproterozoic and to constrain the minerals associated with changing climate. These proxies confirm that the Neoproterozoic climate changed from cool and arid after the deposition of the basal diamictite as indicated by the high K_2O/Al_2O_3 ratio plotting closer to the muscovite line and low CIA values that range from 64-78. The climate changed to an interglacial state where it was warm and humid during the deposition of the XIF as shown by the low K_2O/Al_2O_3 ratio which represents smectite and kaolinite and high CIA values of 80-99, signifying high degrees of weathering under a humid climate. The climate must then have reverted to extremely cold conditions when the top diamictite was deposited. The conditions were likely even colder compared to those in the earlier glaciation as shown by the overall high K_2O/Al_2O_3 ratios of the top diamictite compared to the bottom diamictite.

In order to paint a full picture of what happened in the Neoproterozoic paleobasin during the deposition of XIF, the prevailing conditions of deposition had to be elucidated. These conditions allowed the creation of a genetic model for XIF. From the evidence produced, it is understood that the XIF was probably deposited in an open continental shelf with high detrital input from a nearby continental mass. The Fe and Si in XIF must have been sourced from shallow seawater mixed with

detrital components rich in Al, Si and HFSEs, while Mn may have been derived from either or both sources. Hydrothermal inputs, if present, were not possible to be confirmed using geochemistry. The above features are consistent with many other NIF globally.

It is believed that the marine anoxia that allowed accumulation of dissolved Fe^{2+} and Mn^{2+} in the paleobasin was partly inherited from a reducing Proterozoic ocean and was further accentuated by stagnant basin conditions due to the extensive ice cover. The dissolved Fe^{2+} and Mn^{2+} species accumulated in a chemically decoupled fashion in deeper parts of the basin with dissolved Mn^{2+} accumulating as oxides closer to the coast where detrital input was higher. The oxidation mechanism which was required to oxidise and precipitate the dissolved Fe^{2+} and Mn^{2+} species occurred in two different but overlapping stages. The first was initiated by melting ice sheets as a result of increasing temperatures which released dense oxic plumes that consequently oxidized the Fe^{2+} and Mn^{2+} and precipitated the Fe and Mn oxides respectively. The second oxidation step occurred when the ice cover was completely thawed under extremely hot and humid climate and the sun rays reached the photic zone of the basin. A combination of UV-photo oxidation, anoxygenic photosynthesis and oxidative photosynthesis may have been responsible for further oxidation of dissolved Fe^{2+} and Mn^{2+} to Fe and Mn-oxides in the photic zone of the basin. The hydrological cycle upwelled reduced deep water containing the dissolved Fe^{2+} and Mn^{2+} and mixed it with oxic shallow seawater to precipitate Fe and Mn oxides.

Finally, simple speciation calculations using bulk-rock average chemical composition of the XIF and mineral-specific compositional data, suggest that almost 94% of the total iron can be recovered as magnetite from the rocks, as the silicate fraction only accounts for about 6% of the total iron. The extractable magnetite is expected to be extremely poor in Mn, as all the Mn is accommodated into silicate minerals (garnet and amphibole).

There is no doubt that the Snowball Earth Hypothesis laid fundamental principles and arguments on the climatic, tectonic, ocean-atmospheric and continental conditions of the Neoproterozoic that enabled the deposition of XIF and NIF in general. This hypothesis has given birth to various schools of thought that further seek to furnish new information and refine existing ideas on the environmental conditions of the Neoproterozoic. Some agree with the original hypothesis and provide updates and modifications whilst some completely reject it and provide alternative

explanations. Whatever the case might be the Snowball Earth Hypothesis has opened an ongoing discourse among the science community that has spawned new ideas that will continue to shed light on the ocean-atmosphere redox conditions of the Neoproterozoic and how the Earth has transformed over time. The XIF seems to be one of the custodians of the Snowball Earth Hypothesis and genetic models from Lechte and Wallace (2015) and Klein and Beukes (1993) to shed light and paint a complete picture of the Neoproterozoic.

5.1 Proposed future work

The results of this work suggest that NIFs are important archives for climate and ocean chemistry of the Neoproterozoic, such as:

1. The high weathering rates on the continents as shown by the high CIA index and high siliciclastic components in XIF during glacial retreat;
2. The redox state of the Neoproterozoic paleobasin as seen in relationships between Co and Mn in XIF which is absent in earlier IF deposits of the Paleoproterozoic and Archean. This suggests that the Neoproterozoic atmosphere-ocean system was possibly more oxic than the Paleoproterozoic and Archean but less so than the present-day.

The correlation between Co and Mn in XIF and lack of positive Ce anomalies therefore allows the inference that redox conditions in the Neoproterozoic were possibly more oxic than in the Paleoproterozoic following the G.O.E, but less oxic than modern ocean Mn nodules. Molybdenum (Mo) has been extensively studied more so than Co, because it is believed to behave similarly to Co during Mn oxide formation, but unlike Co, it has more than one stable isotopes and is thus suitable as an isotopic proxy. In XIF, Mo does not show any obvious correlation with neither Fe nor Mn. The work done in this study opens an opportunity for more work to be done using Mo stable isotopes and assess how they might inform us about the redox state and Mn deposition in the Neoproterozoic compared to the Archean and Paleoproterozoic, and potentially constrain further the redox evolution of the Precambrian atmosphere and oceans.

6. REFERENCES

Thomas W.T, 2016. "Paleoenvironmental and paleoclimatic reconstruction of the Witbank coal deposits (Karoo Basin South Africa)" *PhD Thesis*, University of Pretoria, Pretoria, South Africa.

Anbar, A.D., Duan, Y., Creaser, R.A., Kaufman, A.J., Gordon, G.W., Arnold, G.L., Buick, R., Kendall, B., Lyons, T.W., Scott, C. & Garvin, J. 2007, "A Whiff of Oxygen Before the Great Oxidation Event?", *Science,* vol. 317, no. 5846, pp. 1903-1906.

Anbar, A.D., 2008. "Elements and evolution", *Science*, vol. 322, no.5907, pp.1481-1483.

Anhaeusser, C.R. and Walraven, F., 1999. "Episodic granitoid emplacement in the western Kaapvaal Craton: evidence from the Archaean Kraaipan granite-greenstone terrane, South Africa". *Journal of African Earth Sciences*, vol.28, no.2, pp.289-309.

Armstrong, F.A., 2007. "Why did Nature choose manganese to make oxygen?", *Philosophical Transactions of the Royal Society B: Biological Sciences*, vol. 363, no.1494, pp.1263-1270.

Bahlburg, H. & Dobrzinski, N. 2011, "Chapter 6 A review of the Chemical Index of Alteration (CIA) and its application to the study of Neoproterozoic glacial deposits and climate transitions", *Geological Society, London, Memoirs,* vol. 36, no. 1, pp. 81-92.

Baker, H., 2014. Mineral resource estimate for the Xaudum Iron Project (Block 1), Republic of Botswana. *Report prepared for Gcwihaba Resources (Pty) Ltd. by SRK Consulting (UK) Limited UK05835*, p.100.

Baldwin, G. 2014, "The Stratigraphy and Geochemistry of the Rapitan Iron Formation, Northwest Territories and Yukon, Canada", *unpublished PHd thesis*. Laurentian University, Sudbury, Canada

Baldwin, G.J., Nägler, T.F., Greber, N.D., Turner, E.C. & Kamber, B.S. 2013, "Mo isotopic composition of the mid-Neoproterozoic ocean: An iron formation perspective", *Precambrian Research,* vol. 230, pp. 168-178.

Baldwin, G.J., Turner, E.C. & Kamber, B.S. 2012, "A new depositional model for glaciogenic Neoproterozoic iron formation: insights from the chemostratigraphy and basin configuration of the Rapitan iron formation", *Canadian Journal of Earth Sciences,* vol. 49, no. 2, pp. 455-476.

Barton, J.M., Holzer, L., Kamber, B., Doig, R., Kramers, J.D. & Nyfeler, D. 1994, "Discrete metamorphic events in the Limpopo Belt, southern Africa: implications for the application of P-T paths in complex metamorphic terrains", *Geology,* vol. 22, no. 11, pp. 1035-1038.

Basta, F.F., Maurice, A.E., Fontboté, L. & Favarger, P.Y., 2011. "Petrology and geochemistry of the banded iron formation (BIF) of Wadi Karim and Um Anab, Eastern Desert, Egypt: implications for the origin of Neoproterozoic BIF". *Precambrian Research*, vol. 187, no.3, pp.277-292.

Bau, M. & Dulski, S. 1993, "Distribution of yttrium and rare-earth elements in the Penge", *Precambrian Research*, vol.79, pp. 37-55.

Bau, M. & Möller, P., 1993, "Rare earth element systematics of the chemically precipitated component in Early Precambrian iron formations and the evolution of the terrestrial atmosphere-hydrosphere-lithosphere system", *Geochimica et Cosmochimica Acta*, vol. 57, no.10, pp.2239-2249.

Bekker, A., Holland, H.D., Wang, P., Iii, D.R., Stein, H.J., Hannah, J.L., Coetzee, L.L. & Beukes, N.J. 2006, "Dating the Rise of Oxygen", *Nature*, vol.427, pp. 117-120.

Bekker, A., Kaufman, A.J., Karhu, J.A. & Eriksson, K.A. 2005, "Evidence for Paleoproterozoic cap carbonates in North America", *Precambrian Research,* vol. 137, no. 3-4, pp. 167-206.

Bekker, A., Slack, J.F., Planavsky, N., Krapez, B., Hofmann, A., Konhauser, K.O. & Rouxel, O.J. 2010, "Iron formation: The sedimentary product of a complex interplay among mantle, tectonic, oceanic, and biospheric processes", *Economic Geology,* vol. 105, no. 3, pp. 467-508.

Bertine, K.K. & Turekian, K.K., 1973, "Molybdenum in marine deposits", *Geochimica et Cosmochimica Acta*, vol. 37, no.6, pp.1415-1434.

Beukes, N.J. & Klein, C., 1990, "Geochemistry and sedimentology of a facies transition—from microbanded to granular iron-formation—in the early Proterozoic Transvaal Supergroup, South Africa", *Precambrian Research*, vol.47, no.1-2, pp.99-139.

Beukes, N.J. & Gutzmer, J. 2008, "Origin and paleoenvironmental significance of major iron formations at the Archean-Paleoproterozoic boundary", *Reviews in Economic Geology,* vol. 15, pp. 5-47.

Blamey, N.J.F., Brand, U., Parnell, J., Spear, N., Lécuyer, C., Benison, K., Meng, F., and Ni, P., 2016, "Paradigm shift in determining Neoproterozoic atmospheric", *Geology,* vol. 44, pp. 651–654

Block, S., Moyen, J.F., Zeh, A., Poujol, M., Jaguin, J. & Paquette, J.L. 2013, "The Murchison Greenstone Belt, South Africa: Accreted slivers with contrasting metamorphic conditions", *Precambrian Research,* vol. 227, pp. 77-98.

Braterman, P.S., Cairns-Smith, A.G. & Sloper, R.W., 1983, "Photo-oxidation of hydrated Fe^{2+}-significance for banded iron formations". *Nature*, vol. 303, no. 5913, p.163.

Breitkopf, J. 1988, "Iron formations related to mafic volcanism and ensialic rifting in the southern margin zone of the Damara Orogen, Namibia", *Precambrian Research,* vol. 38, no. 2, pp. 111-130.

Broecker, W. S. & Peng, T. H. 1982, "Tracers in the sea", *Geochimica et Cosmochimica Acta*. New York, Lamont-Doherty Earth Observatory: Eldigio Press. doi: 10.1016/0016-7037(83)90075-3.

Buhn, B. & Stanistreet, I.G. 1997, “Insight into the enigma of Neoproterozoic manganese and iron formations from the perspective of super continental break-up and glaciation”, *Geological Society, London, Special Publications,* vol. 119, no. 1, pp. 81-90.

Buhn, B., Okrusch, M., Woermann, E., Lehnert, K. & Hoernes, S. 1995, “Metamorphic evolution of Neoproterozoic manganese formations and their country rocks at Otjosondu, Namibia”, *Journal of Petrology,* vol. 36, no. 2, pp. 463-496.

Burns, R. G. 1976, “The uptake of cobalt into ferromanganese nodules soils and synthetic manganese (IV) oxides”, *Geochimica et Cosmochimca Acta.*, vol. 40, pp. 95–102.

Cabral, A.R., Moore, J.M., Mapani, B.S., Kouboval, M. & Sattler, C.D. 2011, “Geochemical and mineralogical constraints on the genesis of the Otjosondu ferromanganese deposit, Namibia: Hydrothermal exhalative versus hydrogenetic (including snowball-Earth) origins”, *South African Journal of Geology,* vol. 114, no. 1, pp. 57-76.

Cairns-Smith, A.G., 1978, ”Precambrian solution photochemistry, inverse segregation, and banded iron formations”. *Nature*, vol. 276, no 5690, p. 807.

Caldeira, K. & Kasting, J.F. 1992, “Susceptibility of the early Earth to irreversible glaciation caused by carbon dioxide clouds”, *Nature,* vol. 359, no. 6392, pp. 226-228.

Canfield, D.E. 2005, “The early history of the atmospheric oxygen: Homage to Robert M. Garrels”, *Annual Review of Earth and Planetary Sciences,* vol. 33, no. 1, pp. 1-36.

Canfield, D.E., Poulton, S.W., Knoll, A.H., Narbonne, G.M., Ross, G., Goldberg, T., Strauss, H. & Hill, T. 2008, “Neoproterozoic Deep-Water Chemistry”, *Nature,* pp. 949-953.

Carney, J., Aldiss, D.T. & Lock, N.P. 1994, “The geology of Botswana”, *Geological Survey Botswana, Bulletin.* vol. 37, pp. 104–113.

Catling, D.C. & Claire, M.W. 2005, “How Earth’s atmosphere evolved to an oxic state: A status report”, *Earth and Planetary Science Letters,* vol. 237, pp. 1-20.

Catuneanu, O., Wopfner, H., Eriksson, P.G., Cairncross, B., Rubidge, B.S., Smith, R.M.H. & Hancox, P.J., 2005, The Karoo basins of south-central Africa. *Journal of African Earth Sciences*, vol.43, no.1-3, pp.211-253.

Cornu, S., Cattle, J.A., Samouëlian, A., Laveuf, C., Guilherme, L.R.G. & Alberic, P., 2009, "Impact of redox cycles on manganese, iron, cobalt, and lead in nodules", *Soil Science Society of America Journal*, vol.73, no.4, pp.1231-1241.

Cox, G.M., Halverson, G.P., Minarik, W.G., Le Heron, D.P., Macdonald, F.A., Bellefroid, E.J. & Strauss, J.V, 2013, "Neoproterozoic iron formation: An evaluation of its temporal, environmental and tectonic significance", *Chemical Geology,* vol. 362, pp. 232-249.

Cox, G.M., Halverson, G.P., Poirier, A., Le Heron, D., Strauss, J.V. & Stevenson, R. 2016, "A model for Cryogenian iron formation", *Earth and Planetary Science Letters,* vol. 433, pp. 280-292.

Craddock, P. R., Bach, B., Seewald, J.S., Rouxel, O.J., Reeves, E. & Tivey, M.K, 2010, "Rare earth element abundances in hydrothermal fluids from the Manus Basin , Papua New Guinea : Indicators of sub-seafloor hydrothermal processes in back-arc basins", *Geochimica et Cosmochimica Acta*. Elsevier Ltd, vol. 74, no. 19, pp. 5494–5513.

Christie-Blick, N., Sohl, L.E. & Kennedy, M.J, 1999, "Considering a Neoproterozoic snowball Earth; discussion and reply", *Science,* vol. 284, pp. 1087-1087.

Crowley, T.J., Hyde, W.T.& Peltier, W.R., 2001, "CO_2 levels required for deglaciation of a "Near-Snowball" "Earth". *Geophysical Research Letters*, vol. 28, no. 2, pp.283-286.

Crerar, D.A. & Barnes, H.L., 1974, "Deposition of deep-sea manganese nodules. *Geochimica et Cosmochimica Acta*, *38*(2), pp.279-300.

de Wit, M.J., de Ronde, C.E, Tredoux, M., Roering, C., Armstrong, R.A., Green, R.W., Peberdy, E. & Hart, R.J., 1992, "Formation of an Archean continent", *Nature,* vol. 357, no. 6379, pp. 553-562.

Dymek, R.F. & Klein, C., 1988, “Chemistry, petrology and origin of banded iron-formation lithologies from the 3800 Ma Isua supracrustal belt, West Greenland”, *Precambrian Research*, vol.39, no.4, pp.247-302.

Elderfield, H. & Greaves, M.J. 1982, “The rare earth elements in seawater”, *Nature,* vol. 296, no. 5854, pp. 214-219.

Embleton, B.J.J. & Williams, G.E. 1986, “Low paleolatitude of deposition for late Precambrian periglacial varvites in South Australia: implications for paleoclimatology”, *Earth and Planetary Science Letters,* vol. 79, no. 3-4, pp. 419-430.

Evans, D.A., 2000, “Stratigraphic, geochronological, and paleomagnetic constraints upon the Neoproterozoic climatic paradox”. *American Journal of Science*, vol. 300, no.5, pp.347-433.

Eyles, N. & Januszczak, N. 2004, “'Zipper-rift': A tectonic model for Neoproterozoic glaciations during the breakup of Rodinia after 750 Ma”, *Earth-Science Reviews,* vol. 65, no. 1-2, pp. 1-73.

Fairchild, I.J. & Kennedy, M.J. 2007, “Neoproterozoic glaciation in the Earth System”, *Journal of the Geological Society,* vol. 164, no. 5, pp. 895-921.

Feng, L., Huang, J., Lu, D. & Zhang, Q. 2016, “Major and trace element geochemistry of the Neoproterozoic syn-glacial Fulu iron formation, South China”, *Geological Magazine, pp.* 1-10.

Franchi, F. & Mapeo, R.B.M., 2019, “Evolution of an Archaean intracratonic basin: A review of the Transvaal Supergroup lithostratigraphy in Botswana”, *Earth-Science Reviews*. vol.191, pp.273-290.

Frei, R., Gaucher, C., Stolper, D. & Canfield, D.E. 2013, “Fluctuations in late Neoproterozoic atmospheric oxidation - Cr isotope chemostratigraphy and iron speciation of the late Ediacaran lower Arroyo del Soldado Group (Uruguay)”, *Gondwana Research,* vol. 23, no. 2, pp. 797-811.

Freitas, B.T., Warren, L.V., Boggiani, P.C., De Almeida, R.P. & Piacentini, T. 2011, "Tectono-sedimentary evolution of the Neoproterozoic BIF-bearing Jacadigo Group, SW-Brazil", *Sedimentary Geology,* vol. 238, no. 1-2, pp. 48-70.

Frimmel, H.E., 2011, "The Kaigas and Numees formations, Port Nolloth Group, in South Africa and Namibia". *Geological Society, London, Memoirs*, vol. 36, no. 1, pp.223-231.

Fryer, B.J. 1963, "Rare earth elements in iron-formation", *Economic Geology*, pp. 345-358.

Garwood,E.J.& Gregory, J. W. 1898, "Contribution to the glacial geology of Spitsbergen", *Quarterly Journal of the Geological Society*, London, vol. 54, pp. 197–225.

Gaucher, C., Sial, A.N. & Frei, R., 2015, "Chemostratigraphy of Neoproterozoic banded iron formation (BIF): types, age and origin", Chemostratigraphy, pp. 433-449).

Glikson, A.Y. 2008, "Milestones in the evolution of the atmosphere with reference to climate change", *Australian Journal of Earth Sciences,* vol. 55, no. 2, pp. 125-139.

Grobler, D.F. & Walraven, F. 1993, "Geochronology of Gaborone Granite Complex extensions in the area north of Mafikeng, South Africa", *Chemical Geology,* vol. 105, no. 4, pp. 319-337.

Haddon, I.G. & McCarthy, T.S. 2005, "The Mesozoic-Cenozoic interior sag basins of Central Africa: The Late-Cretaceous-Cenozoic Kalahari and Okavango basins", *Journal of African Earth Sciences,* vol. 43, no. 1-3, pp. 316-333.

Haddon, I.G. 2005, "The Sub-Kalahari Geology and Tectonic Evolution of the Kalahari Basin, Southern Africa", *PhD Thesis,* University of the Witwatersrand, South Africa, pp. 1-360.

Halverson, G.P., Hoffman, P.F., Schrag, D.P., Maloof, A.C. & Rice, A.H.N., 2005, Toward a Neoproterozoic composite carbon-isotope record. *Geological Society of America Bulletin*, vol. 117, no. 9-10, pp.1181-1207.

Halverson, G.P. & Shields-Zhou, G. 2011, "Chapter 4 Chemostratigraphy and the Neoproterozoic glaciations", *Geological Society, London, Memoirs,* vol. 36, no. 1, pp. 51-66.

Halverson, G.P., Poitrasson, F., Hoffman, P.F., Nadelec, A., Montel, J.M. & Kirby, J. 2011, "Fe isotope and trace element geochemistry of the Neoproterozoic syn-glacial Rapitan iron formation", *Earth and Planetary Science Letters,* vol. 309, no. 1-2, pp. 100-112.

Harland, W. B.& Rudwick, M. J. S. 1964, "The great infra-Cambrian ice age". *Scientific American*, August, 42–49.

Harland, W. B. 1983, "The Proterozoic glacial record". In: Medaris, L.G., Jr., Byers, W. C., Mickelson, D.M & Shanks, W. C. (eds) Proterozoic Geology. *Geological Society of America*, Memoir, vol. 161, pp. 279–288

Hartman, H., 1984, "The evolution of photosynthesis and microbial mats: A speculation on the banded iron formations". *MBL LECT. BIOL.*

Hoffmann, K. & Prave, A.R. 1996, "A preliminary note on revised subdivision and regional correlation of the Otavi Group based on glaciogenic diamictites and associated cap dolostones", *Communications of the Geological Survey of Namibia,* vol. 11, pp. 77-82.

Hoffman, P.F., Kaufman, A.J., Halverson, G.P. & Schrag, D.P. 1998, "A Neoproterozoic snowball earth", *Science,* vol. 281, no. 5381, pp. 1342-1346.

Hoffman, P.F. & Schrag, D.P. 2002, "The snowball Earth hypothesis: Testing the limits of global change", *Terra Nova,* vol. 14, pp. 129-155.

Hoffmann, K.H., Condon, D. J., Bowring, S.A & Crowley, J.L, 2004, "U–Pb zircon date from the Neoproterozoic Ghaub Formation, Namibia: constraints on Marinoan glaciation", *Geology,* vol. 32, pp. 817–820

Hoffman, P.F. 2005, "28th DeBeers Alex. Du Toit memorial lecture, 2004. On Cryogenian (Neoproterozoic) ice-sheet dynamics and the limitations of the glacial sedimentary record", *South African Journal of Geology,* vol. 108, no. 4, pp. 557-577.

Hoffman, P.F. 2011, “Chapter 2 A history of Neoproterozoic glacial geology, 1871-1997”, *Geological Society, London, Memoirs,* vol. 36, no. 1, pp. 17-37.

Hoffman, P.F. & Halverson, G.P. 2011, “Chapter 36 Neoproterozoic glacial record in the Mackenzie Mountains, northern Canadian Cordillera”, *Geological Society, London, Memoirs,* vol. 36, no. 1, pp. 397-412.

Hoffman, P.F., Macdonald, F.A. & Halverson, G.P. 2011, “Chapter 5 Chemical sediments associated with Neoproterozoic glaciation: iron formation, cap carbonate, barite and phosphorite”, *Geological Society, London, Memoirs,* vol. 36, no. 1, pp. 67-80.

Holland, H.D. 2006, “The oxygenation of the atmosphere and oceans”, *Phil. Trans. R. Soc. B*, vol. 361, pp. 903–915.

Hyde, W.T., Crowley, T.J., Baum, S.K. & Peltier, W.R. 2000, “Neoproterozoic 'snowball earth' simulations with a coupled climate/ice- sheet model”, *Nature,* vol. 405, no. 6785, pp. 425-429.

Ikeda, T. & Tajika, E., 1999, ″A study of the energy balance climate model with CO2-dependent outgoing radiation: Implication for the glaciation during the Cenozoic″, *Geophysical Research Letters,* vol. 26, no.3, pp.349-352.

Ilyin, A.V. 2009, “Neoproterozoic banded iron formations”, *Lithology and Mineral Resources,* vol. 44, no. 1, pp. 78-86.

Irving, E. 1956, “Palaeomagnetic and palaeoclimatological aspects of polar wandering”, *Geofisica Pura e Applicada*, vol. 33, pp. 23–41.

James, H.L. 1983, “Distribution of banded iron-formation in space and time”, *Developments in Precambrian Geology,* vol. 6, pp. 471-490.

Kastin, J.F. & Siefert, J.L. 2003, “Life and the Evolution of Earth’s Atmosphere”, *Nature*, vol. 296, pp. 1066-1067.

Kaufman, A.J., Knoll, A.H. and Narbonne, G.M., 1997, "Isotopes, ice ages, and terminal Proterozoic earth history", *Proceedings of the National Academy of Sciences*, vol. 94, no.13, pp.6600-6605.

Kennedy, M., Mrofka, D. & Von, D.B. 2008, "Snowball Earth termination by destabilization of equatorial permafrost methane clathrate", *Nature,* vol. 453, no. 7195, pp. 642-645.

Key, R.M. & Rundle, C.C. 1984, "The regional significance of new isotopic age from windows through the "Kalahari beds" in Northern Botswana", *Transactions, Geological Society of South Africa,* vol. 84, pp. 51-66.

Key, R.M. & Ayres, N. 2000, "The 1998 edition of the National Geological Map of Botswana", *Journal of African Earth Sciences,* vol. 30, no. 3, pp. 427-451.

Khalil, K.I. & El-Shazly, A. 2012, "Petrological and Geochemical Characteristics of Egyptian Banded Iron Formations: Review and New Data from Wadi Kareim", *Geochemistry: Exploration, Environment, Analysis*, vol 12, no. 2, pp. 105-126.

Kirschvink, J.L. 1992," Late Proterozoic low-latitude global glaciation: the snowball Earth*", The Proterozoic Biosphere,* vol. 52, pp, 51-52.

Klein, C. & Beukes, N.J. 1989, "Geochemistry and sedimentology of a facies transition from limestone to iron-formation deposition in the early Proterozoic Transvaal Supergroup, South Africa", *Economic Geology,* vol. 84, no. 7, pp. 1733-1774.

Klein, C. & Beukes, N.J. 1993, "Sedimentology and geochemistry of the glaciogenic late Proterozoic Rapitan iron-formation in Canada", *Economic Geology,* vol. 88, no. 3, pp. 542-565.

Klein, C. & Ladeira, E.A. 2004, "Geochemistry and mineralogy of Neoproterozoic banded iron-formations and some selected, siliceous manganese formations from the Urucum district, Mato Grosso Do Sul, Brazil", *Economic Geology,* vol. 99, no. 6, pp. 1233-1244.

Klein, C. 2005, “Some Precambrian banded iron-formations (BIFs) from around the world: Their age, geologic setting, mineralogy, metamorphism, geochemistry, and origin”, *American Mineralogist,* vol. 90, no. 10, pp. 1473-1499.

Knauth, L.P. 2005, “Temperature and salinity history of the Precambrian ocean: Implications for the course of microbial evolution”, *Paleogeography, Paleoclimatology, Paleoecology,* vol. 219, no. 1-2, pp. 53-69.

Konhauser, K.O., Amskold, L., Lalonde, S.V., Posth, N.R., Kappler, A. & Anbar, A., 2007, “Decoupling photochemical Fe (II) oxidation from shallow-water BIF deposition”, *Earth and Planetary Science Letters*, vol, 258, no.1-2, pp.87-100.

Konhauser, K.O., Pecoits, E., Lalonde, S.V., Papineau, D., Nisbet, E.G., Barley, M.E., Arndt, N.T., Zahnle, K., & Kamber, B.S., 2009, “Oceanic nickel depletion and a methanogen famine before the Great Oxidation Event”, *Nature,* vol. 458, pp. 750–753.

Kramer, A., Hoffmann, J.E., Xie, H., Manker, C., Hegner, E., Wan, Y., Hofmann, A., Liu, D. & Yang, J. 2014, “Generation of early Archaean grey gneisses through melting of older crust in the eastern Kaapvaal craton, southern Africa”, *Precambrian Research,* vol. 255, pp. 823-846.

Kump, L.R. & Seyfried Jr, W.E., 2005, “Hydrothermal Fe fluxes during the Precambrian: Effect of low oceanic sulphate concentrations and low hydrostatic pressure on the composition of black smokers”. *Earth and Planetary Science Letters*, vol.235, no. 3-4, pp.654-662.

Kurzweil, F., Wille, M., Gantert, N., Beukes, N.J. & Schoenberg, R., 2016. “Manganese oxide shuttling in pre-GOE oceans–evidence from molybdenum and iron isotopes”, *Earth and Planetary Science Letters*, vol. 452, pp.69-78.

Le Heron, D.P., Busfield, M.E., Le Ber, E. & Kamona, A.F. 2013, “Neoproterozoic ironstones in northern Namibia: Biogenic precipitation and Cryogenian glaciation”, *Paleogeography, Paleoclimatology, Paleoecology,* vol. 369, pp. 48-57.

Lechte, M.A. & Wallace, M.W. 2015, “Sedimentary and tectonic history of the Holowilena Ironstone, a Neoproterozoic iron formation in South Australia”, *Sedimentary Geology,* vol. 329, pp. 211-224.

Lechte, M. & Wallace, M. 2016, “Sub-ice shelf ironstone deposition during the Neoproterozoic Sturtian glaciation”, *Geology,* vol. 44, no. 11, pp. 891-894.

Lewis, J.P., Weaver, A.J. & Eby, M. 2007, “Snowball versus Slush-ball Earth: Dynamic versus nondynamic sea ice?”, *Journal of Geophysical Research: Oceans,* vol. 112, no. 11, pp. 1-8.

Li, H., Zhang, Z., Li, L., Zhang, Z., Chen, J. & Yao, T. 2014, “Types and general characteristics of the BIF-related iron deposits in china”, *Ore Geology Reviews,* vol. 57, pp. 264-287.

Liivamagi, S., Somelar, P., Mahaney, W.C., Kirs, J., Vircava, I. & Kirsimak, K. 2014, “Late Neoproterozoic Baltic paleosol: Intense weathering at high latitude?”, *Geology,* vol. 42, no. 4, pp. 323-326.

Link, P.K. & Christie-Blick, N. 2011, “Chapter 38 Neoproterozoic strata of southeastern Idaho and Utah: record of Cryogenian rifting and glaciation”, *Geological Society, London, Memoirs,* vol. 36, no. 1, pp. 425-436.

Lottermoser, B.G. & Ashley, P.M. 2000, “Geochemistry, petrology and origin of Neoproterozoic ironstones in the eastern part of the Adelaide Geosyncline, South Australia”, *Precambrian Research,* vol. 101, no. 1, pp. 49-67.

Ludtke, G., Eberle, D. & van der Boom, G., 1986, “Geophysical, geochemical and geological investigation in the Ngami and Kheis areas of Botswana (1980-1983 Final Report). Botswana Geological Survey”, *Bulletin,* vol.32, pp. 319-319.

Lyons, T.W., Reinhard, C.T. & Planavsky, N.J. 2014, “The rise of oxygen in Earth's early ocean and atmosphere”, *Nature,* vol. 506, no. 7488, pp. 307-315.

Lyons, T.W. & Reinhard, C.T., 2009. Early Earth: oxygen for heavy-metal fans. *Nature*, vol.461, no.7261, p.179.

Macdonald, F.A., Schmitz, M.D., Crowley, J.L., Roots, C.F., Jones, D.S., Maloof, A.C., Strauss, J.V., Cohen, P.A., Johnston, D.T. & Schrag, D.P. 2010, "Calibrating the Cryogenian", *Science,* vol. 327, no. 5970, pp. 1241-1243.

Macdonald, F.A., Strauss, J.V., Rose, C.V., Dudas, F.Ã. & Schrag, D.P. 2010, "Stratigraphy of the port nolloth group of namibia and south africa and implications for the age of neoproterozoic neoproterozoic iron formations", *American Journal of Science,* vol. 310, no. 9, pp. 862-888.

Majaule, T., Hanson, R.E., Key, R.M., Singletary, S.J., Martin, M.W. & Bowring, S.A. 2001, "The Magondi Belt in northeast Botswana: Regional relations and new geochronological data from the Sua Pan area", *Journal of African Earth Sciences,* vol. 32, no. 2, pp. 257-267.

Mapeo, R.B.M., Armstrong, R.A., Kampunzu, A.B. & Ramokate, L.V. 2004, "SHRIMP U-Pb zircon ages of granitoids from the Western Domain of the Kaapvaal Craton, Southeastern Botswana: Implications for crustal evolution", *South African Journal of Geology,* vol. 107, no. 1-2, pp. 159-172.

Mapeo, R. B. M., Kampunzu, A. B. & Armstrong, R. A. 2000, "Ages of detrital zircon grains from Neoproterozoic siliciclastic rocks in the Shakawe area: Implications for the evolution of Proterozoic crust in northern Botswana", *South African Journal of Geology*, vol.103, pp. 156–161.

Mapeo, R.B.M., Kampunzu, A.B., Ramokate, L.V., Corfu, F. & Key, R.M. 2004, "Bushveld-age magmatism in southeastern Botswana: Evidence from U-Pb zircon and titanite geochronology of the Moshaneng Complex", *South African Journal of Geology,* vol. 107, no. 1-2, pp. 219-232.

Martin, H. 1965a, "The Precambrian Geology of South West Africa and Namaqualand", *Precambrian Research Unit Bulletin*, vol.1, University of Cape Town, South Africa

Master, S. & Wendorff, M. 2011, “Chapter 12 Neoproterozoic glaciogenic diamictites of the Katanga Supergroup, Central Africa”, *Geological Society, London, Memoirs,* vol. 36, no. 1, pp. 173-184.

McCourt, S. & Armstrong, R.A. 1998, “SHRIMP U-Pb zircon geochronology of granites from the Central Zone, Limpopo Belt, southern Africa: Implications for the age of the Limpopo Orogeny”, *South African Journal of Geology,* vol. 101, no. 4, pp. 329-329.

McCourt, S., Kampunzu, A.B., Bagai, Z. & Armstrong, R.A. 2004, “The crustal architecture of Archaean terranes in Northeastern Botswana”, *South African Journal of Geology,* vol. 107, no. 1-2, pp. 147-158.

Mhlanga, X. R., (2019), “Unravelling the diagenetic and primary depositional history of the Hotazel Fe-Mn Formation, through the application of mineral chemistry, stable isotopes and speciation geochemistry”, PhD-thesis, Rhodes University, Grahamstown, South Africa.

Mikuski, J.A., Pearson, A., Johnston, D.T., Turchyn, A.V., Farquhar, J., Schrag, D.P., Anbar, A.D., Priscu, J.C. and Lee, P.A., 2009, “A Contemporary Microbially Maintained Subglacial Ferrous” Ocean”, *Science*, vol. 324, no. 5925, pp.397-400.

Moore, M., Davis, D.W., Robb, L.J., Jackson, M.C. & Grobler, D.F. 1993, “Archean Rapakivi granite-anorthosite-rhyolite complex in the Witwatersrand Basin hinterland, southern Africa”, *Geology,* vol. 21, no. 11, pp. 1031-1034.

Murray, J. W. and Dillard, J. G. 1979, ″The oxidation of cobalt (U) adsorbed on manganese dioxide″, *Geochimica et Cosmochimca Acta*, vol. 4, no. 1974, pp.781–787.

Murray, K.J., Webb, S.M., Bargar, J.R., Tebo, B.M., 2007, ″Indirect oxidation of Co(II) in the presence of the marine Mn(II)-oxidizing bacterium bacillus sp. strain SG-1″, *Appl. Environ. Microbiol*, vol, 73, pp. 6905–6909.

Myrow, P.M. & Kaufman, A.J. 1999, "A newly discovered cap carbonate above Varanger-age glacial deposits in Newfoundland, Canada", *Journal of Sedimentary Research,* vol. 69, no. 3, pp. 784-793.

Nesbitt, H.W. & Young, G.M. 1982, "Early Proterozoic climates and plate motions inferred from major element chemistry of lutites", *Nature*, vol. 299, no.5885, pp. 715-717.

North, G.R. 1990, "Multiple solutions in energy balance climate models", *Global and Planetary Change,* vol. 2, no. 3-4, pp. 225-235.

Ohta, A. & Kawabe, I., 2001, "REE (III) adsorption onto Mn dioxide (δ-MnO2) and Fe oxyhydroxide: Ce (III) oxidation by δ-MnO_2". *Geochimica et Cosmochimica Acta*, vol.65, no.5, pp.695-703.

Olivarez, A.M. & Owen, R.M. 1991, "The europium anomaly of seawater: implications for fluvial versus hydrothermal REE inputs to the oceans", *Chemical Geology,* vol. 92, no. 4, pp. 317-328.

Oonk, P.B.H. 2017, Across the Asbestos Hills BIF of the Trasnvaal Supergroup, South Africa. Implications for the origin of BIF. *Phd Thesis*, Rhodes University, Grahamstown,South Africa, pp. 157.

Owens, J.D., Lyons, T.W., Li, X., MacLeod, K.G., Gordon, G., Kuypers, M.M.M., Anbar, A., Kuhnt, W. & Severmann, S. 2012, "Iron isotope and trace metal records of iron cycling in the proto-North Atlantic during the Cenomanian-Turonian oceanic anoxic event (OAE-2)", *Paleoceanography,* vol. 27, no. 3, pp. 1-13.

Panahi, A. & Young, G.M. 1997, "A geochemical investigation into the provenance of the Neoproterozoic Port Askaig Tillite, Dalradian Supergroup, western Scotland", *Precambrian Research,* vol. 85, no. 1-2, pp. 81-96.

Pecoits, E., Gingras, M.K., Barley, M.E., Kappler, A., Posth, N.R. & Konhauser, K.O., 2009, "Petrography and geochemistry of the Dales Gorge banded iron formation: Paragenetic

sequence, source and implications for palaeo-ocean chemistry", *Precambrian Research*, vol.172, no.1-2, pp.163-187.

Pierrehumbert, R.T. 2005, "High levels of atmospheric carbon dioxide necessary for the termination of global glaciation", *Nature,* vol. 429, pp. 646-649.

Pierrehumbert, R.T., Abbot, D.S., Voigt, A. & Koll, D. 2011, "Climate of the Neoproterozoic", *Annual Review of Earth and Planetary Sciences,* vol. 39, no. 1, pp. 417-460.

Posth, N.R., Konhauser, K.O. & Kappler, A., 2013, "Microbiological processes in banded iron formation deposition", *Sedimentology*, vol.60, no.7, pp.1733-1754.

Poujol, M., Robb, L.J., Anhaeusser, C.R. & Gericke, B. 2003, "A review of the geochronological constraints on the evolution of the Kaapvaal Craton, South Africa", *Precambrian Research,* vol. 127, no. 1-3, pp. 181-213.

Preiss, W.V., 2000, "The Adelaide Geosyncline of South Australia and its significance in Neoproterozoic continental reconstruction", *Precambrian Research*, vol. 100, no,1-3. pp.21-63.

Rafuza, S. 2015, "Carbonate petrography and geochemistry of BIF of the Transvaal Supergroup: evaluating the potential of Iron Carbonates as proxies for Paleoproterozoic Ocean Chemistry", *MSc. Thesis Unpublished*. Rhodes University, Grahamstown, South Africa, pp. 90.

Rankin, W. 2015, "Cross-Border Correlation of The Damara Belt in Namibia And Equivalent Lithologies In Northwestern Botswana From Potential Field and Magnetotelluric Interpretations", *MSc. Thesis,* University of Witwatersrand, Johannesburg, South Africa, pp. 573-573.

Reusch, H. 1891. "Skuringmærker og morængrus eftervist i Finnmarken fra en periode meget ældre end 'istiden' (Glacial striae and boulder- clay in Norwegian Lapponie from a period

much older than the last ice age)". *Norges Geologiske Undersøkelse*, vol 1, no. 78–85 (English summary, pp. 97–100).

Rice, A.H.N., Edwards, M.B., Hansen, T.A., Arnaud, E. and Halverson, G.P., 2011. "Glaciogenic rocks of the Neoproterozoic Smalfjord and Mortensnes formations, Vestertana Group, E". Finnmark, Norway. *Geological Society, London, Memoirs*., vol 36 no. 1, pp.593-602.

Rieu, R., Allen, P.A., Plötze, M. & Pettke, T. 2007, "Climatic cycles during a Neoproterozoic "snowball" glacial epoch", *Geology,* vol. 35, no. 4, pp. 299-302.

Sakamoto, T. 1950, "The Origin of Precambrian banded iron ores", *American Journal of Science,* vol. 248, no. 7, pp. 449-474.

Scholz, F., McManus, J. & Sommer, S., 2013, "The manganese and iron shuttle in a modern euxinic basin and implications for molybdenum cycling at euxinic ocean margins", *Chemical Geology*, vol. 355, pp.56-68.

Singletary, S.J., Hanson, R.E., Martin, M.W., Crowley, J.L., Bowring, S.A., Key, R.M., Ramokate, L.V., Direng, B.B. & Krol, M.A. 2003, "Geochronology of basement rocks in the Kalahari Desert, Botswana, and implications for regional Proterozoic tectonics", *Precambrian Research,* vol. 121, no. 1-2, pp. 47-71.

Straub, K.L., Benz, M., Schink, B. and Widdel, F., 1996, "Anaerobic, nitrate-dependent microbial oxidation of ferrous iron". *Applied Environmental Microbiology.*, vol. 62, no.4, pp.1458-1460.

Swanner, E. D., Planavsky, N.J., Lalonde S.V., Robbins, L.J., Bekker, A., Rouxel, O.J., Saito, M.A., Kappler, A., Mojzsis, S.J., Konhauser, K.O, 2014, "Cobalt and marine redox evolution", *Earth and Planetary Science Letters*. Elsevier B.V., vol. 390, pp. 253–263.

Takahashi, Y., Shimizu, H., Usui, A., Kagi, H. & Nomura, M., 2000, "Direct observation of tetravalent cerium in ferromanganese nodules and crusts by X-ray-absorption near-edge structure (XANES)", *Geochimica et Cosmochimica Acta*, vol. 64, no.17, pp.2929-2935.

Tang, J., Fu, H., Yu, Z., 1987, "Stratigraphy, type and formation conditions of the late Pre-Cambrian banded iron ores in south China" *China Journal of Geochemistry*, vol.6, no.4, pp. 331–341

Taylor, S.R., McLennan, S.M., 1985. "The Continental Crust: Its Composition and Evolution" *Blackwell Scientific Publications*.

Templeton, A.S., 2011, "Geomicrobiology of iron in extreme environments", *Elements*, vol. *7*, no. 2, pp.95-100.

Thomson, J. 1871, "On the stratified rocks of Islay". *Report of the 41st Meeting of the British Association for the Advancement of Science,* Edinburgh. John Murray, London, 110–111.

Trendall, A. 2011, "Banded Iron Formations", *Encyclopedia of Geobiology*, pp. 92-103.

Tostevin, R., Shields, G.A., Tarbuck, G.M., He, T., Clarkson, M.O. and Wood, R.A., 2016. Effective use of cerium anomalies as a redox proxy in carbonate-dominated marine settings. *Chemical Geology*, vol. 438, pp.146-162.

Tsikos, H. & Moore, J.M. 1997, "Petrography and geochemistry of the Paleoproterozoic Hotazel iron-formation, Kalahari manganese field, South Africa: Implications for Precambrian manganese metallogenesis", *Economic Geology,* vol. 92, no. 1, pp. 87-97.

Van der Westhuizen, W.A., De Bruiyn, H. & Meintjes, P.G., 1991, "The Ventersdorp supergroup: an overview", *Journal of African Earth Sciences (and the Middle East)*, vol. 13, no.1, pp.83-105.

Walde,D.H.G., Gierth,E.& Leonardos, O. H. 1981, "Stratigraphy and mineralogy of the manganese ores of Urucum, Mato Grosso, Brazil", *Geologische Rundschau*, vol. 70, pp. 1077–1085.

Walemba, K.M.A. & Master, S. 2005, "Neoproterozoic diamictites from the Itombwe Synclinorium, Kivu Province, Democratic Republic of Congo: Palaeoclimatic significance and regional correlations", *Journal of African Earth Sciences,* vol. 42, no. 1-5, pp. 200-210.

Wendorff, M. 2005, "Outline of Lithostratigraphy, Sedimentation and Tectonics of the Tsodilo Hills Group, a Neoproterozoic "Lower Paleozoic Siliciclastic Succession in NW Botswana", *Annales Societatis Geologorum Poloniae,* vol. 75, pp. 17-24.

Whitten, G. F. 1970, "The investigation and exploitation of the Razorback Ridge iron deposit", *Geological Survey of South Australia Reports of Investigations*, vol. 33, pp. 165.

Widdel, F., Schnell, S., Heising, S., Ehrenreich, A., Assmus, B. and Schink, B., 1993, "Ferrous iron oxidation by anoxygenic phototrophic bacteria", *Nature*, vol. 362, no. 6423, p.834.

Woodward, H. P. 1884, "Report on the range to the east of Farina". *Parliamentary Papers for 1884. Government of South Australia*, 40,1–5

Xiao, S. 2004, "Neoproterozoic glaciations and the fossil record", *Geophysical Monograph Series,* vol. 146, pp. 199-214.

Xu, D.R., Wang, Z.L., Chen, H.Y., Hollings, P., Jansen, N.H., Zhang, Z.C. & Wu, C.J. 2014, "Petrography and geochemistry of the Shilu Fe-Co-Cu ore district, South China: Implications for the origin of a Neoproterozoic BIF system", *Ore Geology Reviews,* vol. 57, pp. 322-350.

Young, G.M. 2002, "Stratigraphic and tectonic settings of Proterozoic glaciogenic rocks and banded iron-formations: Relevance to the snowball Earth debate", *Journal of African Earth Sciences,* vol. 35, no. 4, pp. 451-466.

Zhang, J. & Nozaki, Y. 1996, "Rare earth elements and yttrium in seawater: ICP-MS determinations in the East Caroline, Coral Sea, and South Fiji basins of the western South Pacific Ocean", *Geochimica et Cosmochimica Acta,* vol. 60, no. 23, pp. 4631-4644.

Zhang, Q.R., Chu, X.L. and Feng, L.J., 2011, "Neoproterozoic glacial records in the Yangtze Region, China", *Geological Society, London, Memoirs*, vol. 36, no, 1. pp. 357-366.

Ziegler, P. A. 1960, "Fruhpala¨ozoische Tillite in ostlichen Yukon- Territorium (Kanada)", *Eclogae Geologicae Helveticae*, vol. 52, pp. 735–741.

7. APPENDICES

A1. Map of Shakawe showing the sampled localities

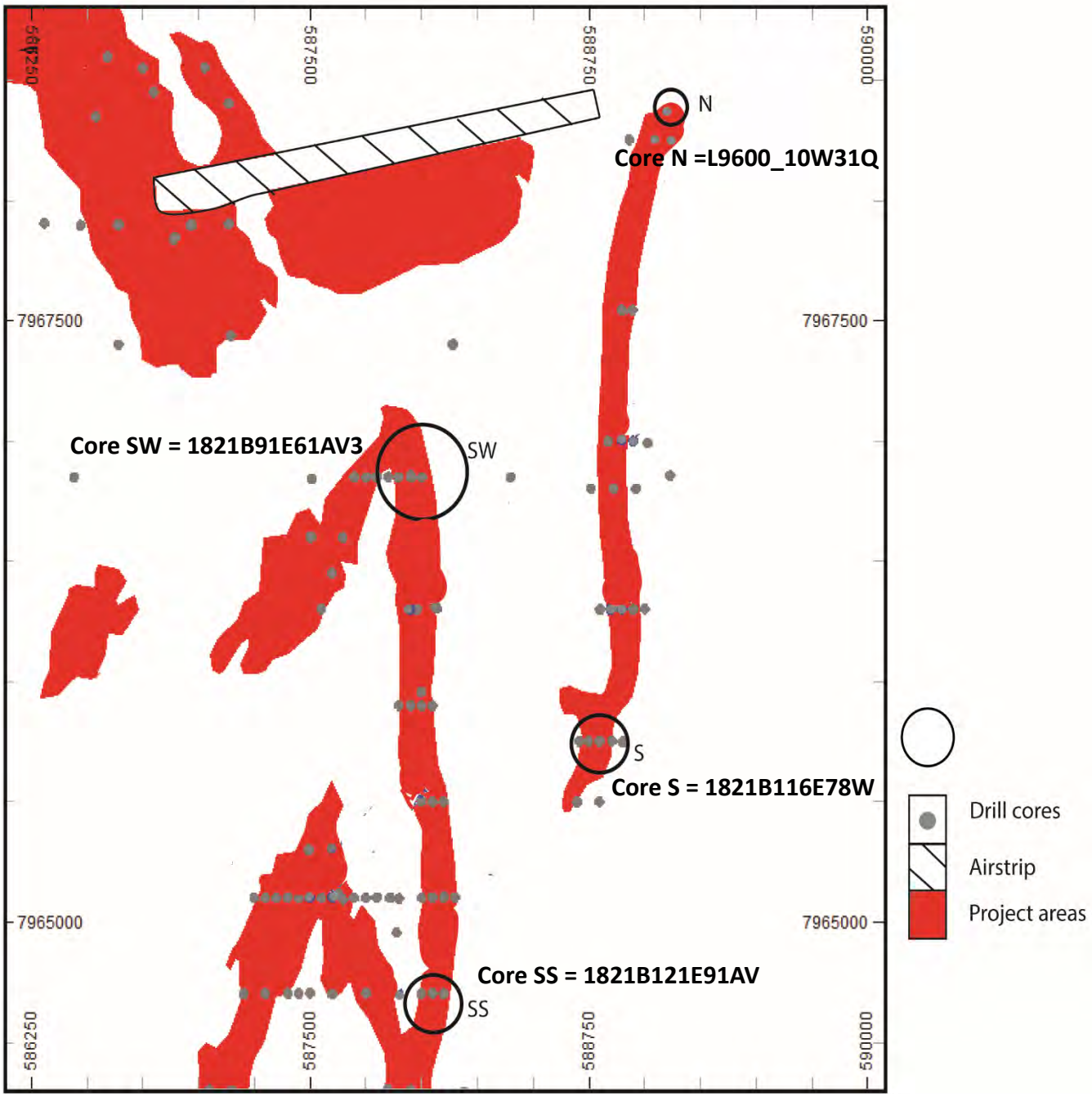

A2. The drill cores of Xaudum Iron-formation and respective samples

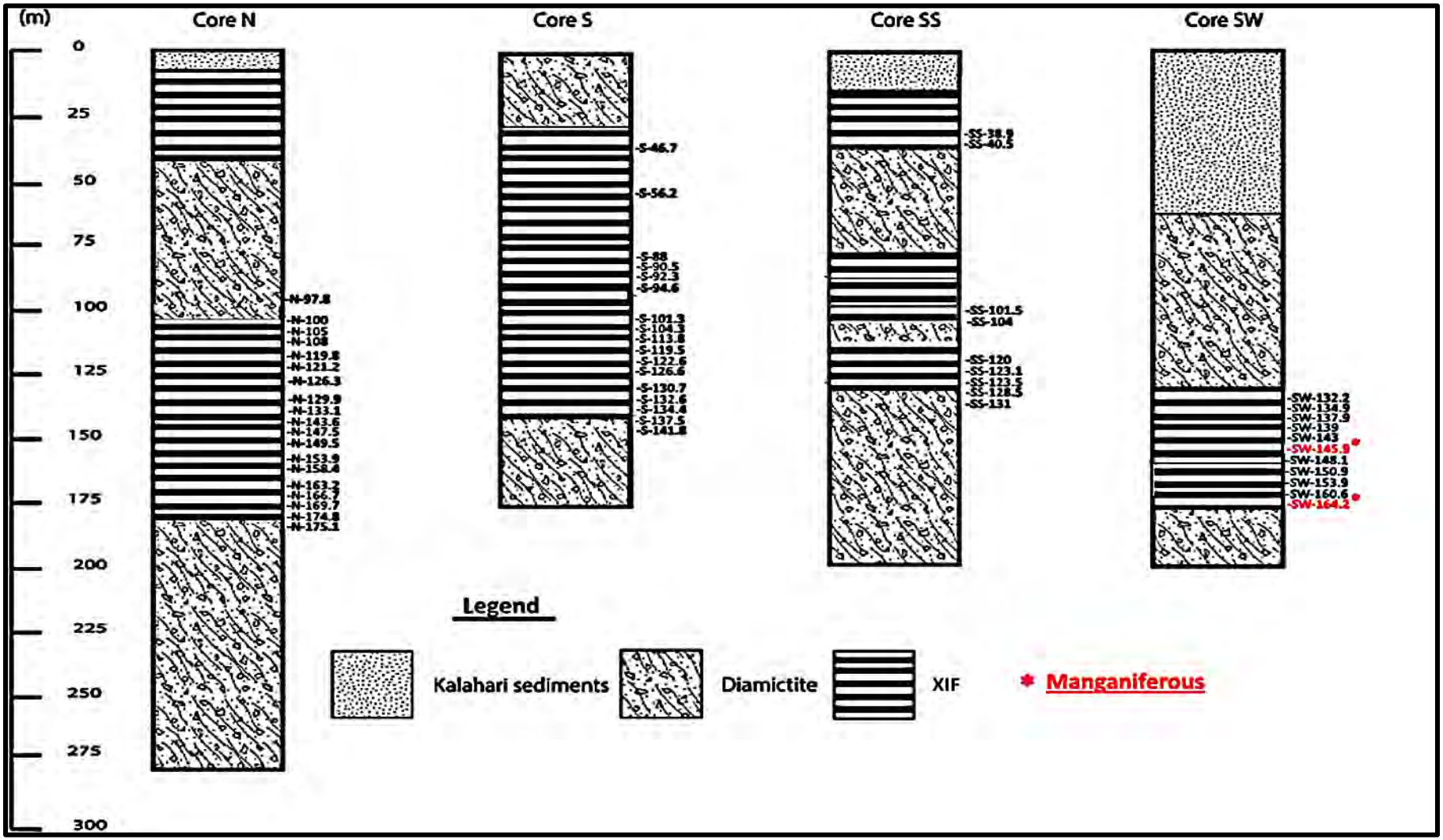

Disclaimer: The XIF facies shown in the drill cores is for demonstrative purpose only. XIF in its true nature is deformed and folded as explained in the local geology.

A3. Whole rock geochemistry

X-Ray Fluorescence (XRF)

Whole rock major and minor element concentrations were measured using fused glass beads prepared in Stellenbosch University. The fused glass beads were made by adding approximately 2g of sample powders into empty and clean crucibles which were weighed. Consequently, the crucible containing the sample powders were ignited in a furnace at 1000°C for 8 hours. The crucibles were left to cool in a desiccator and weighed again. The difference between the two crucible weights are gave the loss on ignition (LOI) which is the measure of volatile compounds structurally bound to the sample and/or compounds added during oxidation. Following the LOI procedure, approximately 0.7g of the ignited sample powder was mixed lithium borate and lithium metaborate flux with a small amount of lithium bromide. The blend was homogenised and melted in a Pt crucible to produce the glass beads. The glass beads were then analysed by a PANalytical Axios Wavelength Dispersive spectrometer fitted a Rh Tube XRF at 3000W using standard techniques. Calibration curves and quality control was obtained using recognised standards from NIST® and SARM®. Analyte peaks intensities were corrected for background using raw intensities measured with SuperQ PANalytical software.

Laser Ablation Inductively Coupled Plasma Mass Spectrometry (LA-ICPMS)

The concentrations of a group of low and several high abundance trace elements including REE were measured using a Resonetic 193nm Excimer Laser Ablation System connected to an Agilent 7700 ICPMS. The analysed trace elements were on polished mounts that were prepared from XRF fusions. For quality control, polished NIST® and mounted standards and recognised reference materials were applied, using standard bracketing. The following LA and ICPMS conditions were met for analytical procedure, and the data was then processed using Glitter software:

Laser:
Resonetics 193nm Excimer laser
Fluence: 8 J/cm2
Frequency: 10 Hz
Spot: 2 spots of 100µm per sample
Ablation gas: He @ 0.35L/min
Ablation time: 15sec background, 35sec ablation

ICP-MS:
Agilent 7700
Carrier gas: 0.9L/min Ar + 0.007L/min Nitrogen

1:10 Sample: Flux ratio

A4. Electron probe micro-analysis (EPMA)

Members of the silicates, oxides and carbonate mineral groups were targeted to acquire precise and quantitative elemental analyses using four wavelength dispersive spectrometers on a JEOL JXA-8230 EPMA at Rhodes University. The beam was produced by a W cathode and excited by a 15kV accelerating potentials at beam currents of 20nA. The beam spot size was less than 1 micron. The elements were measured on K-alpha peaks and counting times were 10s on peak and 5s on background. Natural standards were employed to measure characteristic X-ray. The ZAF matrix algorithm (Heinrich/Duncumb-Reed with FEAST-2005 MACs) was used to correct for differential matrix effects. The total for silicates analysed ranged from 99-100% suggesting optimum analyses.

B1. XIF major element data

Sample	Depth	Fe_2O_3	Mn_3O_4	TiO_2	CaO	K_2O	P_2O_5	SiO_2	Al_2O_3	MgO	Na_2O	LOI	Total
	(m)	(wt.%)											
N-97.80	97.8	78.3	1.0	0.1	1.4	0.0	0.4	18.3	1.9	1.0	0.0	-2.0	100.3
N-100.05	100.05	90.1	0.1	0.0	0.8	bdl	0.4	10.6	0.1	0.1	bdl	-2.6	99.5
N-105.05	105.05	70.6	0.2	0.0	2.0	0.0	1.1	27.6	0.3	0.1	0.0	-1.7	100.3
N-108.80A	108.8	51.3	0.2	0.0	1.1	0.1	0.3	46.5	0.4	1.1	0.0	-0.8	100.3
N-108.80B	108.85	55.9	0.4	0.0	3.6	0.3	0.3	31.8	1.1	3.5	0.1	2.9	100.0
N-119.80	119.8	75.3	0.1	0.1	1.1	bdl	0.2	24.8	0.3	0.4	bdl	-1.4	100.9
N-121.20	121.2	78.5	0.1	0.1	2.5	bdl	1.2	18.8	0.5	0.2	bdl	-0.9	100.9
N-126.30	126.3	76.9	0.2	0.1	0.5	0.2	0.2	19.4	1.8	1.6	0.3	-2.0	99.1
N-129.90A	129.9	52.2	0.1	0.0	1.7	0.0	1.3	44.2	0.4	0.6	0.0	-0.7	99.9
N-129.90B	129.95	89.8	0.1	0.1	1.1	0.0	0.8	9.0	0.4	0.2	0.0	-1.9	99.5
N-133.10	133.1	82.3	0.2	0.1	1.7	0.1	0.7	12.8	0.9	1.0	0.0	-0.5	99.3
N-139.10	139.1	85.2	0.2	0.1	0.9	0.0	0.5	12.3	1.4	1.1	0.1	-1.5	100.4
N-143.60	143.6	21.8	0.1	0.0	3.2	bdl	0.4	69.6	0.3	0.5	0.0	3.1	99.1
N-147.50	147.5	80.9	0.5	0.1	3.1	0.1	0.1	11.5	1.1	1.4	0.3	1.1	100.2
N-149.50	149.5	25.4	0.0	0.0	0.2	bdl	0.1	74.4	0.3	0.1	0.0	-1.0	99.4
N-153.90	153.9	87.3	0.2	0.1	1.7	0.0	0.2	9.3	0.8	0.7	0.3	-1.1	99.5
N-158.40	158.4	82.7	0.2	0.1	1.9	bdl	0.8	15.2	0.5	0.4	0.0	-1.7	100.0
N-163.20	163.2	79.2	0.5	0.1	0.6	0.0	0.2	19.7	0.9	0.3	0.0	-2.4	99.2
N-166.70	166.7	31.0	0.8	0.4	11.3	2.8	1.2	25.7	5.9	6.2	0.3	13.6	99.0
N-169.70	169.7	16.9	0.3	0.0	2.0	0.0	0.2	78.3	0.2	0.0	0.0	1.0	99.0
N-174.20A	174.2	74.6	0.1	0.1	2.9	0.0	2.0	19.0	0.9	1.0	0.1	0.1	100.8
N-174.20B	174.8	47.5	0.3	0.0	1.1	0.0	0.5	45.9	0.7	2.1	0.1	1.4	99.6
N-175.10	175.1	77.2	0.4	0.2	1.7	0.2	1.1	18.8	1.7	1.0	0.1	-2.3	99.9

Sample	Depth	Fe_2O_3	Mn_3O_4	TiO_2	CaO	K_2O	P_2O_5	SiO_2	Al_2O_3	MgO	Na_2O	LOI	Total
	(m)	(wt.%)											
S-46.70	46.7	69.4	0.1	0.1	0.5	0.1	0.3	26.5	1.1	0.2	0.2	2.0	100.5
S-56.20	56.2	85.9	0.5	0.1	0.9	0.1	0.6	12.1	0.2	0.2	0.0	-0.7	100.0
S-88.00	88	80.8	0.7	0.1	0.6	0.1	0.3	16.7	1.6	0.8	0.5	-2.3	100.0
S-90.50	90.5	53.4	1.1	0.1	3.7	0.0	0.2	29.1	2.6	1.3	0.4	7.5	99.4
S-92.30	92.3	66.2	0.5	0.0	0.6	bdl	0.3	31.2	0.3	0.2	0.0	1.2	100.7
S-94.60	94.6	72.1	0.4	0.0	3.0	0.1	0.3	21.2	0.8	1.3	0.1	0.8	100.2
S-101.30	101.3	89.2	0.2	0.1	0.2	0.0	0.0	10.7	1.0	0.2	0.3	-2.7	99.3
S-104.80	104.8	46.8	0.8	0.1	0.9	0.0	0.3	45.5	2.9	2.1	1.4	-1.5	99.4
S-108.30	108.3	63.8	1.0	0.0	6.1	0.1	0.1	17.0	0.6	3.9	0.0	7.1	99.8
S-113.80	113.8	67.0	0.4	0.2	4.4	0.5	3.2	22.8	1.9	1.1	0.1	-1.7	99.9
S-116.10	116.1	79.6	0.6	0.1	3.4	0.0	1.4	11.4	0.3	0.1	0.0	2.9	99.9
S-119.50	119.5	60.0	1.1	0.2	2.0	0.4	0.6	31.9	3.1	1.6	0.2	-1.2	99.9
S-122.60	122.6	58.1	1.7	0.0	2.0	bdl	0.2	35.9	1.3	0.9	0.0	-0.8	99.5
S-126.50	126.5	77.3	0.4	0.1	2.8	0.0	0.1	16.6	1.3	0.7	0.5	-0.2	99.6
S-130.70	130.7	67.2	0.3	0.0	0.3	0.0	0.1	33.5	0.4	0.3	0.0	-1.5	100.8
S-132.60	132.6	81.0	0.4	0.1	3.4	0.2	0.2	10.2	1.1	1.9	bdl	2.2	100.8
S-134.40	134.4	87.0	0.2	0.1	0.2	bdl	0.1	13.3	1.0	0.2	0.3	-2.8	99.5
S-137.50	137.5	73.0	1.4	0.1	2.1	0.0	0.2	21.5	1.4	1.5	0.1	-0.9	100.4
S-141.80	141.8	33.8	0.5	0.6	1.9	1.7	0.5	46.1	11.9	3.0	0.1	-0.3	99.7

Sample	Depth	Fe_2O_3	Mn_3O_4	TiO_2	CaO	K_2O	P_2O_5	SiO_2	Al_2O_3	MgO	Na_2O	LOI	Total
	(m)	(wt.%)											
SW-132.20A	132.2	50.9	1.7	0.2	6.9	0.0	0.4	30.7	2.6	1.7	0.0	4.0	99.2
SW-132.20B	132.8	82.6	0.4	0.1	1.3	0.0	0.8	12.5	0.8	0.3	bdl	1.1	99.9
SW-134.80	134.8	50.5	3.6	0.2	7.5	0.1	0.5	24.9	2.8	2.7	0.0	6.4	99.3
SW-137.60	137.6	81.2	0.7	0.2	0.9	0.4	0.4	12.8	1.3	1.0	0.1	0.4	99.3
SW-139.00	139	80.2	1.0	0.3	0.7	0.4	0.3	12.4	1.7	1.0	0.1	1.2	99.2
SW-143.90	143.9	69.7	1.4	0.2	0.5	0.3	0.2	24.3	1.2	1.8	0.2	1.0	100.9
SW-145.90	145.9	36.5	11.6	0.2	3.8	0.0	0.3	23.2	4.5	3.8	0.0	15.6	99.7
SW-148.10	148.1	28.3	1.3	0.0	0.3	0.1	0.0	67.7	0.4	1.4	0.0	-0.5	99.2
SW-150.90	150.9	64.9	2.2	0.1	1.1	0.4	0.1	25.7	2.5	1.8	0.1	1.9	101.0
SW-153.70	153.7	62.8	1.3	0.2	0.8	0.6	0.5	29.6	2.7	1.9	0.1	-0.3	100.2
SW-157.70	157.7	72.5	1.8	0.2	2.7	0.2	0.5	18.4	2.3	1.0	0.1	0.4	100.1
SW-160.60	160.6	73.4	1.0	0.1	1.3	0.1	0.8	24.9	0.9	0.6	0.0	-2.3	100.8
SW-164.20	164.2	11.5	7.9	0.5	2.4	0.8	0.2	64.1	9.7	1.9	0.0	0.8	99.8

Sample	Depth	Fe_2O_3	Mn_3O_4	TiO_2	CaO	K_2O	P_2O_5	SiO_2	Al_2O_3	MgO	Na_2O	LOI	Total
	(m)	(wt.%)											
SS-38.90	38.9	65.9	0.2	0.0	0.5	0.0	0.3	31.8	0.4	0.3	0.2	-0.1	99.5
SS-40.50A	40.5	82.6	0.7	0.1	2.4	0.8	1.1	8.3	1.5	0.9	0.3	0.6	99.1
SS-40.50B	40.8	50.1	0.3	0.1	1.2	0.3	0.4	45.9	0.7	0.4	0.1	0.4	99.8
SS-101.50	101.5	39.9	0.1	0.3	1.3	0.1	0.8	50.5	6.3	2.2	bdl	-1.0	100.6
SS-104.90	104.9	39.4	0.0	0.0	0.9	0.0	0.6	58.1	0.7	0.5	bdl	-0.8	99.5
SS-120.00	120	44.3	0.1	0.2	4.1	0.0	3.1	44.6	2.5	1.1	0.0	-0.6	99.4
SS-123.10	123.1	32.0	0.1	0.8	7.1	1.7	5.4	44.1	6.6	3.8	0.1	-2.6	99.1
SS-123.80	123.8	79.6	0.0	0.2	1.1	0.1	0.8	17.6	1.8	0.6	bdl	-1.1	100.5
SS-125.00	125	37.8	0.0	0.0	0.5	0.0	0.3	62.9	0.4	0.3	bdl	-2.9	99.4
SS-128.50	128.5	82.1	0.0	0.2	1.0	0.1	0.7	15.4	1.9	0.8	bdl	-2.3	99.9
SS-131.00	131	74.0	0.0	0.1	1.5	0.0	1.2	22.7	0.8	0.1	0.0	0.0	100.5

B2. Diamictite major element raw data

Sample	Depth	Fe_2O_3	Mn_3O_4	TiO_2	CaO	K_2O	P_2O_5	SiO_2	Al_2O_3	MgO	Na_2O	LOI	Total
Top	**(m)**	**(wt. %)**											
N-62.60	62.6	66.2	1.2	0.1	4.8	0.1	0.2	18.7	2.1	1.4	1.0	4.0	99.8
N-67.40	67.4	35.1	0.1	0.0	1.3	0.0	0.5	62.9	0.2	0.0	0.0	-0.7	99.5
N-70.30	70.3	53.0	0.1	0.0	0.3	0.0	0.1	45.0	0.8	0.3	0.1	0.4	100.2
N-72.60	72.6	54.0	0.6	0.2	3.1	0.4	2.0	33.5	3.8	1.1	0.9	0.7	100.2
N-86.80	86.8	71.3	7.3	0.3	1.7	0.2	0.3	9.6	1.0	1.4	0.3	6.7	100.1
N-90.90	90.9	51.4	5.3	0.1	1.4	0.1	0.3	30.9	3.6	0.9	2.0	3.6	99.8
SW-75.70	75.7	7.7	0.1	0.8	2.0	3.0	0.2	62.2	14.9	4.3	2.3	1.4	99.0
SW-90.20	90.2	6.9	0.1	0.7	2.5	2.7	0.1	65.0	14.5	2.9	2.7	1.0	99.1
SW-103.00	103	7.1	0.1	0.7	2.2	2.6	0.1	64.9	14.9	2.9	3.1	0.5	99.2
SW-110.40	110.4	6.4	0.1	0.8	1.8	3.5	0.1	65.0	15.1	2.8	2.2	1.2	99.1
SW-115.60	115.6	7.3	0.1	0.7	2.5	2.6	0.1	65.0	14.5	2.8	2.6	0.9	99.2
SW-121.70	121.7	6.8	0.1	0.8	1.1	3.7	0.1	64.6	15.0	3.5	1.2	2.1	99.0
SW-130.80	130.8	20.9	0.3	0.7	1.6	3.4	0.2	56.2	9.8	3.4	0.1	2.9	99.4
SS-42.30	42.3	36.4	0.3	0.4	4.5	2.3	1.0	39.6	8.0	2.3	2.3	2.1	99.0
SS-47.0	47	41.1	0.1	0.4	1.2	2.0	0.7	43.1	7.7	1.6	2.4	-0.9	99.5
SS-51.50	51.5	26.5	0.2	0.4	2.1	2.4	0.4	53.0	9.5	1.5	2.4	0.7	99.1
SS-58.40	58.4	36.5	0.1	0.8	3.1	2.9	0.7	40.5	9.5	2.0	2.1	0.8	99.1
SS-67.30	67.3	47.2	0.2	0.6	1.8	2.6	0.7	36.7	8.1	2.0	1.5	-0.6	100.8
SS-76.70A	76.7	49.2	0.0	0.0	1.2	0.0	0.5	48.7	0.3	0.1	0.0	0.2	100.3
SS-76.70B	77	72.6	0.2	0.1	3.4	0.4	0.2	19.3	1.2	0.9	0.2	0.8	99.4
SS-79.80	79.8	25.1	0.1	0.5	2.6	2.7	0.3	53.0	10.2	1.8	1.8	1.1	99.2
SS-86.40	86.4	62.3	0.0	0.1	2.2	0.2	1.6	33.1	1.0	0.4	0.0	-1.9	99.1
SS-89.70	89.7	38.5	0.1	0.4	1.9	2.1	1.0	46.0	7.3	2.1	0.1	-0.2	99.2
SS-96.70	96.7	43.5	0.1	0.3	2.6	1.0	1.4	44.1	5.2	1.6	0.5	-0.8	99.4
SS-99.00	99	36.9	0.0	0.1	0.7	0.0	0.5	61.2	0.5	0.6	0.0	-1.1	99.4
Bottom													
N-178.80	178.8	40.8	0.8	0.2	2.8	0.0	0.5	43.0	4.7	3.3	0.0	3.0	99.0
N-182.60	182.6	8.4	0.2	0.6	4.3	2.6	0.2	64.1	12.2	2.4	2.1	2.3	99.3
N-223.80	223.8	8.3	0.3	1.0	4.0	4.9	0.2	54.1	17.4	3.4	2.6	3.0	99.1
N-277.00	277	8.6	0.1	0.9	1.6	3.7	0.1	62.0	15.3	3.6	2.2	0.9	99.1
S-145.70	145.7	26.5	0.7	0.5	8.7	0.0	0.7	43.9	10.7	2.9	0.0	4.6	99.2
SW-187.90	187.9	6.6	0.2	0.8	2.2	2.9	0.2	65.5	14.6	2.2	2.9	1.2	99.3
SS-141.80A	141.8	13.9	0.1	0.5	1.8	2.7	0.9	61.3	12.3	1.4	3.6	0.5	99.1
SS-141.80B	142	24.7	0.1	0.3	0.4	1.6	0.2	67.2	3.7	0.9	0.1	-0.1	99.1
SS-149.00	149	24.2	0.1	0.4	2.7	2.9	1.7	53.2	10.2	1.4	2.3	0.1	99.2
SS-156.10	156.1	21.7	0.1	0.5	1.2	3.4	0.4	56.1	11.4	1.7	2.1	0.4	99.0
SS-163.50	163.5	15.4	0.1	0.5	1.9	1.9	0.5	63.6	12.0	1.3	2.0	-0.1	99.1

B3. LILE raw data

Sample	Depth	K_2O	Rb	Sr	Cs	Ba	Pb
	(m)	(wt. %)	(ppm)				
N-97.80	97.8	0.0	1.1	46.7	0.4	11.6	4.4
N-100.05	100.05	bdl	0.2	104.0	0.1	8.1	21.5
N-105.05	105.05	0.0	0.7	130.4	0.1	11.4	2.6
N-108.80A	108.8	0.1	2.2	47.6	0.8	31.6	1.7
N-108.80B	108.85	0.3	10.1	139.9	4.0	106.8	4.2
N-119.80	119.8	bdl	0.2	41.1	0.1	11.4	3.3
N-121.20	121.2	bdl	0.2	94.7	0.1	10.7	12.7
N-126.30	126.3	0.2	4.8	26.7	4.1	121.4	2.8
N-129.90A	129.9	0.0	0.5	94.5	0.4	14.8	5.8
N-129.90B	129.95	0.0	0.4	55.7	0.3	14.5	1.6
N-133.10	133.1	0.1	2.6	77.7	1.3	60.0	4.3
N-139.10	139.1	0.0	1.3	44.5	1.3	55.4	7.1
N-143.60	143.6	bdl	0.2	132.0	0.1	24.0	14.1
N-147.50	147.5	0.1	2.1	183.9	1.3	30.4	6.7
N-149.50	149.5	bdl	0.2	11.4	0.0	12.1	0.5
N-153.90	153.9	0.0	0.5	73.9	0.3	32.4	2.2
N-158.40	158.4	bdl	0.2	74.0	0.1	15.2	3.3
N-163.20	163.2	0.0	1.0	50.7	0.5	21.7	1.1
N-166.70	166.7	2.8	110.5	359.5	33.1	1269.0	14.1
N-169.70	169.7	0.0	0.3	414.6	0.1	22.4	3.2
N-174.20A	174.2	0.0	1.0	124.8	0.4	16.5	1.8
N-174.20B	174.8	0.0	1.5	46.5	0.6	24.8	1.3
N-175.10	175.1	0.2	4.8	124.3	4.0	125.4	2.8

Sample	Depth	K_2O	Rb	Sr	Cs	Ba	Pb
	(m)	(wt. %)	(ppm)				
S-46.70	46.7	0.1	2.4	25.5	0.1	30.9	3.7
S-56.20	56.2	0.1	1.2	46.0	0.1	8.8	2.2
S-88.00	88	0.1	2.6	37.4	0.7	57.2	2.1
S-90.50	90.5	0.0	0.9	196.0	0.2	9.0	9.3
S-92.30	92.3	bdl	0.4	25.7	0.1	14.5	8.5
S-94.60	94.6	0.1	2.7	98.7	0.8	33.2	3.9
S-101.30	101.3	0.0	1.0	15.2	0.3	18.0	0.9
S-104.80	104.8	0.0	0.7	69.2	0.4	19.1	2.4
S-108.30	108.3	0.1	2.8	223.1	0.9	36.3	7.3
S-113.80	113.8	0.5	12.1	240.2	7.2	516.0	6.9

S-116.10	116.1	0.0	0.6	156.9	0.2	19.0	7.3
S-119.50	119.5	0.4	10.3	85.6	4.6	364.3	12.8
S-122.60	122.6	bdl	0.1	96.9	0.1	10.3	3.4
S-126.50	126.5	0.0	0.4	181.6	0.2	13.9	8.1
S-130.70	130.7	0.0	0.4	14.8	0.1	16.4	1.3
S-132.60	132.6	0.2	5.5	132.1	1.9	71.5	4.9
S-134.40	134.4	bdl	0.4	20.7	0.1	10.7	0.7
S-137.50	137.5	0.0	0.5	110.1	0.1	11.0	5.5
S-141.80	141.8	1.7	56.4	74.7	10.8	671.5	11.8

Sample	Depth	K_2O	Rb	Sr	Cs	Ba	Pb
	(m)	(wt. %)	(ppm)				
SW-132.20A	132.2	0.0	1.2	83.0	0.1	31.5	3.6
SW-132.20B	132.8	0.0	2.6	75.0	0.4	38.6	5.3
SW-134.80	134.8	0.1	4.2	443.1	1.5	73.7	21.2
SW-137.60	137.6	0.4	9.6	66.8	4.2	106.2	3.6
SW-139.00	139	0.4	9.0	48.0	3.0	120.6	8.3
SW-143.90	143.9	0.3	7.1	40.2	2.4	96.0	4.3
SW-145.90	145.9	0.0	0.5	94.4	0.1	27.6	5.7
SW-148.10	148.1	0.1	2.1	17.7	0.7	43.4	2.9
SW-150.90	150.9	0.4	8.6	52.4	2.9	105.2	4.5
SW-153.70	153.7	0.6	16.2	88.9	9.2	195.9	5.2
SW-157.70	157.7	0.2	6.1	167.6	2.4	174.0	6.3
SW-160.60	160.6	0.1	1.8	108.2	0.6	46.8	4.7
SW-164.20	164.2	0.8	27.7	46.5	5.0	117.4	2.2

Sample	**Depth**	**K_2O**	**Rb**	**Sr**	**Cs**	**Ba**	**Pb**
	(m)	**(wt. %)**	**(ppm)**				
SS-38.90	38.9	0.0	0.6	31.0	0.1	30.9	4.3
SS-40.50A	40.5	0.8	10.3	227.5	0.4	180.7	3.5
SS-40.50B	40.8	0.3	3.6	94.8	0.2	86.4	2.0
SS-101.50	101.5	0.1	4.3	77.6	0.9	20.3	1.9
SS-104.90	104.9	0.0	0.3	55.2	0.1	10.3	3.2
SS-120.00	120	0.0	2.1	227.7	0.4	35.3	4.9
SS-123.10	123.1	1.7	84.1	509.9	41.6	1487.5	11.2
SS-123.80	123.8	0.1	3.3	85.1	1.3	27.8	2.2
SS-125.00	125	0.0	0.4	25.3	0.1	9.0	1.2
SS-128.50	128.5	0.1	3.5	76.9	1.8	46.8	1.2
SS-131.00	131	0.0	0.7	62.1	0.2	11.4	1.7

B4. HFSE raw data

Sample	Depth	TiO_2	Zr	Nb	Hf	Ta	Pb	Th	U
	(m)	(wt. %)	(ppm)						
N-97.80	97.8	0.1	12.0	1.0	0.2	0.1	4.4	1.0	0.1
N-100.05	100.05	0.0	3.5	0.4	bdl	0.0	21.5	0.3	0.2
N-105.05	105.05	0.0	6.0	0.4	bdl	0.0	2.6	0.7	0.2
N-108.80A	108.8	0.0	4.9	0.3	bdl	0.0	1.7	1.5	0.1
N-108.80B	108.85	0.0	13.7	1.4	0.2	0.0	4.2	0.9	0.1
N-119.80	119.8	0.1	10.1	0.7	0.2	0.0	3.3	0.4	0.1
N-121.20	121.2	0.1	9.1	0.8	0.2	0.0	12.7	0.8	0.2
N-126.30	126.3	0.1	14.6	1.5	0.3	0.1	2.8	1.5	0.1
N-129.90A	129.9	0.0	6.5	0.6	0.1	0.0	5.8	1.3	0.2
N-129.90B	129.95	0.1	8.2	1.0	0.1	0.0	1.6	0.7	0.2
N-133.10	133.1	0.1	23.8	1.5	0.4	0.1	4.3	0.9	0.2
N-139.10	139.1	0.1	26.0	2.7	0.5	0.1	7.1	1.5	0.2
N-143.60	143.6	0.0	3.3	0.2	0.1	bdl	14.1	0.3	0.0
N-147.50	147.5	0.1	11.8	1.3	0.2	0.0	6.7	0.6	0.1
N-149.50	149.5	0.0	3.4	0.4	bdl	bdl	0.5	0.2	0.0
N-153.90	153.9	0.1	18.2	1.4	0.3	0.1	2.2	0.7	0.1
N-158.40	158.4	0.1	18.0	1.6	0.3	0.1	3.3	1.2	0.2
N-163.20	163.2	0.1	14.3	1.3	0.2	0.1	1.1	0.8	0.1
N-166.70	166.7	0.4	80.5	6.9	2.3	0.5	14.1	3.8	0.6
N-169.70	169.7	0.0	4.7	0.3	bdl	bdl	3.2	0.1	0.2
N-174.20A	174.2	0.1	13.3	1.7	0.2	0.1	1.8	0.8	0.2
N-174.20B	174.8	0.0	9.7	0.9	0.1	0.1	1.3	1.0	0.2
N-175.10	175.1	0.2	33.4	1.4	0.7	0.1	2.8	3.0	0.4

Sample	Depth	TiO_2	Zr	Nb	Hf	Ta	Pb	Th	U
	(m)	(wt. %)	(ppm)						
S-46.70	46.7	0.1	13.9	0.8	0.3	0.0	3.7	1.2	0.4
S-56.20	56.2	0.1	5.4	0.8	bdl	0.0	2.2	0.8	0.4
S-88.00	88	0.1	26.7	1.4	0.3	0.1	2.1	1.5	0.1
S-90.50	90.5	0.1	12.3	0.6	0.1	0.0	9.3	0.5	0.1
S-92.30	92.3	0.0	6.7	0.5	0.1	0.0	8.5	0.7	0.2
S-94.60	94.6	0.0	11.9	1.0	0.1	0.0	3.9	0.7	0.3
S-101.30	101.3	0.1	10.6	1.8	0.2	0.1	0.9	0.4	0.1
S-104.80	104.8	0.1	11.3	0.9	0.3	0.1	2.4	0.9	0.1
S-108.30	108.3	0.0	8.8	0.3	0.1	bdl	7.3	1.2	0.1
S-113.80	113.8	0.2	37.4	3.6	0.9	0.2	6.9	3.5	0.6
S-116.10	116.1	0.1	11.5	0.6	0.1	bdl	7.3	2.1	0.3

S-119.50	119.5	0.2	43.3	3.9	1.1	0.2	12.8	1.5	0.2
S-122.60	122.6	0.0	6.9	0.4	0.1	bdl	3.4	0.5	0.1
S-126.50	126.5	0.1	14.5	0.6	0.3	0.0	8.1	0.4	0.0
S-130.70	130.7	0.0	6.8	0.6	0.1	0.0	1.3	0.4	0.1
S-132.60	132.6	0.1	19.7	1.2	0.3	0.0	4.9	1.4	0.2
S-134.40	134.4	0.1	14.4	1.8	0.3	0.1	0.7	1.2	0.2
S-137.50	137.5	0.1	14.3	1.2	0.3	0.0	5.5	0.7	0.2
S-141.80	141.8	0.6	151.4	9.2	3.9	0.7	11.8	9.1	1.0

Sample	Depth	TiO_2	Zr	Nb	Hf	Ta	Pb	Th	U
	(m)	(wt. %)	(ppm)						
SW-132.20A	132.2	0.2	67.9	4.6	1.3	0.2	3.6	5.3	0.5
SW-132.20B	132.8	0.1	13.1	2.9	0.2	0.1	5.3	1.1	0.4
SW-134.80	134.8	0.2	59.8	3.5	1.1	0.2	21.2	9.5	1.1
SW-137.60	137.6	0.2	35.4	2.5	0.8	0.1	3.6	3.3	1.1
SW-139.00	139	0.3	33.8	8.6	0.7	0.4	8.3	3.2	2.5
SW-143.90	143.9	0.2	42.1	6.4	0.7	0.3	4.3	3.7	2.0
SW-145.90	145.9	0.2	54.7	5.5	1.2	0.3	5.7	2.5	0.4
SW-148.10	148.1	0.0	4.2	0.8	bdl	bdl	2.9	0.5	0.2
SW-150.90	150.9	0.1	37.6	2.1	0.5	0.1	4.5	2.8	1.3
SW-153.70	153.7	0.2	49.9	4.6	1.0	0.2	5.2	6.2	0.8
SW-157.70	157.7	0.2	52.4	2.9	1.1	0.2	6.3	7.6	0.8
SW-160.60	160.6	0.1	10.8	1.4	0.1	0.0	4.7	0.9	0.3
SW-164.20	164.2	0.5	101.5	11.8	2.8	0.7	2.2	6.3	0.9

Sample	Depth	TiO_2	Zr	Nb	Hf	Ta	Pb	Th	U
	(m)	(wt. %)	(ppm)						
SS-38.90	38.9	0.0	8.2	2.1	0.1	0.0	4.3	0.3	0.3
SS-40.50A	40.5	0.1	63.2	3.8	1.2	0.2	3.5	1.0	0.6
SS-40.50B	40.8	0.1	15.5	2.4	0.3	0.1	2.0	1.1	0.3
SS-101.50	101.5	0.3	65.4	5.2	1.6	0.3	1.9	5.2	0.7
SS-104.90	104.9	0.0	11.1	1.8	0.1	0.1	3.2	0.4	0.3
SS-120.00	120	0.2	29.5	4.0	0.6	0.1	4.9	4.0	0.5
SS-123.10	123.1	0.8	85.4	35.5	2.3	0.7	11.2	6.7	5.4
SS-123.80	123.8	0.2	41.5	2.6	0.8	0.2	2.2	2.6	0.5
SS-125.00	125	0.0	6.1	1.7	0.1	0.1	1.2	0.2	0.2
SS-128.50	128.5	0.2	42.8	2.6	0.8	0.2	1.2	2.5	0.6
SS-131.00	131	0.1	20.8	2.2	0.4	0.1	1.7	1.4	0.4

B5. Transition Metals raw data

Sample	Depth	Sc	V	Cr	Co	Ni	Cu	Zn
	(m)	(ppm)						
N-97.80	97.8	5.7	54.1	18.6	13.4	30.7	7.1	26.4
N-100.05	100.05	2.8	35.7	16.5	5.9	13.4	10.3	43.6
N-105.05	105.05	4.3	38.0	20.0	2.8	11.4	11.7	17.4
N-108.80A	108.8	5.1	32.4	20.2	1.8	11.8	13.0	14.5
N-108.80B	108.85	4.7	40.3	19.0	2.8	10.0	7.2	24.4
N-119.80	119.8	3.9	40.8	61.5	2.7	38.1	10.9	19.1
N-121.20	121.2	3.4	36.1	22.5	2.3	12.1	8.9	18.1
N-126.30	126.3	4.9	53.4	25.3	7.6	15.7	7.1	31.0
N-129.90A	129.9	5.8	26.6	33.7	2.5	13.1	17.7	22.9
N-129.90B	129.95	2.1	53.4	24.0	2.3	12.9	13.4	18.9
N-133.10	133.1	5.5	63.5	25.9	3.4	19.0	11.3	33.7
N-139.10	139.1	5.7	61.8	35.2	3.2	16.5	9.6	51.0
N-143.60	143.6	8.3	10.4	25.5	1.3	11.8	9.8	29.4
N-147.50	147.5	4.3	56.4	23.9	7.8	16.1	9.6	23.1
N-149.50	149.5	5.7	22.5	35.1	1.2	15.6	15.9	23.5
N-153.90	153.9	4.1	54.1	23.3	3.6	12.8	15.5	19.3
N-158.40	158.4	3.8	55.5	27.2	3.6	14.6	12.8	30.7
N-163.20	163.2	4.2	53.0	24.8	13.6	13.6	10.2	19.5
N-166.70	166.7	7.5	60.2	43.0	9.0	20.4	9.5	24.8
N-169.70	169.7	5.6	27.4	27.8	3.8	15.6	11.0	11.4
N-174.20A	174.2	4.0	48.1	35.3	4.3	13.8	6.6	35.3
N-174.20B	174.8	5.6	18.7	57.2	2.0	22.2	14.7	38.5
N-175.10	175.1	5.7	72.6	37.4	3.7	10.9	8.3	38.2

Sample	Depth	Sc	V	Cr	Co	Ni	Cu	Zn
	(m)	(ppm)						
S-46.70	46.7	4.5	69.0	50.8	5.1	14.8	14.3	24.4
S-56.20	56.2	3.1	57.1	23.6	12.1	11.5	74.8	34.6
S-88.00	88	6.7	82.9	34.9	14.2	26.3	12.5	40.2
S-90.50	90.5	5.7	48.6	16.0	20.1	22.2	11.7	43.8
S-92.30	92.3	4.0	37.4	23.0	10.3	18.9	400.7	34.9
S-94.60	94.6	3.7	51.7	21.2	3.7	14.1	6.1	29.7
S-101.30	101.3	3.5	73.7	20.0	6.4	17.5	10.0	55.6
S-104.80	104.8	7.3	21.8	22.7	10.8	21.9	8.9	62.7
S-108.30	108.3	3.9	58.2	18.2	5.3	14.3	10.7	43.2
S-113.80	113.8	6.0	50.1	40.8	5.4	14.7	24.9	52.0
S-116.10	116.1	4.3	55.9	22.9	4.4	12.8	13.8	45.9

S-119.50	119.5	7.4	54.8	35.6	26.8	27.6	8.8	45.4
S-122.60	122.6	3.9	57.2	21.4	11.0	19.2	19.5	45.9
S-126.50	126.5	4.4	61.8	22.3	15.0	18.3	9.2	38.4
S-130.70	130.7	4.7	41.9	20.4	3.2	11.7	9.6	23.6
S-132.60	132.6	3.3	65.2	22.7	5.7	17.2	5.1	33.2
S-134.40	134.4	2.8	65.6	37.3	7.0	17.4	8.5	46.7
S-137.50	137.5	5.3	62.4	28.6	18.6	19.1	12.0	47.5
S-141.80	141.8	12.5	82.7	95.4	11.9	50.8	7.9	83.7

Sample	Depth	Sc	V	Cr	Co	Ni	Cu	Zn
	(m)	(ppm)						
SW-132.20A	132.2	7.9	81.4	59.1	44.4	38.0	22.1	90.8
SW-132.20B	132.8	3.5	79.6	40.5	8.1	24.6	28.5	35.7
SW-134.80	134.8	8.5	65.8	52.9	45.9	44.0	13.8	113.5
SW-137.60	137.6	3.7	119.1	44.7	14.9	32.1	18.7	61.5
SW-139.00	139	2.8	170.9	43.8	21.5	32.9	12.8	71.9
SW-143.90	143.9	5.9	109.1	43.1	26.2	40.7	41.0	82.3
SW-145.90	145.9	6.6	19.6	44.0	67.7	41.0	15.2	44.4
SW-148.10	148.1	4.4	8.0	40.6	13.4	28.6	16.2	60.1
SW-150.90	150.9	6.3	124.0	45.9	15.4	27.9	10.6	58.5
SW-153.70	153.7	6.4	68.8	53.5	9.2	27.0	10.6	119.5
SW-157.70	157.7	6.5	104.0	56.2	39.0	44.5	18.2	94.2
SW-160.60	160.6	3.8	90.0	40.8	19.4	28.2	37.7	81.9
SW-164.20	164.2	12.2	42.9	122.4	100.3	108.8	13.7	52.0

Sample	Depth	Sc	V	Cr	Co	Ni	Cu	Zn
	(m)	(ppm)						
SS-38.90	38.9	4.1	43.5	46.4	2.4	22.2	23.9	16.1
SS-40.50A	40.5	6.0	65.9	74.4	22.1	27.1	16.6	33.6
SS-40.50B	40.8	4.8	43.3	46.1	3.3	23.8	13.5	17.5
SS-101.50	101.5	8.5	55.4	58.1	5.6	23.5	12.6	44.5
SS-104.90	104.9	6.8	36.5	22.2	3.1	15.9	149.9	18.3
SS-120.00	120	8.6	41.1	52.1	4.0	17.1	84.2	30.5
SS-123.10	123.1	9.3	23.1	57.1	4.6	33.5	28.3	60.5
SS-123.80	123.8	8.0	72.5	42.8	2.7	18.8	9.7	28.0
SS-125.00	125	5.3	26.1	18.4	1.3	13.4	18.5	19.3
SS-128.50	128.5	7.3	66.7	41.9	2.4	18.9	13.8	31.6
SS-131.00	131	5.0	60.5	30.3	1.4	12.7	13.8	19.5

B6. REE raw data

Sample	Depth	La	Ce	Pr	Nd	Sm	Eu	Gd	Tb	Dy	Ho	Er	Tm	Yb	Lu
	(m)	(ppm)													
N-97.80	97.8	2,2	5,2	0,7	2,9	0,9	0,4	1,1	0,2	1,5	0,4	1,2	0,1	1,4	0,2
N-100.05	100.05	2,0	5,0	0,6	2,9	0,6	0,1	1,0	0,1	1,2	0,3	1,0	0,2	0,9	0,2
N-105.05	105.05	6,8	16,1	1,9	9,0	2,2	0,4	2,7	0,4	3,6	0,8	2,8	0,3	2,5	0,4
N-108.80A	108.8	2,9	6,6	0,8	3,2	0,6	0,1	0,9	0,2	1,4	0,4	1,1	0,1	1,0	0,1
N-108.80B	108.85	1,9	4,2	0,5	2,3	0,4	0,1	0,8	0,1	1,0	0,3	0,9	0,1	0,9	0,1
N-119.80	119.8	2,1	4,3	0,5	2,5	0,5	0,1	0,7	0,1	1,1	0,3	0,9	0,2	0,9	0,1
N-121.20	121.2	5,8	12,9	1,7	7,7	1,7	0,5	2,6	0,5	3,5	0,7	2,5	0,2	2,2	0,3
N-126.30	126.3	6,5	13,7	1,5	6,3	1,1	0,2	1,3	0,2	1,3	0,3	1,0	0,2	1,2	0,2
N-129.90A	129.9	9,3	19,7	2,5	11,8	2,9	0,6	3,2	0,5	3,1	0,7	2,2	0,3	2,1	0,3
N-129.90B	129.95	5,9	12,7	1,5	7,4	1,8	0,4	2,2	0,4	2,7	0,6	1,8	0,3	2,1	0,3
N-133.10	133.1	7,7	16,9	2,0	8,9	2,0	0,5	2,2	0,4	2,8	0,6	2,0	0,3	2,0	0,3
N-139.10	139.1	11,3	23,8	2,7	11,1	2,1	0,4	2,7	0,4	3,7	0,8	2,5	0,3	2,7	0,4
N-143.60	143.6	4,6	9,9	1,3	5,5	1,3	0,2	1,3	0,2	2,1	0,4	1,5	0,2	1,7	0,3
N-147.50	147.5	2,3	4,6	0,5	2,6	0,3	0,1	0,6	0,1	0,8	0,2	1,0	0,1	1,4	0,2
N-149.50	149.5	1,5	2,9	0,3	1,7	0,1	0,0	0,3	0,1	0,6	0,1	0,4	0,1	0,5	0,1
N-153.90	153.9	2,5	5,3	0,6	2,8	0,5	0,1	0,7	0,1	1,1	0,3	1,0	0,1	1,0	0,2
N-158.40	158.4	6,4	13,9	1,7	7,1	1,7	0,4	2,0	0,3	2,6	0,8	2,6	0,3	2,6	0,5
N-163.20	163.2	1,7	3,7	0,4	2,2	0,5	0,1	0,6	0,2	1,1	0,3	1,3	0,2	1,3	0,2
N-166.70	166.7	13,2	25,9	3,1	12,8	2,5	0,6	2,4	0,4	2,4	0,5	1,5	0,2	1,8	0,2
N-169.70	169.7	1,0	2,0	0,3	1,3	0,2	0,1	0,5	0,1	0,5	0,1	0,5	0,3	0,5	0,1
N-174.20A	174.2	12,8	29,4	3,6	14,9	3,4	0,8	4,1	0,7	4,5	1,0	3,4	0,4	3,8	0,6
N-174.20B	174.8	4,3	10,1	1,2	5,1	1,1	0,3	1,2	0,3	2,1	0,5	1,7	0,4	2,0	0,4
N-175.10	175.1	15,2	33,6	4,0	17,4	3,4	0,5	4,5	0,6	5,4	1,2	3,9	0,3	3,4	0,6

Sample	Depth	La	Ce	Pr	Nd	Sm	Eu	Gd	Tb	Dy	Ho	Er	Tm	Yb	Lu
	(m)	(ppm)													
S-46.70	46.7	2,7	6,7	0,7	3,1	0,7	0,2	0,6	0,1	0,9	0,2	0,6	0,1	0,7	0,1
S-56.20	56.2	3,8	8,9	1,1	4,8	0,8	0,2	1,3	0,3	2,2	0,6	2,1	0,3	2,1	0,4
S-88.00	88	2,9	7,0	0,8	3,5	0,8	0,2	1,2	0,2	1,3	0,4	1,2	0,2	1,3	0,2
S-90.50	90.5	2,7	5,9	0,6	2,8	0,7	0,3	0,8	0,1	1,1	0,2	0,8	0,1	1,0	0,2
S-92.30	92.3	3,5	7,3	0,7	3,6	0,9	0,2	0,9	0,1	1,1	0,3	0,7	0,1	0,9	0,2
S-94.60	94.6	1,7	3,7	0,6	2,0	0,5	0,2	0,7	0,2	1,4	0,4	1,2	0,2	1,1	0,2
S-101.30	101.3	2,9	5,6	0,6	2,2	0,2	0,1	0,3	0,1	0,3	0,1	0,3	0,0	0,3	0,0
S-104.80	104.8	2,7	6,1	0,8	3,4	0,9	0,1	0,8	0,1	1,0	0,3	0,7	0,1	0,7	0,1
S-108.30	108.3	3,3	6,1	0,7	2,7	0,5	0,1	0,8	0,1	1,4	0,4	1,3	0,2	1,6	0,3
S-113.80	113.8	30,2	58,6	6,6	28,1	5,3	1,6	6,5	0,8	5,5	1,2	3,6	0,6	3,6	0,6
S-116.10	116.1	12,1	25,5	2,8	12,6	2,6	0,7	3,0	0,6	3,9	1,0	2,9	0,4	2,7	0,4

S-119.50	119.5	12,2	22,9	2,5	10,6	1,8	0,5	1,7	0,3	2,0	0,4	1,5	0,3	1,6	0,3
S-122.60	122.6	2,0	3,8	0,5	2,2	0,7	0,1	0,9	0,2	1,2	0,3	0,9	0,1	1,1	0,2
S-126.50	126.5	1,4	3,2	0,4	1,8	0,4	0,1	0,5	0,1	0,6	0,2	0,6	0,1	0,8	0,1
S-130.70	130.7	2,0	4,3	0,6	2,2	0,5	0,1	0,5	0,1	0,9	0,2	1,0	0,1	1,1	0,1
S-132.60	132.6	15,1	27,5	3,1	12,4	1,8	0,3	1,0	0,1	1,1	0,3	0,8	0,1	1,0	0,2
S-134.40	134.4	2,7	5,9	0,6	2,6	0,3	0,1	0,6	0,1	0,8	0,2	0,7	0,1	0,8	0,1
S-137.50	137.5	2,9	6,1	0,8	3,4	0,8	0,3	1,0	0,2	1,5	0,4	1,4	0,2	1,9	0,3
S-141.80	141.8	27,7	55,6	6,4	24,2	4,8	0,9	4,2	0,5	3,3	0,6	1,6	0,2	1,9	0,3

Sample	Depth	La	Ce	Pr	Nd	Sm	Eu	Gd	Tb	Dy	Ho	Er	Tm	Yb
	(m)	(ppm)												
SW-132.20A	132.2	8,8	17,5	2,0	9,0	1,9	0,4	1,9	0,3	2,6	0,5	2,1	0,3	2,2
SW-132.20B	132.8	3,0	7,4	1,0	5,1	1,4	0,3	2,4	0,4	3,2	0,8	2,3	0,4	2,3
SW-134.80	134.8	9,5	21,6	2,6	12,3	2,9	0,7	3,5	0,5	4,4	1,0	3,2	0,5	3,8
SW-137.60	137.6	5,2	11,2	1,3	6,1	1,4	0,3	1,4	0,2	1,7	0,4	1,4	0,2	1,4
SW-139.00	139	3,0	6,7	0,7	3,6	0,7	0,2	1,0	0,1	0,4	0,1	0,3	0,0	0,2
SW-143.90	143.9	4,8	9,4	1,1	4,5	0,8	0,1	0,7	0,1	0,5	0,1	0,5	0,1	0,6
SW-145.90	145.9	7,4	14,8	1,8	7,2	1,6	0,7	2,2	0,3	2,3	0,5	1,7	0,2	1,6
SW-148.10	148.1	0,3	0,8	0,1	0,4	0,1	0,0	0,2	0,0	0,2	0,1	0,2	0,0	0,3
SW-150.90	150.9	4,7	10,6	1,2	5,0	0,9	0,4	1,1	0,2	1,9	0,4	1,5	0,3	1,7
SW-153.70	153.7	23,8	45,6	4,6	18,2	2,8	0,5	2,7	0,4	2,7	0,7	2,2	0,3	2,2
SW-157.70	157.7	7,6	15,4	1,7	7,7	1,9	0,4	2,6	0,4	3,4	0,9	2,6	0,4	3,0
SW-160.60	160.6	2,3	5,9	0,9	4,4	1,4	0,2	1,8	0,3	2,7	0,6	1,9	0,3	1,9
SW-164.20	164.2	18,7	37,6	4,5	17,2	3,9	1,0	3,6	0,5	3,2	0,7	1,9	0,3	1,8

Sample	Depth	La	Ce	Pr	Nd	Sm	Eu	Gd	Tb	Dy	Ho	Er	Tm	Yb
	(m)	(ppm)												
SS-38.90	38.9	2,4	5,5	0,7	3,1	0,6	0,2	1,0	0,1	1,3	0,3	1,1	0,1	1,2
SS-40.50A	40.5	16,9	36,6	4,8	20,0	4,3	1,1	5,4	0,7	4,6	1,2	3,3	0,5	3,2
SS-40.50B	40.8	8,4	16,8	2,1	8,4	1,8	0,3	2,0	0,3	2,5	0,6	1,8	0,2	2,1
SS-101.50	101.5	20,2	40,3	4,6	18,2	4,0	0,7	3,6	0,5	3,3	0,8	2,1	0,3	1,9
SS-104.90	104.9	6,0	13,0	1,7	6,7	1,7	0,4	2,0	0,3	2,8	0,6	2,1	0,3	1,7
SS-120.00	120	30,1	62,6	7,1	30,1	6,5	2,1	7,3	1,1	6,6	1,3	3,8	0,5	3,3
SS-123.10	123.1	17,6	38,1	4,9	20,7	6,2	2,1	7,3	1,0	6,1	1,0	3,3	0,4	2,6
SS-123.80	123.8	22,0	47,4	5,4	23,1	4,9	0,9	5,4	0,9	5,7	1,2	4,3	0,6	4,3
SS-125.00	125	2,1	3,9	0,4	2,0	0,5	0,1	0,7	0,1	0,9	0,2	0,8	0,1	0,9
SS-128.50	128.5	18,2	38,7	4,4	18,6	4,2	0,8	4,9	0,7	4,9	1,1	3,4	0,5	3,3
SS-131.00	131	11,8	24,2	2,6	12,1	2,9	0,7	3,7	0,6	4,1	0,9	2,8	0,4	2,8

B7. EPMA raw data

Sample and mineral	Al_2O_3	SiO_2	TiO_2	Na_2O	MgO	FeO	MnO	F	CaO	K_2O	Total
	(wt%)										
N-72.60_bt	15.3	39.4	1.3	0.3	13.4	18.2	0.3	0.1	0.1	7.3	95.6
N-72.60_bt 1.2	16.0	38.3	1.4	0.3	13.0	17.9	0.3	0.1	0.1	7.9	95.1
N-72.60_bt 1.3	14.6	41.9	1.0	0.2	12.0	17.9	0.3	bdl	0.1	5.6	93.6
N-72.60_bt 2.2	16.1	39.2	1.7	0.2	13.2	17.5	0.4	0.2	0.1	6.9	95.6
N-72.60_bt 2.3	16.3	38.8	1.6	0.3	13.0	18.1	0.4	bdl	0.1	7.9	96.4
N-72.60_grt 1.2	20.0	38.4	bdl	bdl	2.4	26.3	10.4	bdl	3.1	bdl	100.6
N-72.60_grt 1.3	20.2	38.6	bdl	bdl	2.6	26.4	10.1	bdl	3.0	bdl	101.0
N-72.60_grt 2	20.2	38.4	bdl	bdl	2.4	27.5	9.6	bdl	2.8	bdl	101.0
N-72.60_grt 2.2	20.3	38.3	bdl	bdl	2.7	26.8	10.7	bdl	2.1	bdl	100.9
N-72.60_grt 3	20.5	38.6	bdl	bdl	2.6	27.5	9.5	bdl	2.4	bdl	101.2
N-72.60_grt 3.2	20.3	38.0	bdl	bdl	2.8	26.9	10.1	bdl	2.7	bdl	100.8
N-72.60_grt 3.3	20.0	38.3	bdl	bdl	2.4	26.0	10.4	bdl	3.2	bdl	100.4
N-72.60_grt 4	20.1	38.5	bdl	bdl	2.6	26.5	9.9	bdl	2.9	bdl	100.6
N-72.60_grt 4.2	20.2	38.5	0.1	bdl	2.6	26.0	10.3	bdl	2.9	bdl	100.7
N-72.60_grt 4.3	20.5	38.2	0.1	bdl	2.5	26.9	9.9	bdl	2.9	bdl	101.1
N-126.30_bt 1	18.1	37.9	2.1	0.1	10.1	18.4	0.1	0.1	bdl	7.7	94.5
N-126.30_bt 1.2	18.1	38.7	2.1	0.1	10.4	18.2	0.1	0.1	bdl	7.8	95.6
N-126.30_bt 1.3	18.3	38.6	2.0	0.1	10.5	18.3	0.1	0.0	bdl	7.7	95.6
N-126.30_bt 2	18.3	37.5	2.2	0.2	10.3	18.9	0.1	0.1	bdl	9.2	96.6
N-126.30_bt 2.2	17.9	38.4	2.0	0.2	10.5	18.8	0.1	0.1	bdl	8.7	96.7
N-126.30_bt 2.3	17.9	38.0	2.1	0.1	10.6	18.2	0.1	0.2	bdl	8.6	95.8
N-126.30_bt 3	18.3	37.6	2.1	0.2	10.3	18.7	0.2	0.2	0.1	9.3	96.8
N-126.30_bt 3.3	18.2	38.6	2.1	0.1	10.6	17.9	0.1	bdl	bdl	8.5	96.2
N-126.30_bt 4	18.5	37.8	1.8	0.1	10.3	18.9	0.1	0.2	bdl	9.4	97.2
N-126.30_bt 4.2	18.4	37.6	1.7	0.2	10.0	18.8	0.1	0.1	bdl	9.2	96.3
N-126.30_bt 4.3	18.3	37.5	1.8	0.1	10.3	18.7	0.1	0.1	bdl	9.2	96.0
N-126.30_grt 2	19.5	37.0	bdl	bdl	0.3	40.8	0.6	bdl	1.7	bdl	100.0
N-126.30_grt 2.2	19.7	37.4	0.1	bdl	0.3	40.6	0.7	bdl	1.9	bdl	100.8
N-126.30_grt 3	19.8	37.1	bdl	bdl	0.3	40.8	0.6	bdl	1.6	bdl	100.3
N-126.30_grt 3.2	19.7	37.5	bdl	bdl	0.3	41.2	0.6	bdl	1.6	bdl	100.9
N-126.30_grt 3.3	19.6	37.2	bdl	0.1	0.3	41.1	0.6	bdl	1.9	bdl	100.8
N-126.30_grt 5	20.7	38.6	0.1	bdl	2.0	29.7	0.9	bdl	7.9	bdl	99.9
N-126.30_grt 5.2	20.8	38.3	0.1	bdl	1.8	30.5	1.2	bdl	7.3	bdl	100.1
N-126.30_grt 5.3	20.8	37.8	0.1	bdl	1.9	30.6	2.6	bdl	6.4	bdl	100.4
N-126.30_grt 6	20.5	38.2	0.1	bdl	1.5	31.3	1.9	bdl	6.7	bdl	100.2
N-126.30_grt 6.2	20.5	38.3	0.1	bdl	1.9	30.3	0.8	bdl	7.7	bdl	99.6
N-126.30_grt 6.3	20.5	38.4	0.1	bdl	1.8	31.0	1.3	bdl	7.2	bdl	100.3

N-126.30_grt 7	20.5	38.3	0.1	bdl	1.7	30.8	1.4	bdl	6.5	bdl	99.4
N-126.30_grt 7.2	20.5	38.4	0.1	bdl	1.7	31.2	2.1	bdl	6.0	bdl	99.9
N-126.30_grt 7.3	20.4	38.5	0.1	bdl	1.9	31.7	1.5	bdl	6.8	bdl	101.0
N-126.30_grt 9	20.3	38.6	0.1	bdl	1.5	30.3	3.6	bdl	6.1	bdl	100.4
N-126.30_grt 9.2	20.5	38.4	0.1	bdl	1.6	31.2	1.2	bdl	7.0	bdl	100.0
N-126.30_grt 9.3	20.3	38.5	0.1	bdl	1.5	29.3	4.8	bdl	6.1	bdl	100.7
N-126.30_grt 10	20.6	38.5	0.1	bdl	1.7	30.8	1.2	bdl	7.0	bdl	100.1
N-126.30_grt 10.2	20.4	38.4	0.1	bdl	1.7	30.7	1.8	bdl	6.7	bdl	99.8
N-126.30_grt 10.3	20.7	38.2	bdl	bdl	2.0	30.5	1.3	bdl	7.0	bdl	99.7
N-126.30_grt 11	20.4	37.9	0.1	bdl	1.5	31.4	2.7	bdl	6.0	bdl	100.2
N-126.30_grt 11.2	20.4	38.0	bdl	bdl	1.6	31.3	1.9	bdl	6.6	bdl	100.0
N-126.30_grt 11.3	20.5	38.4	0.1	bdl	1.6	30.8	2.7	bdl	6.0	bdl	100.3

Sample and mineral	Al_2O_3	SiO_2	TiO_2	Na_2O	MgO	FeO	MnO	F	CaO	K_2O	Total
	(wt%)										
S-149.80_*bt 1	18.7	38.3	1.9	0.2	10.4	18.0	0.1	0.2	0.0	7.6	95.5
S-149.80_bt 1.2	19.0	37.7	1.9	0.1	10.5	18.1	0.1	0.2	0.0	7.7	95.9
S-149.80_bt 1.3	18.7	38.1	2.0	0.2	10.4	18.1	0.1	0.0	bdl	7.9	96.4
S-149.80_bt 2	18.6	37.3	1.9	0.2	10.3	18.3	0.1	0.2	bdl	9.5	95.7
S-149.80_bt 2.2	18.5	37.8	1.7	0.2	10.6	17.8	0.1	0.1	bdl	9.3	96.1
S-149.80_bt 2.3	18.6	36.8	1.8	0.1	10.7	18.5	0.1	0.2	bdl	8.4	95.2
S-149.80_bt 3	19.3	38.5	1.8	0.2	10.5	18.2	0.1	0.2	bdl	8.4	97.3
S-149.80_bt 3.2	19.0	38.3	1.8	0.1	10.3	18.0	0.1	0.2	bdl	7.7	95.0
S-149.80_bt 3.3	18.6	37.5	1.8	0.2	10.4	18.6	0.1	0.2	bdl	8.9	96.4
S-149.80_*grt 1	20.6	38.2	0.1	bdl	1.2	30.7	3.9	bdl	5.8	bdl	99.6
S-149.80_grt 1.2	20.5	38.4	0.1	bdl	1.4	29.2	5.2	bdl	6.1	bdl	100.3
S-149.80_grt 1.3	20.3	37.8	0.1	bdl	1.2	28.5	5.5	bdl	5.9	bdl	99.9
S-149.80_grt 2	20.3	38.0	0.1	bdl	1.4	30.4	3.6	bdl	6.1	bdl	99.5
S-149.80_grt 2.2	20.6	38.3	0.1	bdl	1.5	30.8	2.1	bdl	6.6	bdl	100.6
S-149.80_grt 2.3	20.5	38.6	0.1	bdl	2.0	30.2	1.0	bdl	7.6	bdl	100.0
S-149.80_grt 3	20.3	37.7	0.2	bdl	1.2	28.2	6.2	bdl	5.8	bdl	100.1
S-149.80_grt 3.2	20.4	38.2	0.1	bdl	1.8	29.9	4.0	bdl	5.7	bdl	100.2
S-149.80_grt 3.3	20.2	38.4	0.1	bdl	1.3	27.9	5.9	bdl	5.8	bdl	100.0
S-149.80_grt 4	20.5	38.0	0.1	bdl	1.0	29.4	5.6	bdl	5.8	bdl	100.1
S-149.80_grt 4.2	20.2	37.8	0.2	bdl	1.1	29.7	4.9	bdl	6.0	bdl	100.1
S-149.80_grt 4.3	20.0	37.9	0.1	0.0	0.7	26.0	8.7	bdl	6.0	bdl	100.1
S-149.80_grt 5	20.5	38.2	0.1	0.0	1.4	31.3	2.9	bdl	6.2	bdl	100.0
S-149.80_grt 5.2	20.9	38.0	0.1	bdl	1.8	31.3	1.2	bdl	6.7	bdl	100.0
S-149.80_grt 5.3	20.4	38.3	0.1	bdl	1.4	31.4	2.3	bdl	6.1	bdl	100.0

Sample and mineral	Al_2O_3	SiO_2	TiO_2	Na_2O	MgO	FeO	MnO	F	CaO	K_2O	Total
	(wt%)										
SW-145.90_*amph	0.2	52.4	bdl	bdl	7.8	34.8	3.7	0.1	0.2	bdl	99.1
SW-145.90_amph	0.2	51.3	bdl	bdl	7.8	34.9	3.6	bdl	0.2	bdl	98.1
SW-145.90_amph	0.1	51.7	bdl	bdl	7.8	34.6	3.9	bdl	0.2	bdl	98.3
SW-145.90_amph	0.2	51.5	bdl	bdl	7.8	35.0	3.8	bdl	0.2	bdl	98.4
SW-145.90_amph 2	0.2	51.6	bdl	bdl	7.1	34.9	3.8	bdl	0.2	bdl	97.8
SW-145.90_amph 2.2	0.2	51.2	bdl	bdl	7.2	35.1	3.8	bdl	0.2	bdl	97.8
SW-145.90_amph 2.3	0.3	51.5	bdl	0.1	7.3	34.6	3.9	bdl	0.2	bdl	98.0
SW-145.90_amph 3.1	0.2	51.6	bdl	bdl	7.3	35.5	3.8	bdl	0.2	bdl	98.6
SW-145.90_amph 3.2	0.1	51.8	bdl	bdl	7.4	35.6	3.8	bdl	0.2	bdl	99.0
SW-145.90_amph 3.3	0.3	51.6	0.1	0.1	7.2	35.2	4.0	bdl	0.3	bdl	98.7
SW-145.90_amph 4	0.3	52.4	bdl	bdl	9.4	32.1	3.9	bdl	0.2	bdl	98.4
SW-145.90_amph 4	0.3	52.5	bdl	bdl	9.3	32.2	4.0	bdl	0.2	bdl	98.5
SW-145.90_amph 4.1	0.2	52.3	bdl	bdl	9.4	32.3	4.0	bdl	0.2	bdl	98.3
SW-145.90_amph 4.2	0.3	52.5	bdl	bdl	9.4	31.9	3.9	bdl	0.2	bdl	98.2
SW-145.90_amph 5	0.3	52.7	bdl	bdl	9.6	32.2	3.5	bdl	0.2	bdl	98.5
SW-145.90_amph 5.2	0.3	52.9	0.1	bdl	9.8	31.9	4.0	bdl	0.2	bdl	99.2
SW-145.90_amph 5.3	0.3	52.6	0.1	0.1	9.8	32.1	3.8	bdl	0.2	bdl	98.9
SW-145.90_amph 6	0.3	52.8	bdl	0.1	10.3	30.8	3.9	bdl	0.3	bdl	98.5
SW-145.90_amph 6.2	0.2	53.4	bdl	bdl	10.5	30.5	3.8	bdl	0.2	bdl	98.7
SW-145.90_amph 6.3	0.3	53.1	bdl	bdl	10.4	30.4	4.0	bdl	0.3	bdl	98.5
SW-145.90_amph 6.3	0.3	53.1	bdl	bdl	10.4	30.4	4.0	bdl	0.3	bdl	98.6
SW-164.20_amph 2.2	0.2	56.1	bdl	bdl	16.2	21.2	4.7	bdl	0.6	bdl	99.0
SW-164.20_amph 2.3	0.2	55.3	bdl	bdl	16.4	20.5	4.8	bdl	0.9	bdl	98.1
SW-164.20_amph 3	0.1	55.6	bdl	bdl	16.4	21.3	4.6	bdl	0.4	bdl	98.4
SW-164.20_amph 3.2	0.2	55.9	bdl	bdl	16.5	20.9	4.8	bdl	0.8	bdl	99.1
SW-164.20_amph 3.3	0.1	55.3	bdl	bdl	15.5	22.1	5.2	bdl	0.3	bdl	98.5
SW-164.20_bt 1	14.0	38.9	1.6	0.1	11.0	20.4	0.6	0.1	bdl	9.3	96.1
SW-164.20_bt 1.2	14.5	37.2	1.7	0.1	10.7	21.8	0.9	0.1	bdl	8.7	95.6
SW-164.20_bt 1.4	14.8	39.3	1.7	0.1	11.2	19.3	0.6	bdl	bdl	9.8	96.9
SW-164.20_bt 1.5	14.9	39.4	1.7	0.1	11.5	19.5	0.6	0.1	bdl	9.4	97.2
SW-164.20_bt 1.6	14.9	36.6	1.6	0.1	11.6	22.1	0.7	0.2	bdl	7.6	95.2
SW-164.20_bt 4	14.9	39.3	1.6	0.1	12.6	18.1	0.6	0.2	bdl	9.2	96.6
SW-164.20_bt 4.2	14.6	39.9	1.4	0.1	12.9	17.8	0.7	0.3	bdl	8.6	96.3
SW-164.20_bt 4.3	14.6	40.1	1.7	0.1	13.1	17.8	0.7	0.2	bdl	8.7	96.9
SW-164.20_bt 5	14.7	39.6	1.6	0.1	12.9	17.7	0.7	0.1	bdl	9.2	96.5
SW-164.20_bt 5.2	14.5	39.7	1.6	0.1	13.1	18.0	0.7	0.3	bdl	7.9	95.9
SW-164.20_bt 5.3	14.7	39.3	1.7	0.1	13.0	17.8	0.6	0.1	bdl	8.6	95.9
SW-145.90_grt 1	18.5	37.3	0.1	bdl	0.6	21.4	18.3	bdl	2.9	bdl	100.8
SW-145.90_grt 1	18.4	37.8	0.1	bdl	0.6	21.6	18.2	bdl	3.0	bdl	99.6

SW-145.90_grt 1.2	20.0	37.7	0.1	bdl	0.7	22.3	17.0	bdl	2.9	bdl	100.1
SW-145.90_grt 1.3	18.6	37.5	0.2	bdl	0.8	22.5	17.1	bdl	2.8	bdl	100.8
SW-145.90_grt 2	18.6	37.4	0.2	bdl	0.6	21.4	18.4	bdl	2.9	bdl	100.3
SW-145.90_grt 2.2	18.7	37.2	0.1	bdl	0.7	22.5	17.1	bdl	2.8	bdl	100.9
SW-145.90_grt 2.3	18.3	37.4	0.2	bdl	0.5	20.9	18.6	bdl	3.0	bdl	100.6
SW-145.90_grt 3	18.6	37.7	0.1	bdl	0.5	21.7	18.2	bdl	2.9	bdl	100.0
SW-145.90_grt 3.2	19.7	37.5	0.1	bdl	0.5	21.4	18.7	bdl	2.9	bdl	98.5
SW-145.90_grt 3.3	19.5	37.1	0.1	bdl	0.7	22.0	17.3	bdl	2.9	bdl	98.2
SW-145.90_grt 4	19.6	37.3	0.1	bdl	0.7	22.4	17.2	bdl	2.8	bdl	98.3
SW-145.90_grt 4.2	19.5	37.4	0.1	bdl	0.6	22.2	18.1	bdl	2.9	bdl	98.1
SW-145.90_grt 4.3	19.93	37.56	0.03	0.03	0.75	23.21	16.56	bdl	2.17	0.02	100.3
SW-145.90_grt 5	19.52	37.34	0.18	bdl	0.48	22.96	17.44	bdl	2.94	0.02	100.9
SW-145.90_grt 5.2	19.69	37.31	0.19	0.01	0.46	22.51	17.28	bdl	3.08	0.03	100.6
SW-164.20_grt 1	19.98	38.52	0.08	0.03	1.62	17.44	19.97	bdl	3.2	0.02	100.6
SW-164.20_grt 1.3	20.31	38.3	0.07	0.01	1.49	17.73	20.59	bdl	2.88	0.01	100.5
SW-164.20_grt 2	20.23	38.45	0.07	bdl	1.46	17.52	19.91	bdl	3.42	0.03	99.3
SW-164.20_grt 2.2	20.08	38.47	0.12	0.03	1.27	16.67	19.18	bdl	4.75	0.03	100.9
SW-164.20_grt 2.3	20.03	37.73	0.23	bdl	1.18	16.88	20.09	bdl	4.26	0.03	100.4
SW-72.60_grt 3	20.37	38.37	0.06	0.04	1.45	17	19.36	bdl	4.34	0.04	99.8
SW-164.20_grt 3.2	20.42	38.45	0.09	0.03	1.49	17.35	19.73	bdl	3.73	0.05	98.6
SW-164.20_grt 6	20.1	38.09	0.04	0.01	1.34	17.21	20.57	bdl	3.17	0.03	98.3
SW-164.20_grt 6.2	20.16	38.17	0.1	0.02	1.27	17.07	20.52	bdl	3.16	0.04	98.5
SW-164.20_grt 6.3	19.88	37.96	0.11	0.01	1.48	16.46	19.66	bdl	3.71	0.02	98.3
SW-164.20_grt 7	20.21	38.18	0.07	bdl	1.30	17.06	20.11	bdl	3.97	0.03	98.7
SW-164.20_grt 7.2	20.15	37.9	0.04	bdl	1.34	17.11	21.1	bdl	2.71	0.03	98.2
SW-164.20_grt 7.3	19.75	37.73	0.1	0.03	1.01	17.11	20.58	bdl	3.35	0.04	98.3

Sample and mineral	Al_2O_3	SiO_2	TiO_2	Na_2O	MgO	FeO	MnO	F	CaO	K_2O	Total
	(wt%)										
SS-40.50_*chl 3	13.2	32.9	0.1	0.1	25.8	14.9	1.1	bdl	0.1	0.1	88.2
SS-40.50_chl 3.	13.1	33.1	0.1	0.1	26.1	15.0	0.9	bdl	0.1	0.1	88.8
SS-40.50_chl 3.	13.1	33.1	0.1	0.1	25.8	14.7	1.0	bdl	0.0	0.1	88.0
SS-40.50_chl 4	12.3	32.2	0.1	bdl	24.0	17.9	1.3	bdl	0.1	0.1	88.4
SS-40.50_chl 4.	12.5	31.8	0.1	bdl	23.9	17.8	1.2	bdl	0.1	0.1	87.2
SS-40.50_chl 4.	11.6	34.4	bdl	0.1	21.4	16.0	1.0	bdl	0.1	0.2	85.2
SS-40.50_chl 5	11.6	31.6	0.1	bdl	24.4	17.7	1.0	bdl	0.1	0.1	86.9
SS-40.50_chl 5.	11.9	31.3	0.1	bdl	23.7	18.6	1.3	bdl	0.1	0.2	87.7
SS-40.50_chl 5.	12.1	32.5	bdl	bdl	25.0	16.6	1.2	bdl	0.3	0.1	88.3
SS-123.80_grt 1	19.8	37.4	bdl	bdl	1.0	41.1	0.3	bdl	0.4	bdl	99.7
SS-123.80_grt 1.2	20.0	37.5	bdl	bdl	1.1	40.7	0.3	bdl	0.3	bdl	100.1

SS-123.80_grt 1.3	19.7	37.5	bdl	bdl	1.2	41.3	0.3	bdl	0.4	bdl	100.7
SS-123.80_grt 2	19.9	37.2	bdl	bdl	1.3	40.4	0.3	bdl	0.6	bdl	100.4
SS-123.80_grt 2.2	20.1	37.4	bdl	bdl	1.2	41.0	0.3	bdl	0.4	bdl	99.9
SS-123.80_grt 2.3	19.8	37.7	bdl	bdl	1.1	40.9	0.3	bdl	0.4	bdl	100.0
SS-123.80_grt 3	19.9	37.4	bdl	bdl	1.2	41.1	0.3	bdl	0.4	bdl	100.5
SS-123.80_grt 3.2	20.0	37.5	bdl	bdl	1.2	41.2	0.3	bdl	0.4	bdl	100.5
SS-123.80_grt 3.3	19.9	37.1	bdl	bdl	1.2	40.8	0.2	bdl	0.4	bdl	99.7
SS-123.80_grt 4	19.8	37.5	bdl	bdl	1.1	40.9	0.3	bdl	0.5	bdl	100.1
SS-123.80_grt 4.2	19.9	37.4	bdl	bdl	1.2	41.4	0.3	bdl	0.5	bdl	100.7
SS-123.80_grt 5	20.0	37.4	bdl	bdl	1.1	41.3	0.3	bdl	0.4	bdl	100.4
SS-123.80_grt 5.2	19.7	37.4	0.1	bdl	1.2	40.9	0.2	bdl	0.4	bdl	99.9
SS-123.80_grt 5.3	20.0	37.6	bdl	bdl	1.1	38.5	0.6	bdl	2.2	bdl	100.0
SS-123.80_amph 1	0.4	52.4	bdl	bdl	8.0	37.8	0.1	bdl	bdl	bdl	98.7
SS-123.80_amph 1.2	0.3	52.3	bdl	bdl	8.1	38.0	0.0	bdl	bdl	bdl	98.7
SS-123.80_amph 1.3	0.3	52.2	0.1	bdl	8.0	37.8	0.1	bdl	bdl	bdl	98.5
SS-123.80_amph 2	0.3	52.1	bdl	bdl	7.8	37.8	0.1	bdl	bdl	bdl	98.1
SS-123.80_amph 2.2	0.4	52.0	bdl	bdl	8.1	37.4	0.1	bdl	bdl	bdl	98.1
SS-123.80_amph 2.3	0.4	52.2	bdl	bdl	8.1	37.6	0.1	bdl	bdl	bdl	98.3
SS-123.80_amph 3	0.4	52.1	bdl	bdl	8.1	37.7	0.1	bdl	bdl	bdl	98.3
SS-123.80_amph 3.2	0.4	52.0	bdl	bdl	8.1	38.1	bdl	bdl	bdl	bdl	97.9
SS-123.80_amph 3.3	0.3	52.4	bdl	bdl	8.1	37.9	bdl	bdl	bdl	bdl	98.4
SS-123.80_amph 4	0.3	52.3	bdl	bdl	8.0	37.8	bdl	bdl	bdl	bdl	99.4
SS-123.80_amph 4.2	0.3	52.5	bdl	bdl	8.0	38.0	bdl	bdl	bdl	bdl	98.3
SS-123.80_amph 4.3	0.4	52.0	bdl	bdl	8.1	38.0	bdl	bdl	bdl	bdl	98.0
SS-123.80_amph 5	0.4	52.3	bdl	bdl	8.0	37.6	bdl	bdl	bdl	bdl	97.6
SS-123.80_amph 5.2	0.4	52.1	bdl	bdl	8.0	38.0	bdl	bdl	bdl	bdl	97.5
SS-123.80_amph 5.3	0.3	52.3	bdl	bdl	8.2	37.4	bdl	bdl	bdl	bdl	98.2

*bt = biotite; grt = garnet; amph = amphibole; chl=chlorite

B8. CIA values for Xaudum iron-formation

These values are calculated without CaO* because the inclusion of CaO in the formula will cause unrealistic values (Fedo et al. 1995).

Sample	Depth (m)	CIA
N-97.80	97.8	98.38
N-105.05	105.05	91.43
N-108.80A	108.8	80.39
N-108.80B	108.85	94.05
N-126.30	126.3	80.09
N-129.90A	129.9	93.48
N-129.90B	129.95	90.24
N-133.10	133.1	87.88
N-139.10	139.1	90.85
N-147.50	147.5	84.03
N-153.90	153.9	82.12
N-163.20	163.2	94.56
N-166.70	166.7	65.86
N-169.70	169.7	76.92
N-174.20A	174.2	89.11
N-174.20B	174.8	89.16
N-175.10	175.1	86.24

Sample	Depth (m)	CIA
S-46.70	46.7	78.00
S-56.20	56.2	87.42
S-88.00	88	73.83
S-90.50	90.5	87.35
S-94.60	94.6	84.54
S-101.30	101.3	92.73
S-104.80	104.8	67.06
S-108.30	108.3	82.05
S-113.80	113.8	85.92
S-116.10	116.1	87.10
S-119.50	119.5	83.52
S-126.50	126.5	71.12
S-130.70	130.7	95.56
S-137.50	137.5	93.84
S-141.80	141.8	87.43

Sample	Depth (m)	CIA
SW-132.20A	132.2	96.77
SW-134.80	134.8	94.39
SW-137.60	137.6	83.96
SW-139.00	139	98.67
SW-143.90	143.9	70.39
SW-145.90	145.9	99.44
SW-148.10	148.1	78.43
SW-150.90	150.9	82.05
SW-153.70	153.7	85.76
SW-157.70	157.7	86.74
SW-160.60	160.6	91.75
SW-164.20	164.2	92.63

Sample	Depth (m)	CIA
SS-38.90	38.9	69.49
SS-40.50A	40.5	88.27
SS-40.50B	40.8	82.50
SS-120.00	120	98.05
SS-123.10	123.1	79.02
SS-131.00	131	96.39

B9. CIA values for top and bottom diamictite

These values are calculated without CaO* because the inclusion of CaO in the formula will cause unrealistic values (Fedo et al. 1995)

Top diamictite		
Sample	**Depth (m)**	**CIA**
N-62.60	62.6	65.29
N-67.40	67.4	91.67
N-70.30	70.3	85.57
N-72.60	72.6	74.70
N-86.80	86.8	68.13
N-90.90	90.9	63.42
SW-75.70	75.7	73.84
SW-90.20	90.2	72.91
SW-103.00	103	72.17
SW-110.40	110.4	72.65
SW-115.60	115.6	73.42
SW-121.70	121.7	75.23
SW-130.80	130.8	74.10
SS-42.30	42.3	63.67
SS-47.0	47	63.32
SS-51.50	51.5	66.27
SS-58.40	58.4	65.66
SS-67.30	67.3	65.98
SS-76.70A	76.7	85.29
SS-76.70B	77	67.93
SS-79.80	79.8	69.68
SS-86.40	86.4	84.62
SS-89.70	89.7	76.76
SS-96.70	96.7	78.13
SS-99.00	99	96.01

Bottom diamictite		
Sample	**Depth (m)**	**CIA**
N-178.80	178.8	98.01
N-182.60	182.6	72.36
N-223.80	223.8	69.85
N-277.00	277	72.27
S-145.70	145.7	99.03
SW-187.90	187.9	71.69
SS-141.80A	141.8	66.01
SS-141.80B	142	68.69
SS-149.00	149	66.62
SS-156.10	156.1	67.30
SS-163.50	163.5	75.52

B10. Diamictite geochemical relationships

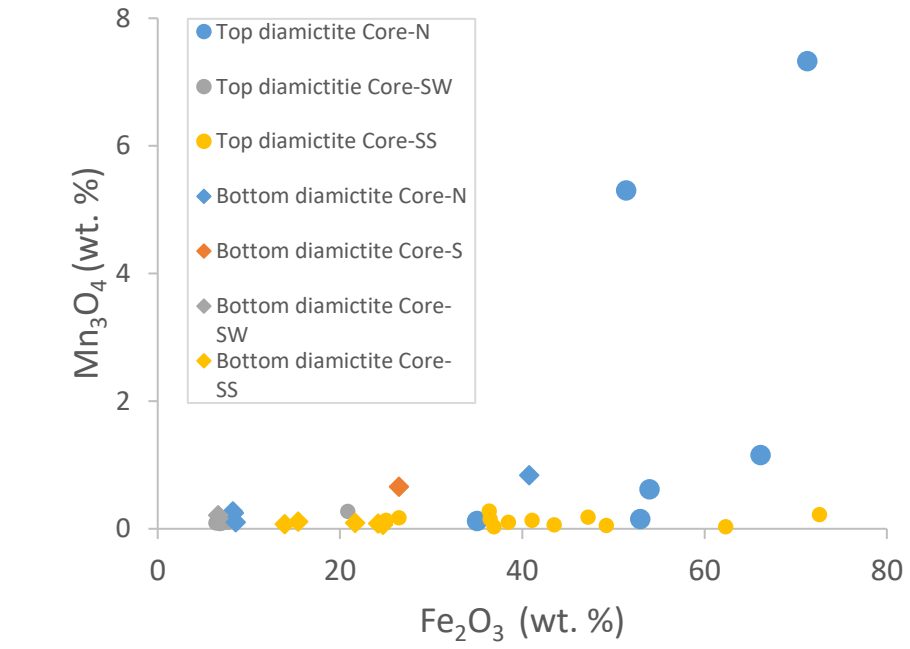

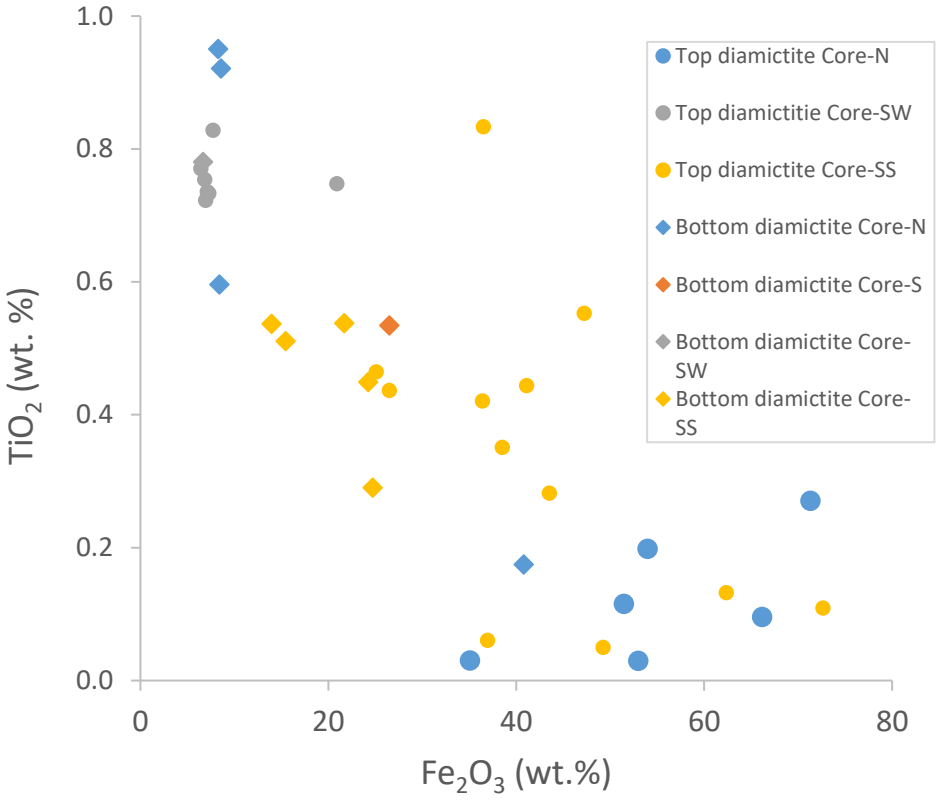

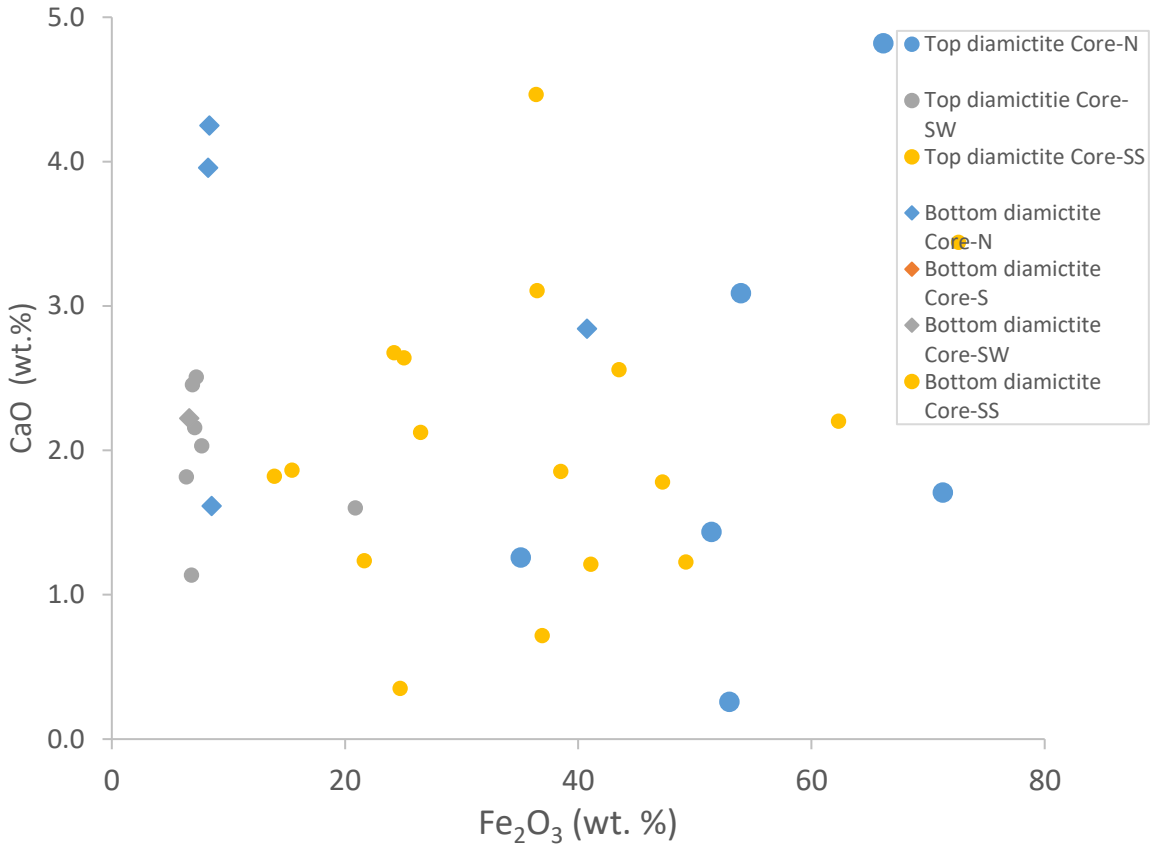
5.0
4.0
3.0
2.0
1.0
0.0
CaO (wt.%)
0
20
40
60
80
Fe2O3 (wt. %)
Top diamictite Core-N
Top diamictitie Core-SW
Top diamictite Core-SS
Bottom diamictite Core-N
Bottom diamictite Core-S
Bottom diamictite Core-SW
Bottom diamictite Core-SS

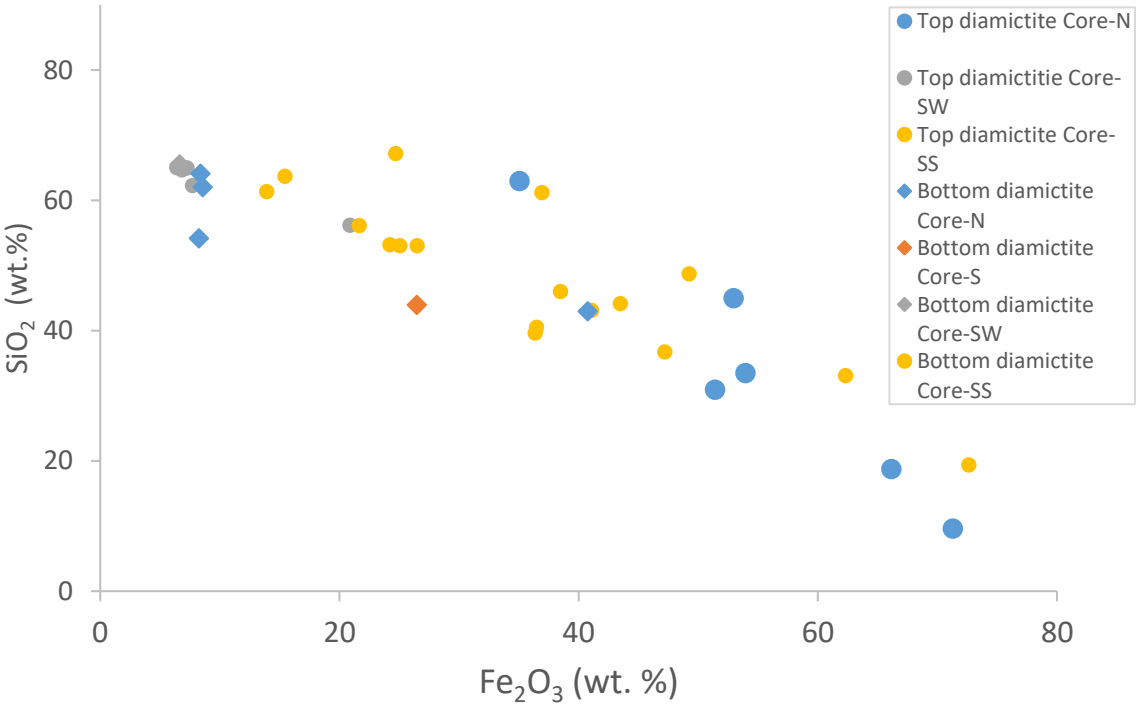
80
60
40
20
0
SiO2 (wt.%)
0
20
40
60
80
Fe2O3 (wt. %)
Top diamictite Core-N
Top diamictitie Core-SW
Top diamictite Core-SS
Bottom diamictite Core-N
Bottom diamictite Core-S
Bottom diamictite Core-SW
Bottom diamictite Core-SS

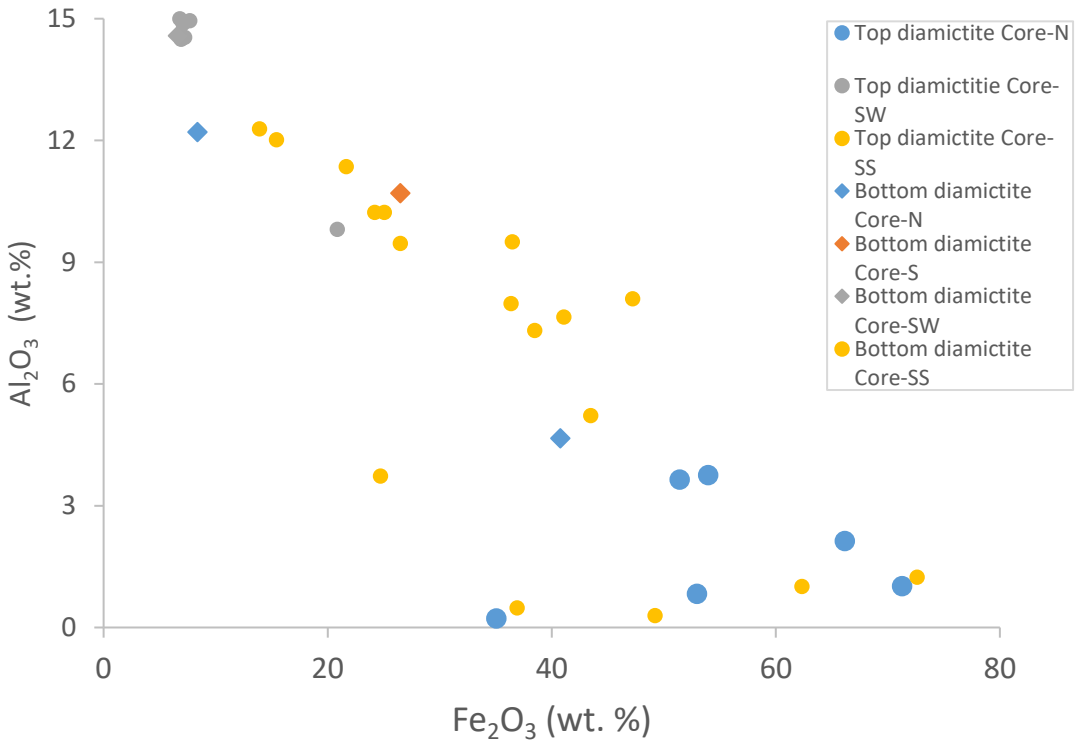
15
12
9
6
3
0
0
20
40
60
80
Al_2O_3 (wt.%)
Fe_2O_3 (wt. %)
Top diamictite Core-N
Top diamictitie Core-SW
Top diamictite Core-SS
Bottom diamictite Core-N
Bottom diamictite Core-S
Bottom diamictite Core-SW
Bottom diamictite Core-SS

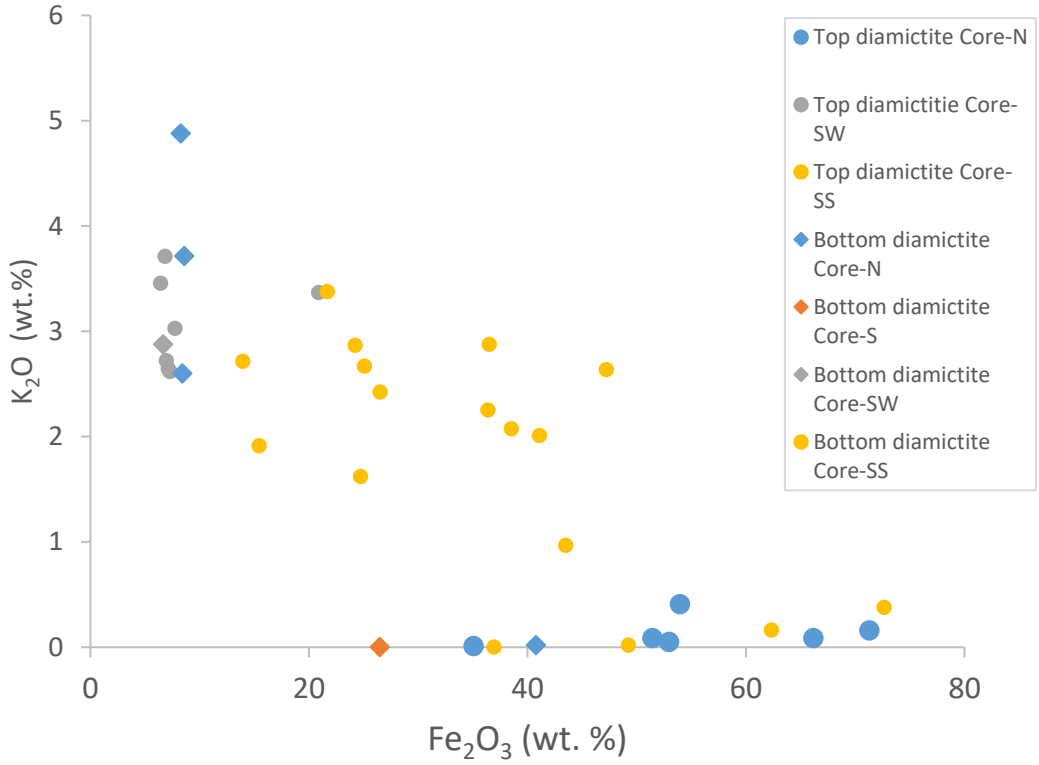
6
5
4
3
2
1
0
0
20
40
60
80
K_2O (wt.%)
Fe_2O_3 (wt. %)
Top diamictite Core-N
Top diamictitie Core-SW
Top diamictite Core-SS
Bottom diamictite Core-N
Bottom diamictite Core-S
Bottom diamictite Core-SW
Bottom diamictite Core-SS

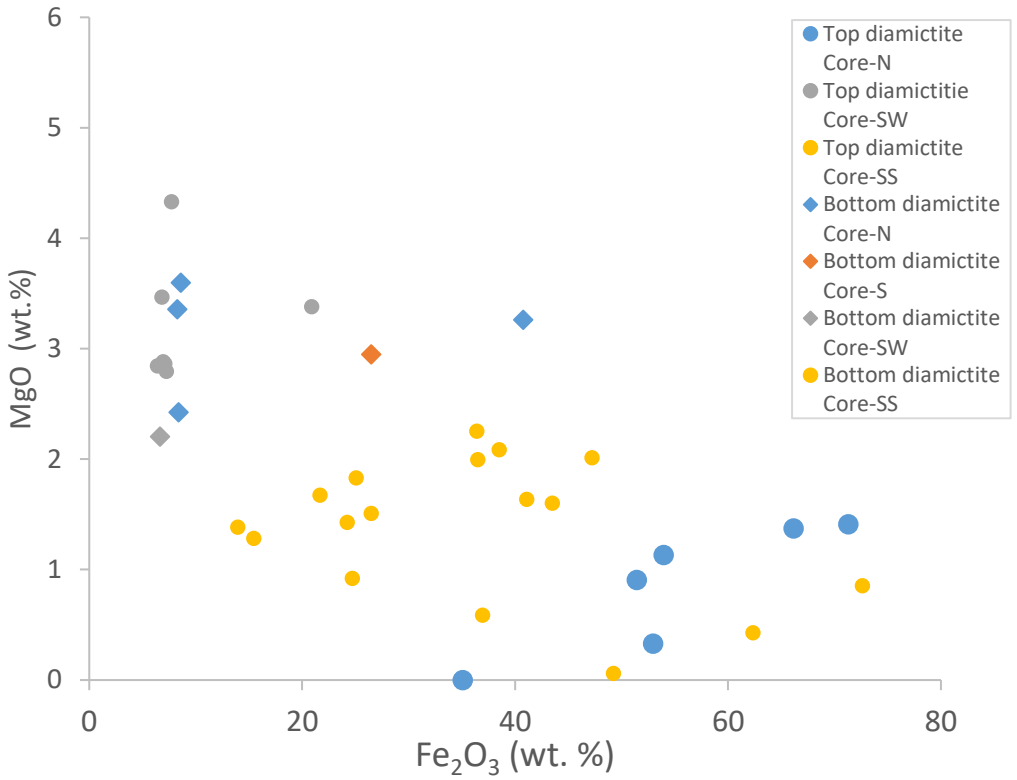
MgO (wt.%)
Fe_2O_3 (wt. %)
Top diamictite Core-N
Top diamictitie Core-SW
Top diamictite Core-SS
Bottom diamictite Core-N
Bottom diamictite Core-S
Bottom diamictite Core-SW
Bottom diamictite Core-SS

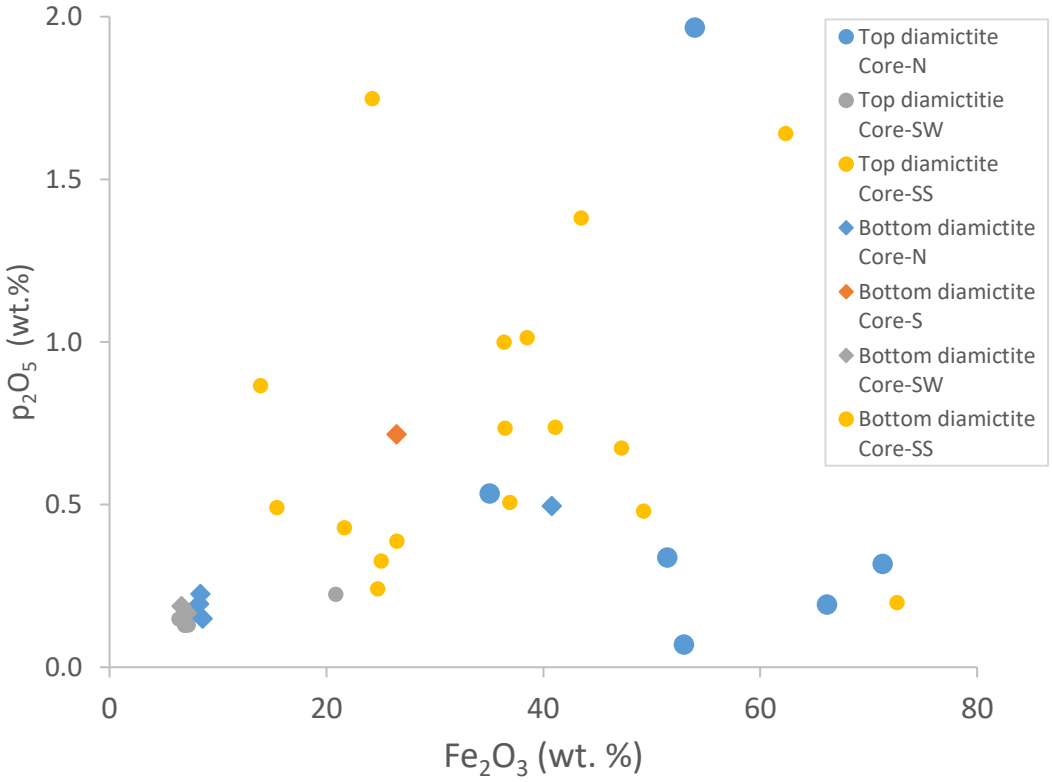
p_2O_5 (wt.%)
Fe_2O_3 (wt. %)
Top diamictite Core-N
Top diamictitie Core-SW
Top diamictite Core-SS
Bottom diamictite Core-N
Bottom diamictite Core-S
Bottom diamictite Core-SW
Bottom diamictite Core-SS

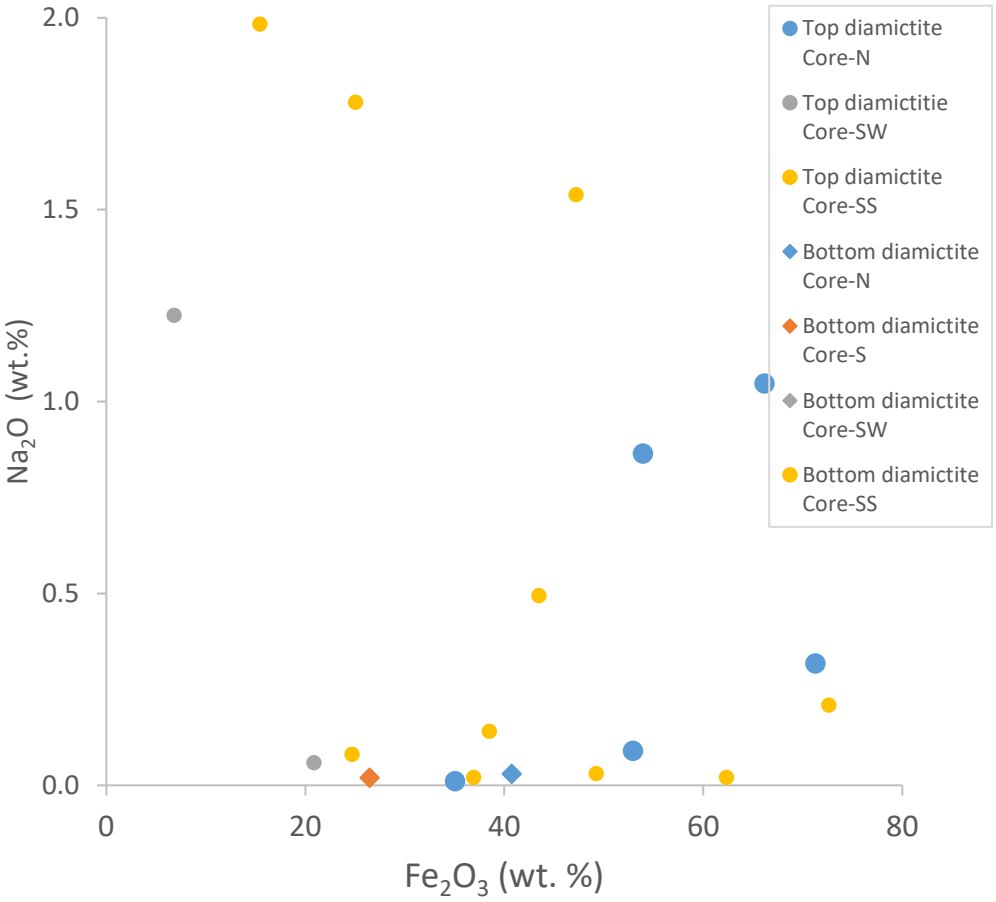
2.0
1.5
1.0
0.5
0.0
Na_2O (wt.%)
0
20
40
60
80
Fe_2O_3 (wt. %)
Top diamictite Core-N
Top diamictitie Core-SW
Top diamictite Core-SS
Bottom diamictite Core-N
Bottom diamictite Core-S
Bottom diamictite Core-SW
Bottom diamictite Core-SS